



School of Systems Engineering

**Estimation of Magnet Separation for Magnetic
Suspension Applications**

by

Maxwell Parfitt

Thesis submitted for the degree of Doctor of Philosophy

**PhD in Computer Science
School of Systems Engineering**

June 2013

University of Reading

Dedication

This entire work is dedicated to my Grandfather Ian Gow who sparked my interest in Engineering at an early age, by letting me join him in his workshop and setting me mechanical problems to solve.

He taught me many of the processes, that I used for the testing rig manufacture, described in this thesis.

For all that he has done for me, he has my eternal gratitude!

Abstract

This thesis describes a form of non-contact measurement using two dimensional hall effect sensing to resolve the location of a moving magnet which is part of a ‘magnetic spring’ type suspension system. This work was inspired by the field of Space Robotics, which currently relies on solid link suspension techniques for rover stability. This thesis details the design, development and testing of a novel magnetic suspension system with a possible application in space and terrestrial based robotics, especially when the robot needs to traverse rough terrain. A number of algorithms were developed, to utilize experimental data from testing, that can approximate the separation between magnets in the suspension module through observation of the magnetic fields. Experimental hardware was also developed to demonstrate how two dimensional hall effect sensor arrays could provide accurate feedback, with respects to the magnetic suspension modules operation, so that future work can include the sensor array in a real-time control system to produce dynamic ride control for space robots. The research performed has proven that two dimensional hall effect sensing with respects to magnetic suspension is accurate, effective and suitable for future testing.

Original Authorship

I confirm that this is my own work and the use of all material from other sources has been properly and fully acknowledged.

Maxwell Ralph Parfitt

17th June 2013

Acknowledgments

I would like to acknowledge both of my supervisors, Dr Gerard McKee for helping start my journey into a PhD and Professor William Harwin for his help to finish the PhD and draw together my research.

I would also like to thank the support and technical staff at the University of Reading, who helped take my designs from the drawing board and into the real world for testing.

I would like to thank my girlfriend Noeleene Mallia for her unending patience and dedicated proof reading services, without her help I would never have finished!

Thanks to my family, who in their own special way, have motivated me to complete my research.

To everyone else who has helped along the way, my deepest thanks!

Table of Contents

Dedication	ii
Abstract	iii
Acknowledgments	v
Table of Contents	x
List of Tables	xi
List of Figures	xix
Nomenclature	xx
1 Introduction	1
1.1 Background and Motivation	2
1.1.1 Suspension Systems used in Space Robotics	3
1.2 Research Aims	4
1.3 Research Methodologies	4
1.4 Research Contributions	6
1.5 Thesis Structure	6

2	Literature Review	9
2.1	Uses of Suspension	10
2.1.1	History of Suspension	10
2.1.2	Review of Modern Suspension Designs	11
2.2	Space Robotics	17
2.2.1	Suspension used in Space Robotics	17
2.3	Space robotics environmental considerations	29
2.3.1	Temperature Cycling	29
2.3.2	Gravity	30
2.3.3	Space	32
2.3.4	Dust and Wind	32
2.3.5	Atmospheric Pressure	34
2.3.6	Radiation	35
2.4	Permanent Magnet and Electromagnetic Systems	36
2.5	Summary	42
3	Theory	44
3.1	Magnetic field theory	45
3.1.1	Maxwell equations	45
3.1.2	Lorentz force law	47
3.1.3	Magnetic dipole moment	48
3.1.4	Current loop equations	48
3.1.5	Far field approximations	49
3.2	Force between magnets	50
3.2.1	Magnetic dipole force in a magnetic field	50
3.2.2	Gravity analogue equations	50
3.2.3	Gilbert Model for Magnetic Repulsion Force	51

3.3	Sensor calibration using a Helmholtz coil	52
3.3.1	Helmholtz coil Derivation	53
3.3.2	Helmholtz coil specifications	56
3.4	Hall Effect Sensing	58
3.5	Magnetic field measurement using a 2D Hall Effect Array	60
3.6	Chapter Summary	61
4	Magnetic Simulations & Validation Experiments	63
4.1	Simulation Types and Accuracy	66
4.1.1	Types of Simulation	67
4.1.2	Meshing and Solver Accuracy	68
4.1.3	Boundaries and Boundary Conditions	70
4.2	Simulation of a Single ID54 Magnet	71
4.3	Simulations of two ID54 Magnets	76
4.4	FEMM of Helmholtz coil	78
4.5	Chapter Summary	79
5	Experimental Setup	81
5.1	Sensor Calibration	81
5.2	Experimental Rig Development	84
5.2.1	Test Rig 1	84
5.2.2	Test Rig 2	87
5.2.3	Test Rig 3	92
5.3	Final Hardware Design for Data Capture	96
5.3.1	TR4 Hardware	97
5.3.2	TR4 Software	103
5.3.3	TR4 Experimental Setup and Configuration	113

5.4	Chapter Summary	117
6	Results and Analysis of Experimental Data	119
6.1	Sensor Calibration	120
6.2	Experimental Testing Rigs	121
6.2.1	Test Rig 1	121
6.2.2	Test Rig 2	127
6.2.3	Test Rig 3	130
6.3	Final Testing Rig TR4	133
6.3.1	Single magnet calibration swing from guide tube end	134
6.3.2	Single magnet calibration swing from mechanical limit	138
6.3.3	Results after data calibration	141
6.3.4	Dual magnet suspension results	144
6.4	Curve Fitting	151
6.5	Magnet Separation Algorithm Development	153
6.6	Magnet Separation Algorithm Results	156
6.7	Chapter Summary	169
7	Conclusion & Future Work	171
7.1	Main Findings	171
7.1.1	TR1 and Gilbert Model conclusions	172
7.1.2	FEMM magnetic field modeling conclusion	173
7.1.3	Magnet Separation Algorithm Conclusions	174
7.2	Contributions	175
7.3	Limitations of Work	178
7.3.1	Possible improvements to Hardware	178
7.3.2	Possible improvements to Software	179

7.3.3	Testing in a ‘Space’ environment	180
7.4	Future Work	181
	Bibliography	182
	Appendices	195
A	Helmholtz Coil Full Derivation	195
B	Helmholtz Coil Manufacture	199
C	Single Hall Effect sensor calibration using a Helmholtz Coil	206
D	Group Calibration of Sensors	208
E	Simulink models for data capture	216
F	Test Rig 4 SolidWorks models for manufacture	219
G	Work log for the manufacture of Test Rig 4	230
H	TR4 Circuit and PCB	242
I	Published paper from ASTRA 2011 conference proceedings	247
J	Published poster presentation from ASTRA 2011 conference	254

List of Tables

2.1	Comparison between planets in our solar system	31
3.1	Comparison of Standard Wire Gauge (SWG) characteristics	57
4.1	Comparison between simulated and measured results, where X_{mm} denotes the Probe position from the magnets central axis in mm , M_{mT} is the measured magnetic field strength in mT and F_{mT} is the simulated magnetic field strength in mT from FEMM	76
5.1	Properties of magnets used with TR1	85
5.2	PIC18F87K22-I ADC channel configuration	106
5.3	Files used for calibration and data analysis	111
6.1	6 th order polynomials of the magnets used with TR1	123
C.1	Table showing the Magnetic Field Strengths in Tesla (T) with respects to Displacement (mm). Column headings: Dis (Displacement), FEMM (FEMM Software), Cal (Calibrated Hall Probe) and SS49E (SS49E Sensor)	207
D.1	Hall Effect Sensor Data for Group Calibration	215
H.1	Bill of materials for TR4 PCB	243

List of Figures

1.1	Rocker-Bogie suspension wheel positions on different terrain profiles [1]	3
1.2	A cybernetics approach to meeting design goals and evaluating research	5
2.1	Leaf-spring suspension system (dimensions in inches)	10
2.2	Torsion Bar Suspension Diagrams	11
2.3	Nylon torsion bar on robotic test platform	12
2.4	Constant and Progressive pitch coil springs	13
2.5	The AUDI Semi-Active magnetically damped suspension system [2]	14
2.6	Normal air ride seat suspension response compared to the active Bose Ride suspension system [3] for a single bump and a 100 yards traveled along a road	16
2.7	Original drawing from the Bickler Rocker-Bogie patent [4]	18
2.8	Different applications of Whiffletrees	19
2.9	Second World War Navy PV-1 Balance Computer [5]	20
2.10	Rocker-Bridge latch pawl of the MER mobility system used to lock the rocker-bogie during deployment [6]	21
2.11	NASA MER and ExoMars Spoked Wheel Designs	22
2.12	Six of the seven suspension concepts tested [7]	23
2.13	ExoMars Flexible Wheel Design [8]	24
2.14	NASA ATHLETE mobility system [9]	25

2.15	Six wheel radius turning used in Rocker-Bogie chassis designs [10]	27
2.16	High speed bogie lifting $\approx 1m/sec$ [11]	28
2.17	Ground and air temperature variations over a two Sol period (Data from NASA/JPL-Caltech/CAB)	30
2.18	Wind direction and pressure data from Sol 75 (Data from NASA/JPL-Caltech/CAB)	33
2.19	Pressure variations experienced on the Martian surface (Images from NASA/JPL-Caltech/CAB/Ashima Research/SWRI)	34
2.20	Atmospheric pressure variation and radiation exposure over a five Sol period (Data from NASA/JPL-Caltech/CAB)	35
2.21	Inner workings of the High-Performance Magnetic Gear [12]	37
2.22	Inner workings of a Magnetic Clutch [13]	39
2.23	Response of two permanent magnets in repulsion: two blocks of barium ferrite, $15 \times 10 \times 2.5cm$, at rest position $3.5cm$ gap [14]	40
2.24	Biologically Inspired Ant Research - LabANT [15]	42
3.1	Magnetic dipole field representation around a small current loop, plotted using VectorFieldPlot (VFPlot) [16]	46
3.2	Fields associated with a current loop	49
3.3	Gravity analogue for force between two magnetic poles	51
3.4	Two concentric cylindrical permanent magnets held so that the bottom magnet is fixed and the top magnet can only move in the z-axis	52
3.5	Magnetic field on the axis of a circular current	53
3.6	Graph showing magnetic field strength of B_1 , B_2 and full Helmholtz coil	55
3.7	Dimensions for a Helmholtz coil with respect to equation 3.25	56
3.8	Hall effect sensing system diagram	59

3.9	The four possible hall effect results from varying the magnetic field and current directions	60
4.1	Simulation of a rubber ball on a solid flat surface	64
4.2	Grid types used in simulations	69
4.3	Comparison between unstructured 2D and 3D meshes	69
4.4	Comparison between discretized and irregular boundary representation	70
4.5	ID54 Simulation model with the different solver approaches	72
4.6	Comparison between the Planar and Asymmetric solutions	73
4.7	Comparison between the FEMM simulation and measured results . . .	74
4.8	FEMM model for the dual ID54 magnet simulations	77
4.9	FEMM simulation results for magnet separations: 40mm, 20mm and 0mm	78
4.10	Model and simulation results for the Helmholtz coil	79
5.1	3D Printed Helmholtz bobbin and Helmholtz coil	83
5.2	Hall effect probe displacement test of the Helmholtz coil	84
5.3	Various size magnets mounted in Delrin holders for TR1	86
5.4	Load Cell with TR1 in place ready for experimentation	87
5.5	Diagram showing dimensions of plastic used for TR2	89
5.6	First edition Hall Sensor Array for TR2	90
5.7	Second edition of TR2 sensor placement	90
5.8	Algorithm idea to find midpoint between magnetic fields	91
5.9	TR3 showing the connections, veroboard mounting and close up of the sensors super glued into a custom CNC machined profile	93

5.10	Virtual x and y axis sensing point of TR1, TR2 and TR3 using y axis sensor group 1 compared to the no shift sensing point in TR3 using y axis sensor group 2	94
5.11	The TR3 module connected to 3 Quanser data capture cards	95
5.12	TR4 top and side elevations showing the ADC PCB attached to sensors	97
5.13	The TR4 PCB design sent for manufacture	100
5.14	The TR4 PCB after manufacture and testing	101
5.15	Positions of hall effect sensors when mounted on testing rig	102
5.16	Push pin calibration board attached to the data capture module	103
5.17	Application of the C18 code to count turns going onto the 3D printed Helmholtz coil bobbin	104
5.18	The custom TR4 data logging user interface written in C#	107
6.1	FEMM simulation of field magnitude (in Tesla) plotted against mea- surement point displacement from center of the Helmholtz coil (in mm) with experimental results for the calibrated hall probe and the SS49E hall effect sensors	120
6.2	Comparison curves showing separation between magnet faces (mm) plotted against magnetic field strength (in Tesla) for the 8 magnets tested with TR1; ID17, ID20, ID21, ID23, ID34, ID43, ID44 & ID54 . .	122
6.3	Polynomial curve fit of the ID17 and ID54 magnet repulsive force profiles	124
6.4	Comparison between the ID54 real world data and the Gilbert Model for magnetic repulsion	125
6.5	Comparison between the 8 magnets tested with TR1	126
6.6	Results from magnetic separation algorithm for the first version of TR2	128
6.7	Results from magnetic separation algorithm for the second version of TR2	129
6.8	Plots showing all 24 data channels recorded by TR3	132

6.9	Raw voltage data from TR4's 24 sensor channels when a single magnet is passed through the TR4 guide tube	136
6.10	Data from the first single magnet calibration experiment with the raw voltage values converted into Gauss	137
6.11	Raw voltage data from TR4's 24 sensor channels when a single magnet is passed through the TR4 guide tube from the mechanical testing limit	139
6.12	Data from the second single magnet calibration experiment with the raw voltage values converted into Gauss	140
6.13	Comparison between the raw data (shown as dotted lines) and the calibrated and scaled data (the solid lines) from the first single magnet calibration experiment	142
6.14	Comparison between the raw data (shown as dotted lines) and the calibrated and scaled data (the solid lines) from the second single magnet calibration experiment	143
6.15	Video stills from Matlab showing magnet separation, measured magnetic field magnitude and angle at each sensor group	146
6.16	Graph showing TR4 experimental data with the fixed magnets exposed face located at sensor zero	147
6.17	Graph showing TR4 experimental data with the fixed magnets exposed face at sensor zero plus $1.05mm$	148
6.18	Graph showing TR4 experimental data with the fixed magnets exposed face at sensor zero plus $5mm$	149
6.19	Graph showing TR4 experimental data with the fixed magnets exposed face at sensor zero plus $6.05mm$	150
6.20	Matlab plot of a single y-axis data channel, with the zero crossing selected and a line tangent plotted at that point	151

6.21	Far field fit approximation of real world data using gradient at x-axis crossing point	152
6.22	Calculated results of magnet location algorithm plotted against expected results for the first experimental data run with TR4	158
6.23	Calculated results of magnet location algorithm plotted against expected results for the second experimental data run with TR4	159
6.24	Calculated results of magnet location algorithm plotted against expected results for the third experimental data run with TR4	160
6.25	Calculated results of magnet location algorithm plotted against expected results for the fourth experimental data run with TR4	161
6.26	Calculated magnetic field midpoints for sensor group pairs, overlay of original algorithm separation prediction (blue line) and expected data (red line)	161
6.27	Calculated magnetic field midpoints for all sensor groups, overlay of original algorithm separation prediction (blue line) and expected data (red line)	162
6.28	Curves produced through analysis of field angle at known sensor loca- tions and displacement of the free moving magnet	163
6.29	Diagram showing the parameter names used in equations 6.10 - 6.13 to modify the far-fit magnetic algorithm and determine field angles at defined points along the x-axis, y-axis with known magnet separation .	164
6.30	Curves produced by Matlab function, <code>angfun(x,y,S)</code> , for the sensors distributed along the x-axis with respects to the field angle for a range of magnet separation displacements	166
6.31	Clarified view of S-shaped curves for $10mm$ increments ranging from 0 to $60mm$	167

6.32	Clarified view of S-shaped curves for 10mm increments ranging from 61mm to 100mm	168
A.1	Graph showing magnetic field strength of B_1 , B_2 and full Helmholtz coil	197
B.1	3D Printing of the Helmholtz coil bobin	199
B.2	Rotation counting using a magnet attached to the lathes chuck and a SS49E sensor	201
B.3	Fully wound Helmholtz coil after wire turns had been added to the 3D printed bobin	202
B.4	Coil counting display built on a PIC development board to process the analog input from the SS49E sensor	203
B.5	Translation stage and experimental setup to move the hall sensing devices through the Helmholtz coil	204
B.6	Close up of Calibrated hall probe within the Helmholtz coil	205
C.1	FEMM simulation and Hall Effect measurements of the Helmholtz Coil	206
D.1	Plot of 24 ADC channels provided voltage against voltage measured after group calibration test	215
E.1	TR2 Data logging Simulink model	216
E.2	TR3 Data logging Simulink model	217
E.3	TR3 analog input handling Simulink model	218
G.1	Raw material used for the construction of Test Rig 4	231
G.2	The lathe used for manufacture with acrylic being turned	231
G.3	Acrylic tube after preparation with lathe	232
G.4	The cutting jig to hold the guide tube in the CNC milling machine during cutting	232

G.5	Guide tube in cutting jig ready for the first profile to be machined . . .	233
G.6	Cutting the first profile into the guide tube	234
G.7	The guide tube after the first program had been completed	234
G.8	Guide tube during the second and third cutting profile programs	235
G.9	Guide tube after the second and third cutting profile programs	235
G.10	The guide tube after machining and washing to remove coolant and swarf	236
G.11	Manufacturing one of the TR4 magnet holders from Delrin	236
G.12	Measurement to insure the magnet holder matches design tolerances . .	237
G.13	The cleaner the surface of the Delrin, the lower the friction	237
G.14	Location hole positioned through the magnet holder	238
G.15	Magnet holder located within the guide tube	239
G.16	Component parts of TR4	239
G.17	TR4 magnet holder with magnet and side view of guide tube with both magnet holders mounted	240
G.18	TR4 with sensors mounted on the guide tube	241
H.1	TR4 Data capture, processing and transfer Schematic	244
H.2	TR4 PCB with ground planes (Top Layer, Red, Bottom Layer, Blue) .	245
H.3	TR4 PCB with no ground planes (Top Layer, Red, Bottom Layer, Blue)	245
H.4	TR4 PCB after population with components	246

Nomenclature

The following abbreviations and terms used in this Thesis are included here in alphabetical order.

Mathematical Notation Used

Δv	Thrust required to accelerate against gravity
\mathbf{B}	Magnetic field
\mathbf{E}	Electric field
\mathbf{H}	Magnetizing field
s	Any closed surface
$d\mathbf{A}$	A vector normal to the direction of the magnetic field with a tiny magnitude
\oint_C	A line integral around a closed curve C
\int_S	A 2D surface integral over S enclosed by C
$d\mathbf{l}$	A differential of curve C
\mathbf{J}	Total current density
$\nabla \cdot$	Magnetic field divergence
$\nabla \times$	The curl operator
F	Force

q	Point charge
\mathbf{v}	Velocity
$\underline{\mathbf{m}}$	Magnetic dipole moment
p	Magnetic pole strength
ℓ	Vector separating the poles in a magnetic dipole
\hat{r}	Unit radial vector
\hat{a}	Unit vector normal to a current loop
μ	Permeability of the surrounding medium
μ_0	The permeability of free space ($4\pi \times 10^{-7} \approx 1.257 \times 10^{-6} \text{ T}\cdot\text{m/A}$)
$q_{m_{PoleNumber}}$	Magnetic pole strength for the pole: $m_{PoleNumber}$
x	Displacement or separation (Meters)
R	Magnet Radius (Meters)
t	Magnet Thickness (Meters)
M	Magnetic Field (Direction arrow shown)
B	Magnetic Field Strength (Tesla T)
V	Voltage (Volts V)
\mathbf{R}	Resistance (Ohms Ω)
I	Current (Amperes A)
n	Number of complete wire turns in a coil
ρ	Resistivity of a Conductor per meter ($\Omega \cdot m$)
\underline{n}	Magnetic North Seeking Pole
\underline{s}	Magnetic South Seeking Pole
T_g	Glass Transition Point of a thermoplastic
T_m	Melting Transition Point of a thermoplastic

Abbreviations Used

2D	Two Dimensional
2.5D	Two and a Half Dimensions
3D	Three Dimensional
7-SEG	Seven Segment Display
ABS	Acrylonitrile butadiene styrene
ADC	Analog to Digital Converter
ATHLETE	All-Terrain Hex-Limbed Extra-Terrestrial Explorer
BAT	Battery
CAD	Computer Aided Design
Caltech	California Institute of Technology
CAM	Computer Aided Manufacture
CCD	Charge Coupled Device
CNC	Computer Numerically Controlled
CSV	Comma Separated Values data file
CTS	Clear to Send - UART Flow Control
DAC	Digital to Analog Converter
DC	Direct Current
DXF	Drawing Exchange Format
EDL	Entry Decent and Landing
EEPROM	Electrically Erasable Programmable Read Only Memory
EMF	Electromotive force
ESA	European Space Agency
FEA	Finite Element Analysis
FEM	Finite Element Method

GUI	Graphical User Interface
I/O	Input / Output
LPM	Locomotive Performance Model
MER	Mars Exploration Rover
MSL	Mars Science Laboratory
NASA	National Aeronautics and Space Administration
NCMG	Non-Contact Magnetic Gear
NdFeB	Neodymium
PC	Personal Computer
PCB	Printed Circuit Board
PDD	Pseudo Direct Drive from Magnomatics
PIC	Programmable Interface Controller
PVA	Polyvinyl alcohol
RAM	Random Access Memory
RGB	Red, Green, Blue color values
RTG	Radioisotope thermoelectric generator
RTS	Request to Send - UART Flow Control
RX	Receive
SmCo	Samarium-Cobalt
Sol	Martian Day
SPP	Serial Port Profile
SSE	School of Systems Engineering, University of Reading
TX	Transmit
UART	Universal Asynchronous Receiver / Transmitter
WEB	Warm Electronics Box

Chapter 1

Introduction

The need to transport objects and people across terrain has always been hampered by rough surfaces and difficulty in adapting machines to the natural environment. This thesis proposes a novel suspension solution with low friction and integrated displacement measurement. The suspension mechanism develops earlier work by Richard McElligott [15] which considers magnets in repulsion. The displacement measurement is based on resolving the magnetic field angles that surround two identical magnets that have been placed in repulsion and locked to a common axis of travel, using two dimensional hall effect sensing and novel algorithms.

The current state of suspension systems used in space robotics motivated the research as current solutions have major limitations which could be improved. The solution developed would require additional considerations such as operation under low pressures, transit through the vacuum of space, thermal cycling due to sun exposure, radiation exposure due to reduced atmospheric protection and power consumption before it could be considered for space applications, however it has had limited testing on Earth based mobile robots [15].

Mobile robotics has been a rapidly growing field of research since the early 1950's,

when W. Grey Walter created machines [17] he called turtle robots. These robots were capable of responding to external light sources and exhibited what he called “free will” [18]. Over the next 30 years mobile robots became larger but remained mainly tethered to mainframe computers, such as ‘Shakey’ from the Stanford AI lab [19], which reduced their maneuverability. The size and design of these robots meant that they were limited to a laboratory environment, due largely, to a lack of adaptability in their mobility systems. Further advances in robotic hardware and software design came in the 1980’s, with the Stanford Cart [20], when faster computers and more flexible robot chassis designs meant that mobile robots could leave the laboratory and enter the real world. It was now only a matter of time before mobile robots could carry enough processing power and equipment to become useful scientific tools for use here on Earth and for planetary exploration.

This thesis contains a variety of mathematical symbols, notations and abbreviations that support the research performed, which are described in the Nomenclature section, page number xx.

1.1 Background and Motivation

Space exploration rovers such as the NASA MER [21], NASA MSL [22] and ESA ExoMars [23] currently have their top speed limited to around 10cm/s to reduce the impact forces experienced when the rovers wheels come into contact with an obstacle [11], as well as enabling object avoidance vision processing to be completed for route planning without having to constantly stop the rovers motion whilst driving. If rovers are ever to move faster on the surface of other planets it is necessary to reduce the force experienced when traversing objects, such as rocks, thus protecting the scientific payload and rover mobility systems from damage.

1.1.1 Suspension Systems used in Space Robotics

The current space exploration rover designs that are being used by NASA and the ESA all use solid linkage suspension based on the Rocker-Bogie mobility system that was designed and patented by Donald Bickler [4] in 1989. The Rocker-Bogie suspension maintains a relatively constant weight and therefore traction on all wheels, even if one wheel is substantially higher or lower than the others. There is no need for a soft spring type suspension in this configuration, which is very important in space robotics, as designs try to maximize the robots traction between the wheels and the surface that it is traversing. The body of the rover is connected to a pivot joint, so the rovers body will only rise and fall a fraction of the amount that an individual wheel does, which is demonstrated in figure 1.1 with the blue box representing the rovers body.

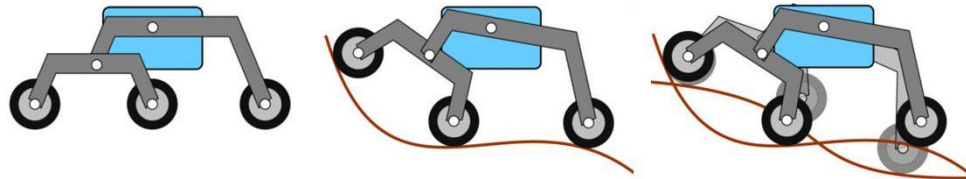


Figure 1.1: Rocker-Bogie suspension wheel positions on different terrain profiles [1]

The solid link rocker-bogie suspension is simple to model and construct as there are no actively controlled or powered joints once they have locked into place during deployment [6], but the major drawback with solid link suspension is that impact forces and high frequency vibrations transfer through the chassis of the rover to the electronics and science equipment which could cause damage. To try and compensate NASA introduced spoked wheels that could flex under load, to give some compliance and soften the ride, but these wheels can only do so much and thus the top speed of the rover is limited.

This begs one of the questions that is addressed by this thesis:

- *What can be done to isolate a system from mechanical impacts and vibrations?*

1.2 Research Aims

The research aims can be articulated through the following questions.

Research Questions:

- (1) *Can the magnetic ‘spring’ effect be measured and analyzed accurately?*
- (2) *Can a good analytical model be found to define the magnetic spring characteristics?*
- (3) *Could the magnetic ‘spring’ effect be utilized in suspension systems for space robotics to increase the space rovers capability?*
- (4) *Can the current inaccuracy in single magnet localization using Hall Effect sensing be improved by employing more sensors or by changing the sensing orientation?*
- (5) *Is there a way to accurately localize two magnets using Hall Effect sensing and thus accurately know their separation?*

The aim of this thesis is to demonstrate how magnetic compliance can be applied to any mobility system. It has been specifically targeted at the field of Space Robotics which motivated this research, to enable faster and smoother traversal over complex terrains, without transferring excessive forces and high frequency vibrations through to either a passenger or a rovers payload.

1.3 Research Methodologies

This research is targeted towards the development of a new measurement system, which can be used in partnership with magnetic compliance suspension, to determine suspension displacement with novel non-contact techniques and algorithms. The research was performed in parallel streams, such that after each stage of development

the results from both analytical models and physical measurements, recorded through experimentation, could be directly compared.

The ideal solution for the development of the experimental hardware would have been to create extensive computational models before physical development was started, but due to time constraints this was performed in parallel to the physical design, as this allowed for confirmation of the computer models through direct testing on the hardware. This approach ensured that the computational models were accurate to the experimental ground truth, whilst confirming the suspension measurement system operated as expected. Additional computer modeling was performed using commercial FEA and FEM software packages, to add a third system to test results against, thus confirming experimental data along with the algorithms developed to determine the suspension systems displacement.

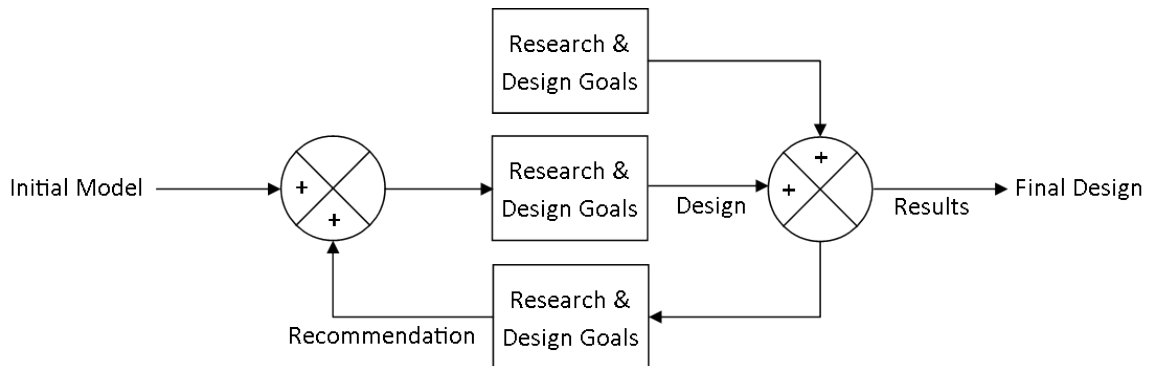


Figure 1.2: A cybernetics approach to meeting design goals and evaluating research

The research therefore followed the classic approach used in feedback theory, where the initial model ideas are the input to the system, which pass through the design process to provide results, which were compared against the expected project goals. This comparison created the feedback that could improve the model through further development, with the final result emerging from the system after a number of design iterations to meet the project goals, figure 1.2.

With the advancement of research performed the research methods sometimes had to be modified to adapt to the new knowledge created. If the research methods varied significantly due to changes in knowledge, a note was included in the relevant experimentation section, sections 5.1 to 5.3.

1.4 Research Contributions

There are four original research contributions described in this thesis:

- (1) *Analysis of magnetic suspension for use in suspension systems*
- (2) *Algorithm development and testing to calculate separation of two identical magnets through analysis of magnetic fields surrounding the magnets*
- (3) *Creation of experimental testing hardware to validate the magnet separation algorithm*
- (4) *Experimental data generation and analysis using novel techniques*

1.5 Thesis Structure

The structure of this thesis is detailed below, with brief descriptions of chapter content and the key ideas or results found.

Chapter 2 provides a literature review that outlines key papers used to define and support the research performed for this thesis. The papers include historic paradigms that are the basis of equations used and more recent research review papers that describe specific mechanical and hardware systems. Each review includes a short summary of the key points and how they are relevant to this thesis. The chapter ends with a summary of key points and poses some questions that need to be addressed

through the research performed for this thesis.

Chapter 3 outlines the various mathematical approaches and mechanical concepts considered in the research performed for this Thesis. The chapter introduces equations that underpin the research performed in magnetic and electromagnetic systems, such as the Gilbert model for magnetic force calculation.

Chapter 4 describes simulations and system modeling performed to support the research. The software package FEMM is described and this chapter explains how simulations can be affected by model declaration and model accuracy. This chapter also outlines essential experiments to confirm and validate the simulations performed, which ensure that further experimentation is accurately calibrated.

Chapter 5 describes experiment setup to support and confirm the theoretical premise of this thesis. The first section discusses the experimental approach to sensor calibration and goes on to follow the development of three initial testing rigs. The experimentation performed with the initial testing rigs leads onto how the final testing rig evolved from design iterations.

Chapter 6 outlines the main experimentation results, which are described and analyzed, along with curve fitting and algorithm development. The analysis defines choices made for each revision of the experimental testing rigs and includes descriptions of experimental success and shortcomings. The chapter also analyzes the accuracy of the Gilbert model by comparing the expected theoretical and measured real world results. An analysis of the final testing rigs data draws some conclusions on the experimental processes performed. The calibrated data was taken from the final testing rig and curve fitting was conducted to analyze how accurate experimental models are at predicting magnetic fields. The data is also passed through a modified magnet separation approximation algorithm, developed originally for the second test rig, to analyze the algorithms performance at locating a free magnet by measuring the

magnetic fields present in the final testing rig.

Chapter 7 draws the thesis together with discussion on experimental process, data generated and results after data analysis. The magnet location algorithm and data curve fitting are concluded, with insights into possible future uses of the magnet location algorithm and suitability of the data capture hardware. The chapter ends with a review of research questions, to ensure that the expected goals have been achieved by the research performed for this thesis.

Chapter 2

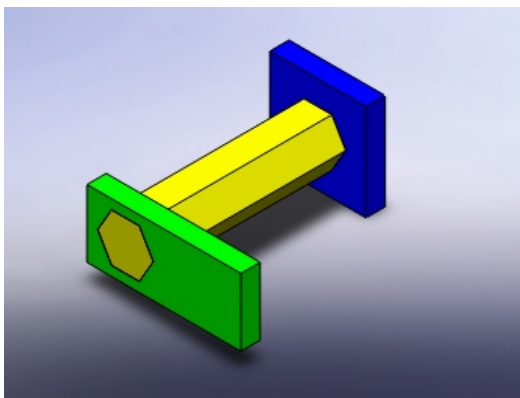
Literature Review

This chapter reviews published material including summaries of key papers that are relevant to the research performed for this thesis. The fields covered include space robotics, mechanical and electromagnetic suspension and mechanical transmission. The chapter begins with a review of suspension systems and their uses, section 2.1, including a brief overview of suspension history and space robotics. The following section looks into space robotics, section 2.2, including the different forms of solid link suspension used by space based rovers. Section 2.3 discusses the environmental considerations for suspension systems and robotics when exposed to the extreme conditions of space travel. This is followed by a review of permanent and electromagnetic suspension systems, section 2.4, along with key references that form the basis for continued research in this thesis. The electromagnetic suspension systems review looks at possible application areas such as electromagnetic bearings, magnetic stirrers, magnetic mechanical transmission, anti-vibration mounts and transport systems. The chapter ends with a summary of key points, section 2.5, which pose questions that need to be answered through the research performed for this thesis.

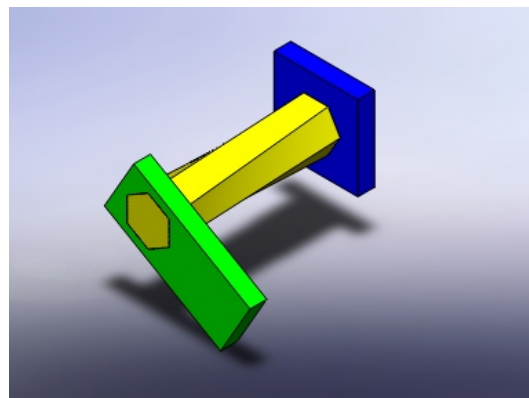
The leaf spring, figure 2.1, is made up from layers of curved metal plates called leaves, which are laminated together and attached to the load at either end by eyes. The wheel mounting is attached to the central bolt and bottom plate so that as the load increases more leaves are flexed to increase suspension force, springing back once the load has been removed. This is a basic type of suspension and requires a lot of force to bend the plates so is normally used for heavy applications that do not require complex linkages, such as truck suspension.

2.1.2 Review of Modern Suspension Designs

Modern suspension techniques rely on more than just metal plates in a leaf-spring configuration, such as torsion bars and coil springs which are more compact and dampers to dissipate energy that would otherwise be transferred through to the load. Torsion bar suspension, figure 2.2, works by twisting a solid bar that has one end fixed to the chassis and the other attached to the input load such as a wheel. The torsion bar experiences a reactive force when a load is applied to the free end of the bar, which can be calculated if the properties of the bar are known, so it can be tuned for the application it is used in.



(a) Torsion bar under no load



(b) Torsion bar with load applied

Figure 2.2: Torsion Bar Suspension Diagrams

Torsion bars are generally heavy as they need a large cross section to support the load applied to the end without warping or snapping and much like the leaf suspension they require a substantial load when made from metal. Experiments have been done with Nylon in place of metal torsion bars in the Space Robotics Lab at Reading University, figure 2.3, but whilst the Nylon could operate with lighter loads it did not have the same operating temperature range as metal and therefore would not be practical for general use. The Nylon torsion bars were fixed to the chassis of a test platform using brass bushing with a pin driven through the bar to stop it from rotating.

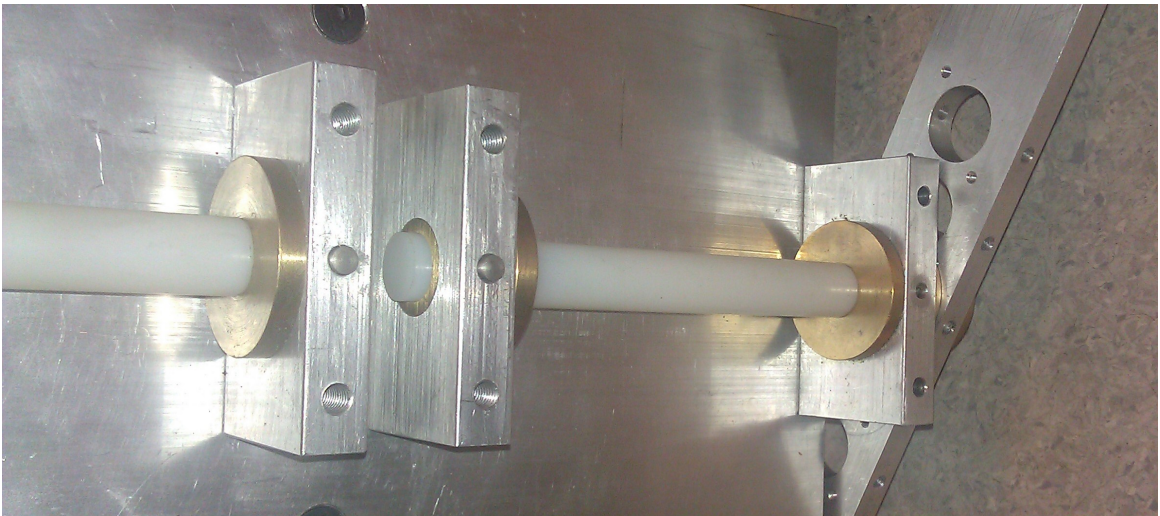


Figure 2.3: Nylon torsion bar on robotic test platform

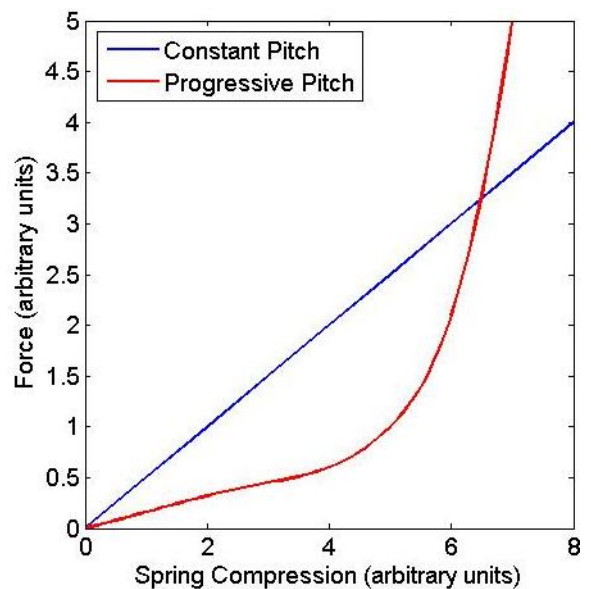
The output end of the Nylon bar was clamped into another brass bushing with a pin to stop rotation, which could be fixed into multiple positions on the suspension arm. This was done so that the same torsion bar could be tested under different operating conditions and loads. Coil springs are more commonly found in modern cars due to their size and performance and operate on the same principle as the torsion bar suspension by introducing a twist to the coils as they are compressed.

Coil springs can have both constant pitch where the coils are equally spaced and thus have a constant force to compression ratio, as well as progressive pitch where the coils

get tighter closer to the end of the spring, figure 2.4. The advantage of progressively wound coils is the force required to compress the spring once the tightly wound coils have become solid, where the coils are touching and therefore not compressing further, is greater. These progressively wound springs are found in most small and medium sized road vehicles that have to account for variable road conditions and cornering effects on the suspension such as mopeds, motorcycles, cars and push bikes with integrated suspension.



(a) Progressive coil springs



(b) Force of constant and progressive pitch springs

Figure 2.4: Constant and Progressive pitch coil springs

All of these suspension systems integrate a damper, also known as a shock absorber or dashpot, to dissipate kinetic energy and smooth the suspensions response to physical displacements. Dampers are essential for controlling the ride quality of a vehicle, as without some form of damping the suspension system would oscillate about its natural frequency causing motion sickness and, more importantly, variable traction between the surface of the road and the tyre which could massively effect the vehicles handling. Damping force is normally generated by restricting the flow of oil past, or through,

a piston. This rate of flow determines how responsive the suspension system is to physical displacements and how long it takes to recover from a large displacement. The flow rate is normally fixed so has to be tailored to the vehicle, so that it responds to the vehicle mass and passenger load. As this type of damping is dependent on oil flowing, the suspension dynamics can change dramatically with large variations in temperature, such as if the oil gets too cold it becomes very viscous which would cause the suspension system to take too long to respond to physical displacements, or even seize up completely. To avoid this, companies that manufacture dampers chose oil that will operate in the expected environmental conditions of the vehicle. For extreme environments, such as high pressure underwater exploration, the dampers are specially made to ensure that they meet the required specifications.

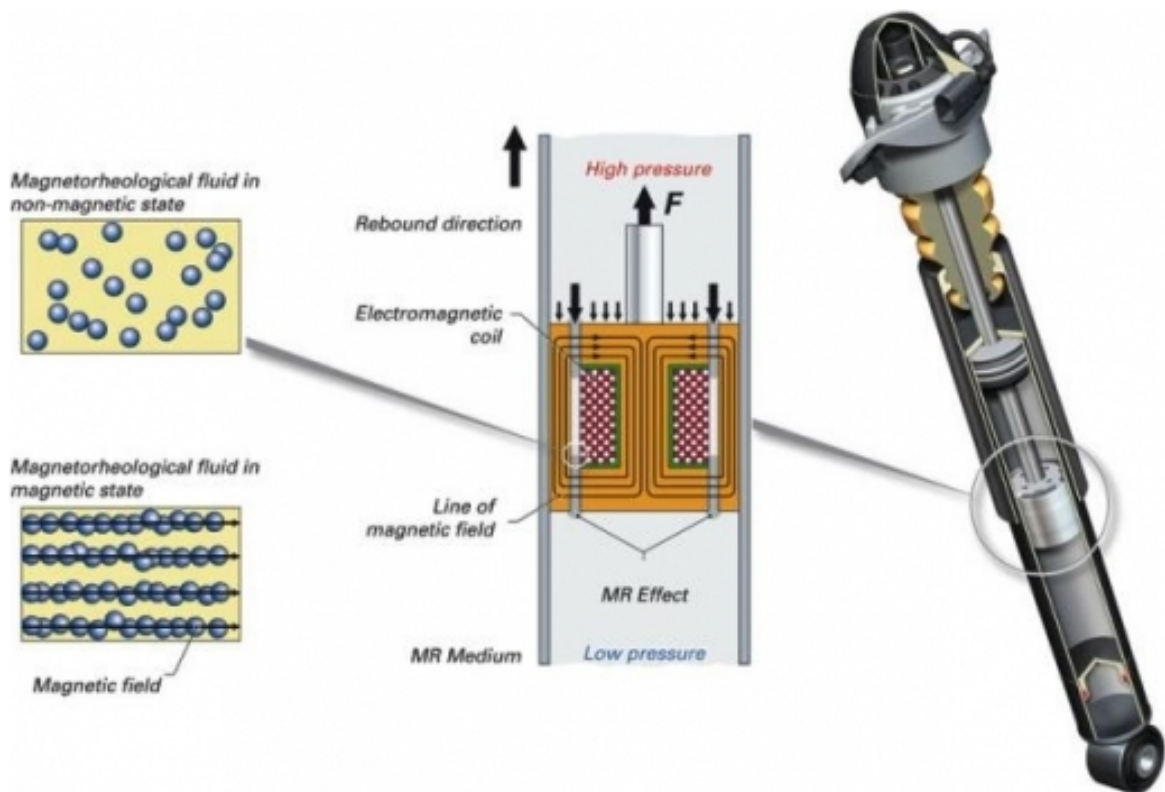


Figure 2.5: The AUDI Semi-Active magnetically damped suspension system [2]

The car manufacturer AUDI, introduced a range of ‘magnetic’ dampers in 2010 [2]

which can respond to road conditions and dynamically change the damping coefficient of the suspension. The oil within the damper has been replaced by a synthetic hydrocarbon fluid which has micro magnetic particles suspended within the fluid. These particles are roughly a tenth of the diameter of a human hair and distributed evenly through the fluid. When a current is passed through an electromagnetic coil surrounding the damper the magnetic particles align, figure 2.5, which resist flowing through the damper thus increasing the damping coefficient. This change can occur in milliseconds and therefore it can change the cars suspension dynamics to account for heavy braking, fast cornering, large bumps and even vibrations from the road surface. The AUDI suspension system uses a Skyhook algorithm [24] to adjust the control loop for each wheels damping so that the wheels' contact with the road is maximized.

Another suspension system that has been developed recently, white paper published in 2010, is the Bose Ride system [3] which actively controls an electromagnetic actuator to dynamically change the height of a truck drivers' seat. This system was developed to improve the working conditions for long distance truck drivers, who frequently have to take time off due to medical problems related to road vibration experienced during driving [3]. The system works by reading the road profile in front of the trucks' wheels, so that when a dip or a bump is encountered the suspension reacts in the opposite direction to counteract the motion that a normal air suspended drivers' seat would not account for. This action can be seen in the comparative motion diagram, figure 2.6, generated from real world testing. The drivers' head position remains at a similar level even when experiencing disturbances to the suspension system, therefore large shocks are not transferring through to the drivers' body.

Unfortunately none of the above systems of motion damping can be adapted for use with space robotics as normal fluid and the AUDI damper systems both rely on fluid within the dampers to flow, which would be a problem on the surface of Mars as, for

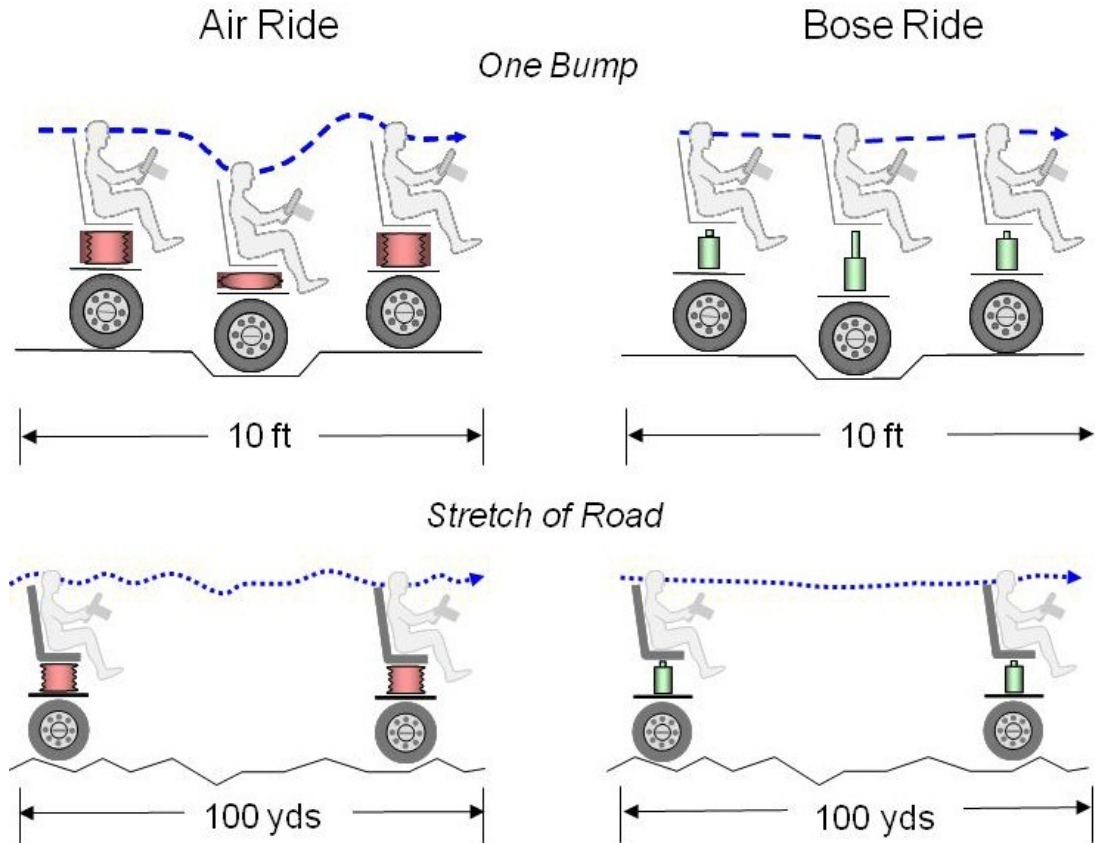


Figure 2.6: Normal air ride seat suspension response compared to the active Bose Ride suspension system [3] for a single bump and a 100 yards traveled along a road

example, the average temperature would be too low and would freeze the oil used, section 2.3. The Bose system requires a continuous $50W$ of power to operate, which is more power than the MER drive train consumes whilst moving. As power is a limited resource on space rovers, the NASA MSL rover Curiosity has a maximum power output from its RTG of $125W$; thus the Bose system is not efficient enough to be considered for space robotics suspension.

2.2 Space Robotics

Space robots such as the NASA MER's are scientists' eyes, ears and remote testing labs on other planets, implementing various sensors and tools to test samples to determine what planets, such as Mars, are actually like. These tests range from simple atmospheric tests such as measuring wind speed, ambient surface radiation and temperature, to geological studies of rock samples using x-ray spectroscopy to excite and characterize the minerals from their emitted spectra. Some tests also look for the building blocks of life, such as carbon-based organic compounds, along with sensors to test for water deposits that are either in a frozen or liquid form. For the purposes of this review the systems and sensors described are all used within space rover mobility systems such as surface interaction sensors and encoders.

2.2.1 Suspension used in Space Robotics

The Rocker-bogie suspension system [4], described in section 1.1.1, gets its name from the rear arm of the mechanical linkages, labels 65 & 65A in figure 2.7, which is able to rotate from side to side around a central pivot point.

This rocker-bogie linkage allows the mobility system to keep all 6 wheels in contact with the surface, whilst maintaining a near constant force between each of the wheels and the ground, even if one of the wheels was substantially higher or lower than the others. Experimentation performed at the California Institute of Technology [25] improved the efficiency of the rocker-bogie system by introducing a differential gear between the two sides of the chassis, which increased the robot's stability and has become the de facto standard for most space rover mobility systems including the ESA ExoMars and all current NASA mars rovers.

The Rocker Bogie suspension system is mechanically equivalent to the design of

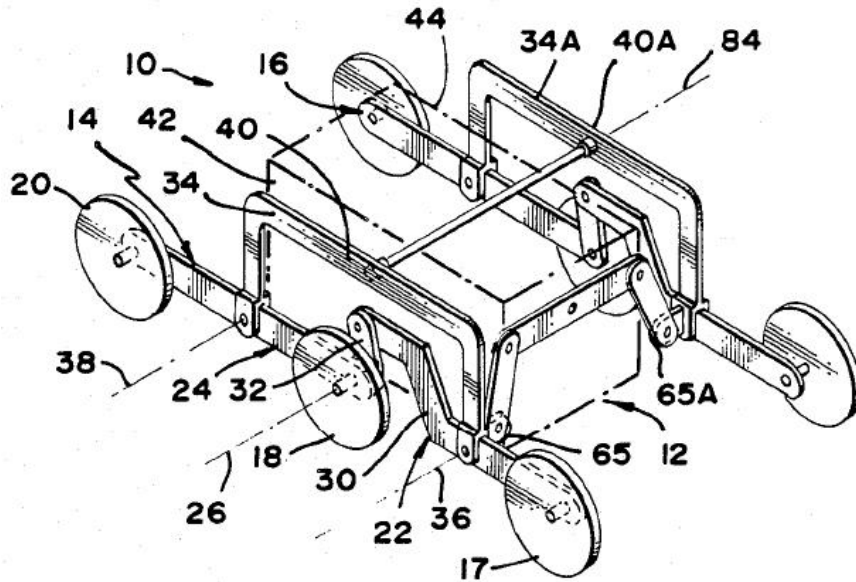


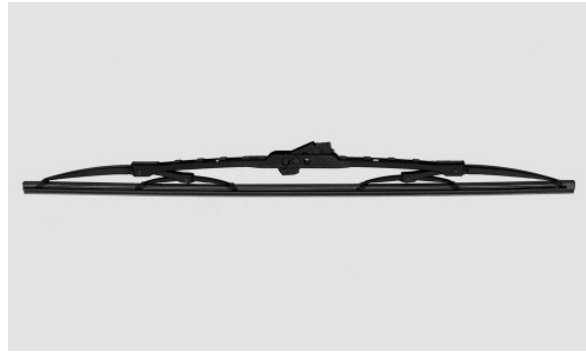
Figure 2.7: Original drawing from the Bickler Rocker-Bogie patent [4]

Whiffletree's which can be used to share loads between beasts of burden, figure 2.8a, produce an equal load along the length of a windscreen wiper, figure 2.8b, perform simple mechanical computing calculations, figure 2.8c [26] and perform digital to analog conversions, figure 2.8d [27] [28] [29] [30]. In early computation whiffletrees were used for addition, figure 2.8c, as the motion of push rods that are mechanically linked through a set of pivots produces a proportional motion that is relative to the displacement of each rod. Analog computing extends the use of whiffletrees by combining many interlinked sets of whiffletrees to produce complex outputs. During the Second World War it was necessary to quickly calculate the balance of military planes when they were loaded with bombs and fuel, figure 2.9, such that by adjusting the position of the 19 knobs on the front panel the operator moved combinations of whiffletrees, figure 2.9d, to produce a loading profile which displayed instantly on the two output dials.

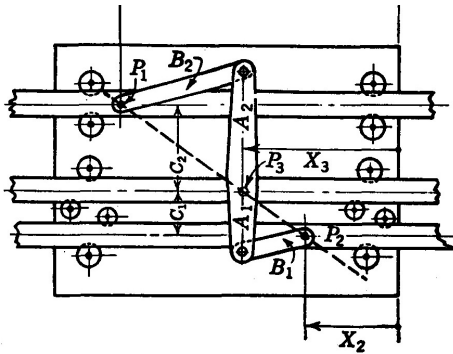
This approach was extended to computer printer interfaces used in the early 1960's



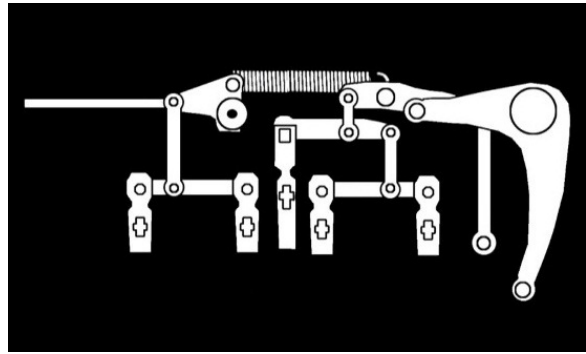
(a) Load sharing between horses



(b) Equal load along length of a wiper blade



(c) Mechanical adder using linkages [26]



(d) DAC using linkages [27] [28] [29] [30]

Figure 2.8: Different applications of Whiffletrees

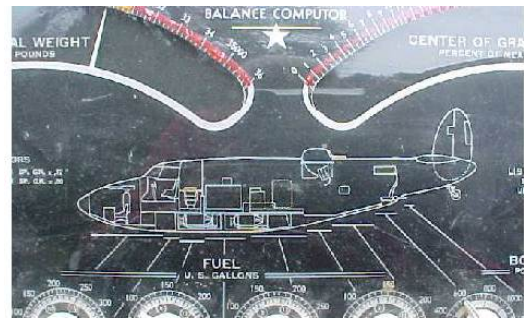
such as the IBM Selectric typewriter [27]. The whiffletrees converted digital inputs, produced by solenoids, to analog movements of cables that governed the printer head position [28] and rotation [29] [30].

The motion created by solid linkage whiffletrees is relevant to the rocker bogie suspension system as the whiffletree kinematics can be directly incorporated into the dynamic models used to predict the motion of a rocker bogie as it traverses uneven terrain. These kinematic models however are of no use if the rover is not capable of fitting into the planetary delivery system.

To get space rovers to other planets the mobility system must fit into both the delivery rocket and the planetary lander system, which normally means the rovers mobility system is stored in a folded or compressed configuration [6], which the rover deploys



(a) Front view of panel



(b) Enlarged view of detail



(c) View of bomb loading dials



(d) Rear view of panel

Figure 2.9: Second World War Navy PV-1 Balance Computer [5]

once at the destination planet. The MER mobility system had the ability to unfold its suspension once on the Martian surface which then latched into position, figure 2.10, activating a microswitch to indicate successful deployment of the joint.

Whilst performing correctly during the deployment phase of the MER's mission, NASA concluded [6] that the system complexity could have been reduced by removing the microswitches in the latch assembly, the blue box in the bottom right of figure 2.10, and using motor current feedback instead to measure when the latch was correctly engaged.

The MER's had some limited suspension built into their design through the choice of materials used in construction of the chassis as well as flexible spoked wheels to absorb some of the surface impacts. The MER chassis was fabricated from tapered titanium box beams [25] which allowed a small amount of flexing, much like the torsion bar

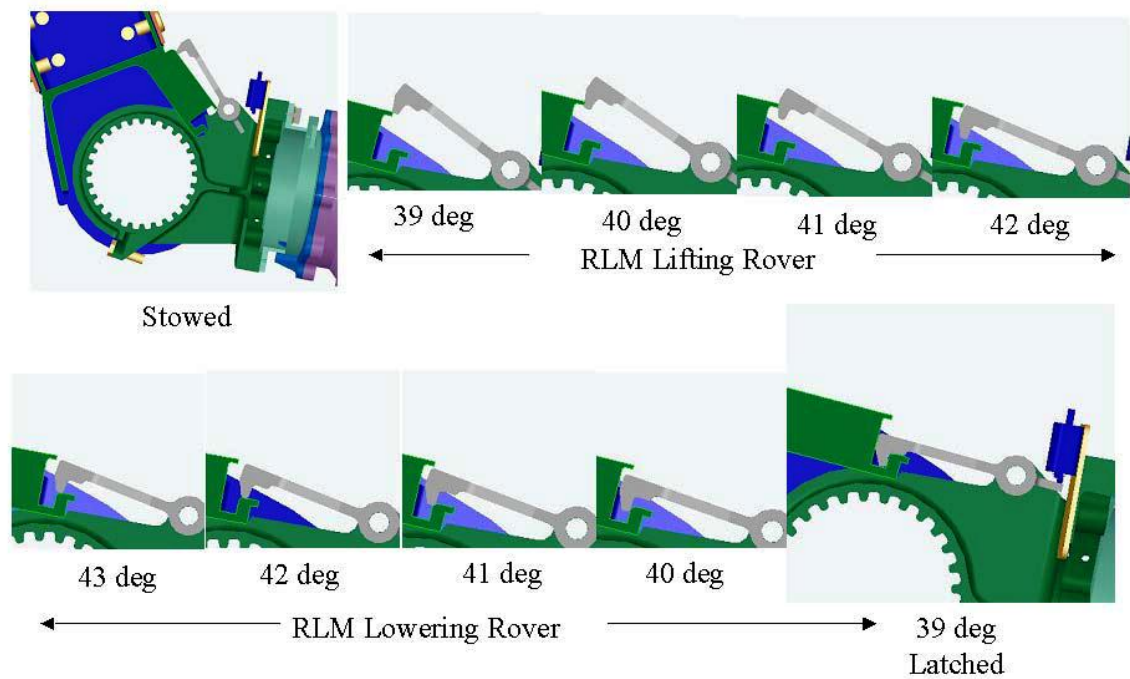


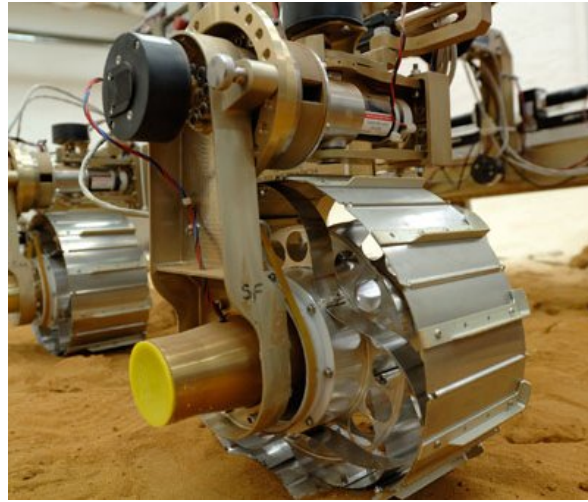
Figure 2.10: Rocker-Bridge latch pawl of the MER mobility system used to lock the rocker-bogie during deployment [6]

suspension principle, to give the rover “a ride somewhere between a luxury vehicle and a truck”. The spoked wheel design [31] attached the outer paddle wheel to the inner motor drive hub, figure 2.11a, so that as the wheels impacted rocks on the surface some of the kinetic energy was absorbed by the aluminum spokes and the orange Solimide foam, which doubled as a hub cap to stop rocks and debris from jamming the driving and steering actuators.

The ExoMars rover, designed for the ESA by Astrium, is a self-contained rover in which all six wheels are driven with the ability to pick the wheels up and ‘walk’ with them. The ExoMars rover chassis includes some features not previously seen on other Martian based rovers [32], including adaptive metallic wheels which are flexible, figure 2.11b, in order to reduce energy consumption and protect the rover from terrain



(a) Closeup of the MER wheel



(b) ExoMars wheel with mobility system

Figure 2.11: NASA MER and ExoMars Spoked Wheel Designs

impacts, a passive 3-bogie arrangement, wheel walking capability to negotiate terrain that would stop standard wheels and 6-wheel steering to give better terrain handling, maneuverability and the ability to crab.

Many locomotive ideas were considered for the ExoMars project however a passive 6-wheel configuration was chosen since it offers good mobility whilst traversing the Martian surface. Seven suspension concepts were researched; RCL concepts C,D and E, CRAB, 3-Bogie, V-Bogie (figure 2.12) and the Rocker-Bogie.

The RCL-C type was rejected due to a suspension problem when climbing obstacles that was corrected with the RCL-E design, which had an independent transverse rear bogie to overcome the RCL-C suspension problem, however this configuration was rejected due to poor static stability caused by the straight linkage configuration, which produced an equal reaction on both wheels of a bogie when on a slope. The RCL-D and CRAB types were also rejected due to their poor static stability. The 3-Bogie configuration was introduced as it improves the static stability of the rover by allowing differential wheel reactions on the bogie by removing the linkages from the

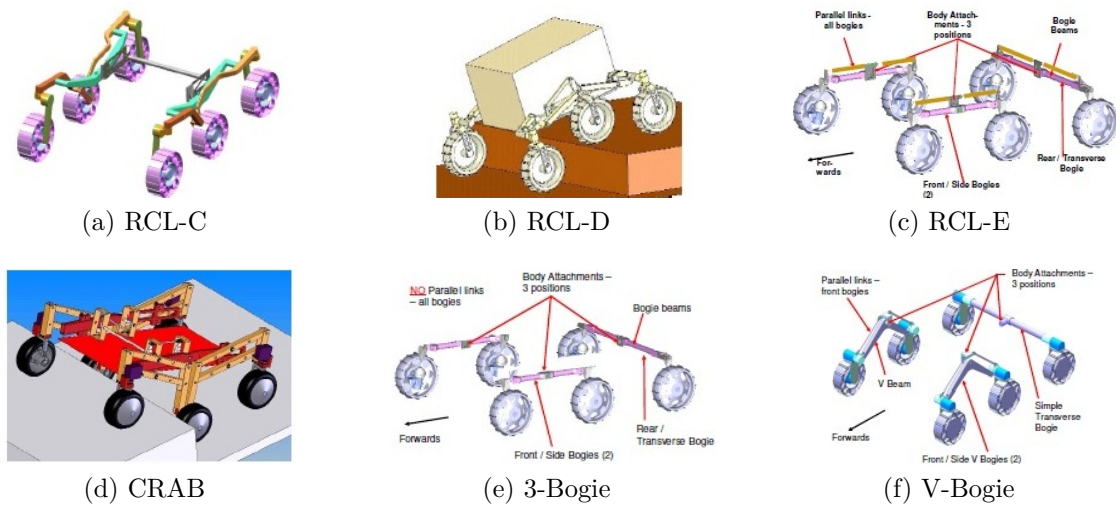
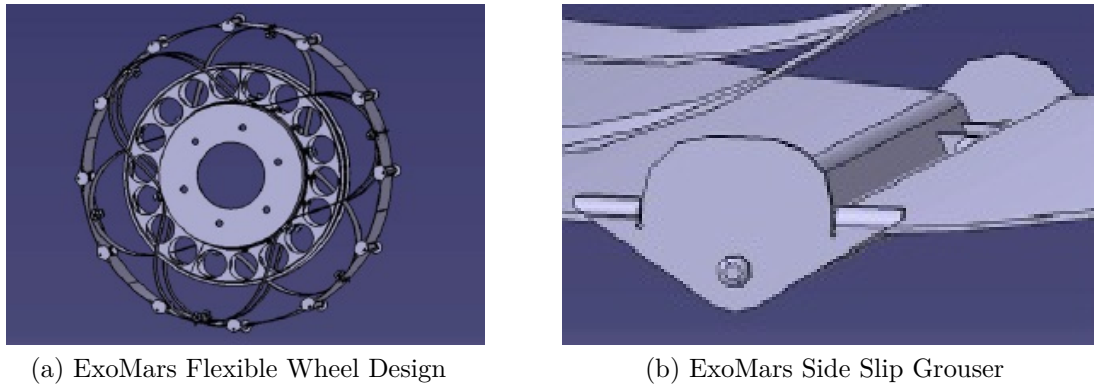


Figure 2.12: Six of the seven suspension concepts tested [7]

RCL-E configuration. The V-Bogie configuration was proposed to solve the potential 3-Bogie design flaw that could result in bogies overturning when the leading wheels are blocked, but the V-Bogie configuration was found to be inferior to both the 3-Bogie and Rocker-Bogie configurations at climbing steps because of the higher pivot position, which pushed the leading wheels downwards. The static stability and performance of the Rocker-Bogie system was found to be no better than the 3-Bogie system, but the 3-Bogie concept was found to be the lightest and simplest configuration and hence was chosen for the ExoMars project [7].

The ExoMars wheels differ to the MER's design [8], figure 2.13, as they are made from multiple parts rather than a single block of machined aluminum and react to the ground more like normal rubber tyres that you would find in a car. Both the MER and ExoMars wheels are manufactured out of metal because rubber is an organic material, which could contaminate organic samples and has less durability than metal for long missions that involve large variations in negative temperature environments.

Flexible wheels were chosen for the ExoMars testbed since flexible wheels provide a



(a) ExoMars Flexible Wheel Design

(b) ExoMars Side Slip Grouser

Figure 2.13: ExoMars Flexible Wheel Design [8]

larger rolling radius than a rigid wheel with the same diameter. They also improved traction performance so a smaller wheel could achieve big wheel performance. The performance criteria used for the wheels included overall traction resistance, drive torque and energy consumption. Various tests performed on slopes between $15^\circ - 20^\circ$ on a range of soil types with wheel diameter $0.2m - 0.3m$ and width $0.4m$ showed that flexible wheels provide superior traction performance compared to rigid wheels under identical conditions [32]. Further work restricted the diameter to $0.25m$ and it was determined that a target stiffness of $11kPa$ was to be used [7]. To increase traction the flexible wheel design incorporates grousers, figure 2.13b, which are mounted across the profile of the wheel to improve rolling traction as well as on the sides of the wheel to reduce lateral slippage. The optimum grouser configuration used in the ExoMars testbed utilized 12 grousers of height $4mm$ and side-grousers for lateral resistance to limit lateral slip [32]. Following further gradeability tests [33] on varied slopes and different grousers a modification to the wheels was found to be necessary. By altering the height of the grousers to $8mm$ the Locomotive Performance Model (LPM) was able to climb slopes as high as 18° uphill and downhill. The LPM with $8mm$ grousers successfully overcame obstacles at speed $2cm/s$. With the modified grousers, the LPM was able to climb obstacles that were $0.25m$ tall with relative ease. Very little wheel

spin was seen and the grousers were not levering the rover up the step [33].

The rover is required to be statically stable on an inclined plane of up to 40° as this ensures stability for operation on uneven terrain with slopes up to 25° and the presence of rocks. Static stability is dependent on suspension arrangement and it is lost when any of the wheels contact force curve drops below zero [7].

Other experimental suspension systems based on the rocker-bogie design exist for space robotics [34] [35], which all have slightly different linkage mechanisms but no significant advantages over the current designs being used by ESA and NASA.



(a) Climbing cliff face



(b) Drilling with wheel attachment

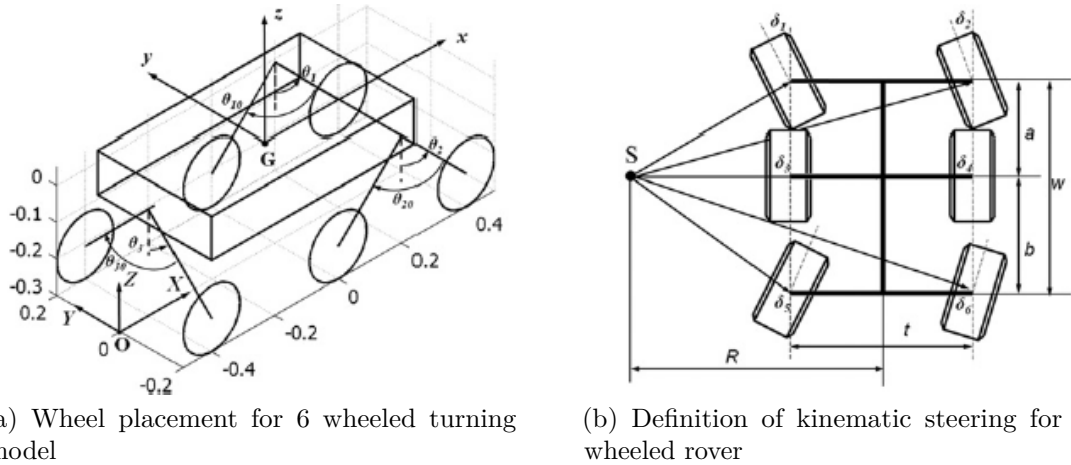
Figure 2.14: NASA ATHLETE mobility system [9]

The ESA ExoMars design currently allows the wheels to be locked and lifted from the surface, so it can be used as a walking type motion [36], which has also been employed by NASA on their ATHLETE mobility system [9]. The ExoMars uses the wheel walking to increase its slope climbing ability so when its wheels start to bury themselves due to slope dynamics, the wheels can be individually actuated using a walking motion found more commonly in small insects to pull the rover up the slope. The NASA ATHLETE platform has a much greater capability to lift its wheels due to more degrees of freedom within each leg, figure 2.14, which enables the rover to pick

its way over objects that are too big to drive over, figure 2.14a, or to navigate areas that a driving wheel would get stuck at such as a boulder field. The NASA ATHLETE also has the ability of extra functionality from its legs, as each wheel actuator has the ability to attach tools to the wheel hub's power take off connector, figure 2.14b. This enables each leg to use tools such as drill attachments to take core samples and place sub terrain sensors, circular saw attachments to cut down into the surface of a rock to expose internal geology to study and gripper attachments that can be controlled by either running the wheel forwards or in reverse to open and close the gripper.

These extra degrees of freedom in the ExoMars and NASA ATHLETE platforms allow for enhanced driving capability on rough terrain as well as the ability to turn each wheel individually so that the rover can move in a 'Crab' like fashion, but the original rocker bogie design shown in figure 2.7 does not include the ability to change the direction of any of its wheels [4]. This problem was overcome by adding steering to the four outer wheels, whilst keeping the central wheels in alignment with the rovers turning radius. This means that rovers such as the NASA MERs that utilize the original rocker bogie suspension do not have the capability to 'Crab', instead they have to turn about a radius, figure 2.15, which requires some additional work to ensure the wheels are pointed in the correct direction.

Figure 2.15 shows an example of the rocker bogie suspension turning about a radius which is defined by the center point S . The wheels are marked by 6 rectangles, with their direction of travel marked by a dotted line. The rover can turn due to the four corner wheels each resolving their own angle and as such none of the wheels drag or slip. If the four turning wheels all used the same angle then the rover would dig into the surface of the planet, because the drive from the wheels would create lateral loading on the outside edges of all the wheels. This looks like a simple mathematical problem to solve, but is made more complex when the rovers wheels are not operating



(a) Wheel placement for 6 wheeled turning model

(b) Definition of kinematic steering for a 6 wheeled rover

Figure 2.15: Six wheel radius turning used in Rocker-Bogie chassis designs [10]

on a perfectly flat surface, such that a lifted wheels drive angle would change due to the rocker bogie suspension systems dynamics. This radius path wheel turning is also used by rovers that have a greater number of actuated wheels, such as the ExoMars and NASA ATHLETE platforms, and is often the preferred way to turn the rovers as the rovers rotation can be used to bring objects of interest into view, whilst using less power than the ‘crab’ motion as fewer wheels need to be turned simultaneously.

The rocker bogie suspension system has a major limitation of speed, as any impacts that the wheels experience is transferred through the solid linkage assembly to the rovers internal electronics and instrumentation, as well as the possibility of flipping the bogie over under impact conditions. Most of the rovers that have used rocker bogie suspension have compensated for this problem by either reducing the top speed that the rover travels at, including flexible materials in the rovers construction, or by including suspension into the wheels directly, but even with these fixes the top speeds of the NASA Sojourner [37], MER [25] and MSL [38] platforms were only $2mm/s$, $4 - 8mm/s$ and $50mm/s$ respectively.

Research to increase surface traversal speed performed by the School of Aerospace

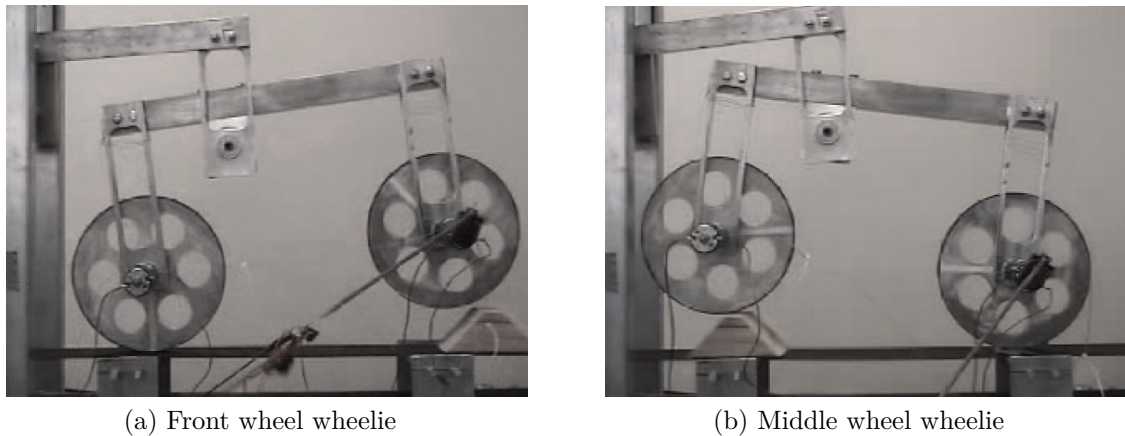


Figure 2.16: High speed bogie lifting $\approx 1m/sec$ [11]

and Mechanical Engineering, University of Oklahoma, tried to run a rocker bogie at near human walking pace ($\approx 1m/sec$) under laboratory conditions [11]. This research demonstrated that it was possible to lift individual wheels, attached to a bogie, from the ground by adjusting the drive speed of other wheels within the rover, figure 2.16. Using closed loop control, the system lifted the front wheel to avoid an obstacle of known height and shape by driving the middle bogie wheel faster than the rear wheel, figure 2.16a, so that once the front wheel was clear it could then be run slower than the rear wheel to lift the middle bogie wheel which the obstacle was approaching, figure 2.16b. This system worked under laboratory conditions, but did not account for the final trailing wheel that smacked into the obstacle at full speed, which would damage instrumentation and run the risk of snapping the rear wheels mounting. The proposed solution to this was to have a second bogie so that the rear wheels could mimic the front bogies motion, but this would require eight driving wheels which would increase the weight and power requirements along with the size of the rover, therefore this solution would not be feasible for space robotics. The system was not tested on soft surfaces such as sand and mud, as the drive control model required known friction coefficients between the wheels and the surface to provide the correct amount of power

to the lifting wheels.

This confirms the question discussed in section 1.2:

- *What can be done to isolate the rover from impacts and vibrations created by the rovers mobility system as it moves over the surface of another planet?*

2.3 Space robotics environmental considerations

All forms of exploration have their unique challenges, for example the crushing pressure experienced with underwater exploration [39] or the trajectory control of unmanned space craft [40]. With respect to space robotics that are used to explore different planetary bodies, the destination will have its own unique properties that will hinder a robot's performance, such as very loose micro-dust surfaces as found on the Moon [41] and vast temperature ranges as found on Mars, section 2.3.1. This section outlines some harsh conditions that Space Robotic Rovers face when they deploy and traverse the Martian terrain as well as the initial journey to Mars.

2.3.1 Temperature Cycling

Temperature cycling can cause stress on components and materials [42], so the design and testing phase for space robotics must take this into account, especially if visiting some of the more distant planets, table 2.1. The surface of Mars experiences a range of temperatures throughout a Martian year and has a clear daily pattern ranging between $\approx -140^{\circ}C$ and $\approx 31^{\circ}C$. A two Sol plot of surface and air temperatures, figure 2.17, shows the temperature range experienced by the MSL mission between the 15th and 17th August 2012, clearly showing that the Martian surface experiences a greater

variation in temperature than the air.

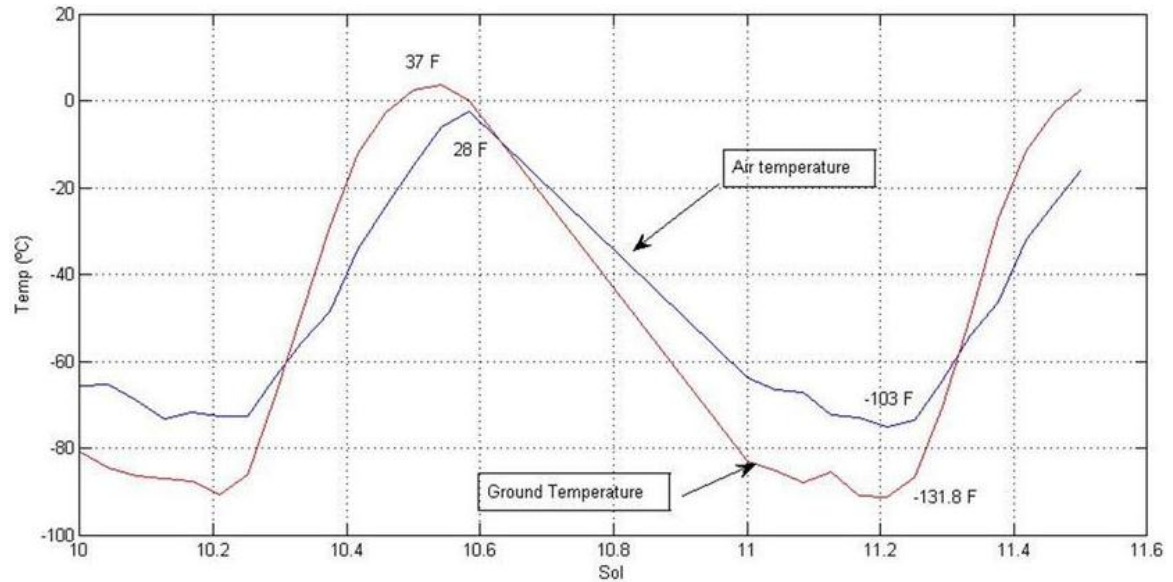


Figure 2.17: Ground and air temperature variations over a two Sol period (Data from NASA/JPL-Caltech/CAB)

The temperature variations on Mars means that all Martian rovers have to contain their electronics in a insulated box, the Warm Electronics Box (or WEB for short), so that a near constant temperature can be maintained. This is done using a combination of heat from the RTG and heating elements, along with a cooling system to regulate the WEB's internal temperature. Components such as the batteries are most efficient when kept within a narrow temperature range and the constant temperature helps protect fragile components found within some of the scientific instruments, which can also lose accuracy if rapidly cooled or heated.

2.3.2 Gravity

Mars has a lower magnitude gravity compared to the gravity on Earth, table 2.1, for example an object that weighs $100kg$ on earth will only have the apparent weight of $37.3kg$ on Mars. This lower gravity environment has some benefits such as reduced

load on the rovers motors which makes traversal of terrain easier, so that the rover requires less power to move and can use smaller motors. The rover is also capable of carrying a larger payload and can use lighter materials in its construction due to not being subjected to the stresses found under Earth gravity. If the rover was part of a sample return mission the return rocket would need less fuel to escape the effects of Martian gravity than a rocket launching from Earth. The lower gravity environment however makes it more difficult for the rover to initially land on the surface, as any landings that use deployable air bags to cushion the rovers surface impact will result in the rover bouncing across the Martian surface for a lot longer. The rover would also have lower traction between its wheels and the Martian surface due to not having the same weight as on Earth where it was tested.

Planet	Approximate Temp Range ($^{\circ}C$)	Gravity relative to Earth	Distance from the Sun (AU)
Earth	-89 to 58	1.000	1.000
Mercury	-220 to 420	0.378	0.387
Venus	437 to 469	0.907	0.723
Mars	-140 to 31	0.377	1.520
Jupiter	-128 to 4	2.360	5.200
Saturn	-153 to -23	0.916	9.580
Uranus	-214 to -205	0.889	19.200
Neptune	-223 to -220	1.120	30.050
Pluto	-238 to -228	0.059	39.240

Table 2.1: Comparison between planets in our solar system

2.3.3 Space

Space travel is a difficult endeavor due to the complexity of launching, which has killed people on a number of occasions [43], navigating using various tracking techniques [44] [45], using gravity to accelerate and decelerate [46] [47] and then if you have managed to get close to a planet, finally getting a space vehicle to land on the surface in one working piece [48] [49]. Dr Charles Elachi [50] stated ‘After traveling 450 million kilometers, the rover Spirit arrived at Mars within 80 meters of its intended landing site which is the equivalent of teeing off in Los Angeles and sinking a hole in one in St Andrews Scotland, and the hole on Mars was moving at 60,000 mph!’

For the purpose of this thesis, let us assume that the rover has made it successfully to Mars and has deployed onto the Martian surface without incident. Now that the rover is on the surface it will be subjected to dust storms, Martian winds, hot and cold temperature cycling, lower gravity as well as a lower pressure atmosphere compared to Earth. The following sections describe why some of these environmental conditions might be a problem for a Martian rover such as Dust and Wind, section 2.3.4, Temperature Cycling, section 2.3.1, Gravity, section 2.3.2, Atmospheric Pressure, section 2.3.5 and Radiation, section 2.3.6.

2.3.4 Dust and Wind

Whilst a space rover is being constructed the laboratory is kept as dust free as possible as a small speck of dust could cause major problems for the rover, for example the optics systems could become blurred or blocked if part of the CCD sensor was obscured by dust, thus stopping light reaching it. Whilst in space dust is not so much of a problem, but once the rover has landed dust can cover solar panels which reduces the life of the rover [51], it can get into scientific instruments, optics and even seize

motors. The entry decent and landing sequence (EDL) [48] [49] for the latest NASA rover MSL, named Curiosity, utilized a sky crane that hovered 20 meters above the surface of Mars to minimize the interaction of the rocket motors with the surface to try and reduce the amount of dust stirred up during the landing process. The MSL rover was then lowered on a tether to the surface from the sky crane, as the rocket motors on the sky crane could blot out the rovers view of the surface and create excessive contamination of the rover and surrounding area if it hovered any lower.

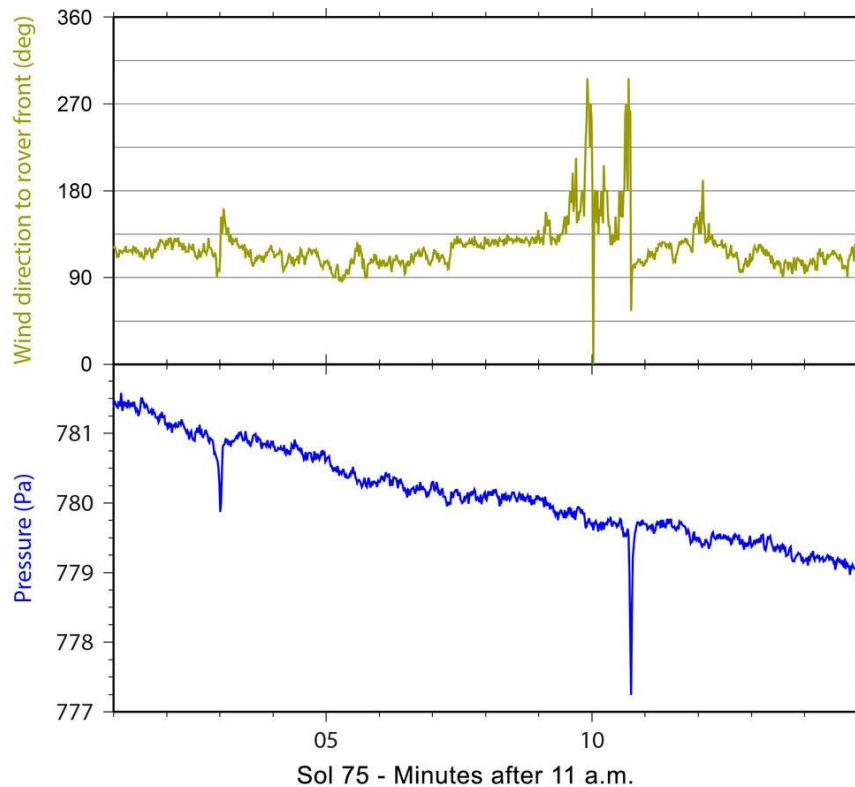


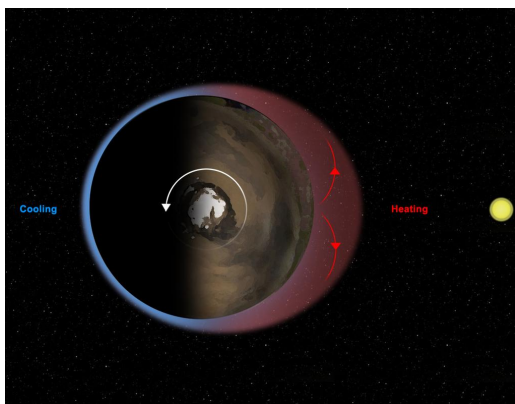
Figure 2.18: Wind direction and pressure data from Sol 75 (Data from NASA/JPL-Caltech/CAB)

Surface measurements taken with both the NASA MER and MSL rovers support visual observations that wind is experienced on the surface of Mars. This was seen when the solar panels that powered the MER Spirit, started to produce more power after the rovers cameras captured what looked like a dust devil [52] cleaning dust from

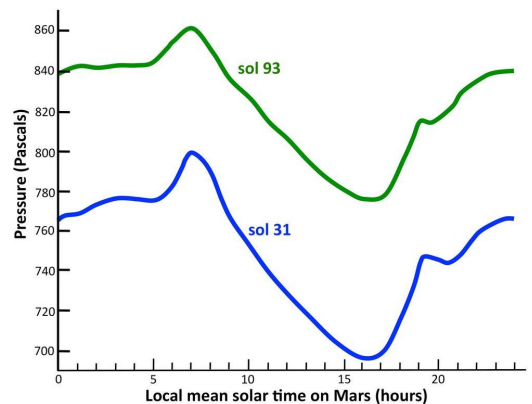
the solar panels. The weather instruments on MSL have also measured wind direction and pressure fluctuations that could only be caused by whirlwinds, figure 2.18. This can be seen in the data as a sudden drop in pressure, as the whirlwind passed over the rover, coupled with a rapid change in wind direction.

2.3.5 Atmospheric Pressure

Variations in atmospheric pressure can cause issues for rovers with sealed compartments or sealed sample containers. Most sealed parts of a rover require a pressure compensation valve with a filter to remove any contaminants such as dust. On Mars there are large variations in surface pressure due to a ‘Thermal Tide’, figure 2.19a. As the sun heats the Martian atmosphere, the air expands towards the sun creating a negative pressure underneath it, which draws in colder air from the other side of Mars, thus causing lower pressure on the ‘dark’ side and higher pressure on the side facing the sun which can be measured, figure 2.19b.



(a) Thermal tides on Mars



(b) Pressure cycle on Mars for one Sol

Figure 2.19: Pressure variations experienced on the Martian surface (Images from NASA/JPL-Caltech/CAB/Ashima Research/SWRI)

2.3.6 Radiation

The magnetosphere and atmosphere surrounding Earth keeps us relatively safe from cosmic radiation, but on Mars where there is no Magnetosphere and a limited atmosphere the risk of radiation is much higher. To ensure that the hardware on space rovers operate correctly and lasts for the duration of the mission, items such as the processors and memory chips have to be hardened against radiation. The dose of radiation that Martian rovers experience depends on the atmospheric pressure, figure 2.20, as increased pressure provides higher protection against radiation. The data, figure 2.20, shows how the daily pressure cycle (blue points plotted in Pascal) coincides with the total radiation exposure (red line) from both charged particles and neutrons. This data is important to analyze and understand, as it will be critical information if humans are ever to set foot on Mars.

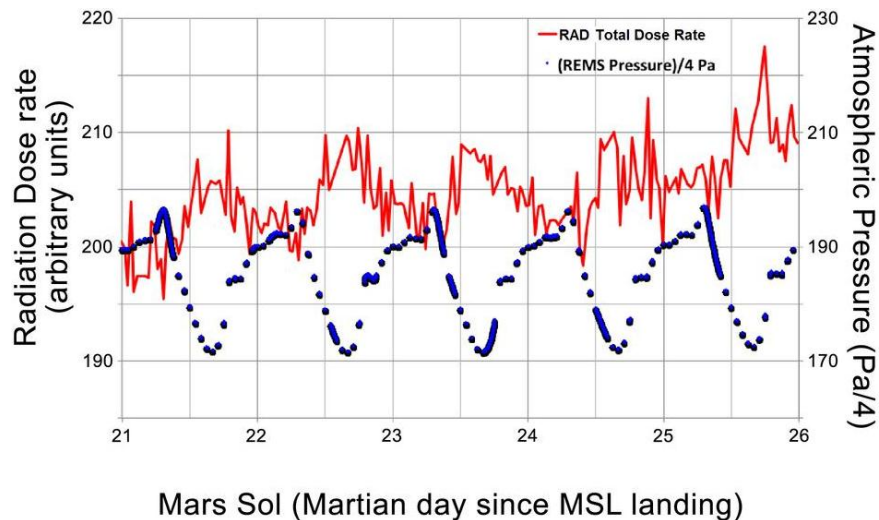


Figure 2.20: Atmospheric pressure variation and radiation exposure over a five Sol period (Data from NASA/JPL-Caltech/CAB)

2.4 Permanent Magnet and Electromagnetic Systems

There are many applications that permanent magnets and electromagnetic systems are used for, including mechanical linkages that can disengage under high loads, high speed low friction bearings for machinery that require long maintenance free lifespans, laboratory equipment such as pumps and stirrers to avoid contamination from grease, equipment that has to operate in harsh or dangerous environments such as underwater motors or agitators inside flammable gas tanks and mass transit systems that utilize magnetic levitation. This section describes some of the above and how they are related to the research performed for this thesis.

Mechanical linkages in drive trains normally utilize some form of shaft coupling and bearing supports to ensure the smooth operations of mechanical components. These are used within space robotics to transfer power from drive motors to the wheels through a series of gears to increase the torque output from the motor known as Harmonic Drives [53]. The NASA MER platform had 33 motorized actuators, of which 19 had incorporated harmonic drives [54]. Harmonic Drives utilize both bearings and couplings to compensate for wear and misalignment of the drive shafts, as well as using specially formulated lubricants due to running at sub-zero temperatures on other planets [55], which meant that the motors required heating to ensure that the lubricant would flow across all gear teeth within the Harmonic Drive. Harmonic drives have a lot of parasitic losses such as friction, so the life expectancy of the rover is reduced and has relatively low efficiency. Magnetic couplings and bearings can be employed to solve some of these problems as magnetic couplings operate with minimal friction. Most of the friction comes from the bearings used to mount the couplings, whilst magnetic bearings can run with no friction under certain conditions. Emerging technologies such

as the Non-Contact Magnetic Gear (NCMG) [56], the High-Performance Magnetic Gear [12], figure 2.21, Magnomatics Magnetic Gears [57] [58] and Pseudo Direct Drive (PDD) [59] use the interactions between permanent magnets and a stator to produce drive or passive gearing without friction. These devices do not require lubrication to operate due to there being very low friction between the internal components, so they can run for the life of the product without requiring maintenance. The drives also have the capability of disengaging from the load if there was a problem such as over-torque, where the required torque would damage the drive train. This is done by changing the distance between two magnetized plates so that the linkage can provide a clutch like variable torque transmission [60], figure 2.22.

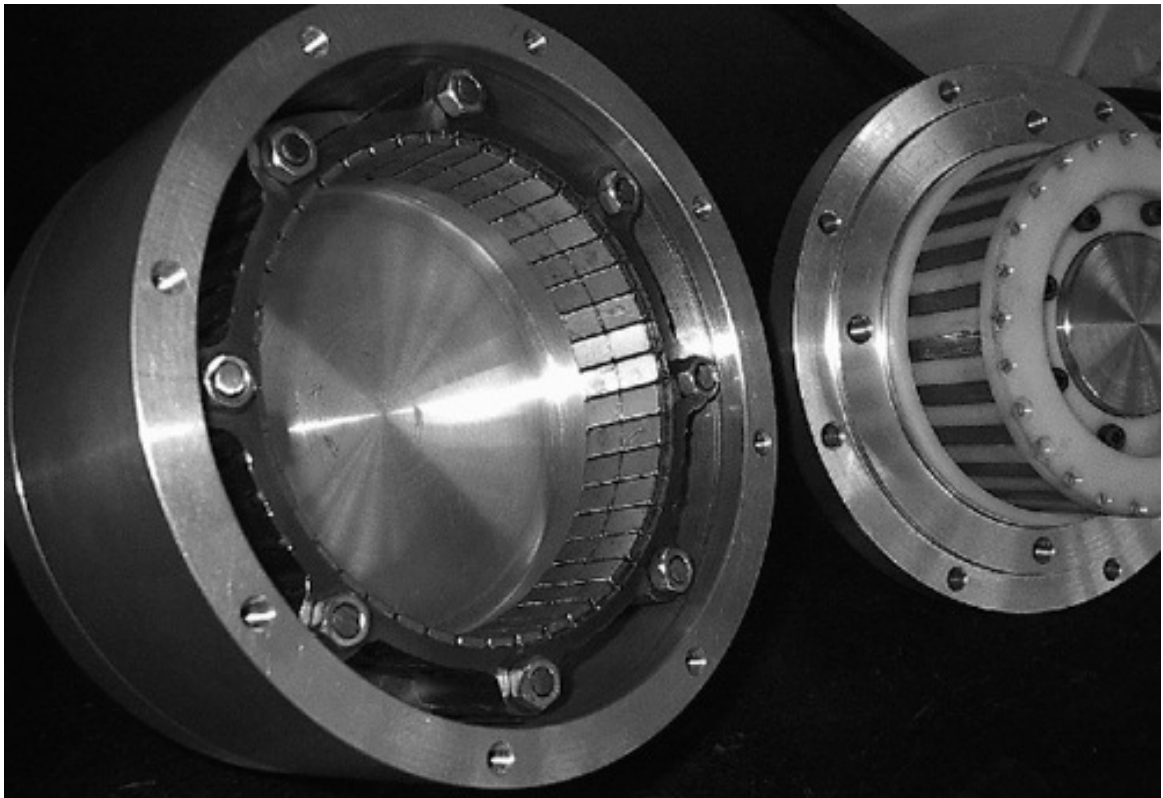


Figure 2.21: Inner workings of the High-Performance Magnetic Gear [12]

These devices are of great interest in the fields of renewable energy, marine propulsion,

automotive and aerospace applications, energy storage flywheels and many other sectors that require gearing or transmission with minimal friction. These could replace the current Harmonic Drives in space rovers once they have passed all experimental testing stages, but are showing early promise. The main consideration for these magnetic gears is the maximum environmental temperature that they would be exposed to, as once a magnet is heated past its Curie point it becomes demagnetized and thus would no longer operate, for example a sintered *NdFeB* magnet has a Curie point of $\approx 310^{\circ}\text{C}$ [61]. Conditions specifically on the surface of Mars would not reach this Curie point, so these devices would be suitable for Martian terrain exploration.

Friction is a major problem in high speed bearings, so electromagnetic solutions have been found to either support or stabilize rotating shafts, such as energy-storage flywheels [62] and small impellers used in artificial blood pumps [63]. The problem with electromagnetic bearing solutions is the complexity required in the control systems to keep the bearings operating correctly [64], as the bearing dynamics change due to temperature variations among other things.

The ability to rotate an output shaft using coupled magnets [13], figure 2.22, with no physical connection to a motor allows for drive to be transferred through surfaces, such as drive being transferred to propellers on a boat without the need to have large heavy water seals to avoid leaks around the propellers drive shaft, as well as the ability to agitate a gas within a pressurized container without the risk of grease contamination or sparks from the motor that could ignite flammable contents [65]. These magnetic gears and drives have obvious applications in the field of robotics, but the research performed for this thesis is more interested in possible ways that magnets can be applied to suspension applications.

There has been a lot of research over the years into electromagnetic suspension, with little interest in permanent magnets due to their high cost and relatively low strength.

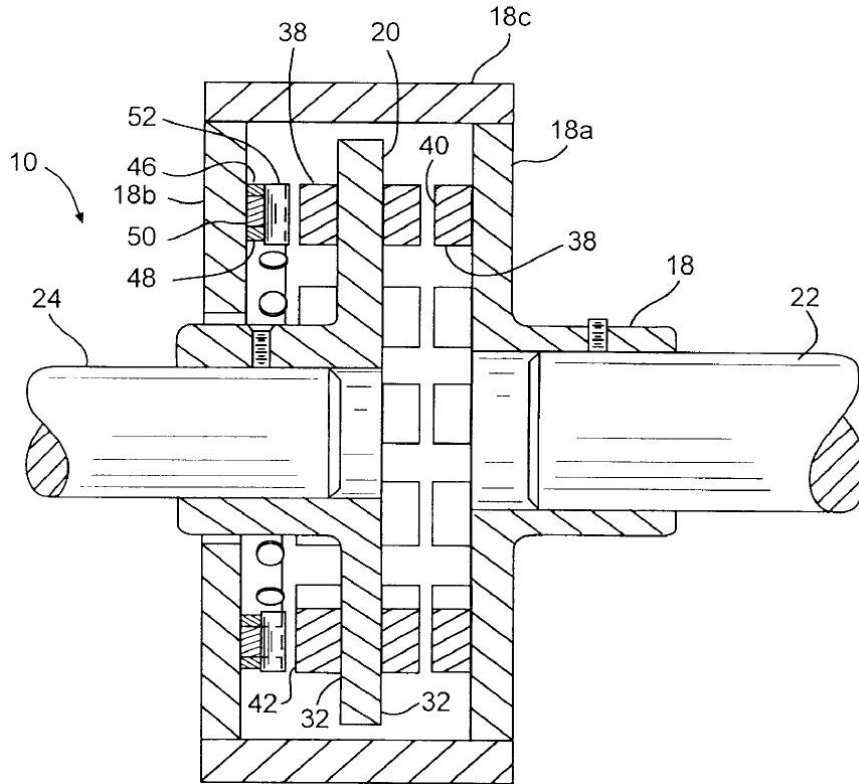


Figure 2.22: Inner workings of a Magnetic Clutch [13]

Early research using permanent magnets to support vehicles was performed in the 1960's [66] but was abandoned due to the low strength of magnetic materials available. Samarium-Cobalt ($SmCo$) magnets revived the research [67], but the cost of these magnets meant that it was prohibitively expensive to be used on a large scale. The advent of Neodymium ($NdFeB$) magnets enabled some small-scale [68] and full size demonstrations [69] of vehicles that were levitated using permanent magnets, but both approaches required additional electromagnetic control to stabilize the levitation. It is impossible to levitate a permanent magnet without additional control and thus energy, but it is possible to reduce the degrees of freedom that the magnet or control can move in. This approach [70] required active control of a motor, that was limited to a single degree of freedom, to balance a table levitated on a number of magnets. The

results of this research showed that stable operation was not very practical and the suspension oscillated for a long time after a disturbance. This problem had already been solved [14] by introducing a material such as aluminium between the supporting magnets, figure 2.23, so that as the table oscillated, Lorentz forces were generated in the aluminium which dissipated energy (through heat) and thus caused damping within the system.

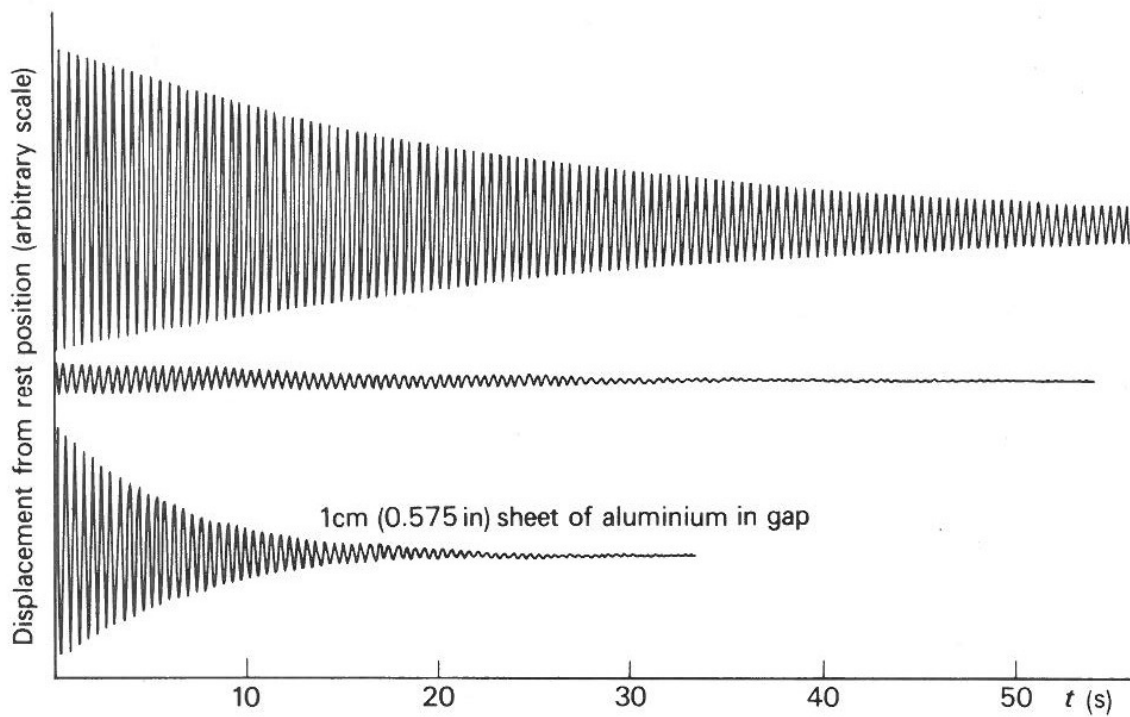


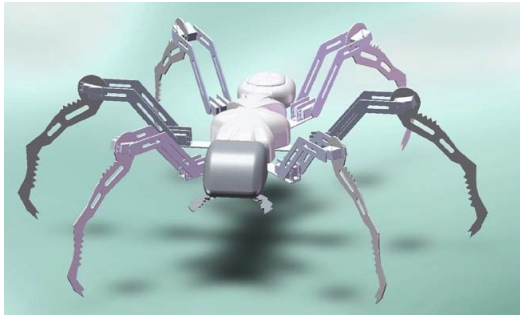
Figure 2.23: Response of two permanent magnets in repulsion: two blocks of barium ferrite, $15 \times 10 \times 2.5\text{cm}$, at rest position 3.5cm gap [14]

If magnets are limited to a single axis of motion, a ‘spring’ like device can be created [71]. This ‘spring’ effect can be affected by materials placed around the device, so damping could be introduced to the device for example by encasing it within an aluminium tube. The aluminium tube solution is considered to be passive damping as the damping cannot be changed once the tube is in place, but there are other approaches to introduce damping that could be controlled. To introduce an active

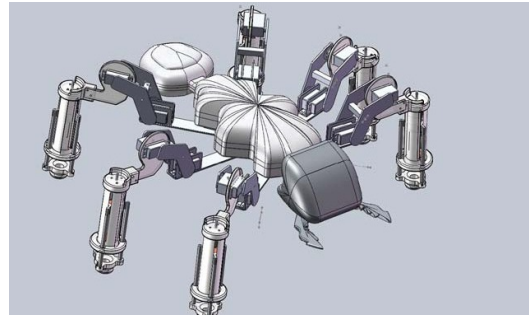
damping to the magnetic ‘spring’, an electromagnetic coil could be wound around the device so that when the electromagnetic field is adjusted, by changing the current flowing through the coil, the magnets within the device would respond to the change in magnetic field. This method is crude and would require a lot of additional power to effect the strong permanent magnets within the magnetic ‘spring’. A better solution would use the same coil, but instead of introducing a current to the coil, the field would be damped using a controllable variable resistive load. This load would be attached to the two ends of the coil to dissipate the voltage, generated due to Faraday’s Law when a permanent magnet passes through the coil of wire, thus damping the magnets’ motion.

The ‘spring’ effect can be modeled using theories noted in chapter 3, but there is very little experimental data available to confirm if the assumptions made for the analytical models are true. Previous research performed at the University of Reading [15] looked at designing a biologically inspired ant’s leg, figure 2.24 which incorporated magnets to provide compliance within the leg. The research performed basic analysis of magnetic fields between multiple magnets, but the repulsive force fitting equations that were created as part of the research only applied to a specific type of magnetic setup, which did not use standard cylindrical permanent magnets and so leads to three further research questions:

- *Can the magnetic ‘spring’ effect be measured and analyzed accurately?*
- *Can a good analytical model be found to define the magnetic spring characteristics?*
- *Could the magnetic ‘spring’ effect be utilized in suspension systems for space robotics to increase the space rovers capability?*



(a) LabANT with inelastic legs



(b) LabANT legs with magnetic compliance

Figure 2.24: Biologically Inspired Ant Research - LabANT [15]

2.5 Summary

This literature review has demonstrated that there is currently a major lack of experimental data for the magnetic ‘spring’ effect, as well as a comprehensive repulsive force equation to approximate how two cylindrical magnets react to each other when locked to a single degree of freedom along their axis. To address this lack of data, extensive measurements performed under experimental protocols are required, which will build up a library of force curves for Neodymium magnets of different sizes and magnetization densities with respect to separation. These force curves will then be used to create new analytical models that will model magnetostatic interactions between two cylindrical Neodymium magnets in repulsion.

Hall effect sensing, described in section 3.4, can be used to approximately localize a magnet in a single dimension, but due to the properties of magnetic fields and sensor characteristics there needs to be a more robust method to localize magnets using Hall Effect sensing. If multiple magnets are present within the system, the single hall sensor approach cannot distinguish between them, thus creating inaccuracy in measurement and leading to two additional research questions that need to be answered:

- *Can the current inaccuracy in single magnet localization using Hall Effect sensing be improved by employing more sensors or by changing the orientation of the sensors?*
- *Is there a way to accurately localize two magnets using Hall Effect sensing and thus accurately know their separation?*

Section 1.2 consolidates the above research questions, so that they can be referred back to in the conclusion, chapter 7.

Chapter 3

Theory

The design of any system requires an understanding of the underlying mathematics which govern and define the system's characteristics. This chapter sheds light on the equations and theoretical processes used for the verification of equipment and data produced from experimentation. Section 3.1 states some of the underlying magnetic field theory including two of the Maxwell equations; Stokes' divergence theorem and Ampere's law, along with Lorentz forces, magnetic dipole equations and elliptic integrals. Section 3.2 describes the Gilbert Model used for magnetic force calculation, which was used for initial testing and analysis of the expected magnetic fields. This is followed by section 3.3 which explains how Helmholtz coils can be used for sensor calibration and includes a mathematical derivation to define the properties of a Helmholtz coil. Section 3.4 describes the process for determining magnetic field strength using hall effect sensing, with section 3.5 describing how an array of 2D hall effect sensors can extract field magnitude and angle from raw magnetic field measurements, which is the basis of research explored by this thesis.

3.1 Magnetic field theory

This section states some of the magnetic field theories used to calculate forces between magnets. There are a number of notations, symbols and variables used in this section, which are all described in the Nomenclature section, page number xx.

3.1.1 Maxwell equations

Maxwell's equations work in partnership with Lorentz force law to underpin classical electromagnetism. The equations are a set of partial differentials and describe how magnetic fields are created and affected by other fields, electrical currents and point charges.

Two of the Maxwell's equations relevant to this thesis are discussed.

Stokes' divergence theorem (Equivalent Gauss Law)

Gauss law can be briefly stated as “there are no magnetic monopoles”, instead any magnetic field from a material is generated by a dipole. A dipole can be represented as loops of current, but most recognize them as magnetic field lines that can extend to an infinite distance but do not begin or end, figure 3.1.

The differential and integral forms, equations 3.1 and 3.2, for Gauss Law of magnetism are mathematically equivalent, such that the same number of magnetic field lines enter and exit a piece of material with magnetic properties

$$\nabla \cdot \mathbf{B} = 0 \tag{3.1}$$

$$\oint_S \mathbf{B} \cdot d\mathbf{A} = 0 \tag{3.2}$$

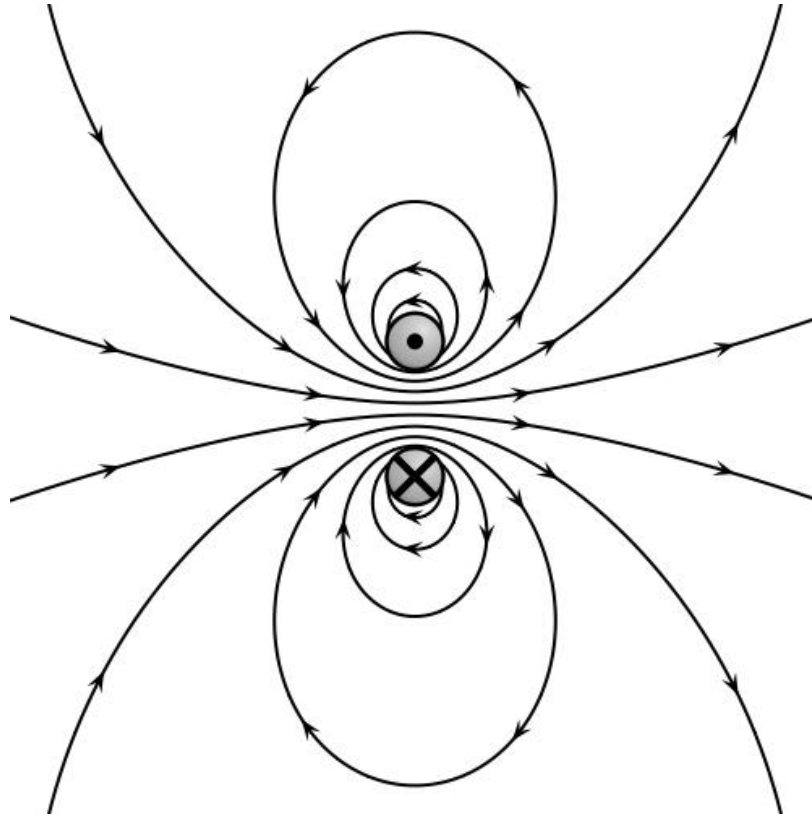


Figure 3.1: Magnetic dipole field representation around a small current loop, plotted using VectorFieldPlot (VFPT) [16]

where $\nabla \cdot$ is the field divergence, \mathbf{B} is the magnetic field, S is any closed surface and $d\mathbf{A}$ is a vector normal to the surface S at a given point with infinitesimal magnitude, thus a differential of S .

Ampere's law

Ampere's law, equation 3.3, relates the flow of current through a loop to the magnetic field generated around the loop. The equation contains a time component to account for fast changes in current but as this thesis only concentrates on quasi static magnetic fields, which do not change position rapidly, the second half of the equation can be dropped leaving equation 3.4

$$\oint_C \mathbf{H} \cdot d\mathbf{l} = \int_S \mathbf{J} \cdot d\mathbf{A} + \frac{d}{dt} \int_S \underline{D} \cdot d\mathbf{A} \quad (3.3)$$

$$\oint_C \mathbf{H} \cdot d\mathbf{l} = \int_S \mathbf{J} \cdot d\mathbf{A} \quad (3.4)$$

where \oint_C is a line integral around a closed curve C , \int_S is a 2D surface integral over S enclosed by C , $d\mathbf{l}$ is a differential of curve C and \mathbf{J} is the total current density. This can be written in a differential form, equation 3.5, as long as the field is constant in time and therefore not changing

$$\nabla \times \mathbf{B} = \mu_0 \mathbf{J} \quad (3.5)$$

where $\nabla \times$ is the curl operator.

3.1.2 Lorentz force law

Lorentz forces due to an electromagnetic field, equation 3.6, are the forces acting on a point charge that is moving through a magnetic or electric field.

$$\mathbf{F} = q(\mathbf{E} + \mathbf{v} \times \mathbf{B}) \quad (3.6)$$

where F is the force acting on a point charge q moving with velocity \mathbf{v} through external electric \mathbf{E} and magnetic \mathbf{B} fields.

Lorentz forces are responsible for creating electromotive forces (EMF) when a conductor is passed through a magnetic field. For some materials such as aluminium these forces are significant enough to observe by holding a strong magnet in your hand and rapidly passing it across an aluminium plate.

3.1.3 Magnetic dipole moment

A current loop has a magnetic dipole moment \underline{m} , equation 3.7 and figure 3.2, such that the magnetic moment is projected along the current loop's axis

$$\underline{\mathbf{m}} = Ia^2\pi\hat{\mathbf{a}} \quad (3.7)$$

where I is the current flowing round the current loop, $a^2\pi$ is the current loop area and $\hat{\mathbf{a}}$ is the unit vector normal to the current loop with radius a .

3.1.4 Current loop equations

A solution to Maxwell's equations for a circular current loop uses elliptic integrals and is given in equations 3.8 and 3.9, which approximates near magnetic fields using the complete elliptic integral of the first kind $K(k)$, the complete elliptic integral of the second kind $E(k)$ and the magnetization strength B_0

$$\underline{B}_z = B_0 \frac{a}{\pi\sqrt{Q}} \left[E(k) \frac{a^2 - \rho^2 - z^2}{Q - 4\rho a} + K(k) \right] \quad (3.8)$$

$$\underline{B}_\rho = B_0 \frac{az/\rho}{\pi\sqrt{Q}} \left[E(k) \frac{a^2 + \rho^2 + z^2}{Q - 4\rho a} - K(k) \right] \quad (3.9)$$

where

$$k^2 = \frac{4a\rho}{(\rho + a)^2 + z^2} = \frac{4a\rho}{Q} \quad (3.10)$$

and

$$Q = (\rho + a)^2 + z^2 \quad (3.11)$$

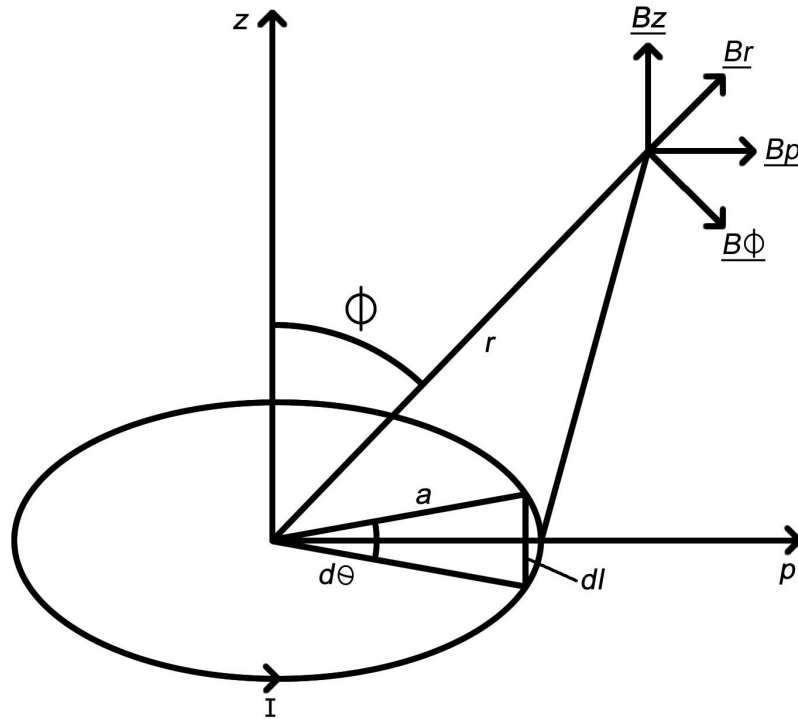


Figure 3.2: Fields associated with a current loop

3.1.5 Far field approximations

If r is significantly large compared with a , the elliptic equations can be approximated with equations 3.12 and 3.13

$$\underline{B}_r = \frac{\mu I a^2 \sin \phi}{4 r^3} \quad (3.12)$$

$$\underline{B}_\phi = \frac{\mu I a^2 2 \cos \phi}{4 r^3} \quad (3.13)$$

where r is the separation between two magnetic poles and I is the current flowing around the loop.

3.2 Force between magnets

The following sections describe a number of approaches for the calculation of force between two magnets.

3.2.1 Magnetic dipole force in a magnetic field

The force of a magnetic dipole positioned within a magnetic field can be computed with equation 3.14 [72]

$$\underline{F} = \nabla(\underline{\mathbf{m}} \cdot \underline{\mathbf{B}}) \quad (3.14)$$

which can be simplified using Boyer's form [72] to equation 3.15

$$\underline{F} = (\underline{\mathbf{m}} \cdot \nabla)\underline{B} \quad (3.15)$$

where $\underline{\mathbf{m}}$ is the magnetic dipole moment and \underline{B} is the magnetic field.

It is difficult to use Boyer's form [72] in practice, but there are other approximations such as the Gilbert model to calculate the force between two magnets.

3.2.2 Gravity analogue equations

The force between two magnetic poles [73], equation 3.16 and figure 3.3, results in either a positive or a negative value that represents a repelling or attracting force respectively

$$F = \frac{\mu q_{m_1} q_{m_2}}{4r^2\pi} \hat{\underline{r}} \quad (3.16)$$

where μ is the permeability of surrounding medium, q_{m_1} & q_{m_2} are the magnetic pole

strengths, r is the separation between q_{m_1} & q_{m_2} and \hat{r} is the unit radial vector.

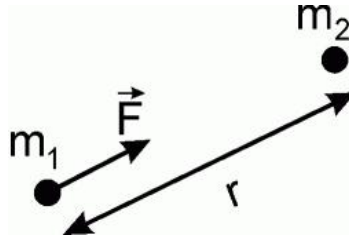


Figure 3.3: Gravity analogue for force between two magnetic poles

3.2.3 Gilbert Model for Magnetic Repulsion Force

The Gilbert model assumes that magnetic charges near the poles of a magnet are responsible for the forces between two, or more, magnets. This assumption is technically incorrect, but the Gilbert model does provide a relatively close match to real world observations. Gilbert provides a form for cylindrical magnets in repulsion [74], equation 3.17, as long as the magnets are aligned along the same axis, figure 3.4

$$F(x) = \frac{\pi\mu_0}{4} M^2 R^4 \left[\frac{1}{x^2} + \frac{1}{(x+2t)^2} - \frac{2}{(x+t)^2} \right] \quad (3.17)$$

where R is magnet radius, t is magnet thickness, M is the magnetization of the magnets and x is the separation between the magnets repelling faces.

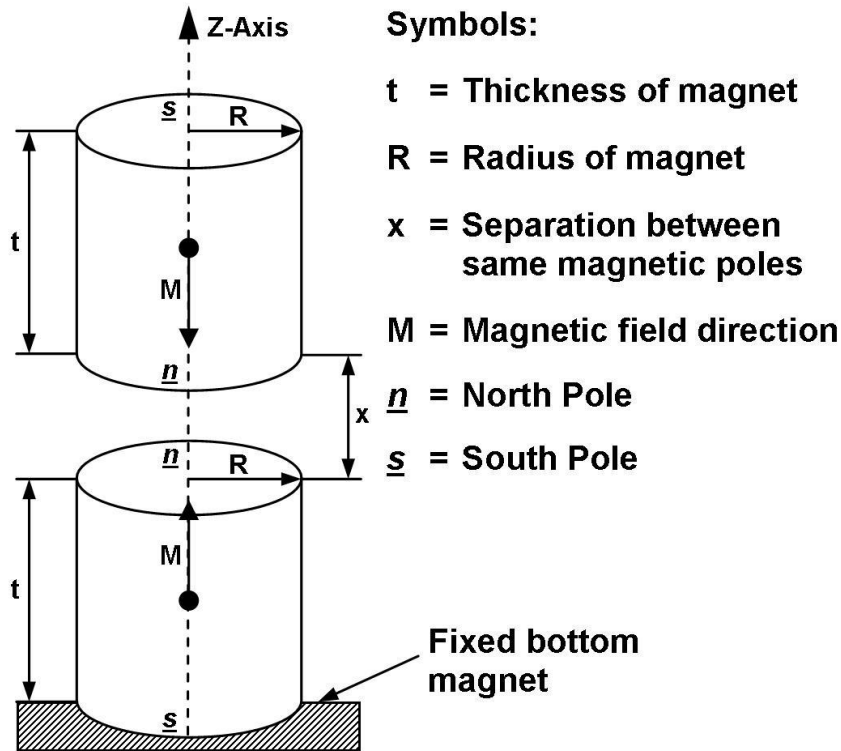


Figure 3.4: Two concentric cylindrical permanent magnets held so that the bottom magnet is fixed and the top magnet can only move in the z-axis

3.3 Sensor calibration using a Helmholtz coil

Helmholtz coils, named after a German physicist Hermann von Helmholtz, produce a constant near parallel magnetic field over a large area and are often used for calibration of devices which are subjected to magnetic fields. Helmholtz coils are recognizable from their physical properties, as the separation between the two coils is equal to the coil radius, with a mathematical model, equation 3.24, such that a Helmholtz coil can be tailored to specific requirements. The coils each contain a similar number of turns and are both supplied by the same constant DC current source, normally the coils are wired in series, so that they both produce a magnetic field in the same direction.

3.3.1 Helmholtz coil Derivation

To calculate the magnetic field of a current loop (figure 3.2), equation 3.18 is derived from Biot-Savart's Law [75]. The differential form (equation 3.18) is integrated for the full loop causing all the elements that are perpendicular to the axis to cancel, simplifying to equation 3.19

$$dB = \frac{\mu_0 I}{4\pi} \frac{dl \times \hat{r}}{r^2} \quad (3.18)$$

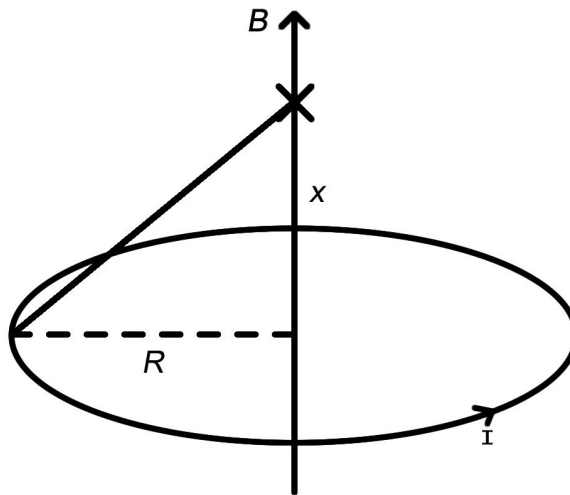


Figure 3.5: Magnetic field on the axis of a circular current

$$B = \frac{\mu_0 I R^2}{2(R^2 + x^2)^{3/2}} \quad (3.19)$$

where B is the magnetic field strength, μ_0 is the permeability of free space, I is the current flowing around the loop, R is the loops radius and x is the axial distance from the loop.

To calculate magnetic field strength B for multiple wire turns (figure 3.5) at any point x along the central axis of the loop, also known as the axial field, equation 3.19 is adapted, assuming that the cross section of the coil is a point, the equation can be

extended to include multiple wire turns n as seen in equation 3.20.

$$B = \frac{\mu_0 n I R^2}{2(R^2 + x^2)^{3/2}} \quad (3.20)$$

The central point between the coils is the point of interest in a full Helmholtz coil and as the separation between the coils is equal to the radius $x = R$, it can be determined that the coils must be positioned from this midpoint at $x \pm R/2$ which can be substituted into equation 3.20 to produce equation 3.21.

$$B = \frac{\mu_0 n I R^2}{2(R^2 + (x \pm (R/2))^2)^{3/2}} \quad (3.21)$$

Which, by separating out the constants, can be re-written as

$$B = \frac{\mu_0 n I R^2}{2} \left(\frac{1}{(R^2 + (x \pm R/2)^2)^{3/2}} \right). \quad (3.22)$$

By assigning B_1 to the magnetic field strength due to coil 1 and B_2 to the magnetic field strength due to coil 2, the magnetic field strength B can be defined by $B = B_1 + B_2$.

Since B_1 and B_2 are given by

$$B_1 = \frac{\mu_0 n I R^2}{2} \left(\frac{1}{(R^2 + (x - R/2)^2)^{3/2}} \right)$$

and

$$B_2 = \frac{\mu_0 n I R^2}{2} \left(\frac{1}{(R^2 + (x + R/2)^2)^{3/2}} \right)$$

the magnetic field strength at any point can be found by equation 3.23

$$B = \frac{\mu_0 n I R^2}{2} \left(\frac{1}{(R^2 + (x - R/2)^2)^{3/2}} + \frac{1}{(R^2 + (x + R/2)^2)^{3/2}} \right). \quad (3.23)$$

By varying the value of x it is now possible to calculate the magnetic field strength at any point along the axial field which can be seen in figure 3.6.

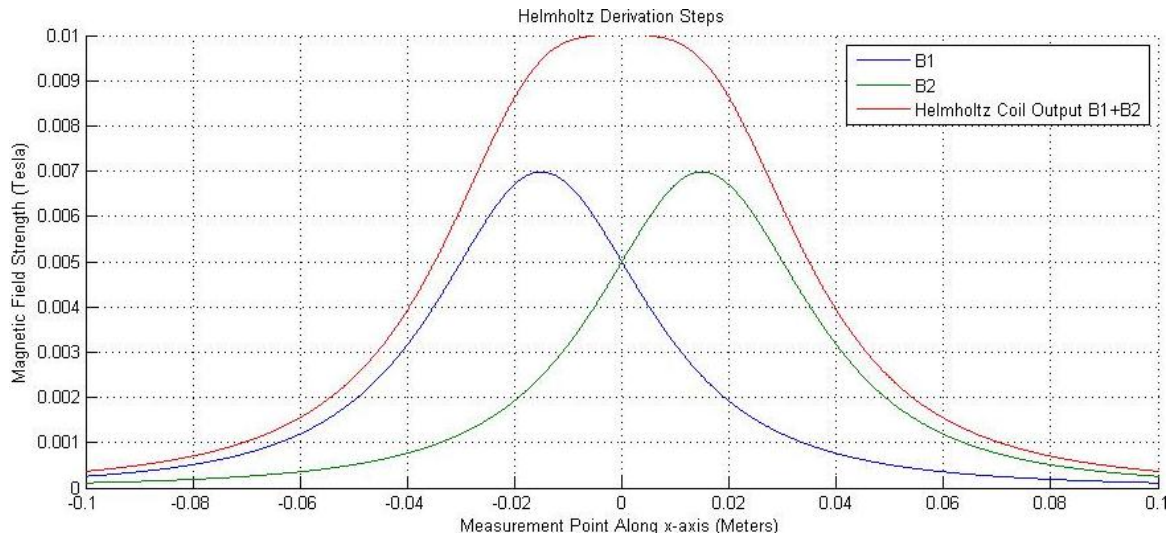


Figure 3.6: Graph showing magnetic field strength of B_1 , B_2 and full Helmholtz coil

This equation 3.21 can now be simplified to produce the final Helmholtz coil model seen in equation 3.24. The simplification steps are explained in appendix A.

$$B = \left(\frac{4}{5}\right)^{3/2} \frac{\mu_0 n I}{R} \quad (3.24)$$

The simplified equation can now be rearranged to solve for other factors such as current required to drive the coil or the number of turns needed to produce a magnetic field of specific magnitude (equation 3.25).

$$n = \frac{RB}{(4/5)^{3/2} \mu_0 I} \quad (3.25)$$

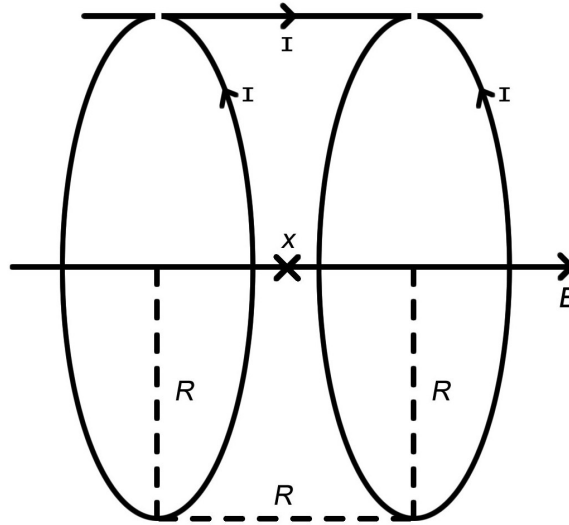


Figure 3.7: Dimensions for a Helmholtz coil with respect to equation 3.25

3.3.2 Helmholtz coil specifications

The mathematical model of the Helmholtz coil in the previous section details the expected field characteristics from known parameters, but does not take into account the physical creation of the coils. To create a Helmholtz coil certain considerations such as the gauge of wire are required, otherwise the coil could overheat or be too bulky to fit in the required area. To calculate the required length of wire L in meters needed for each coil, the circumference of the coil is multiplied by the number of turns (3.26) calculated in equation 3.25.

$$L = 2\pi Rn \quad (3.26)$$

To calculate the Helmholtz coil power dissipation, $P = I^2 \mathbf{R}$, the wire resistance for the coils needs to be known. The larger the diameter the wire is, the lower the resistance per meter, table 3.1. The coils total resistance is proportional to wire length giving equation 3.27.

SWG	Resistance (Ωm^{-1} at 20°C)	Diameter (mm)
14	0.00532	2.108
16	0.00831	1.630
18	0.01480	1.220
20	0.02630	0.914
22	0.04340	0.711
24	0.07030	0.558
26	0.10500	0.457
28	0.15500	0.376

Table 3.1: Comparison of Standard Wire Gauge (SWG) characteristics

$$P = I^2 r L \quad (3.27)$$

To produce a coil with a cross section that is roughly square in shape, the number of turns n first needs to be square rooted $S = \sqrt{n}$ to find a starting number. This starting number S is then used to locate the non-negative integers on either side of the real number, floor f and ceiling c . If the non-negative integers f and c when multiplied together are greater than the number of turns n then the correct ratio has been found, otherwise increment the c and repeat the process until the result is larger than n .

In psudo code this looks like:

```
while ((f * c) < n) { c = c + 1 } return (f, c)
```

The final step is to then calculate the area required for the coils to be located in, which is easily done by taking f and c and multiplying them by the wires diameter d , equation 3.28.

$$\begin{bmatrix} f \\ c \end{bmatrix} d = \begin{bmatrix} \text{coil dimension in x} \\ \text{coil dimension in y} \end{bmatrix} \quad (3.28)$$

This section has explained how to calculate both the mathematical model and the physical characteristics of a Helmholtz coil and as such enables the design and use of a Helmholtz coil for calibration and measurement tasks performed during the research described in this thesis.

3.4 Hall Effect Sensing

Hall Effect sensing is used for many applications that require a high level of repeatability and reliability. It has many applications ranging from non-contact measuring of glass and paper thickness to contactless position and rotation sensing of a motor shaft. Hall effect sensing is achieved by passing a known constant current through a conductive plate, figure 3.8, so that when a non-parallel external magnetic field is applied, the electrons in the plate experience a Lorentz Force. This force curves the path of the electrons, figure 3.9, which creates a charge imbalance between the sides of the plate that can be measured and amplified.

Hall effect sensing is very reliable but the Hall element will only produce a charge imbalance with respect to the observed magnetic field magnitude. Thus if the magnetic field is angled then the Hall sensor will not measure the full field magnitude. Another problem with Hall effect sensing is that magnets are never exactly the same, so the field observed from one magnet could be very different to another, thus each magnet will require a calibration routine before use.

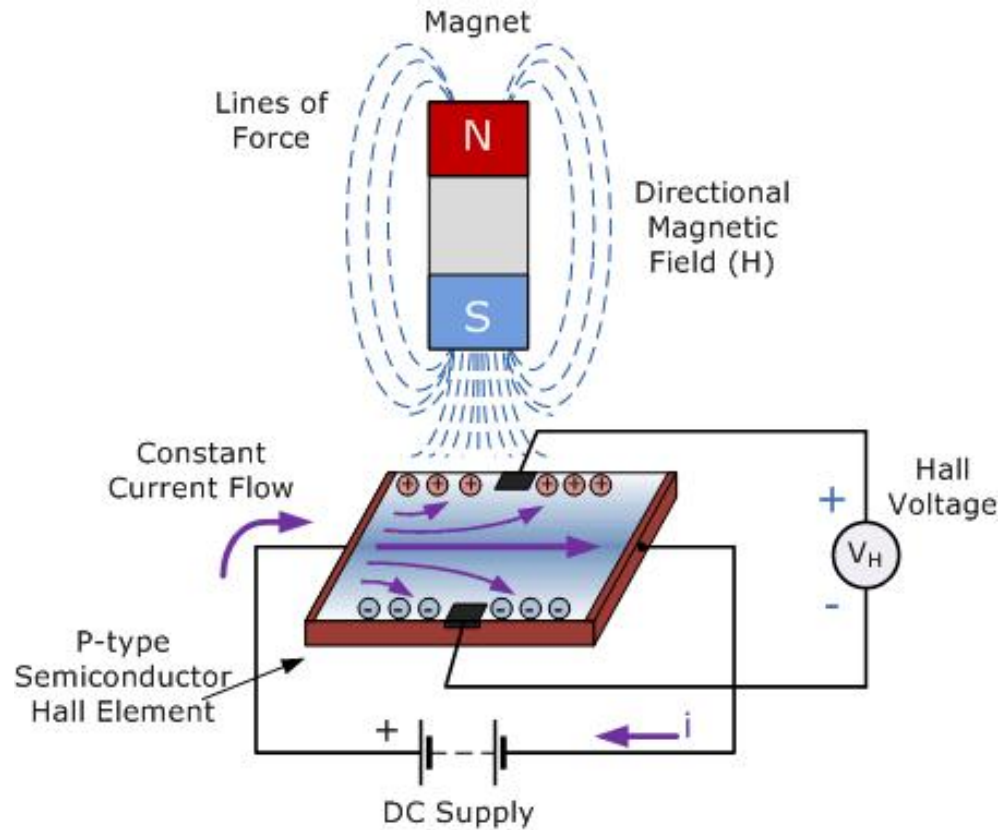


Figure 3.8: Hall effect sensing system diagram

Figure 3.9, displays the four configurations, A to D, of magnetic field (4) and current direction (5), with the electron path displayed as blue balls flowing in a loop (1) passing through the hall element (2), between two magnets (3).

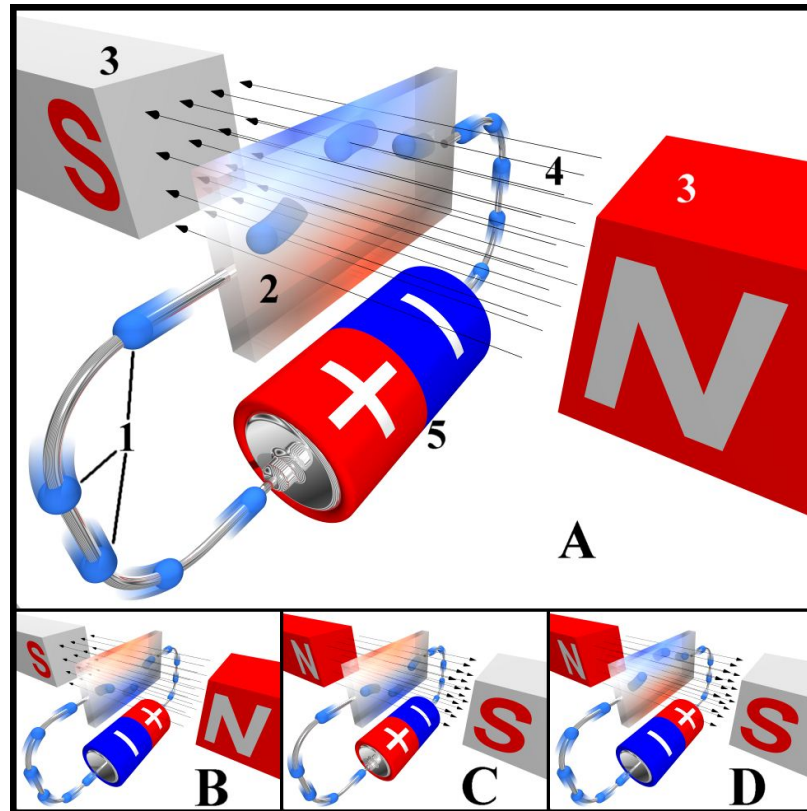


Figure 3.9: The four possible hall effect results from varying the magnetic field and current directions

3.5 Magnetic field measurement using a 2D Hall Effect Array

As the hall effect sensor can only measure field magnitude in a single axis, any positional or angular misalignment will greatly effect the observed magnetic field; so by using two hall effect sensors mounted perpendicular with respect to each other, the two field magnitudes can be resolved. Knowing the field magnitudes for example in the x-axis and y-axis, the relationship between the magnitudes, using trigonometry, can be calculated in terms of the magnetic field angle θ and magnitude B , equations 3.29 and 3.30

$$\theta = \tan^{-1} \frac{B_y}{B_x} \quad (3.29)$$

$$B = \sqrt{B_x^2 + B_y^2} \quad (3.30)$$

where B_x and B_y are the magnitudes measured by each Hall Effect Sensor.

This sensor fusion resolves the magnetic field angle and magnitude at a single point where the two sensors are located. If multiple groups of sensors are distributed along the x-axis, an approximate magnetic field profile can be generated from the data. This leads to scalable sensing which enables the solution to fit the application. The sensing can be performed using a microprocessor, so that the data is processed in real-time and will give an instantaneous result.

This approach was tested using four 2D sensor groups, section 5.2.2, which led to the development of an algorithm to approximate a free magnet's location using magnetic field measurements. This algorithm assumed that the magnets used were identical with their motion constrained to a single shared axis, with one magnet fixed in space, figure 3.4.

3.6 Chapter Summary

The equations and theoretical processes described in this chapter form the basis for continued work within this thesis. The first section on Maxwell equations allows for the calculation and predicted of expected output from theoretical models used to verify experimental results, but also gives insight into the expected outcomes of sensor calibration. This leads onto the analysis of the Gilbert Model which is widely used to describe the force between two perfect magnets, both in attraction and repulsion. The

Gilbert Model however is not a true representation of the force between magnets as proven through experimental processes, described in section 5.2.1, with the results and analysis discussed in section 6.2.1. The mathematical derivation of the Helmholtz coil describes the underlying theory which can be used in further experimentation, section 5.1, to calibrate the Hall Effect sensors in a magnetic field of known magnitude and direction. The theoretical results from the derived equations matches the real world experimental data, section 6.1, to a high degree of accuracy and was also confirmed through FEA techniques, section 4.4. The final section of this chapter explains the process of Hall Effect sensing which forms the basis for continued experimentation and data recording. The Hall Effect allows the magnitude of a magnetic field perpendicular to the Hall Element to be measured, but this does not take into account the direction of the field. To improve on this sensing limitation a second Hall Effect sensor is added, allowing for the determination of both field angle and magnitude at the Hall sensing point. This additional sensor provides a wider range of possible readings to be taken. When the Hall Effect sensors are used in pairs, that have been distributed along an axis parallel to the motion of a magnet, algorithms created for this thesis, section 6.5, enable the location of a moving magnet to be determined. In conclusion, this chapter provides a solid base for continued experimentation through the thorough understanding of the existing mathematical models for the field of magnetics, as well as measurement techniques that are relevant for non-contact sensing of a magnets location.

Chapter 4

Magnetic Simulations & Validation Experiments

In modern Computer Aided Design (CAD), simulation techniques play a large part in design verification through the use of various techniques. It is essential when performing simulations that the system is modeled correctly, but also understood as most errors during simulation come from a lack of understanding. With the advent of CAD packages that include FEM/FEA tools it has become possible to produce simulations with little understanding of the calculations that are used, leading to simulation errors which may look correct to the user but are very wrong. The common mistakes made when performing simulations [76] are:

- Too much detail of the models simulated
- Incorrect material specifications when defining the simulation model
- Incorrect resolution of the simulations mesh solver
- Incorrect units used in constrains such as boundary conditions
- Programming language selection not suitable for application area

- Unverified or invalid models due to lack of understanding
- Incorrect initial simulation conditions
- Prematurely halted simulations

To ensure that any model simulated is accurate the model should only contain the items necessary for the simulation, reducing the number of iterations required by the simulation solver. This reduction will also greatly reduce the memory load on the computer used as large simulations can require Gigabytes of storage, as well as increase the rate of simulation due to extraneous data being suppressed. This is also true of incorrectly defined materials used in the simulation as each material has its own set of properties, each of which requires additional processing and memory storage. If a simulation, for example, of a solid rubber ball sitting on a flat immovable surface (Figure 4.1) is to be modeled, the material within the surface does not need to be known as only the surface properties such as friction coefficient are needed to solve the simulation. This principle extends to all simulations, so the system model needs to be understood before the simulation is configured.

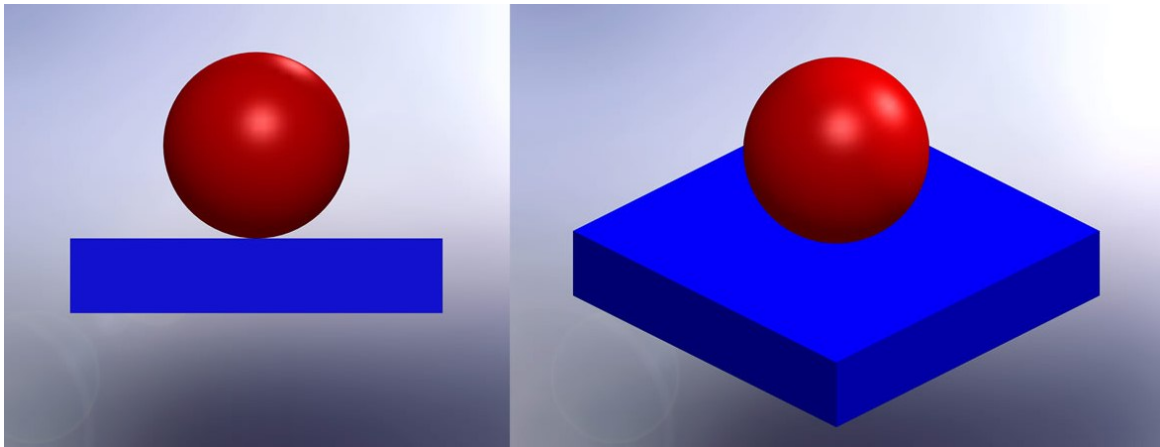


Figure 4.1: Simulation of a rubber ball on a solid flat surface

When creating a Finite Element simulation model it is necessary to define a minimum size or maximum angle, in the case of triangular meshes, for the solver to use. These values define the mesh resolution of the solver for approximation of the results. The value choices here are critical, as a mesh that is too sparse can miss possible structural elements and thus produce incorrect results; a very dense mesh can take an extremely long time to solve, to the point where the computer can run out of resources whilst trying to solve the model. There have been a number of cases in history where a simulation or calculation error involving the conversion of units, for example millimeters and inches [77], has caused the failure of equipment or the loss of entire missions. This is not just limited to mathematical mistakes but also the selection of software or programming language used in a simulation, as these employ different approaches to solving simulations that can produce very different results.

There is generally a lot of faith put into results from simulations [78], so it is essential for any piece of simulation software to be extensively tested and compared to known or measured real world data that the experimenter has available, thereby verifying that the software chosen is suitable for the application required by the experimenter. If the simulation is dependent on any initial conditions, for example time, then these have to be included as accurately as possible within the model otherwise errors will accumulate in the results, whilst still looking accurate. A key point to the success of a simulation is the run time, as a prematurely halted simulation could stop half way through or completely miss a critical factor such as an instability or a harmonic vibration. This would then require the entire simulation to be run again, taking more time and computing power, which whilst not sounding like the end of the world could cost a company millions of pounds to purchase additional time on a supercomputer or computing grid.

There are many different software packages available for simulation of magnetic fields,

but these can cost in excess of £12,000 (at time of writing thesis) for the high end solvers with simple to use GUI's (Graphical User Interfaces), with mid range products costing between £3,000 and £10,000. As the cost of software was not factored into the costs of this PhD, the software available for research purposes included a school research license of SolidWorks 2012 (upgraded over the years from SolidWorks 2009) and FEMM. SolidWorks is a 3D solid modeling package with limited integrated FEM solving ability and FEMM is an open source electro-magnetic FEM/FEA solver, which is able to model magnetic fields in 2D and 2.5D.

The goal of this chapter is to introduce the types of simulation used to support this thesis including ways to increase simulation accuracy, section 4.1, followed by the simulations performed of the ID54 magnet (chosen in section 5.2.1) that is used in experimentation, sections 4.2 - 4.3. The chapter concludes with simulations performed to verify the Helmholtz coil characteristics which confirms the FEMM simulation accuracy for 2.5D electromagnetic problems, section 4.4.

4.1 Simulation Types and Accuracy

This section looks at different simulation types, how different factors affect simulation accuracy and describes ways to increase accuracy in simulations. When a simulation is conceived certain conditions must be considered as these drastically change the type of simulation that is performed, section 4.1.1. Simulation accuracy is normally a compromise between the time required to perform a simulation and the capabilities of the computer performing the simulation. If a complex simulation is required but output accuracy only needs to be on a millimeter scale, then there is no point running the simulation at micrometer accuracy. This may be an obvious point but it is important detail to get correct as simulation solvers calculate their results by operating on a

mesh, section 4.1.2 which is not always defined as a simple grid. Simulations require a scope to solve within as it is impossible in practice to simulate everything that physically surrounds an object, so the scope is limited by a boundary. In simulations involving electromagnetic interactions the problem's boundary also needs to have some conditions defined, section 4.1.3, to correctly limit any fields that are present within the simulations scope.

4.1.1 Types of Simulation

When a simulation is conceived a system model is required to be able to perform the simulations. System models can be 3D representations of objects, equations that return or process data, algebraic systems or statistical models. Simulations also can also be grouped into types [79]:

- 'Discrete Event Simulations' where the simulation waits for events to happen and is dormant between these events, for example a vending machine simulation would not perform any processing before or after dispensing an item
- 'Agent-Based Modeling' where multiple smaller simulations are part of a greater model or problem to be solved, for example modeling the interactions between neurons in a brain
- 'Monte Carlo Simulations' where random samples are used to manipulate simulation parameters to solve stochastic or deterministic problems that are not determined by time
- 'Continuous Simulations' which represent a system, over time, by effecting inputs to differential equations or partial differential equations. One example of these are 'Lotka-Volterra Equations', also known as predator-pray simulations, which

are used to look at how different elements interact using a pair of non-linear, first-order, differential equations, for example a model of how two species interact in an environment

The research performed for this thesis includes Continuous and Discrete Event simulations, that use a range of software including Matlab for data analysis and visualization of data, SolidWorks for 3D modeling of components and static analysis of test rig mechanics, and FEMM for 2D and 2.5D magnetic problem solving.

4.1.2 Meshing and Solver Accuracy

Simulation and solver accuracy is especially important for complex multi-dimensional problems such as 2D, 2.5D and 3D models, so accuracy normally refers to the mesh used to solve these problems. Grids and meshes are used to approximate the shape and structure of the model to be solved so that partial differential equations that have been ‘discretized in space’ [80], can be applied to the mesh and solved. The grid or mesh can be created as either a structured or unstructured grid, figure 4.2, but considerations have to be made when writing the numerical algorithm, as a numerical algorithm designed to run on a structured grid will not run on an unstructured grid, whilst one that was designed for an unstructured grid will run on both grid types.

Both SolidWorks and FEMM use the unstructured grid type for their simulation solvers, with FEMM using triangular meshing to solve its 2D and 2.5D problems and SolidWorks using Tetrahedral meshing solve its 3D problems, figure 4.3. Triangular meshing can be performed in a number of ways including the Bubble mesh method [81] and the Delaunay refinement algorithms [82]. Both methods create a set of tessellated triangles that fill the model area, such that the outline and detail are approximated. The same method is performed by SolidWorks, but instead uses Tetrahedrons to fill

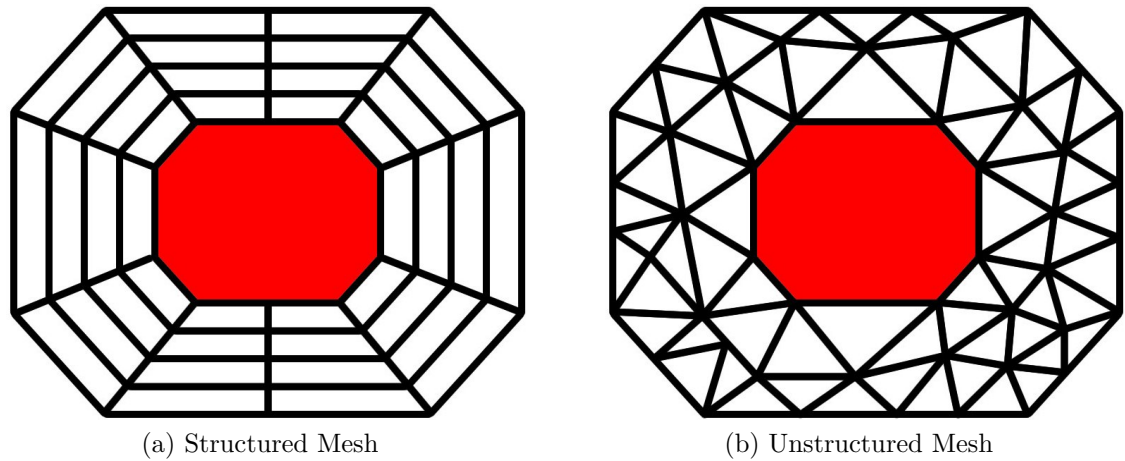


Figure 4.2: Grid types used in simulations

the model in 3D to approximate its shape. All meshes rely on a few key factors such as maximum internal angle and mesh size to determine how their algorithm operates, therefore a mesh with a low maximum internal angle value would keep breaking the largest triangles down until all triangles in the mesh satisfied the maximum internal angle requirement. Depending on the size of the model and the required accuracy of the mesh, a model could have any number of mesh points generated for it but the higher the number of mesh points generated the longer the simulation would take to complete.

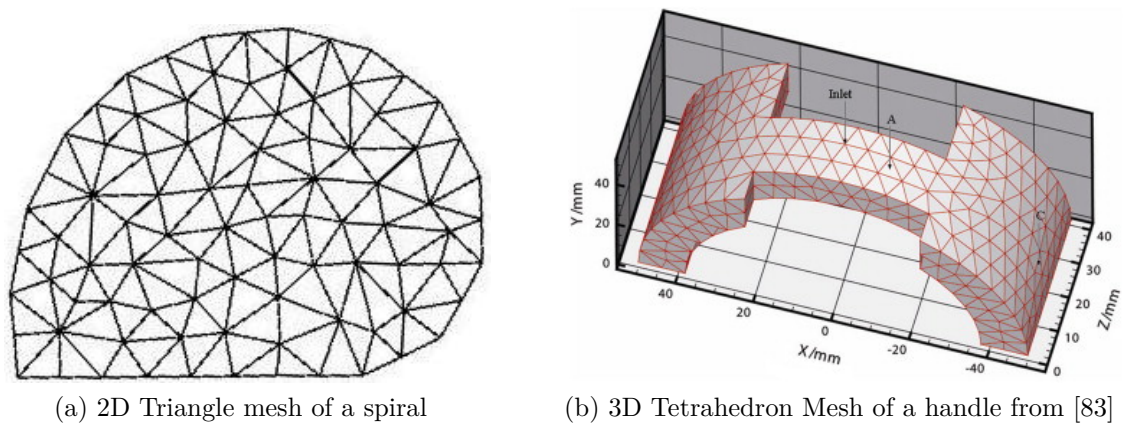


Figure 4.3: Comparison between unstructured 2D and 3D meshes

4.1.3 Boundaries and Boundary Conditions

Simulations require a scope to limit the duration of the simulation and limit the simulations complexity. When working with magnetic field simulations, the magnetic fields are required to satisfy suitable conditions on the boundary of the domain [84]. These boundary conditions can be grouped into four different types with different conditions required for each; Dirichlet, Neumann, Periodic and Anti-periodic. The simulations performed for this thesis use a hybrid mixed boundary type [85] based on the Neumann and Dirichlet types as all fields simulated with FEMM are bounded by a curve. Boundaries can be represented as either discretized steps or as an exact boundary curve using irregular spacing, figure 4.4 [86]. The FEMM software forms its unstructured solving mesh within the boundary condition and represents the boundary by using irregular spacings.

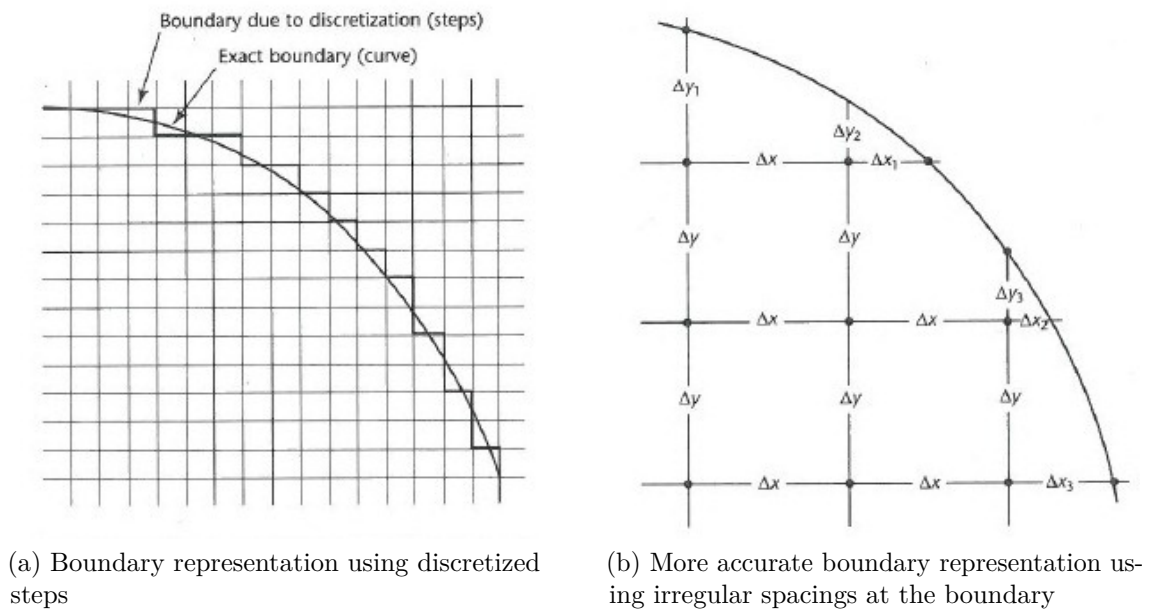


Figure 4.4: Comparison between discretized and irregular boundary representation

4.2 Simulation of a Single ID54 Magnet

The magnet chosen for experimentation, section 5.2.1, is composed of grade N42 Neodymium ($\text{Nd}_2\text{Fe}_{14}$). The grading refers to the magnets material composition, where the number after the “N” is the strength of magnetization, which is essential to know so that the correct model characteristics can be used in simulations. Defining a simulation requires some other characteristics to be known, such as what the problem type is, the scope of the simulation, the units involved, the solver precision and meshing properties. The simulation problem types available in the FEMM software are ‘Planar Solving’ and ‘Asymmetric Solving’, 2D and 2.5D respectively, so that the problem can be approached in different ways. Caution is required when defining the model and choosing the correct simulation type, as both problem types will solve but one will be accurate with the other not matching real world measurements. To show the differences in solving a simple problem, a model of a single magnet with the same characteristics as the ID54 magnets used in testing, figure 4.5, is solved using both methods and shows the differing results, figure 4.6, even though the model started as the same for both.

The differences between the results are due to how the FEMM software treats the model area depending on the problem type, for example the planar type problem has an additional option of depth in its setup and is projected up perpendicular to the model page, much like looking at a box from above, where as the asymmetric type problem revolves the model around the vertical axis to form a cylinder in this case, thus the difference between 2D and 2.5D modeling.

Figures 4.6a and 4.6b show the graphical representation of magnetic field magnitude, the colors indexed by the legend, as well as the magnetic field lines, where a huge difference in field shape between the two results is visible. The red lines displayed in

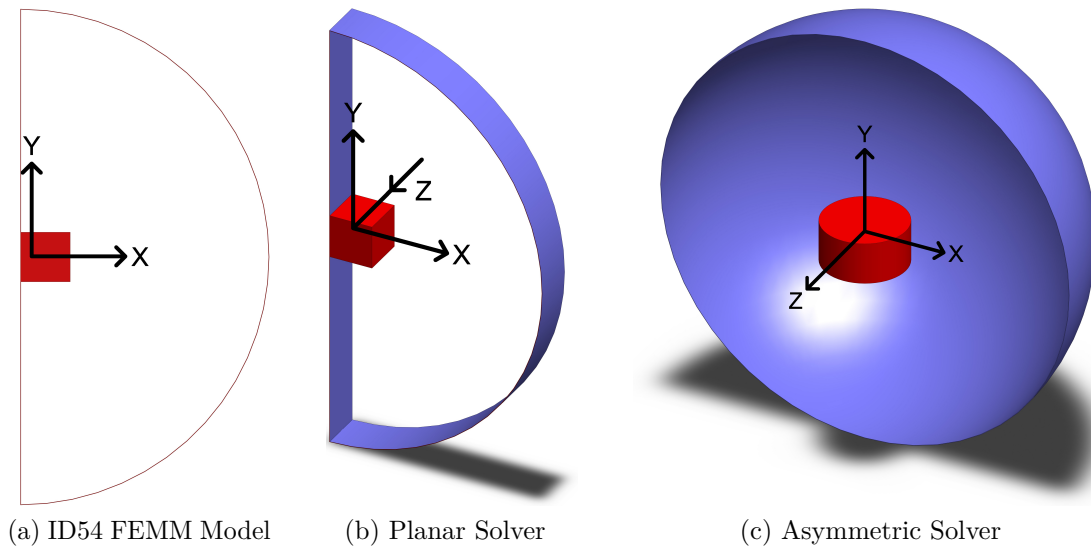
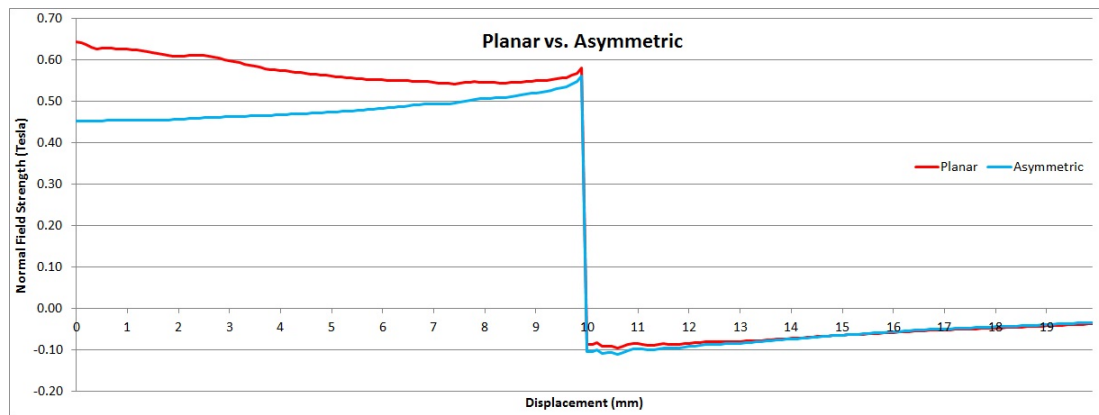
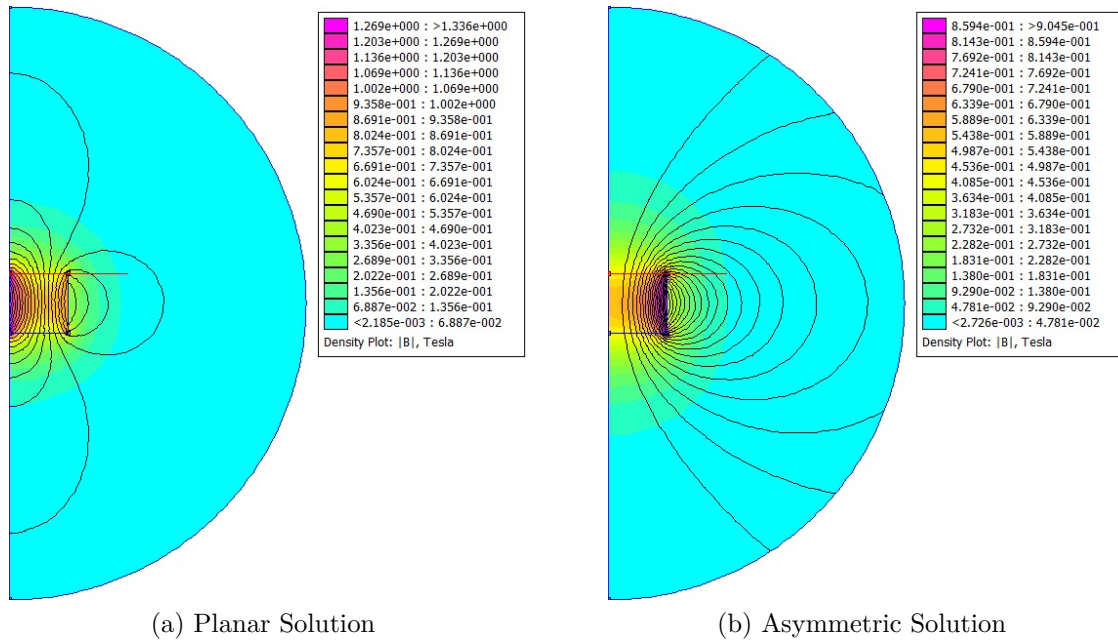


Figure 4.5: ID54 Simulation model with the different solver approaches

figures 4.6a and 4.6b were used to define the output profile from the FEMM solver, so that data could be retrieved and compared. Figure 4.6c shows a comparison between the two simulations, denoted by the red line in figures 4.6a and 4.6b, which are plotted as the normal field strength (T) against the displacement (mm). The characteristics of the ID54 magnets are known, so the expected normal magnetic field strength should be $0.46T$ at the surface of the magnet, which matches the field simulated by the asymmetric solver as expected as the ID54 magnets are cylindrical rather than cube shaped.



(c) Data Comparison between the Planar and Asymmetric Solvers

Figure 4.6: Comparison between the Planar and Asymmetric solutions

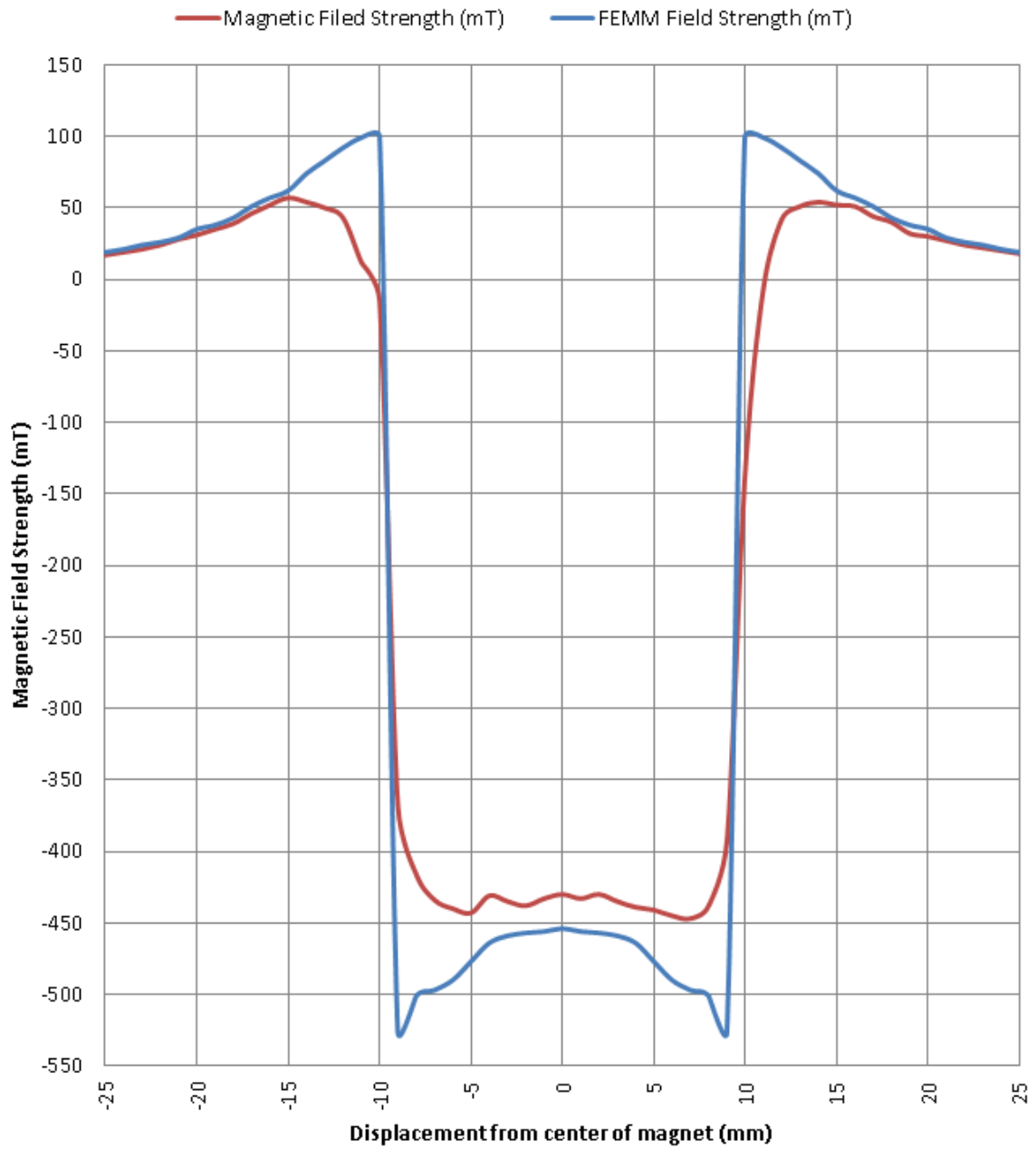


Figure 4.7: Comparison between the FEMM simulation and measured results

Validation Experiment of Single ID54 Magnet

To confirm the simulation results, a simple test using a calibrated Hall probe was devised, where the probe was passed in a straight line over the surface of the ID54 magnet traversing the central axis of the magnet and extending $\pm 25mm$ from the central axis, with readings taken at mm increments, figure 4.7. The differences between the measured and simulated results are due to a number of factors including the thickness and angle of the Hall probe, the hall probes accuracy and the positional accuracy during experimentation. Comparison between simulated and measured results, Table 4.1, shows the FEMM software is capable of accurately simulating the models required for this thesis, therefore FEMM was chosen as the tool for further simulations. The table headings have been shortened to fit the table onto the page, so the column heading X_{mm} denotes the Probe position from the magnets central axis in mm , M_{mT} is the measured magnetic field strength in mT and F_{mT} is the simulated magnetic field strength in mT from FEMM.

X_{mm}	M_{mT}	F_{mT}	X_{mm}	M_{mT}	F_{mT}	X_{mm}	M_{mT}	F_{mT}
-25	17	19	-8	-416	-501	9	-393	-526
-24	19	21	-7	-434	-497	10	-135	100
-23	21	24	-6	-440	-490	11	-6	99
-22	24	26	-5	-443	-477	12	42	92
-21	28	29	-4	-431	-464	13	51	83
-20	31	35	-3	-435	-459	14	54	74
-19	35	38	-2	-438	-457	15	52	62
-18	39	43	-1	-433	-456	16	51	57
-17	46	51	0	-430	-454	17	44	51
-16	52	57	1	-433	-465	18	40	43
-15	57	62	2	-430	-457	19	32	38
-14	54	74	3	-435	-459	20	30	35
-13	50	83	4	-439	-464	21	27	29
-12	43	92	5	-441	-477	22	24	26
-11	12	99	6	-445	-490	23	22	24
-10	-15	100	7	-447	-497	24	20	21
-9	-368	-526	8	-438	-501	25	18	19

Table 4.1: Comparison between simulated and measured results, where X_{mm} denotes the Probe position from the magnets central axis in mm , M_{mT} is the measured magnetic field strength in mT and F_{mT} is the simulated magnetic field strength in mT from FEMM

4.3 Simulations of two ID54 Magnets

Section 4.2 proved the accuracy of FEMM as a simulator of magnetic fields using experimental data to confirm the results. This section uses FEMM to produce a range of simulations to display the expected fields found between two identical ID54 magnets in repulsion that share a common axis. These simulations are experimentally confirmed using the experiments described in chapter 5, with the results of experimentation and data analysis described in chapter 6. The FEMM model for these simulations, figure 4.8, was created using the same parameters as the simulations described in the last section to ensure correct simulation parameters. The ID54 magnet characteristics (radius r and thickness t) and the separation between the magnet faces, x , are all defined in mm to ensure accuracy. The magnets are aligned along their central axis,

so that the the asymmetric solver can be used, with the magnetization directions set at $\pm 180^\circ$ to define the internal characteristics of the ID54 magnets.

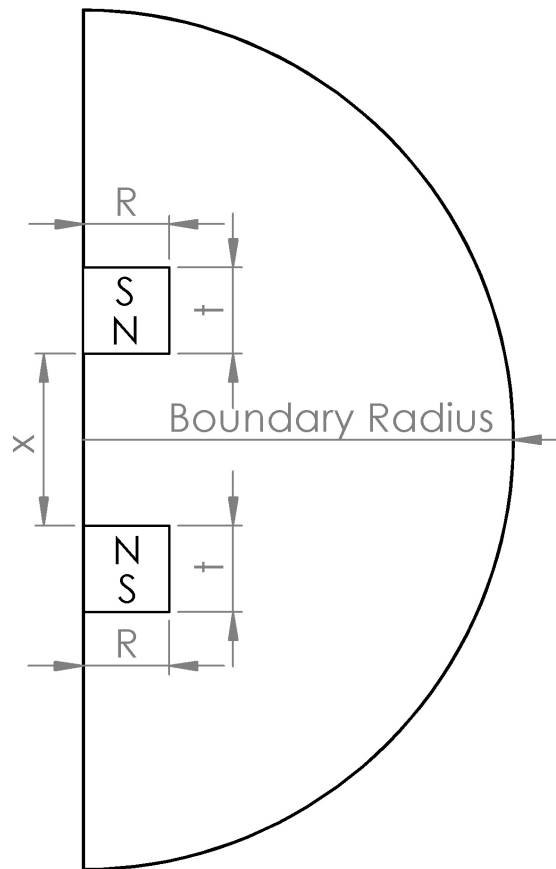


Figure 4.8: FEMM model for the dual ID54 magnet simulations

The dual magnet model was simulated multiple times, with the separation between the two magnets being reduced each time until the magnet faces were touching, which provided a good range of magnetic field data to evaluate. The simulations at magnet separations $40mm$, $20mm$ and $0mm$, show magnetic field lines but the magnetic field strength color gradient has been removed for clarity, figure 4.9.

Figure 4.9 shows the expected magnetic field results for multiple magnet separations, which are used as a benchmark for data analysis, chapter 6, as well as reference during algorithm development, chapter 6.4.

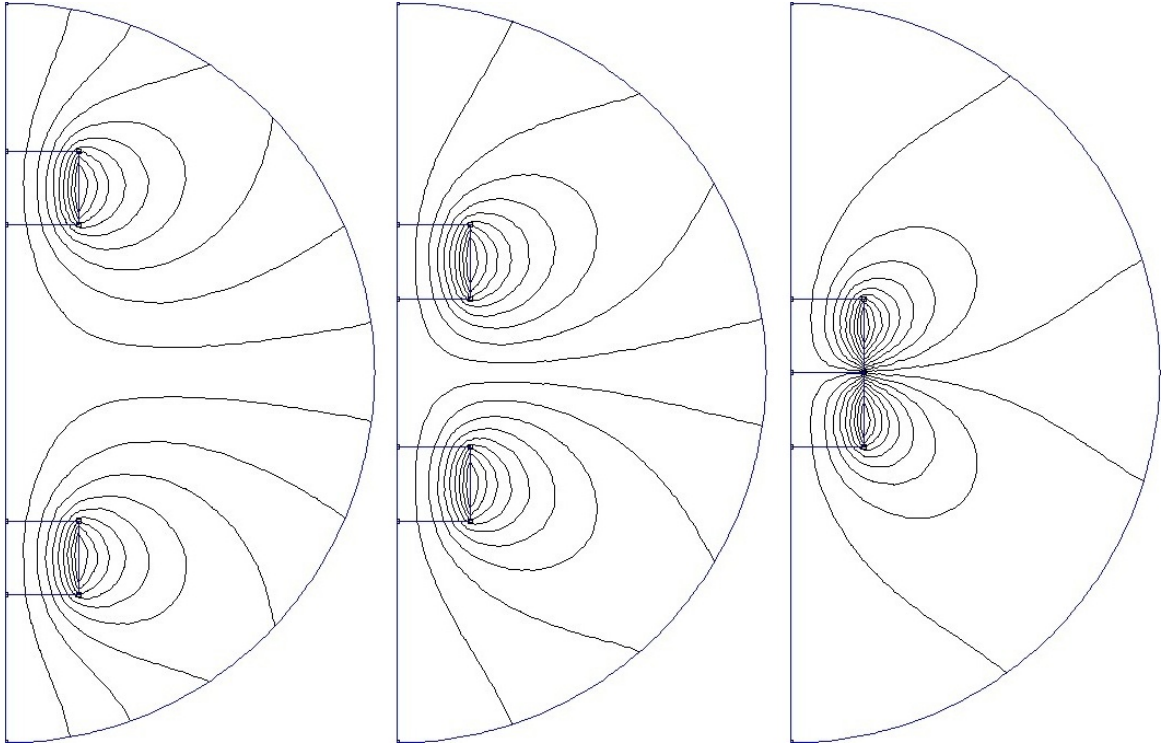


Figure 4.9: FEMM simulation results for magnet separations: $40mm$, $20mm$ and $0mm$

4.4 FEMM of Helmholtz coil

Section 3.3 describes a Helmholtz coil that was designed to facilitate sensor calibration, so to confirm the theory a FEMM model was created and simulated, figure 4.10.

The FEMM model of the Helmholtz coil uses the same parameters described in section 3.3 for coil dimensions and coil current. The output from the simulation was defined using the horizontal red line, so that a comparison between the theory, simulation and measured results, figure 6.1 in section 6.1, shows that all approaches give the same results as expected.

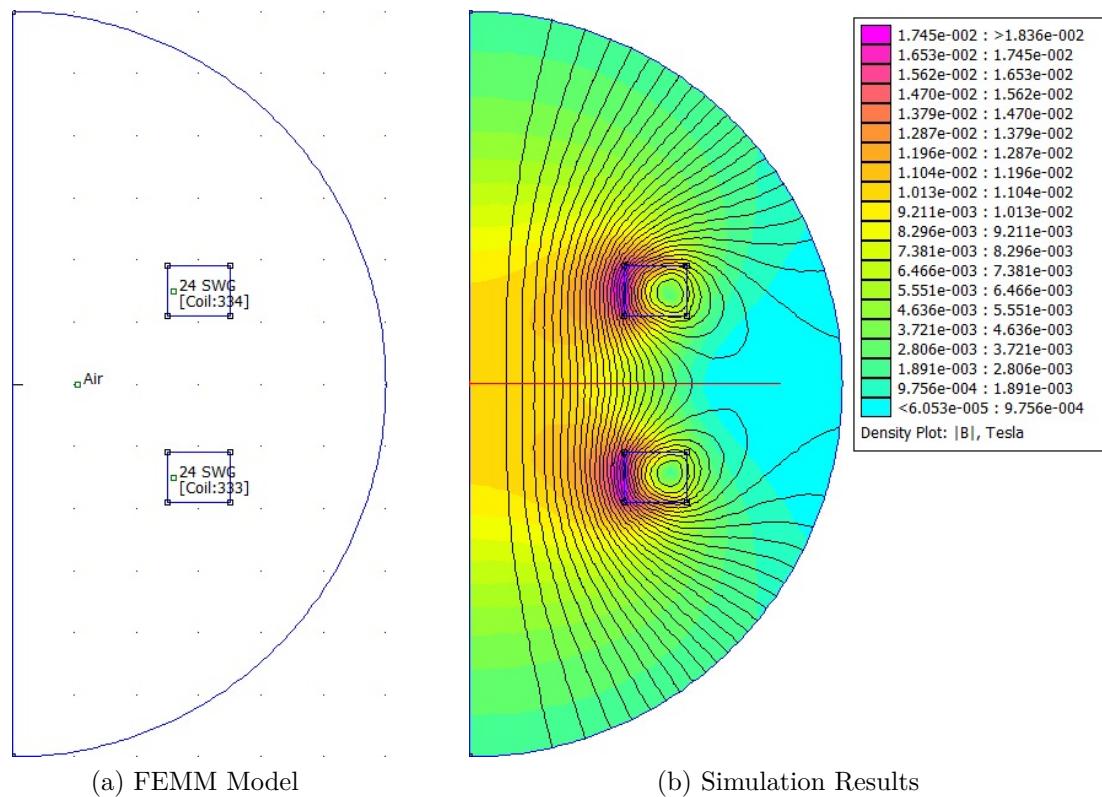


Figure 4.10: Model and simulation results for the Helmholtz coil

4.5 Chapter Summary

This chapter has introduced simulation techniques used in FEM and FEA based software packages, including ways to ensure accurate simulation results are produced from a vast array of possible simulation settings. The simulation approaches discussed in this chapter have allowed accurate simulations to be performed to confirm research results analytically.

Simulations using FEMM confirm the expected field strength of a single ID54 magnet, section 4.2, as well as expected field properties, such as field shape, through comparison with real world results.

The simulation of two ID54 magnets in repulsion, section 4.3, helped to visualise the expected magnetic fields interacting between the two magnets which aided in the

development of the magnet separation algorithm, section 6.5.

The chapter ends with a FEMM simulation of the Helmholtz coil, section 4.4, which will be used to calibrate the Hall Effect sensors, the results of which show a high degree of similarity to the real world results, section 6.1.

To conclude, this chapter has shown that simulations can produce very accurate results using analytical approaches such as FEM and FEA, as long as the simulations are fully defined using the correct starting conditions and parameter choices.

Chapter 5

Experimental Setup

This chapter describes the experiments performed which support and confirm the theoretical premise of this thesis. The experiments were:

1. Simple calibration steps (section 5.1) to ensure that measurement equipment was reading correctly and testing accuracy
2. The initial testing rigs (section 5.2) to determine the optimum characteristics of sensors and magnets used with the final testing rig
3. The final experiment (section 5.3) to confirm that two dimensional Hall Effect sensing is an accurate way to predict the location of a free magnet

A Helmholtz coil was fabricated to validate sensor calibration and four test rigs, TR1-TR4, were constructed and tested. The results of these experiments are presented in Chapter 6.

5.1 Sensor Calibration

Sensor calibration is essential for accurate readings to be taken during experimentation. From the simulations performed in Chapter 4 a Hall Effect sensor, SS49E manufactured

by Honeywell, was chosen from a range of Hall Effect sensors due to its sensing characteristics. The SS49E operates on a 5 volt DC supply and provides a sensing range of ± 1000 Gauss (equivalent to ± 0.1 Tesla) with a linear output of 1 to 4 volts DC. This made it an ideal choice due to the strength of magnets used and the rate that magnetic field strength drops off with distance. The SS49E is also very simple to interface with, as a single 5 volt supply and ground produce a low noise analog voltage output due to its thin film resistor construction which can be tied directly into an ADC or a PIC. To ensure that the sensors confirm the theory and simulations are accurate some simple tests, sections 5.1 & 5.3.1, were performed to confirm that all sensor channels were accurate.

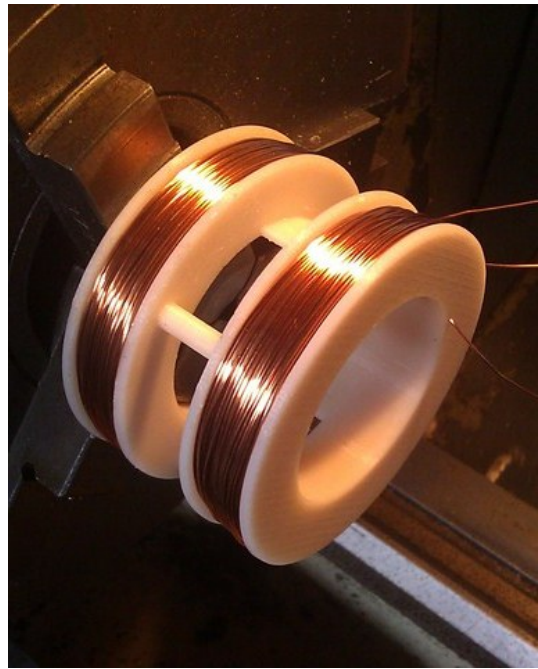
Single Hall Effect sensor in a Helmholtz coil

To confirm that the chosen SS49E sensors performed as expected, they were used in conjunction with a Helmholtz coil. The Helmholtz coil used for calibration testing was created using the same physical parameters as the one defined in section 3.3. The coil was manufactured by winding the coils onto a 3D printed bobbin, figure 5.1. For details of manufacture see Appendix B.

Once the coils had been wound onto the bobbin and connected in series, a DC supply was attached to produce the magnetic field. The specifications of the Helmholtz coil required a 1A DC power supply to produce the required 100 Gauss (0.01 Tesla) field. To create these conditions the Helmholtz coil was connected to a stabilized laboratory power supply which was limited to provide a maximum of 1A current even if a higher voltage was selected. The field was checked using a calibrated Hall probe, which confirmed a field magnitude of 100 Gauss at the center of the Helmholtz Coil (figure 5.2).



(a) 3D printing the Helmholtz bobbin



(b) Helmholtz bobbin with windings

Figure 5.1: 3D Printed Helmholtz bobbin and Helmholtz coil

The next test performed echoed the simulation done previously, section 4.4, to confirm the cross axis field of the Helmholtz coil. This test used the calibrated hall effect probe, figure 5.2, with field magnitude readings taken at $1mm$ increments as the probe was translated perpendicular to the field direction starting from the center of the coil. This test was repeated using the Honeywell SS49E hall sensor to confirm its operating parameters. The results of this testing, figure 6.1 in section 6.1, show a good correlation between the simulation results and the measurements taken with the two different hall effect devices, thus proving that the sensor is calibrated correctly and is suitable for further experimentation.

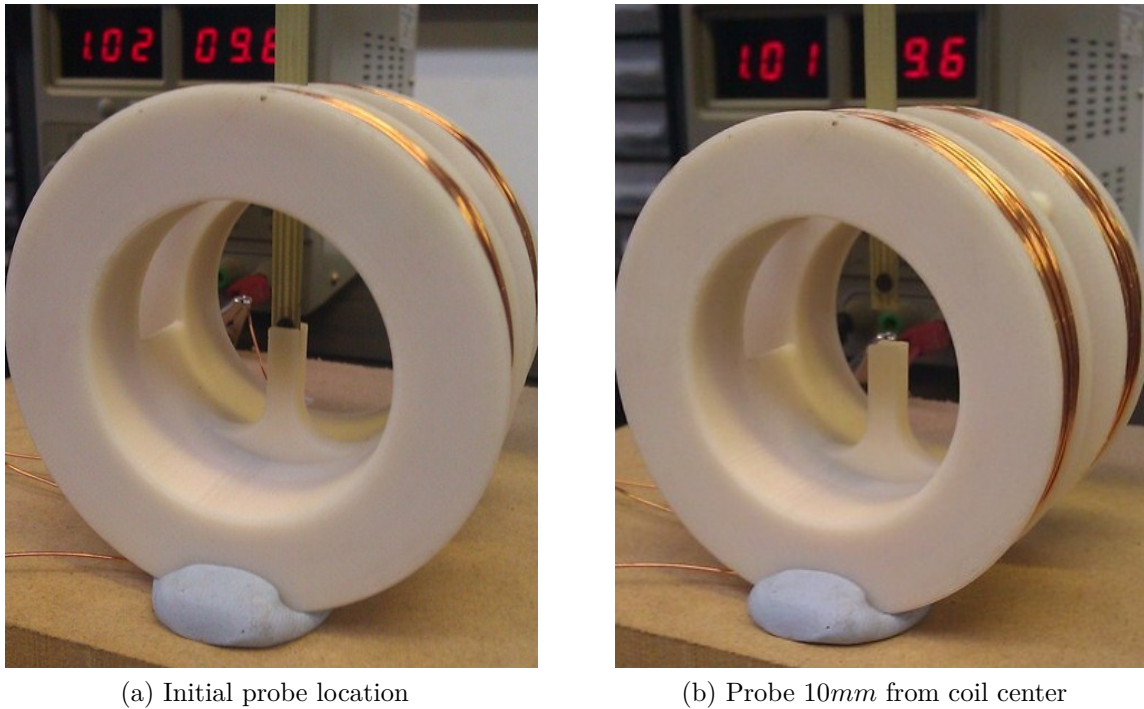


Figure 5.2: Hall effect probe displacement test of the Helmholtz coil

5.2 Experimental Rig Development

The manufacture of instrumentation hardware to support this thesis required a number of revisions before the final design could be fully defined. The following sections explain how each of the test rigs operated, including interfacing with recording equipment and the expected targets and outcomes from the experimentation. From this point onwards the test rigs are referred to as a number with the prefix ‘TR’, for example Test Rig 4 will be referred to as ‘TR4’

5.2.1 Test Rig 1

The first testing rig was a simple suspension system with no incorporated data recording devices which had the ability to test a range of magnets with various diameters and thicknesses. An experimental goal for TR1 was to determine the most suitable magnet

for continued experimentation as there were many to choose from, with a second goal to experimentally derive an equation to express the repulsive force in Newtons between the two magnets due to the inaccuracy of the Gilbert Model described in section 3.2. The magnets considered are given in table 5.1. This section describes the mechanical design and experimental setup required for running these tests to satisfy the goals stated with the results of experimentation located in section 6.2.1.

Magnet ID	Thickness (mm)	Diameter (mm)	Magnet Strength (Tesla)
ID 17	1	5	0.20
ID 20	5	5	0.59
ID 21	10	5	0.46
ID 23	1	6	0.20
ID 34	30	8	0.66
ID 43	5	10	0.51
ID 44	10	10	0.52
ID 54	10	20	0.46

Table 5.1: Properties of magnets used with TR1

The design of TR1 required the ability to lock two magnets, configured to repel each other (i.e. both north poles facing, with a single axis of motion) so that they could be moved back and forth in increments and have the repelling force measured in Newtons. The experiment required the magnets to only interact with each other and not with external disturbances to their magnetic fields, so each magnet was mounted in its own plastic holder made from Delrin (Polyoxymethylene) [87]. This approach was chosen due to the range of magnet dimensions to test and because it reduced the complexity of the experiment by holding them all in a standard size container, figure 5.3, which

could then be slotted into the rig for testing.

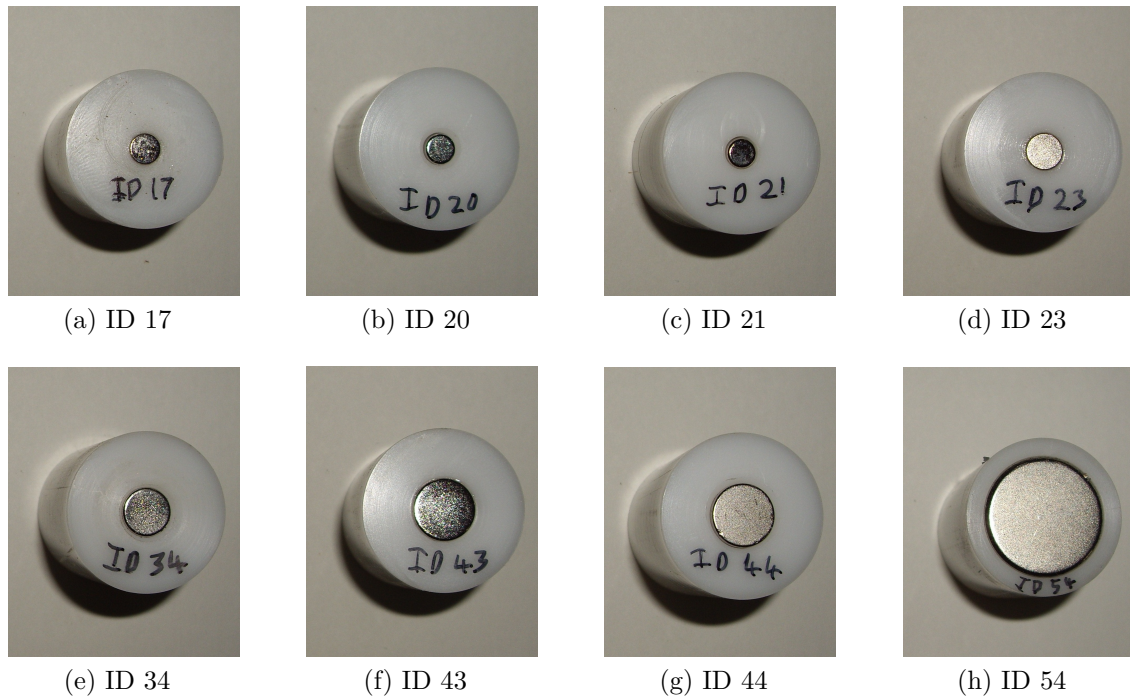


Figure 5.3: Various size magnets mounted in Delrin holders for TR1

The testing rig utilized a 1kN (kilonewton) load cell that could record the force experienced at set increments, so as the magnets were brought closer together the force was recorded automatically by the software. The software could be instructed to record multiple test runs automatically, so that repeatability testing could be performed to account for disturbances and calculate how stable the magnets are. To isolate the magnets from the steel frame of the load cell the plastic magnet holders were designed to fit into spacers made from mahogany. Mahogany was chosen due to its impressive strength under compression, simplicity to machine into useful holders and non-magnetic properties. The mahogany spacers were turned on a lathe to ensure that they both aligned along a central axis and both had a friction fit slot for the plastic magnet holders to locate into, making sure that the magnets were correctly positioned and would not fall out. The load cell with TR1 in position, figure 5.4, was compressed

until the magnet faces were touching which became the zero position.



Figure 5.4: Load Cell with TR1 in place ready for experimentation

Once the zero position had been recorded by the computer the 2 magnets were then drawn apart to a distance of 50cm (0.5 meters) which was set as position 1, at which point the computer was instructed to compress the magnets to position zero whilst recording the force at 1mm increments. When complete the load cell would be returned to position 1 and the test would be repeated to record repeatability data. This work was published as a paper, Appendix I, as well as a poster presentation, Appendix J, but included the Gilbert model as describe in section 3.2. This oversight can be seen in the comparison graph, figure 6.4, which shows the results of a test run against the incorrect model.

5.2.2 Test Rig 2

The motivation for TR2 takes the basic setup of TR1 and tries to expand on the design to produce a suitable suspension device with some limited integration of sensors and incorporating the ID54 magnets within the design. TR2 has a fixed magnet much like

the TR1 setup with the second magnet able to move freely along the axis shared with the fixed magnet, so design considerations had to be made so that the mechanism did not hinder the magnets motion relative to each other. The design also called for the use of materials that would not affect the magnetic fields of the magnets, for example ferrous metals so that the observed motion was a true representation of the magnetic interactions between the fields of the two magnets. This material choice extends to metals that are non-magnetic, for example Aluminum, which when moved through a static magnetic field or introduced to a moving magnetic field generates Lorentz forces within its structure which cause a damping effect on the system [67].

The system needed to have as little friction as possible as not to hinder the moving parts and the use of grease or oil had to be avoided as they can change the dynamics of the system. The design proposed and manufactured was created out of two types of plastic, as plastic does not affect the magnetic field in a measurable way with relation to the scale of this experiment. The plastics chosen were clear acrylic, to enable viewing of the magnets interactions and, as before, the magnet holders were made from Delrin [87] (Polyoxymethylene) due to its high strength in compression and low friction coefficient. To lock the magnets to a single axis of motion and for simplicity during manufacture, extruded Acrylic tube with a wall thickness of 3mm for strength was selected to slide over a Delrin rod with an outside diameter that was just smaller than the inside diameter of the acrylic tube (figure 5.5). This choice of materials enabled the magnets to repel each other whilst the free magnet in its holder could move with relatively little friction.

The creation of TR2 allowed for hall effect sensors to be placed on the outside of the acrylic tube so that the initial testing could be performed. This testing was designed to see if two hall effect sensors positioned perpendicular to each other could be used to approximate the location of the magnets. This rig had 4 sensor groups, figure 5.6,

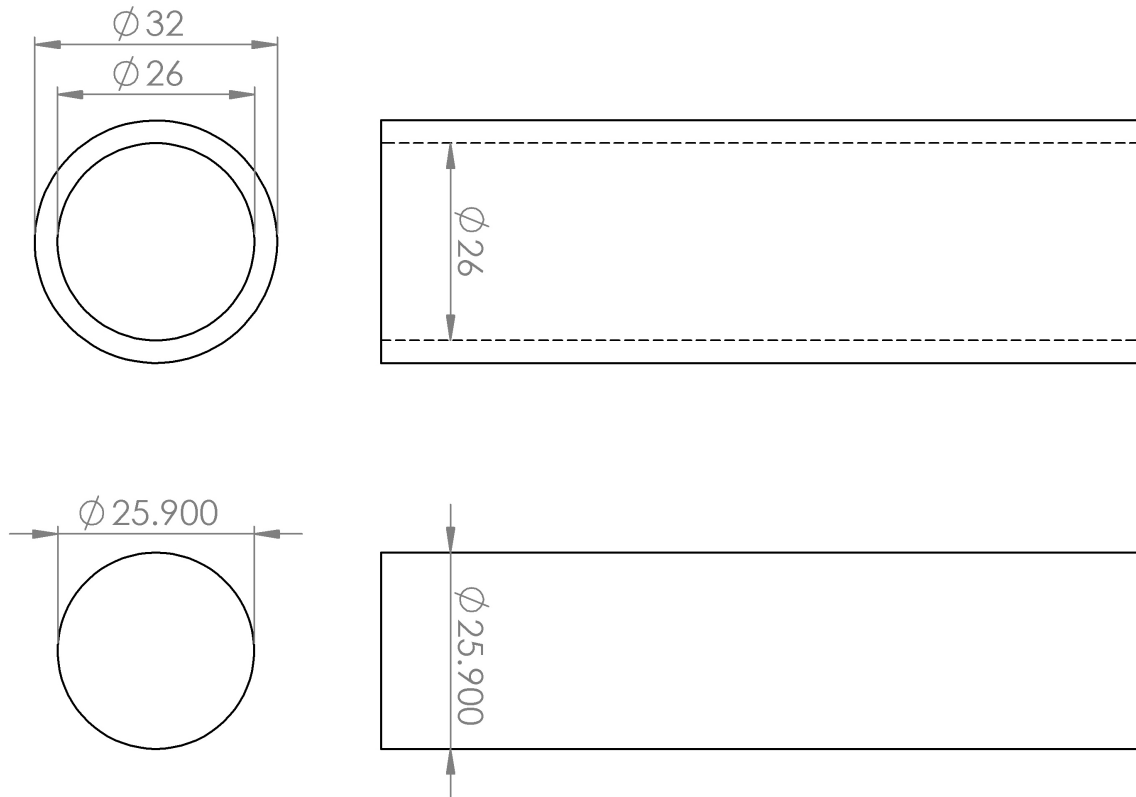


Figure 5.5: Diagram showing dimensions of plastic used for TR2

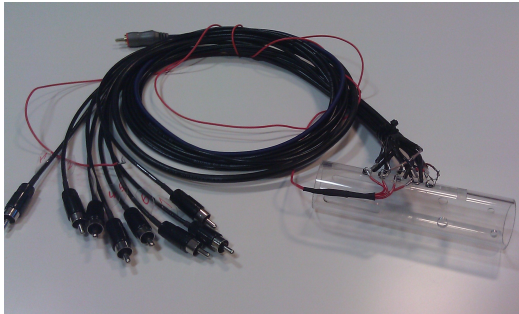
containing two of the SS49E hall effect sensors (the black blocks attached to the PCB) arranged so that each group could measure the field magnitude in both the x -direction and y -direction in Cartesian coordinates. The connectors shown in figure 5.6 from left to right are sensors 1 to 8 followed by the power connector.

This initial PCB was held in place with Bluetack so that it could be quickly removed, but the PCB could shift during testing due to the weight of the ribbon cable, so a second edition of the hardware was created where the sensors were super glued into a profile cut along the outside of the tube, figure 5.7. Both editions of the test rig were connected to a Quanser data capture card that was linked to a computer to record data at 10 bit accuracy, however the Quanser boards were limited to recording 8 analog channels simultaneously. The data capture was driven with a Simulink model,

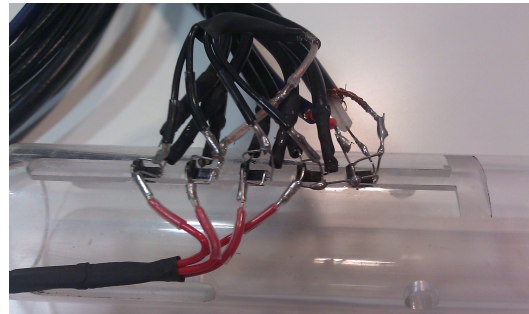


Figure 5.6: First edition Hall Sensor Array for TR2

Appendix E, which recorded data to a CSV file for later analysis.



(a) Super glued hall sensor array



(b) Close up of hall sensor array

Figure 5.7: Second edition of TR2 sensor placement

The second edition of the TR2 electronics used shielded coaxial cable to suppress some of the electrical noise that was observed coming from the first edition of the electronics via the ribbon cable. Whilst the coaxial cable did reduce some of the electrical noise the flying lead connections to the sensors required additional insulation and solder joints, leading to a rig that frequently experienced broken connections and shorts. The second edition also included an additional sensor pair to extend the positions that

data could be recorded at, but was still limited by the 8 data channels of the Quanser boards. The super glued sensors did improve the sensor groups positional accuracy, which can be seen in the results comparison between the first and second editions data in figure 6.6.

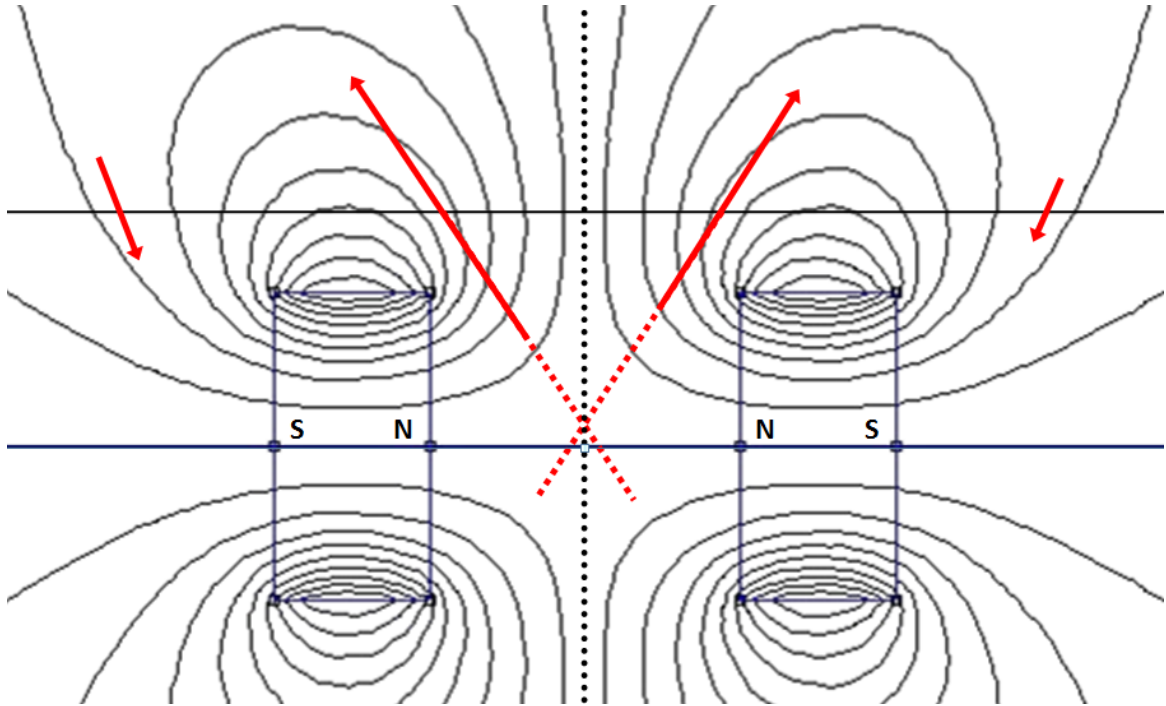


Figure 5.8: Algorithm idea to find midpoint between magnetic fields

The graphs in figure 6.6 were produced with an initial algorithm that was developed to locate the midpoint between two magnets in repulsion. The algorithm resolved the field angle and magnitude at each sensor group and located the group where the fields diverged, thus finding the rough position of the field midpoint. Taking the field angle and magnitude of the sensor groups either side of where the magnetic field diverged and extending their vectors until they crossed gave the approximate midpoint between the fields, figure 5.8, so that by doubling this value, the free magnets face could be located. The final algorithm used by TR4 described in section 6.4 is based on this initial work. The design of TR2 showed the possibilities of the equipment, with an initial and

rough position for the free magnet being estimated by the algorithm. However due to signal noise and poor sensor positional accuracy TR2 required a redesign to solve the following problems:

1. More sensors are required to improve the usable magnet displacement range of the test rig
2. A PCB is required to provide structural support to the sensing system and better connectivity to sensors
3. Sensor positioning needs to be more accurate to improve algorithm performance
4. Longer guide tube so magnets are not restricted by physical limits
5. Greater flexibility in fixed magnet positioning to enable a range of experiments to be performed with different initial conditions for sensor positioning

Overall TR2 was a positive step in the development of equipment for this thesis, but the design of TR3 had to address the problems listed above.

5.2.3 Test Rig 3

The five main problems found with TR2 detailed at the end of section 5.2.2 required TR3 to be designed. The design of TR3 called for a greater range for measurements to be taken, so that the magnets could be passed through the entire device and be recorded along its length. Due to the limitation of the Quanser data capture boards, the total number of sensors had to be divisible by 8 so that multiple Quanser data capture boards could be utilized. By increasing the number of sensors, the flying lead approach used to connect the second edition of TR2 to the Quanser boards was no longer feasible due to the high pin connection density, thus an efficient way of

providing bus power and ground with signal management was required. To improve the connectivity between the sensors and the wires, the sensors in TR3 terminated on strips of veroboard to give structural rigidity, bus power and simple interfacing to the sensor channels, figure 5.9. This arrangement allowed for 3 times more data channels compared to TR2, whilst reducing the overall sensor array depth by $20mm$.



(a) TR3 with all its connectors



(b) Close up of TR3 with 2 magnets

Figure 5.9: TR3 showing the connections, veroboard mounting and close up of the sensors super glued into a custom CNC machined profile

Sensors were positioned inside custom CNC machined profiles to increase the sensor groups positional accuracy. These profiles were positioned so that the sensor groups center was located directly over the face of the fixed magnet, which is used as the zero displacement reference during testing. The design of TR3 used 8 groups of sensors spaced at $10mm$ increments from the surface of the fixed magnet, which gave measurements along the length of the device. The decision to have an additional y -axis sensor per group was made to try and reduce the distance between the centers of the hall effect elements. This means that the virtual sensing point in TR1 and TR2 between the x and y axis, figure 5.10, was removed in all of the groups on TR3 to get a true reading of field angle and magnitude by using the second y axis sensors. TR3 could also replicate the results of TR1 and TR2 by using the first y axis sensor in each sensor group, to give direct comparison of results.

As before the sensor channels were connected to Quanser data capture boards, figure

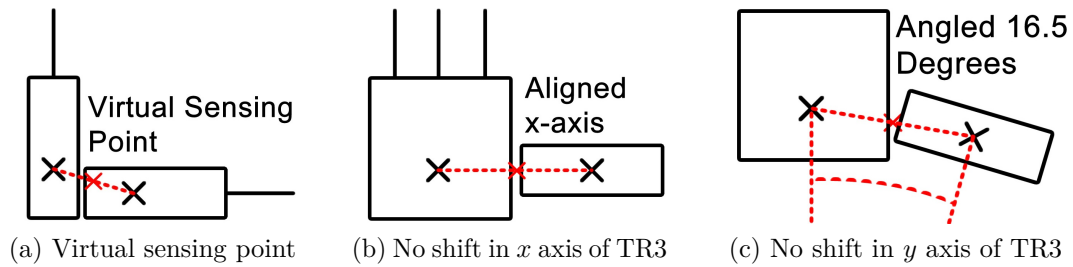


Figure 5.10: Virtual x and y axis sensing point of TR1, TR2 and TR3 using y axis sensor group 1 compared to the no shift sensing point in TR3 using y axis sensor group 2

5.11, but due to there being 24 channels ($8 \times x$ axis and 2 sets of $8 \times y$ axis) TR3 had to be connected to three Quanser board at the same time to distribute the data recording. This caused a few synchronization problems as the three Quanser data capture boards were attached to three different computers. To compensate for this the data capture Simulink model for TR2, Appendix E, was modified to take a debounced (single event) digital trigger input to drive the data capture. This digital trigger was provided by a hand held switch that was connected in parallel to the three Quanser data capture boards, so that when the switch was depressed the digital trigger caused all three computers to record the data at the same time.

TR2 suffered from hard physical limits if the free magnet was released when under load, and as such the acrylic tube of TR3 was increased in length by $25mm$ to support greater displacements without mechanical interference. The guide tube also had three additional mounting points for the fixed magnet included in the design, so that it could be positioned in the following locations:

1. The face of the fixed magnet positioned directly under the x -axis and second y -axis sensing points (original position)
2. The face of the fixed magnet displaced by $1.05mm$ so that it is under the virtual sensing point between the x -axis and first y -axis sensing points

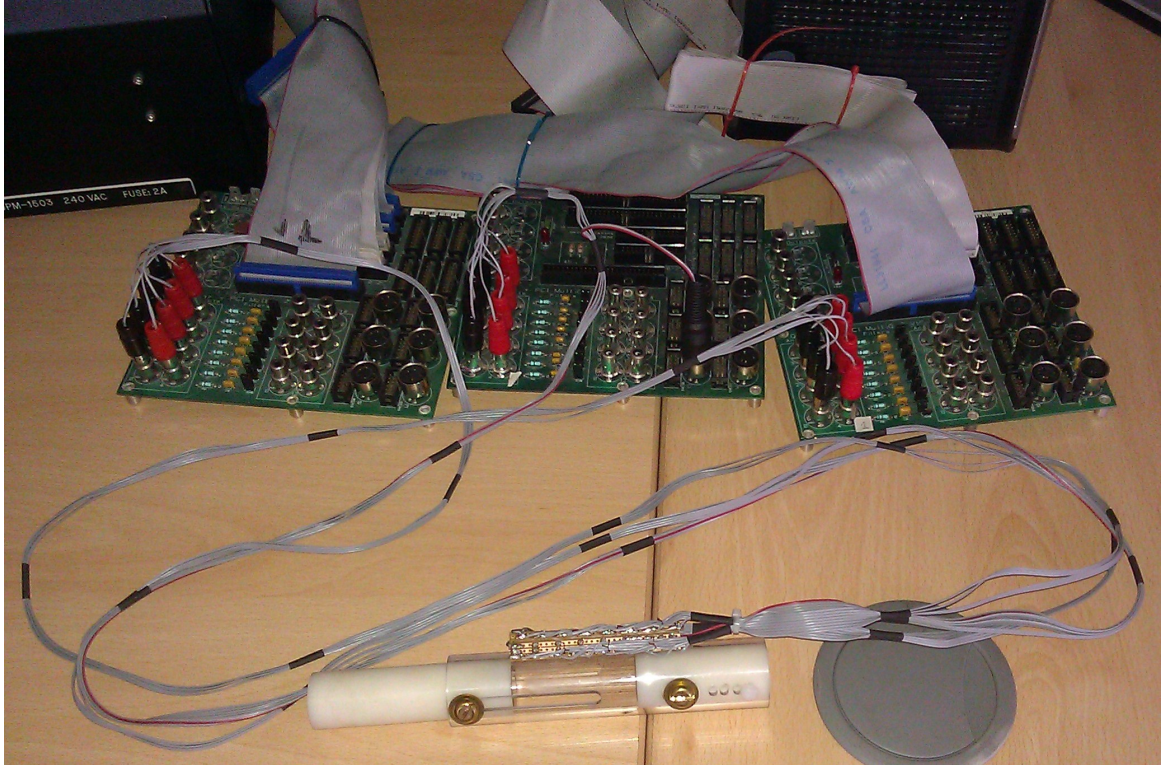


Figure 5.11: The TR3 module connected to 3 Quanser data capture cards

3. The middle of the fixed magnet is positioned under the x-axis and second y-axis sensing points (displacement of $5mm$ compared to the original position)
4. The middle of the fixed magnet is positioned under the virtual sensing point between the x-axis and first y-axis sensing points (displacement of $6.05mm$)

These positions were obtained by inserting a holding pin into the correct mounting hole and through the correct hole in the fixed magnet holder, thus enabling a wider range of tests to be performed with the test rig. TR3 was tested briefly, but because of the difficult data recording approach it was abandoned in favor of designing TR4. This was due to a number of reasons including the additional complexity incurred with the use of an external trigger which required meticulous logs of click counting to be kept, the need for the three computers to be relocated to the room containing the

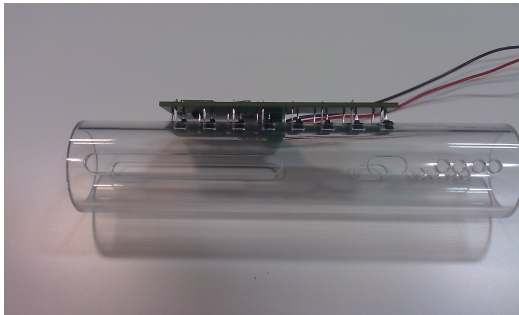
load cell test equipment and the additional signal noise generated by connecting three separate computers to a common ground. Section 6.2.3 shows the substandard quality data produced by TR3 and the data logs can be found on the DVD included with this thesis.

5.3 Final Hardware Design for Data Capture

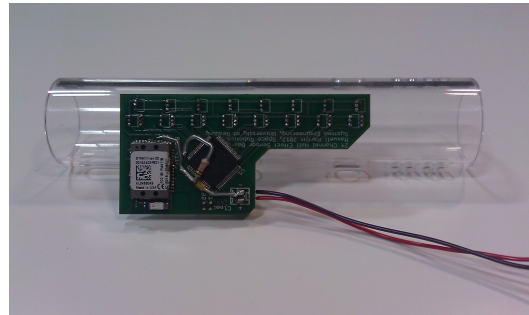
TR4 was designed to correct the flawed data capture system that was tolerated with TR2 and abandoned with TR3. The flaw was caused by a combination of faulty wiring which lead to short circuits, long signal traces that incurred signal noise and signal degradation as well as the complex data capture system which required synchronization across three computers. The data capture on TR4 is performed by a PIC with 24 12-bit ADC channels. The 12-bit ADC processes 4096 individual voltage steps, giving a conversion resolution of $1.22mV$ per step across the $5V$ input range. This provides more accuracy than the Quanser board which only records at 10-bit accuracy ($4.88mV$ per step over the $5V$ input range). The PIC and the sensors are connected to the same PCB, with the longest signal trace measuring $20mm$, attenuating a maximum of $0.1mV$ signal amplitude. All signal traces are shielded and routed to avoid power and communications lines to minimize signal noise. The communications from TR4 to the data logging computer utilize Bluetooth radio, due to the small PCB footprint size, communications range and data transfer rates. This allowed software on the data logging computer, section 5.3.2, to request readings from TR4 via the Bluetooth radio link so that TR4 could run from a battery rather than a smoothed DC mains supply thus reducing noise from the power supply.

The construction of TR4, detailed fully in Appendix G, was performed to tighter tolerances than TR3 which made sensor placement more accurate. The sensor locations

were defined by custom CNC machined profiles, so sensor placement was accurate to $\pm 0.05mm$ compared to TR3 which was $\pm 0.1mm$. The system was a lot smaller than TR3 as it only required a laptop to run the data capture software and Bluetooth link compared to the 3 separate data capture computers and interfaces used with TR3, thus making TR4 very portable.



(a) Side view of the TR4 module



(b) Top view of the TR4 module

Figure 5.12: TR4 top and side elevations showing the ADC PCB attached to sensors

5.3.1 TR4 Hardware

The mechanical design of TR4 is practically identical to TR3, but has improved manufacturing tolerances and electronics. TR4 was built from the same plastic stock as TR3, but to increase accuracy the aligning and positioning of tools before cutting was performed with more precision. Section 5.3.1 describes the electronics designed for TR4 to improve the TR3 data capture system, including details of the power supply, Bluetooth communications and PIC chosen. Section 5.3.1 details the PCB that was developed from the TR4 circuit diagrams, including the choices made to reduce electronic noise with board layout. Section 5.3.1 describes the group calibration testing process, as TR4 required all 24 sensor channels to be calibrated with respects to each other to avoid incorrect data and to ensure that the channels operated as expected. Final technical drawings of TR4 are included in Appendix F and the SolidWorks files

used are included on the thesis DVD. Manufacturing details of TR4 are included in Appendix G. The Schematic and PCB for TR4 are included in Appendix H and the Eagle CAD files are included on the thesis DVD.

TR4 Schematic

The main problem with TR3 that had to be addressed was the electrical noise that was generated by both the computers that TR3 was connected to and the long signal traces; so to avoid these problems TR4 was designed to run from a battery and keep signal traces as short as possible. The TR4 circuit power was provided by a 5V battery pack to supply the required current for the TR4 circuitry, whilst not introducing high frequency noise that a smoothed DC power supply would. The 5V supply was passed through a voltage regulator to provide 3.3V required by the Bluetooth communications module to operate correctly. The voltage regulator, ST Microelectronics *LD117AS33TR* [88], output was smoothed further by two decoupling capacitors which reduced the chance for voltage spikes whilst performing the ADC with the PIC.

The Bluetooth communications module, *BTM411* [89], interfaced directly with the PIC UART to provide 2 way communications between the PIC and the computer. The Bluetooth modules CTS and RTS pins were connected together as the PIC did not require communications flow control to be implemented. The communications between the PIC and the Bluetooth module operated at different logic levels, so to compensate the RX line on the Bluetooth module (TX line of the PIC) was pulled down through a 3.3V zener diode so that the PIC did not overload the Bluetooth module. The PIC used with TR4, the PIC18F87K22-I [90], was chosen for the following reasons:

1. Can record data over the full 0 – 5V output range of Honeywell SS49E sensors
2. Integrated 12-bit ADC for improved resolution compared with Quanser boards

3. Large RAM and EEPROM to store program and ADC data
4. Integrated UART module for communications
5. Surface mount package with high pin density for small circuit footprint
6. Low power usage to negate effects of data capture current

The circuit schematic also had a custom module created for the 24 Honeywell SS49E sensors which made the development of the schematic and PCB simpler to understand, rather than having 24 individual sensor modules that required connecting and positioning. The TR4 schematic was converted into the TR4 PCB using Eagle CAD, which reduced the chance of processing and translation errors and enabled the ability to make revisions whilst keeping both files synchronized.

TR4 PCB Layout

The PCB design software, Eagle CAD, utilized the TR4 schematic to import the correct components into the PCB layout editor to avoid incorrect components being included or components being missed. The import process allows for custom PCB footprints to be generated which was necessary for both the Bluetooth Module and the Sensor arrangement, as neither had a PCB footprint in the Eagle CAD library. The sensor positioning PCB footprint was done using a custom sensor layout for one sensor group, which was replicated seven times every $10mm$ to give the required 24 channels. This enabled the sensors to be imported as one part for simplicity when positioning them on the PCB. The Bluetooth module required some additional constraints to be included in its PCB footprint as the integrated antenna needed to be positioned with no copper surrounding it, so a 'keep out' area was included in its PCB footprint to avoid copper under the module.

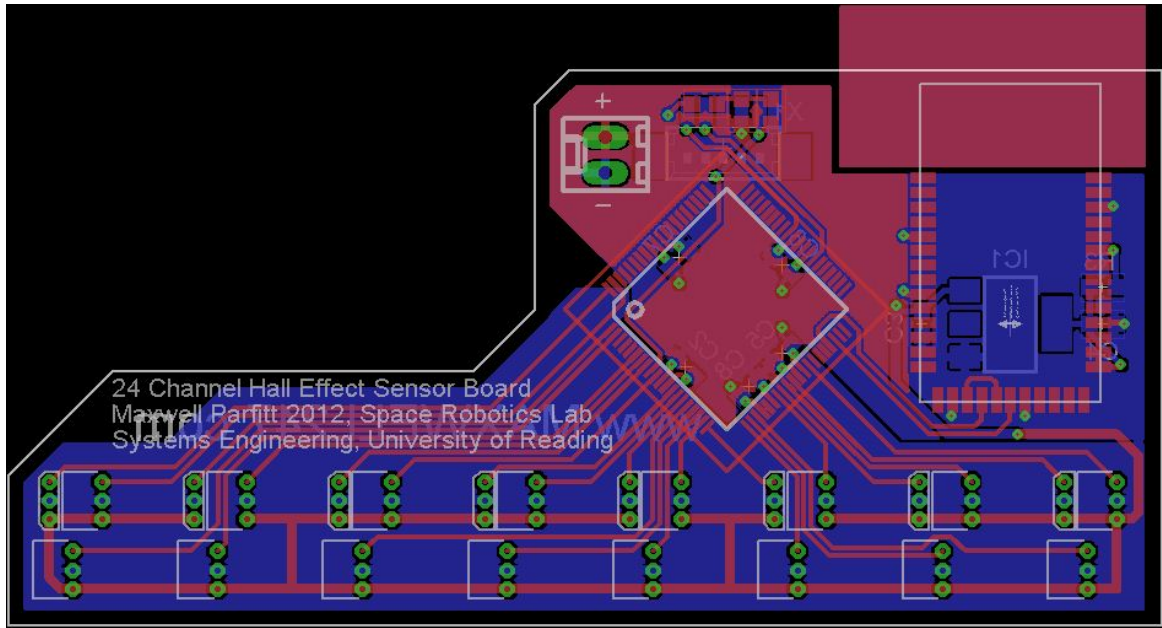


Figure 5.13: The TR4 PCB design sent for manufacture

There are a number of techniques that have been used to reduce electrical noise in the PCB design, including separate ground planes for digital and analog signals to avoid noise generated by digital communications being detected on the analog inputs that are connected to the ADC, decoupling capacitors included close to the power supplies of the Bluetooth module and the PIC chip to provide a local power store, no analog signal lines crossing over power lines to avoid any noise coming from the power supply and no ground loops that can cause unexpected voltage spikes and strange device behavior. The final PCB design for TR4, figure 5.13, was manufactured professionally with a dual sided board and through hole plating to give the most accurate results. The boards were then assembled using flow soldering facilities at the University of Reading, figure 5.14, and tested to see if all channels worked correctly (section 5.3.1).

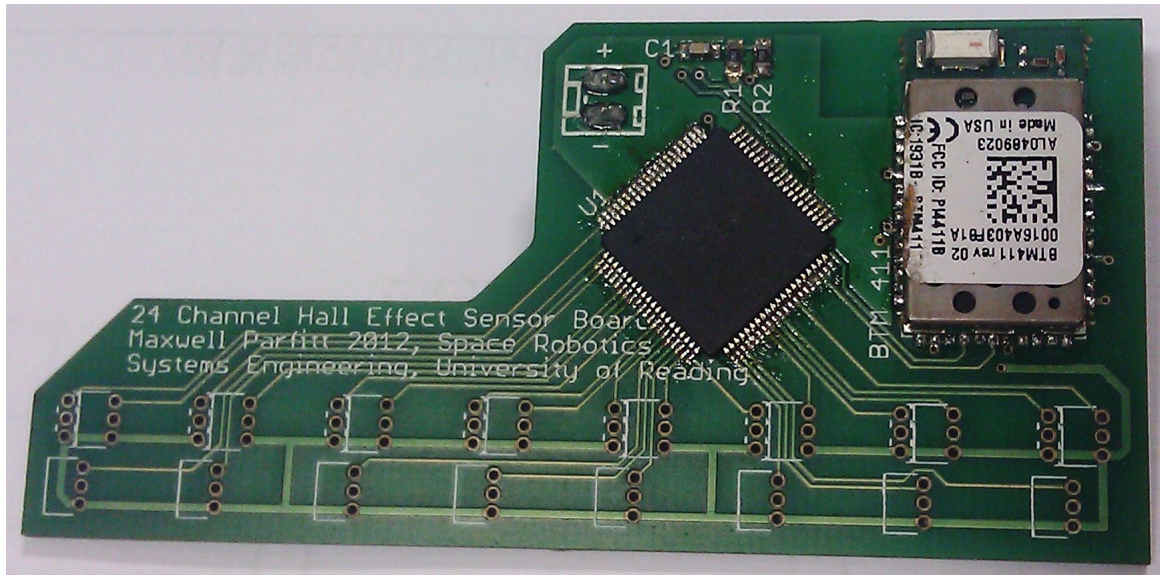


Figure 5.14: The TR4 PCB after manufacture and testing

Group calibration of TR4 sensor channels

The electronics used in the final test rig, section 5.3, utilized 24 of the SS49E hall effect sensors in 8 orthogonal pairs with 8 calibration sensors. The sensor placement, figure 5.15, enables the sensors to record data with known positioning of the hall element center [91] within each sensor group. The hall element center is the exact location where measurements are taken within the sensors packaging, as such it is important to account for this when locating the sensors to give a precise offset for the sensor casing. The first pair of sensors were placed as close to each other as possible in a row to minimize the differences in readings between them, but due to the casing size this was not as close as required. To solve this problem the second y-axis sensor was positioned so that the hall element center was at the same displacement in both the y-axis and the x-axis. This was done by rotating its location around the tube, figure 5.15, so that it experienced an equivalent field as the x-axis sensor.

The group calibration experiment ensured that all sensor channels on the microprocessor

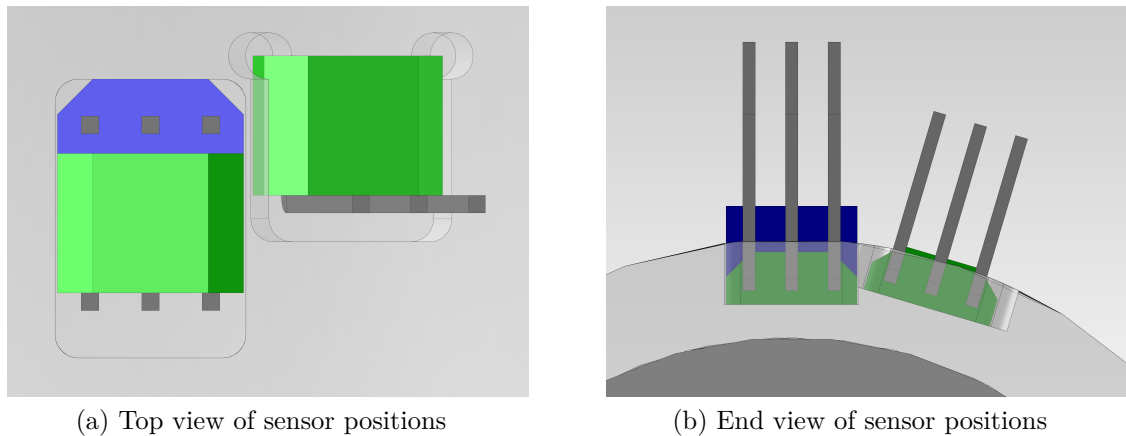


Figure 5.15: Positions of hall effect sensors when mounted on testing rig

recorded data for the full 5V input range of the SS49E sensors, as well as ensuring that all channels produced equal values when exposed to the same voltage. To perform this test a variable millivolt reference source was connected simultaneously to all input channels of the data capture board using push pins before the SS49E sensors were soldered in place, figure 5.16. These pins fitted through the holes that the SS49E sensor legs would be positioned through, so that the data capture board could also check that all the channels work. The first group test proved that all the channels worked through repeated readings taken as the input to all channels was pulsed logic high followed by logic low. The next test checked the PIC's ADC accuracy by starting at 0V and progressively incrementing the millivolt reference by 10mV, taking a reading after each increment until 5V was reached. The testing proved that all ADC channels on the PIC had a maximum variance of $\pm 1.5mV$ which when connected to the Honeywell SS49E is equivalent to ± 1.071 Gauss (± 0.107 millitesla). The data and graph from this test can be found in Appendix D.

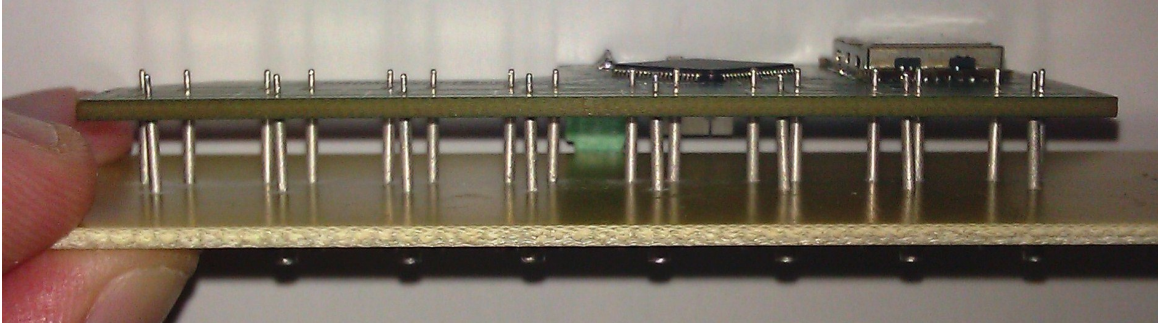


Figure 5.16: Push pin calibration board attached to the data capture module

5.3.2 TR4 Software

TR4 required three different pieces of software to be developed to cover the firmware on the PIC, the data logging using C# and the data analysis using Matlab. This section describes the C18 code that the PIC ran during the Helmholtz coil manufacture and the code used to communicate with TR4 via Bluetooth whilst performing ADC to record data from TR4. This is followed by a description of the data logging software including data storage and graphical output and ends with a description of the Matlab code that was developed to sort, process and analyze the data from TR4, including visualization routines that were developed to display the data in an intelligent manner.

C18 Code Description for PIC Firmware

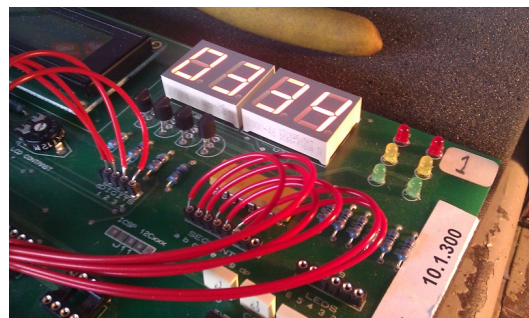
The C18 compiler for C was used to program the PIC hardware used in both the manufacture of the Helmholtz coil and the experimentation with TR4. It was chosen due to an accessible school license and previous experience programming in the MPLab environment with the C18 compiler. The code listing for all PIC C18 software developed for this thesis is on the DVD included with this thesis. The Helmholtz coil manufacture C18 software was developed to run on the V2.0 PIC Millennium Board due to the 7-Seg display and simple interface to attach analog sensors. The software utilized the

input from a spare SS49E hall effect sensor to detect a magnet attached to the lathe's chuck, figure 5.17, that was used to wind the coils onto the 3D printed Helmholtz coil bobbin.

As the chuck rotated the magnet passed the SS49E sensor causing a detectable change in the ADC value, so that with some digital filtering the value displayed by the 7-Seg display on the V2.0 PIC Millennium Board was incremented. If the reset button was pressed the count started from zero again, so that the next coil could be wound. This approach was essential as the Helmholtz coil bobbin required precisely 667 coils to be wound onto it (one coil of 333 turns, the other of 334 turns), which would have been very time consuming to wind manually as well as a high chance of losing count.



(a) View showing the magnet rotating past the SS49E sensor



(b) The V2.0 PIC Millennium Board 7-Seg Display

Figure 5.17: Application of the C18 code to count turns going onto the 3D printed Helmholtz coil bobbin

TR4 required custom C18 code to be developed to facilitate the experiments required for this thesis, with the full code listing included on the thesis DVD.

The key parts of the code that required development were the ADC data capture routines to reliably and accurately record data using the PIC ADC and the Bluetooth communications control to interface with the Laird Technologies BTM411 Bluetooth module [89] [92]. The Bluetooth module used the 'AT' command interface, such that all configuration commands sent to the device started with the letters 'AT'. This made

the interface code very simple as it could be stored as a string rather than individual ASCII or Hexadecimal characters and can be found in the ‘Bluetooth_Setup’ code on the DVD. The code required for Bluetooth setup includes device initialization, naming the device, enabling security and pass-codes, making the device discoverable and connectible, enabling the SPP and finally enabling auto answer so that when a connection is made from the data logging computer the Bluetooth module becomes a transparent link allowing data to flow freely in both directions. The PIC18 series chip chosen for experimentation in section 5.3.1 has 24 ADC channels but no re-mappable peripherals as found in the PIC24 series of chip, so the port mapping had to be done at the same time as the PCB design to make sure that the ACD channels matched the sensor locations. Table 5.2 displays the PIC ADC channel configurations used in the C18 code to assign the correct I/O pins to data recording channels.

Sensor	PIC Port	I/O Pin	Chan	Sensor	PIC Port	I/O Pin	Chan
X_1	AN22	80	a	Y_{15}	AN15	19	m
X_2	AN21	1	b	Y_{16}	AN3	27	n
X_3	AN17	8	c	Y_{17}	AN1	29	o
X_4	AN5	13	d	Y_{18}	AN4	33	p
X_5	AN10	15	e	Y_{21}	AN20	2	q
X_6	AN14	20	f	Y_{22}	AN19	6	r
X_7	AN2	28	g	Y_{23}	AN9	16	s
X_8	AN0	30	h	Y_{24}	AN8	17	t
Y_{11}	AN23	79	i	Y_{25}	AN7	18	u
Y_{12}	AN18	7	j	Y_{26}	AN13	21	v
Y_{13}	AN16	10	k	Y_{27}	AN12	22	w
Y_{14}	AN11	14	l	Y_{28}	AN6	23	x

Table 5.2: PIC18F87K22-I ADC channel configuration

The data collection could either be performed a single channel at a time, useful if there was data corruption during transmission to the data logging computer, or sequentially across all channels on request from the data logging computer. These behaviors depended on the message packet received from the data logging computer software via the Bluetooth link, where the message packet was a single control character. The control character ‘!’ was used to trigger the “read all channels” behavior while the lowercase letters ‘*a* to *x*’ referred to individual channels X_1 to Y_{28} , table 5.2. When a control character was received the C18 code raised an interrupt that jumped into the ADC routine, which checked the control character to see what action was required. If the control character was for a single channel the PIC sent the channel number back to the data logging computer, while the ADC registers were configured to read the specified channel followed by a $10ms$ delay to allow the ADC to charge and stabilize. Once the ADC module had stabilized a reading was taken, stored in two 8-bit registers, and transferred to the communications output buffer to be transferred to the computer. This was repeated ten times for each request from the data logging computer so that data analysis could take an average of all readings for accuracy. Between each communication packet the PIC included a comma to help the data logging software store the data and all messages were finished with a checksum of the message, to enable instant communications error checking by the data logging computer. If this all completed correctly the PIC went back into standby mode to await the next command, but if there was an error it would repeat the whole process to correct errors. If an exclamation mark was received for the control character the PIC ran the same process as the single channel behavior, except that it started from channel X_1 and used a for loop to step through all 24 channels. The data returned was all comma separated so

that the data logging computer could store it efficiently, and was simpler to debug manually if there was a problem.

C# Code Description for Data Logging Software

TR4 required custom data logging software to be created to connect to and control the data capture from TR4, whilst storing the data in a CSV format to be used in later data analysis. The data logging software utilized the powerful C#.net programming environment because it was necessary to display data from TR4 in a graphical format for debugging reasons, whilst efficiently communicating with TR4 via a Bluetooth serial link to capture the data. The data capture software was built as three modules which integrate through the user interface form, figure 5.18, to provide communications, visual data output and data logging tools for the user.



Figure 5.18: The custom TR4 data logging user interface written in C#

The user interface layout includes a communications control section, a data logging section and the graphical output section. The communications control section, located at the top left of the form, comprised of a button which checked the status of the communications link to see if the correct serial port was open and operating, if not it

re-opened the correct port and tried again. This button used the top combo box in this group to choose the serial port it was connecting to, so that if the device changed serial port it could still be found and resolved. The button then called the data request and capture function, by sending the ‘!’ control character to TR4 to request data from all channels, which when received passed through data validation and verification functions to check if the data was received correctly. If the data was corrupted for any reason, the software discarded the data and requested TR4 to provide the data again. Once the data had been confirmed as correct the data logging software added it to the data logging list structure ‘myReadings’ to store the data efficiently. The ‘myReadings’ list structure used a custom data class called ‘Readings’ to store individual entries, which allowed the software to be multi-threaded for efficiency and enabled data locking, so that the software could not change and read the data simultaneously to avoid errors. The next section of the user interface was the data logging section which worked in partnership with the communications control as it provided additional data to be stored in the logged data, for example the force and separation between the two magnets. The up-down boxes, ‘X Step Value(mm)’ and ‘X Separation (mm)’, allowed for initial test conditions to be included in the data so that every time a reading was taken, the X Step value was added or subtracted (depending on sign) to the X Separation value which was logged. This saved a lot of time in data analysis as the X Separation values was already included with the data rather than needing to be added after testing. ‘The Force (N)’ textbox was needed to enter the measured force between the two magnets manually as the load cell could not be interfaced with directly, so to streamline that data capture when the value had been changed, pressing the ‘Enter’ key on the keyboard called the same function as the ‘Take Reading’ button to log the data.

Once all testing had been completed the ‘Dump Data to File’ button called a function

to create CSV files that contained the data. Two files were created by this function, as at the time the data analysis required was not fully understood. The files contained the same recorded data, but one contained the raw data directly received from TR4 and the other was converted to the voltage that TR4 recorded, which turned out to be the data that was used in the final data analysis. The filenames followed the same structure 'Name_Day.Month.Year_Hour.Minute.Second.csv' where 'Name' was either 'RAW' or 'Data' depending on the data contained within it. This structure was logical when experimenting as the data could be located for specific tests if the time of the the experiment was known. The final section of the user interface was the graphical output area at the bottom of the form. This graphical area was dynamically created to operate on its own thread for efficiency and was updated every time a reading was received.

The display, figure 5.18, shows a sample set of data recorded by TR4 across all 24 channels. The display was used for debugging reasons as major discrepancies in the data could be seen graphically. As TR4 returned ten readings per channel, 240 readings in total, the graphical area displayed the maximum and minimum values as a bar, with the average of the ten readings displayed as a point. This average was performed on the computer as a computer is much more capable at division and averaging than a PIC chip is, therefore the average for each channel was also stored in the CSV data file. The last item on the form to describe is the second combo box on the left of the screen, containing the number 200, which was used as a vertical scaling factor for the graphical output during software testing, but was not required during experimentation as the value 200 covered all possible input ranges from experimentation. The C# software performed its task superbly and produced all the CSV data files that were used in later data analysis and algorithm testing. The full C# code listing for the data logging and graphical output is included on the thesis DVD along with the CSV

data files that were produced by the software.

Matlab Code Description for Data Analysis and helper script files

The analysis of data from TR4 was performed using custom scripts written for Matlab. Matlab was chosen due to its mathematical processing power and graphical output. All Matlab ‘m’ files and code used with TR4 are described in this section and can be found on the thesis DVD. The TR4 Matlab code is broken down into helper functions 5.3.2, calibration functions 5.3.2, data management functions 5.3.2 and graphical display functions 5.3.2.

Matlab Helper Functions

The helper functions developed for TR4 were designed to make the data analysis simpler and more efficient. The first helper functions developed, ‘ $deg = rad2deg(rad)$ ’ and ‘ $rad = deg2rad(deg)$ ’, converted between degrees and radians as the latests version of Matlab no longer contains these very useful functions. These functions were used heavily in the algorithm developed for TR4 and in the graphical display of data when converting between raw data and usable graphics in Cartesian coordinates. The second helper function, ‘ $[r, g, b] = RGB('COLORNAME')$ ’, downloaded from the MathWorks website [93] performs a lookup of known color names and returns the corresponding RGB color triple. This helped build up a custom color map so that all graphics produced utilized the same colors, especially useful when plotting multiple lines on a graph and requiring the same colors to be linked to specific channels in all graphs. The final helper function created, ‘ $Out = scaledata(Input, Min, Max)$ ’ applied a scaling factor to recorded data to help with the curve fitting. The function was called with ‘Input’ which could be a vector, matrix or dataset, ‘Min’ the lowest value to return and ‘Max’ the maximum value to return. The output of the function

took the ‘Input’ and returned it exactly scaled between ‘Min’ and ‘Max’.

Matlab Data Management Functions

The data management functions were included as part of the main Matlab file for TR4 rather than in a function of their own as the data produced during testing was too varied to handle efficiently. The data management functions utilized a switch function to choose which data was to be loaded and was driven with the variable ‘EXPno’. Table 5.3 shows the experiment number with the calibration and data files that were loaded for data analysis. These files were all generated by TR4 and can be found on the thesis DVD, including the main Matlab file ‘LoadCSV_Calibrated.m’.

EXPno	Calibration File	Data File
0	First 24 lines of Data File	SecondTest(150mm).mat
1	Cal_Data_Exp_1.mat	Data_Exp_1_R.mat
2	Cal_Data_Exp_1.mat	Data_Exp_2_MAT.mat
3	Cal_Data_Exp_1.mat	Data_Exp_3_MAT.mat
4	Cal_Data_Exp_1.mat	Data_Exp_4_MAT.mat
5	Cal_Data_Exp_1.mat	Data_Exp_5_MAT.mat

Table 5.3: Files used for calibration and data analysis

Once the calibration and data files had been loaded it was necessary to call the calibration function described in section 5.3.2 for EXPno 1 to 5 as they used a separate calibration file. EXPno 0 had its calibration data stored within the data file as the first 24 readings, so these were extracted and assigned to calibration variables $X1cal, X2cal, \dots, X8cal, Y11cal, Y12cal, \dots, Y18cal$ and $Y21cal, Y22cal, \dots, Y28cal$. These calibration variables were used by the other experiments too, but were generated using the calibration functions. The next step in the data management switch functions

was to describe the location offsets of the sensors in the x-axis and y-axis, which were stored in the variables ‘SenX’ and ‘SenY’, followed by the file name used by the Matlab ‘VideoWriter’ so that the final data processing could be visualized as a video. The video output was a very useful way to see how the data changed as the magnets were moved and displayed how the algorithm works. The videos are included on the thesis DVD with experiment descriptions encoded into the video frames.

Matlab Calibration Functions

The calibration function ‘CalData’ took data from the calibration data files described in section 5.3.2 and returned the correct calibration data to be used for the data analysis. The calibration function was called using the following code:

```
[X1cal, X2cal, X3cal, X4cal, X5cal, X6cal, X7cal, X8cal, ...  
Y11cal, Y12cal, Y13cal, Y14cal, Y15cal, Y16cal, Y17cal, Y18cal, ...  
Y21cal, Y22cal, Y23cal, Y24cal, Y25cal, Y26cal, Y27cal, Y28cal] ...  
= CalData(Cal);
```

The calibration data is loaded into a variable ‘Cal’ by the data management function which is used as the input to this function, which is then processed to return the calibration variables shown above. The calibration data passed to this function is normally the result of ten calibration runs, so the function also averages the input for each channel to provide the most accurate calibration data as possible.

Matlab Graphical Display Functions

Matlab is a powerful mathematical data crunching program, but also has a variety of output methods by using the figure environment. The figure environment was used during the data analysis for both graph plotting and diagram drawing which can all be

captured as a frame and used with the Matlab ‘VideoWriter’ to build up animations a frame at a time. The main scripts developed for use with the TR4 data analysis were to display the following:

1. All 24 data channels of raw data grouped into the 3 sets of sensors (X,Y1,Y2) so that the displacement of the free magnet was plotted against the measured Hall Effect voltage
2. All 24 data channels of raw data grouped into the 3 sets of sensors (X,Y1,Y2) so that the displacement of the free magnet was plotted against the Magnetic field strength measured in Gauss
3. All 24 data channels of scaled data grouped into the 3 sets of sensors (X,Y1,Y2) so that the displacement of the free magnet was plotted against the measured Hall Effect voltage
4. All 24 data channels of scaled data grouped into the 3 sets of sensors (X,Y1,Y2) so that the displacement of the free magnet was plotted against the Magnetic field strength measured in Gauss
5. Plot of the displacement in *mm* against the measured force between magnets in Newtons
6. Animation to show all channels with resolved field angles and magnitudes superimposed over a wire frame representation of TR4. This also doubled as the TR4 magnet location algorithm output to see how well the algorithm performed.

5.3.3 TR4 Experimental Setup and Configuration

This section describe the experimentation performed with TR4 to confirm the theories and test if it is possible to accurately locate a free moving magnet by purely

observing the magnetic fields surrounding a fixed magnet of known position. Before all experiments were performed, the TR4 sensors were logged to record the background magnetic field interferences found in the testing area, which was important to account for external environmental disturbances that may change between experimental runs.

Experiment 1: Single magnet calibration swing from guide tube end

This experiment utilized the calibrated load cell, used for experimentation with TR1, section 5.2.1, to accurately translate the free magnet through the guide tube with the SS49E sensors mounted, so that a magnetic profile could be recorded for each of the hall effect sensors. The testing data was logged at $0.5mm$ increments, using the TR4 data recording hardware, as this resolution created very precise curves for use with the calibration functions described in section 5.3.2. The raw data had to be calibrated to account for any misalignment of the sensors and variations in the sensors themselves due to manufacturing processes and was an additional calibration step with respects to the environmental calibration that was already performed.

The experiment was performed by positioning the face of the magnet, in its Delrin holder, at the end of the guide tube which was $40mm$ from the eighth sensor pairs sensing center (not the virtual sensing point). This distance was chosen due to physical limits of the translation stage and the magnet holders length, to allow for the maximum displacement range to be recoded by TR4. The system was then translated to a maximum displacement of $150mm$ with data recorded every $0.5mm$. The recorded data, figure 6.9 in section 6.3, was converted from the raw voltage into gauss, figure 6.10, using equation 5.1.

$$GaussValue = \frac{RawVoltage \pm CalibrationDataforChannel}{SensorVoltageRange/ADCResolution} \quad (5.1)$$

This provides the measured gauss value, but this needed to be corrected by using

the Matlab helper function ‘ScaleData’ so that all sensor readings were between the expected maximum and minimum values, which corrects for any sensor misalignment or defects, figure 6.13 in section 6.3.

Experiment 2: Single magnet calibration swing from mechanical limit

The same experimental process, as found in section 5.3.3, was used for this experiment, but instead of starting to record data from the end of the guide tube, 40mm from the central sensing point of the eighth sensor group, this experiment was run from the mechanical limit of the testing rig when the magnet was fully inserted into the guide tube with the translation stages motion reversed. This choice was to check if the direction of motion would have any bearing over the data recorded. This experiment’s results, section 6.3.2, are recorded using the same orientation as the dual magnet experimentation, section 5.3.3.

Experiment 3: Dual magnet suspension (in load cell)

Once the initial tests had been completed using TR4, which produced the calibration data for the 24 sensor channels, continued experimentation could be performed with two magnets in repulsion. This testing was broken down into four experiments as the fixed magnet could be locked into four different positions, a design feature inherited from the TR3 hardware, section 5.2.3, that was never tested, to achieve the following experimental positioning:

1. Using the first mounting hole for the fixed magnet, the fixed magnets exposed surface was positioned directly under the x-axis and second y-axis sensing points, thus the sensor origin.
2. The second mounting hole displaced the fixed magnets position by 1.05mm so

that the exposed magnet face was positioned under the virtual sensing point between the first x-axis and y-axis sensing points.

3. The third mounting hole displaced the fixed magnet by $5mm$ from the sensor origin, so that the magnets exposed face was located half way between the first and second sensor groups.
4. The final fixed magnet mounting position was a total displacement of $6.05mm$ from the sensor origin, thus positioning the exposed magnet face half way between the first and second virtual sensing points.

These positions allowed for a full range of tests to be performed with TR4, to see if the magnet location algorithm could adapt to different initial conditions and if the initial conditions changed the accuracy of the algorithm. The four experiments all followed the same experimental protocol to ensure consistency and accuracy of the recorded data, section 6.3.4. The experimental protocol when broken down into steps took the following form:

1. Take initial calibration readings with no magnets within the sensing range of TR4 to enable suppression of background and environmental disturbances in the final testing data.
2. Install fixed magnet into testing rig using the mounting points corresponding to the experiment being performed and lock in position using the nylon thread and nuts.
3. Mount the moving magnet onto the load cell such that it will pass into the guide tube without touching the side walls which could cause spikes in the repulsion force measurements.

4. Translate the moving magnets position across the full range of motion to check for any interferences which could cause inaccuracy in data recording.
5. Position the moving magnet so that its exposed face is touching the fixed magnets exposed face and zero the load cells translation stage.
6. Set this point in the load cells motion control software as point 'A'.
7. Move the load cell to $100mm$ displacement so that the free magnet is positioned at the end of the guide tube and set this point in the load cells motion control software as point 'B'.
8. Zero the load cell, so that the mass of the free magnet and its holder with respects to gravity are accounted for.
9. Take a reading with the TR4 data acquisition software and wait for the data to be transfered to the recording computer.
10. Instruct the load cell motion control software to move in $0.5mm$ increments from point 'B' to point 'A', taking a reading of the repulsive force each time it stops.
11. Repeat the previous two steps until the magnets are touching.
12. Command the load cell motion control software to return to point 'B' and repeat the process a number of times for each fixed magnet location to record the experimental average, thus giving data to calculate mean error of data recorded.

5.4 Chapter Summary

The experiments described in this chapter were designed to confirm the theoretical premise of this Thesis, ensuring that the results gathered and analysed in the following

chapter were of the highest quality.

The experimental process for the Hall Effect sensor calibration, section 5.1, was devised to ensure that all measurement equipment was reading correctly and testing accuracy, whilst also confirming that the simulations were providing results that accurately predict the real world data. This also confirmed that the FEA and FEM techniques have been adopted correctly for future simulations.

The experimental testing rigs, section 5.2, that have been described flowed organically in their development. This was due to recommendations being made after each testing rig had been constructed and tested, to ensure that the next testing rig addressed any issues found during experimentation.

The final experimental testing rig, described in section 5.3, combined all recommendations from the initial testing rigs to confirm that two dimensional Hall Effect sensing is an accurate way to predict the location of a free magnet. The data gathered from the final testing rig through hardware and software, described in sections 5.3.1 and 5.3.2 respectively, enabled the magnet separation algorithm to be designed, section 6.5, as well as producing unique data that can be shared with the scientific community.

The results from all testing procedures described within this chapter are displayed in Chapter 6. The data produced by TR4 required additional curve fitting and calibration steps, which are described in Chapter 6.4.

Chapter 6

Results and Analysis of Experimental Data

This chapter displays, analyzes and explains raw data generated by the experiments described in Chapter 5. Wherever possible, similar data series use the same colors, so results can be visually compared between various data plots.

The structure of this chapter is as follows:

1. Results from sensor calibration, section 6.1
2. Results from experimental testing rigs, section 6.2
3. Results from final testing rig TR4, section 6.3
4. Curve Fitting of data, section 6.4
5. Magnet Separation Algorithm Development, section 6.5
6. Magnet Separation Algorithm Results, section 6.6

To save space in the main text, extra simulations and experimental results are included in the appendices. See section 1.5 for the full list of appendices.

6.1 Sensor Calibration

Each experimental method described in chapter 5 produced a range of analog data, with a minimum resolution of 10-bits over a $5V$ range, which equates to $\approx 4.883mV$ difference between samples. The data recorded by TR4 described in section 5.3 was logged using a 12-bit ADC over a $5V$ range, as such the accuracy of data produced by the final test rig is higher with $\approx 1.22mV$ difference between samples.

Single Hall Effect sensor in a Helmholtz Coil

To ensure that the sensors within TR4 were calibrated correctly, the Helmholtz coil described in section 5.1 was used. The calibration results gathered by the Helmholtz coil experiment, figure 6.1, show a good correlation between the simulated FEMM data and measurements taken with both the calibrated hall probe and the SS49E sensor. This data was acquired using a calibrated translation stage so that the readings were accurately recorded at mm intervals. The full data listing for these results, table C.1, can be found in Appendix C.

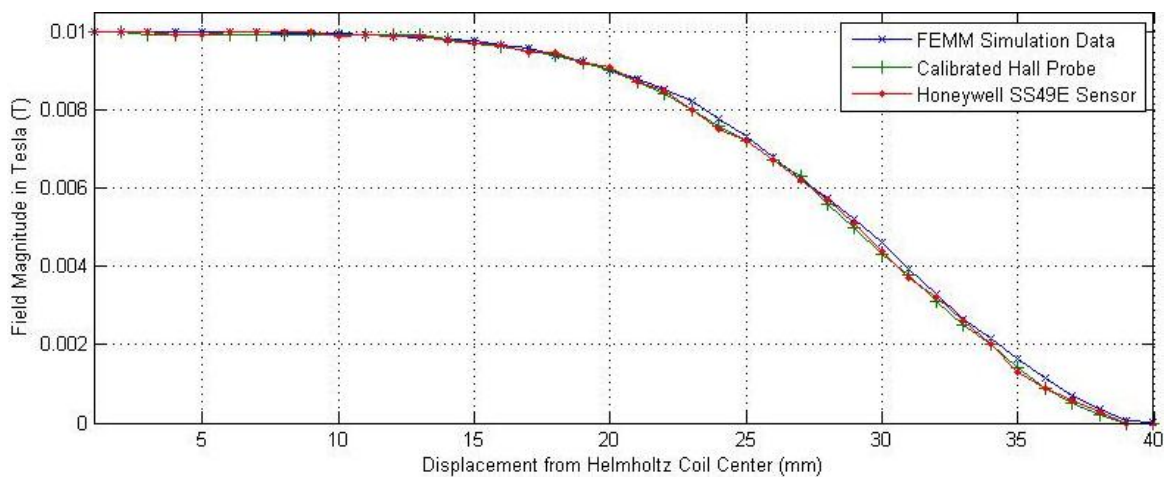


Figure 6.1: FEMM simulation of field magnitude (in Tesla) plotted against measurement point displacement from center of the Helmholtz coil (in mm) with experimental results for the calibrated hall probe and the SS49E hall effect sensors

There are some minor variations between the results which can be attributed to rounding errors with the data recording equipment and the data conversion algorithms, but the shape of all results curves match which proves that the SS49E sensors perform correctly and are correctly calibrated. This enables future experimentation to be performed with confidence in the SS49E sensors and their sensing characteristics.

6.2 Experimental Testing Rigs

This section describes and analyzes the results from tests performed with the experimental testing rigs TR1, TR2 and TR3. The equipment used for experimentation included a $1kN$ computerized load cell, to log force and separation data of the magnets directly to a CSV file, as well as the Quansar data capture system, linked via Simulink to Matlab for data recording of the hall effect sensors at 10-bit resolution between 0 and 5 volts.

6.2.1 Test Rig 1

The goal of TR1 was to experimentally derive magnetic repulsion force curves for various magnet pairs with respects to their separation, such that a magnet could be selected for continued experimentation and tested against the current Gilbert magnetic force model. The magnets tested ranged in size and magnetization density, table 5.1, from the very small ID17 magnet which was $1mm$ thick with a $5mm$ diameter and a magnetic field strength at its surface of $0.20T$, to the ID54 magnet which was $10mm$ thick with a $20mm$ diameter and a magnetic field strength at its surface of $0.46T$. When all the force curves were compared, it was clear that the ID54 magnet was the strongest in repulsion with ID17 producing the weakest response, figure 6.2.

The first goal of this experimentation was to derive an approximate repulsive force

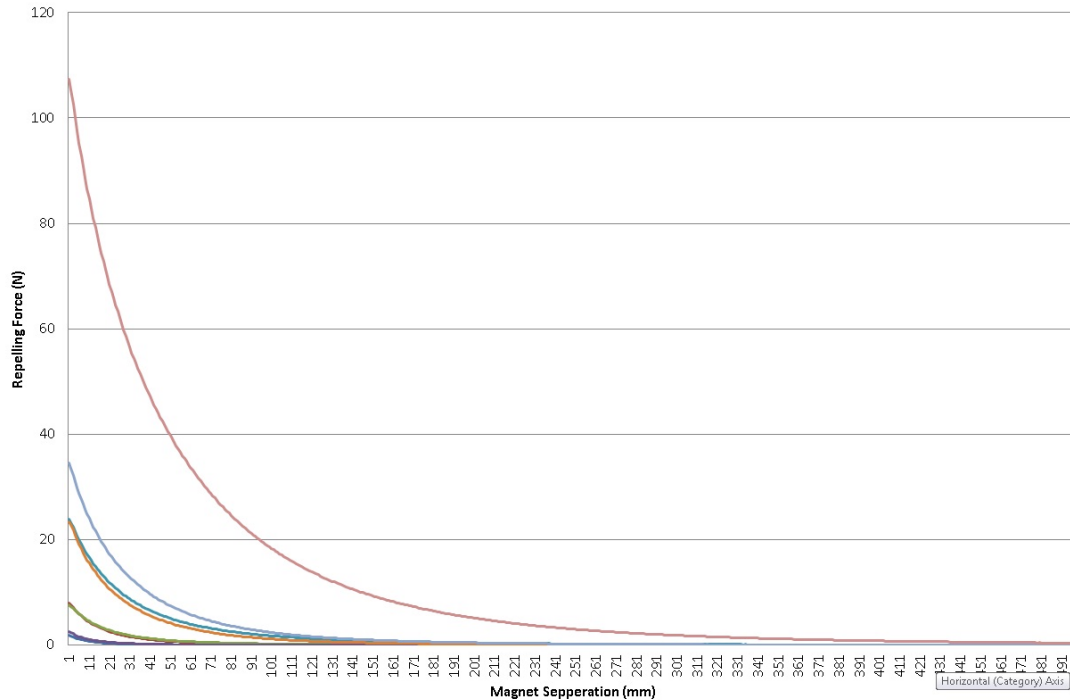


Figure 6.2: Comparison curves showing separation between magnet faces (mm) plotted against magnetic field strength (in Tesla) for the 8 magnets tested with TR1; ID17, ID20, ID21, ID23, ID34, ID43, ID44 & ID54

model of each magnet type with respects to their separation, but when attempting to fit a curve to the real world magnet data the non-linearity of the magnets and their response meant that a high order polynomial was required to describe their response, as the data could not be fitted with a logarithmic series. The polynomials derived to express the real world magnet data curves were 6^{th} order polynomials, table 6.1.

The 6^{th} order polynomials provided a basic representation of the data, figure 6.3, but lacked accuracy without using a higher order polynomial. The representative polynomial curves of ID17 and ID54, figure 6.3, follow the same shape as the real world data with relatively good curve fitting for the ID54 magnet under $5mm$ separation. The measurement accuracy of low repulsion forces cause the real world data to become zero, which causes the oscillating response as the polynomials try to represent data

Magnet ID	Polynomial
ID 17	$0.48359 - 0.22091x + 0.03232x^2 - 2.12309 \cdot 10^{-3}x^3$ $+ 0.06938 \cdot 10^{-3}x^4 - 1.10242 \cdot 10^{-6}x^5 + 6.78970 \cdot 10^{-9}x^6$
ID 20	$3.00713 - 1.30810x + 0.18674x^2 - 0.01209x^3$ $+ 0.39126 \cdot 10^{-3}x^4 - 6.17519 \cdot 10^{-6}x^5 + 3.78425 \cdot 10^{-8}x^6$
ID 21	$3.15957 - 1.34411x + 0.18984x^2 - 0.01221x^3$ $+ 0.39381 \cdot 10^{-3}x^4 - 6.19911 \cdot 10^{-6}x^5 + 3.79166 \cdot 10^{-8}x^6$
ID 23	$0.72163 - 0.32537x + 0.04729x^2 - 3.09432 \cdot 10^{-3}x^3$ $+ 0.10085 \cdot 10^{-3}x^4 - 1.59962 \cdot 10^{-6}x^5 + 9.83842 \cdot 10^{-9}x^6$
ID 34	$12.76193 - 5.08859x + 0.69676x^2 - 0.04405x^3$ $+ 1.40498 \cdot 10^{-3}x^4 - 0.02195 \cdot 10^{-3}x^5 + 1.33555 \cdot 10^{-7}x^6$
ID 43	$11.61328 - 4.80865x + 0.66955x^2 - 0.04271x^3$ $+ 1.36919 \cdot 10^{-3}x^4 - 0.02147 \cdot 10^{-3}x^5 + 1.30900 \cdot 10^{-7}x^6$
ID 44	$18.56939 - 7.48278x + 1.02831x^2 - 0.06511x^3$ $+ 2.07765 \cdot 10^{-3}x^4 - 0.03247 \cdot 10^{-3}x^5 + 1.97558 \cdot 10^{-7}x^6$
ID 54	$74.31065 - 26.7556x + 3.47289x^2 - 0.21277x^3$ $+ 6.64816 \cdot 10^{-3}x^4 - 0.10241 \cdot 10^{-3}x^5 + 6.16618 \cdot 10^{-7}x^6$

Table 6.1: 6th order polynomials of the magnets used with TR1

with zero magnitude. Due to the inaccuracy between the 6th order polynomials and the real world data, better curve fitting equations and approaches need to be developed through further experimentation to accurately represent the force between two magnets in repulsion.

When the ID54 real world data is compared to the Gilbert model, described in section 3.2.3, it is clear that the curves are a very different shape, figure 6.4. This is due to the Gilbert model not accounting for a number of factors including the two magnets magnetization strength. When the two magnets are brought close to each other the magnets try to demagnetize each other to some extent, depending on how magnetically ‘hard’ the magnets are, thus reducing the maximum possible repulsive force that they can produce due to temporary loss of magnetic field strength. This shows that the

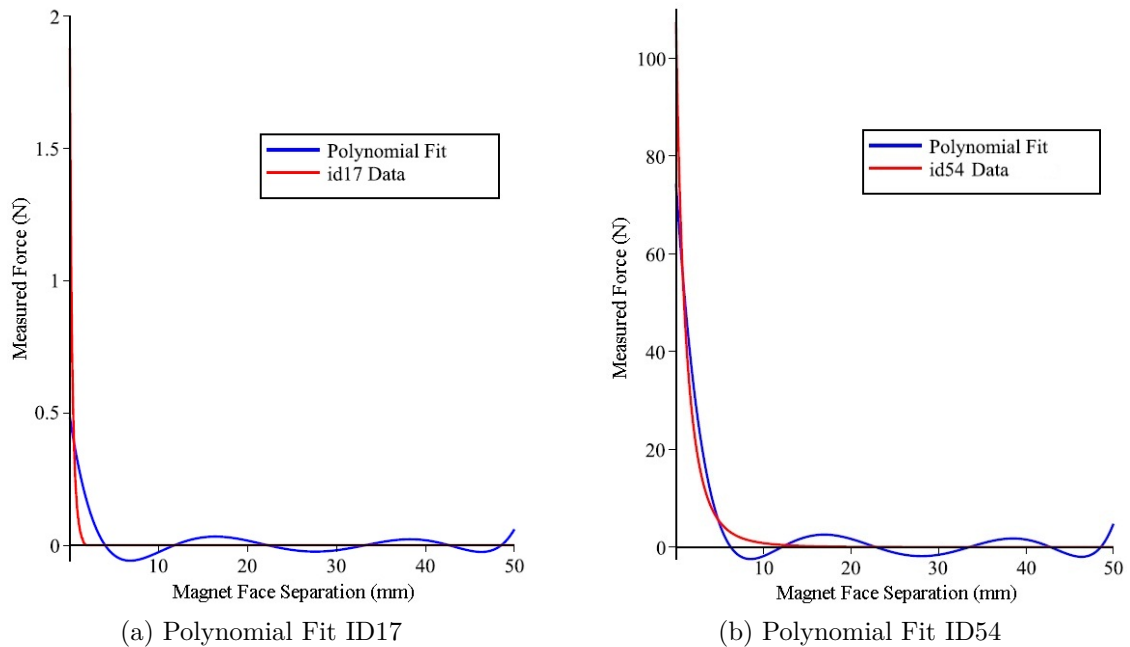


Figure 6.3: Polynomial curve fit of the ID17 and ID54 magnet repulsive force profiles

Gilbert model is inaccurate when the magnets are close together and as such the Gilbert model should only be used to represent magnets that are a good distance apart, thus the Gilbert model is a ‘far fit’ model, which can be used for different experimental scenarios and models.

By applying the Gilbert model to all magnets and analyzing where the real world data crosses the Gilbert model data, $\approx 6mm$ separation in figure 6.4, some characteristics of the magnets can be extracted. Analysis of crossing points between the theoretical and real world data, when plotted against magnetic flux density for all magnets, figure 6.5, shows a strong correlation of results between magnets with proportional dimensions. The trend lines generated show how closely they fit the data and are assigned to magnets with similar proportions such as; magnets with a diameter greater than their thickness ($d > t$), magnets with a diameter less than than their thickness ($d < t$) and magnets with equal thickness and diameter ($d = t$). This analysis will allow

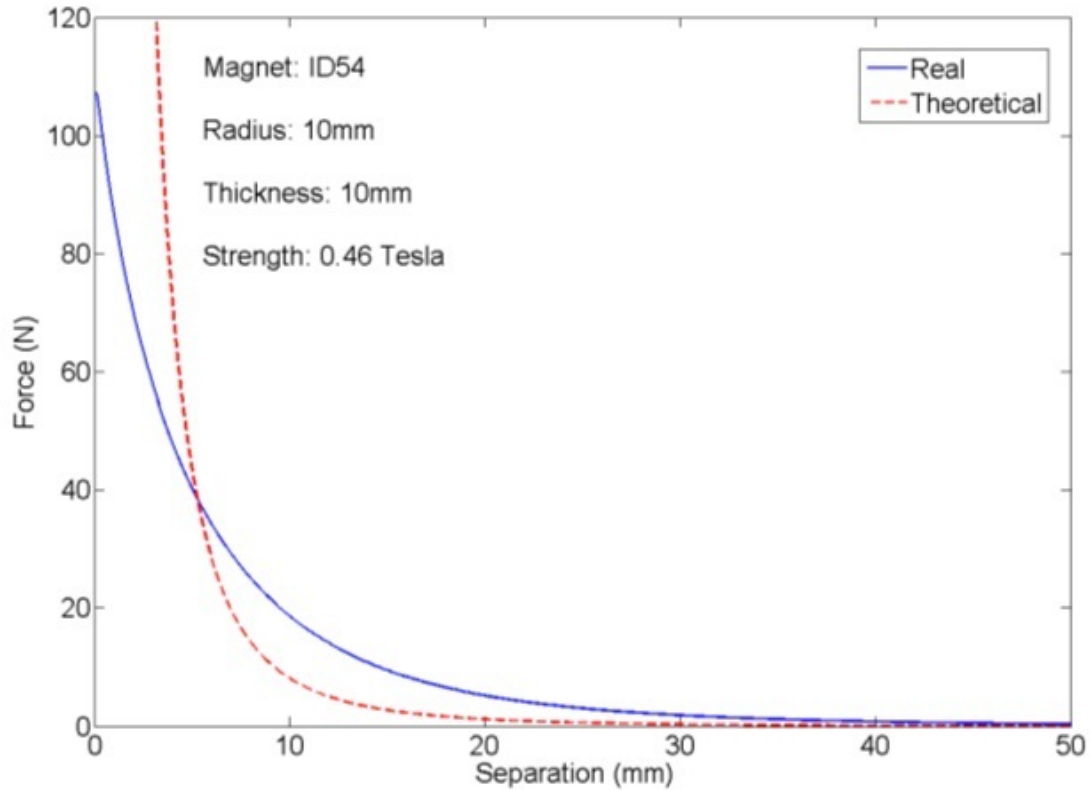


Figure 6.4: Comparison between the ID54 real world data and the Gilbert Model for magnetic repulsion

categorization of an unknown magnet from its force profile by matching against these results.

The experimentation using TR1 resolved the choice of magnet for continued experimentation, the ID54 magnets in table 5.1 (20mm diameter, 10mm thick, 4600 Gauss (0.46T) with a Ni-Cu-Ni protective coating) were chosen as they produced a useful repulsive force, sufficient to support a load of $5kg$ with a maximum repulsive force of $10.8kg$, as well as having enough magnetic field strength to be measured around the device. The magnets were also a good size to work with and easily mountable in the Delrin holders, making them portable and relatively lightweight.

The design of TR2 could now be finalized to incorporate the ID54 magnets and the

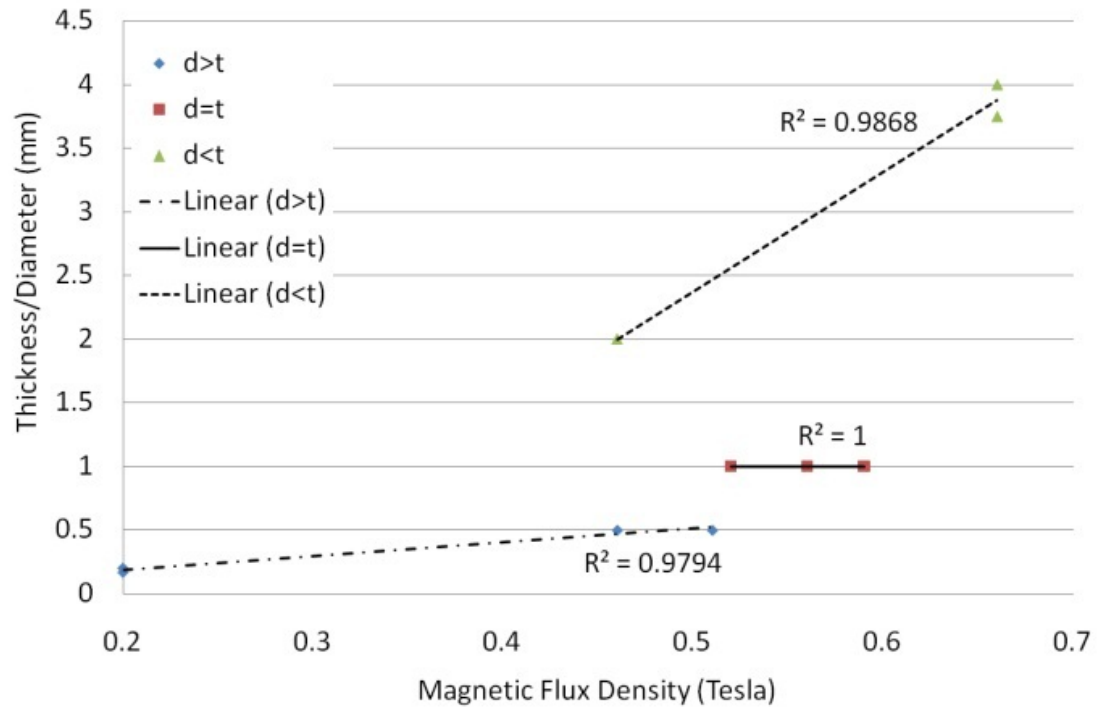


Figure 6.5: Comparison between the 8 magnets tested with TR1

SS49E hall effect sensors to monitor the magnetic fields surrounding the magnets.

6.2.2 Test Rig 2

The design of TR2 was based on the results from experimentation with TR1, such that the ID54 magnets were incorporated into the design and non-magnetic materials were used in the construction of TR2. The Honeywell SS49E sensors were chosen to measure the magnetic fields around the ID54 magnets as their measurement range, ± 1000 gauss (0.1 Tesla), would give a decent response with respects to the observed magnetic fields. The SS49E sensors positioning had to be far enough away from the magnets so that the hall effect sensing element would not saturate due to excessive magnetic field strength, but close enough so that the sensors produced accurate results across a full range of measurements. The positioning of the SS49E sensors in TR2 was determined through some initial tests and simulations (section 4.2) such that mounting the sensors on the plastic guide tube, 15mm from the central magnet axis, provided the optimal positioning for the sensors. To obtain the positioning of the sensors a slot the same width of the SS49E sensors was milled into the side wall of the guide tube, so that the sensors would fit into the groove, at the required displacement from the central axis. The SS49E sensors were mounted into this slot using the process described in section 5.2.2, such that they were arranged into 4 groups of sensors, with each sensor group having two sensors mounted at 90° (perpendicular) to each other to measure the magnetic field in both the x and y-axis in Cartesian coordinates. The sensors data within TR2 was recored using a Quansar data capture board, connected to a PC running Matlab and Simulink, so that data could be logged directly to a CSV file.

Data recoded with the first edition of the TR2's sensing hardware, figure 5.6, had some major inaccuracies, as the data capture was performed on a desk (close to the capture equipment and PC) using a ruler and measurements by eye for magnet displacement,

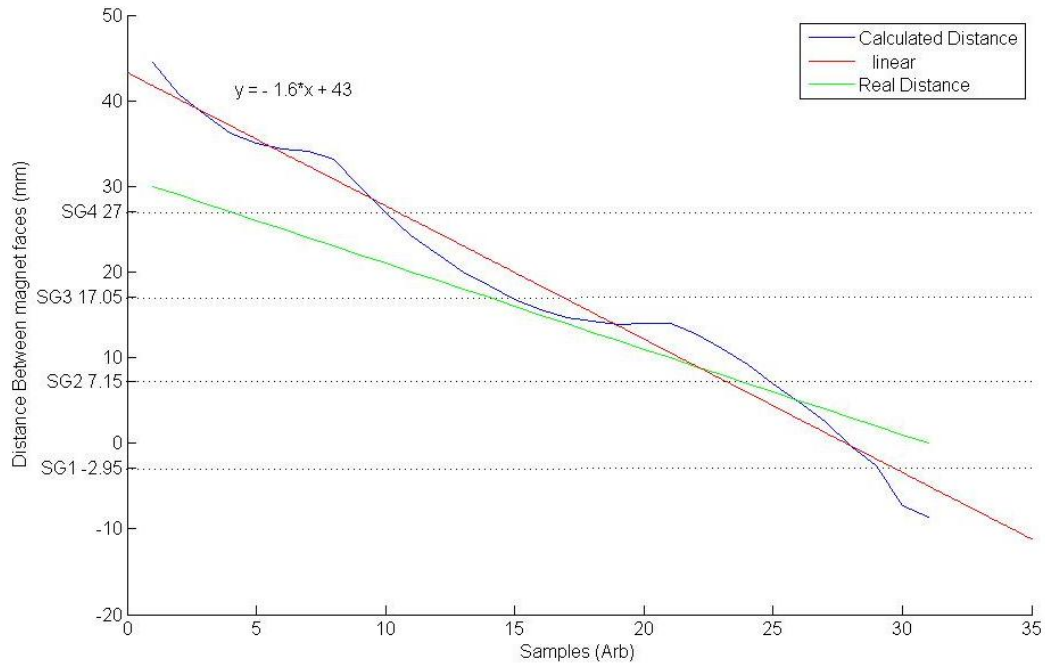


Figure 6.6: Results from magnetic separation algorithm for the first version of TR2

rather than being displaced using a calibrated translation stage. The sensors were soldered into a prototype PCB, manufactured in-house, which was mounted using two ‘blobs’ of Bluetack that caused the PCB to slip under the weight of the ribbon cable used to connect the sensors to the Quansar board. The sensors were only held against the surface of the guide tube, rather than being bonded to it, so their relative position to each other was not very precise and could move up to 2mm out of position. The data was transferred back to the Quansar board using a meters length of unshielded ribbon cable, which incurred electrical interference from the testing environment. All these factors created unsatisfactory data, figure 6.6, which led to the second edition of the sensing hardware, figure 5.7.

The data recorded by the second edition of sensors was more accurate as the sensors could not move relative to each other, due to being super glued in position, but these were still positioned by eye so the sensors were not equally spaced. The electrical noise

experienced with the first edition of the hardware was reduced through the use of coaxial cable to transfer the analog voltages from the sensors back to the Quansar board, figure 5.7. The second edition of the sensing hardware was an improvement with respects to the first edition, but was less robust and frequently experienced broken connections due to the weight of the coaxial cable hanging from the sensors leads. The TR2 data capture system was limited to 8 analog channels so, taking the above points into consideration, TR3 was designed to enable more sensors to be used simultaneously and solve some of the reliability issues found with TR2.

The approximate magnet separation algorithm described in section 5.2.2 was tested using data recorded with the second edition of TR2's hardware, figure 6.7.

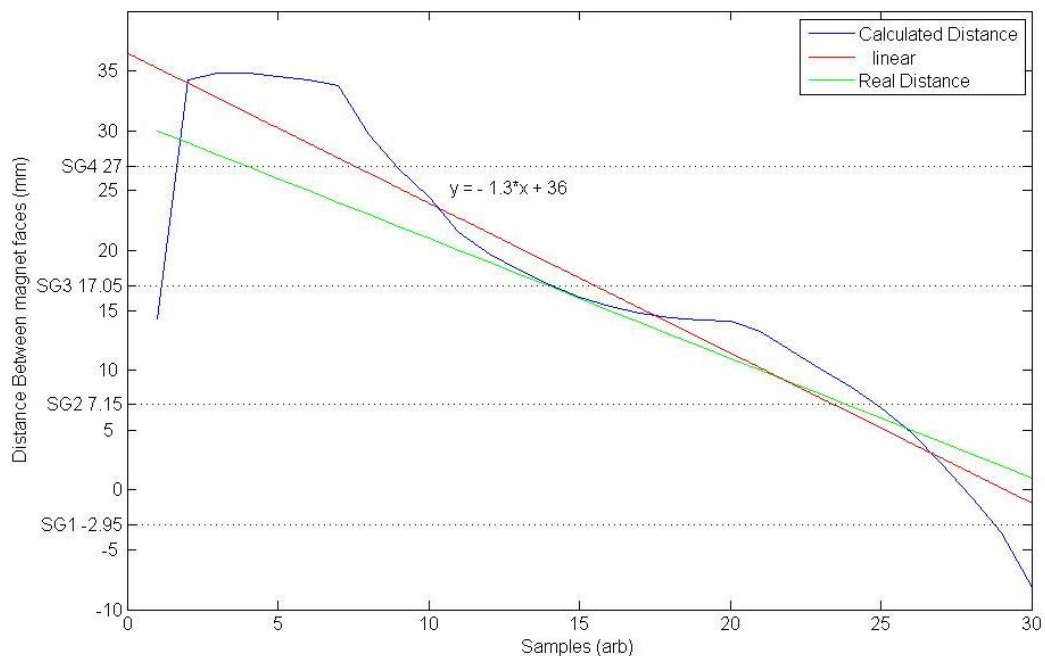


Figure 6.7: Results from magnetic separation algorithm for the second version of TR2

The green line represents the expected separation between the magnet faces, with the blue line showing the output from the algorithm and the red line showing the line of best fit for the processed data. The line of best fit equation $y = -1.6x + 43$ is visibly different to the expected result $y = -x + 30$, but the processed data is relatively close

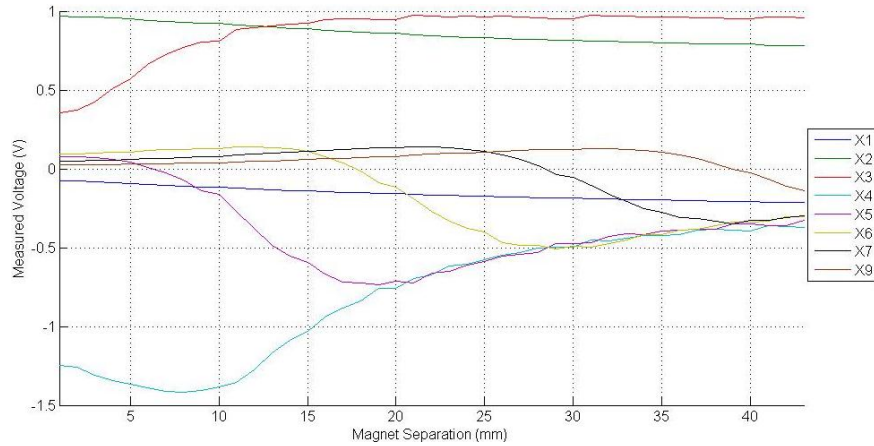
to the expected considering there was a lack of sensor positional accuracy, noise within the data and inaccuracy of positional displacement of the magnets. The processed data compared to the expected results shows a positive step towards being able to locate the position of an unknown magnet from magnetic field measurements, but the data necessary to test the algorithm fully required the development of TR3.

6.2.3 Test Rig 3

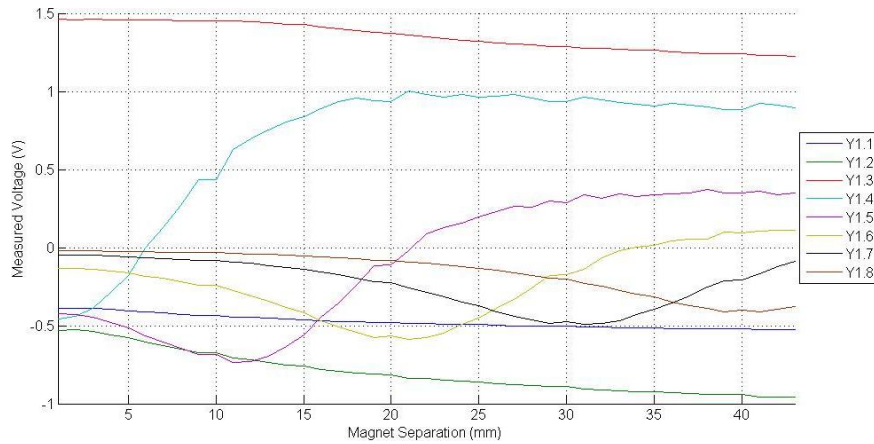
The TR3 design massively improved the positional accuracy of the sensors as they located into CNC milled slots, within $\pm 0.1mm$ of their target location and were held in place with super glue, with all sensors connecting to a cable delivery system to remove the chance of signals either shorting or breaking. The cable delivery system did improve the reliability of the test rig, but the data capture system caused addition problems. The TR3 guide tube and orientation slots were extended to resolve an issue with the magnet holder reaching its physical limits during operation, which allowed for a full range of data readings to be taken even under extreme displacements of the free moving magnet. As discussed in section 5.2.3, TR3 did not live up to expectations with regards to data capture, as such the results, figure 6.8, show a notable increase in signal noise, due in part to the long and unshielded signal traces but predominantly from interference created by connecting 3 computers to a common ground. The data capture system also relied on a hand held microswitch to take snapshots of the sensors data, which caused some errors during the data recording process as occasionally the Quansar data boards missed the trigger signal and as such didn't record the required data. The errors due to missed readings are visible, figures 6.8b & 6.8c, between $8 - 10mm$ and $18 - 20mm$ as a flat spot in the data, with the noisy signal data detracting from the expected smooth data curves. Another problem found with TR3 and its data capture system was the need to consolidate the data recorded into a single

data file as the data was captured using three separate measurement computers. This data consolidation took a long time to perform, even when using scripts to automate most of the process, so additional experimentation became impractical.

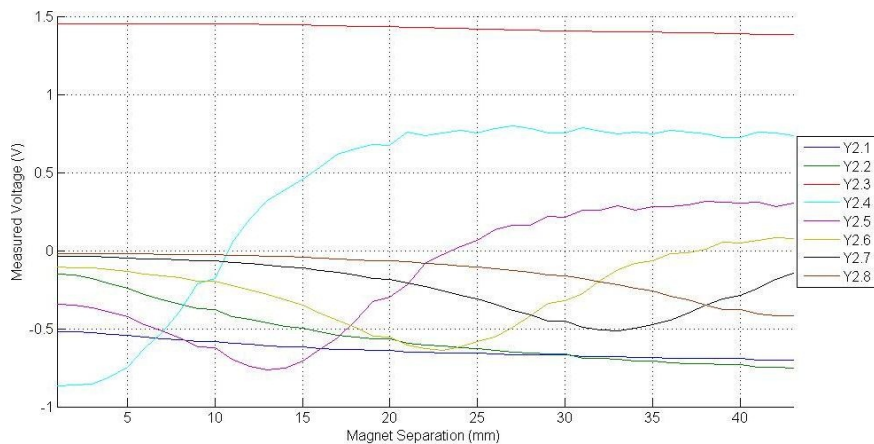
The testing with TR3 was abandoned due to the flawed data capture system that was tolerated when used with TR2 (a single Quansar capture board setup was far simpler to synchronize), which lead rapidly to the design of TR4 which included on board data capture and conversion to move away from the Quansar data capture system. This was an essential step as the approximate magnet separation algorithm required higher quality data than TR2 and TR3 could produce, with the expanded functionality of recording 24 channels of data simultaneously, perform data averaging from multiple experimental runs and reducing the overall size of the device so that 3 computers were not required for testing.



(a) TR3 Data produced by the X group of SS49E sensors measuring magnetic field strength in the x-axis



(b) TR3 Data produced by the Y1 group of SS49E sensors measuring the y-axis with sensor housing offset creating the virtual sensing point



(c) TR3 Data produced by the Y2 group of SS49E sensors measuring the y-axis with corrected sensor offset to remove virtual sensing point

Figure 6.8: Plots showing all 24 data channels recorded by TR3

6.3 Final Testing Rig TR4

The final testing rig developed for experimental purposes, TR4, was built upon the solid mechanical base that TR3 introduced but had a completely redesigned approach to data acquisition. The data acquisition was performed using an embedded microprocessor from Microchip [94], the PIC18F87K22 [95], which enabled sequential recording of 24 analog channels at 12-bit resolution over the 0 – 5 volt range. The PIC chip is capable of taking these readings over 100 times a second, but TR4 did not use the PIC to its full capability and only took ten readings when requested by the TR4 management software. This meant that TR4 sent back ten sets of raw data per analog channel that could be used for data analysis and accuracy checking, thus TR4 produced 240 data points per set of readings.

To reduce the size of the data acquisition system all data was relayed back to a laptop, running custom data management software written in C#, via a Bluetooth link. This meant that TR4 could run off a battery supply and not incur any coupled noise from either a smoothed AC/DC power supply or a data communication cable to the computer, thus improving the quality of data acquired. The analog signal paths were also massively shortened compared to TR3, as the maximum signal trace on the PCB was 5cm, with all analog data lines being surrounded by a ground shield to further reduce noise. The experiments performed, described in section 5.3.3, produced data that was of far higher quality compared to all previous test rigs which enabled much greater analysis and algorithm refinement than was possible before.

The following sections describe and analyze data from experiments performed, as described in section 5.3.3.

6.3.1 Single magnet calibration swing from guide tube end

The data capture system for TR4 had been proven to operate through the group sensor calibration test, Appendix D, but this tested the sensor channels before the 24 SS49E sensors had been soldered to the TR4 PCB. This meant that additional testing was required to check sensor accuracy and test the data recording range of all 24 sensor channels. The experiment was performed, as described in section 5.3.3.

The results were recorded by the TR4 data acquisition hardware at 12-bit resolution and $0.5mm$ increments with the data plotted, figure 6.9, as voltage against magnet location. The data capture system recorded a calibration set of data before the magnet was introduced, which enabled the subtraction of the $\approx 2.5V$ offset produced by the normal operation of the SS49E sensors. This offset represents the hall effect reading when no field is acting upon the hall sensing element, so voltages lower than this offset represented a negative magnetic field direction. The data produced was also grouped into sensor types; x-axis, y-axis virtual sensing point and y-axis central sensing point. When plotted on axis with the same scale the data is visually impressive.

Taking the eighth sensor in the x-axis, X_8 in figure 6.9 (plotted in blue), the graph shows how the magnetic field observed gently increases in a positive direction before sharply dropping to a negative field magnitude, $\approx -1.45V$, which then follows an almost symmetric slope back to near $0V$. The minimum data point of X_8 centers around a $40mm$ displacement, which was expected as the X_8 sensor is positioned $40mm$ from the end of the guide tube which is where readings were taken from. The next sensor, X_7 (plotted in black), follows a very similar curve to the X_8 data but is displaced by $10mm$. This is expected as the sensors are positioned every $10mm$ and are both mounted with the same orientation. This pattern is replicated across the entire data set of x-axis sensors, with very minor variations in the minimum field magnitude point, thus proving that the sensors are accurately placed along the x-axis.

There is however some inconsistency in the magnitude between channels, very clearly seen on channel X_4 (plotted in cyan), due to the SS49E sensor not sitting flush to the guide tube. This was caused by the super glue curing too quickly to allow for accurate placement of the sensor, as such X_4 is sitting on a ‘blob’ of super glue and not positioned as accurately as the other sensors.

The response from the first and second y-axis sensors both have the same curve shape, but are translated by $1.05mm$ as expected due to their positioning on the outside of the guide tube. The second y-axis sensor group also has a slightly smaller amplitude due to being mounted further from the magnets central axis. This was to remove the virtual sensing point by aligning the hall element center with the x-axis hall element. Due to the direction of data recording, X_8 to X_1 , the response curves of the two y-axis plots are the reverse of what is expected when the second magnet is included. The first y-axis sensor group data shows an smaller magnitude recorded by sensor $Y_{1,1}$ with an increased magnitude for $Y_{1,8}$. The reduced magnitude of $Y_{1,1}$ is due to another blob of super glue with the increase in magnitude of $Y_{1,8}$ caused by the sensors internal characteristics from manufacture and falls within the expected sensor accuracy. The second y-axis sensor group data shows $Y_{2,1}$ is also affected by a blob of super glue. The raw data can be converted, using equation 5.1 in section 5.3.3, from voltage to Gauss to give more meaningful results, figure 6.10. The converted data is correctly scaled as seen in the simulations performed, section 4.2, thus can be considered the ground truth data. This single magnet testing is important to ensure that the profiles of all sensors were known under the same test conditions, so that errors caused by positional misalignment and sensor manufacturing differences can be corrected for, section 6.3.3.

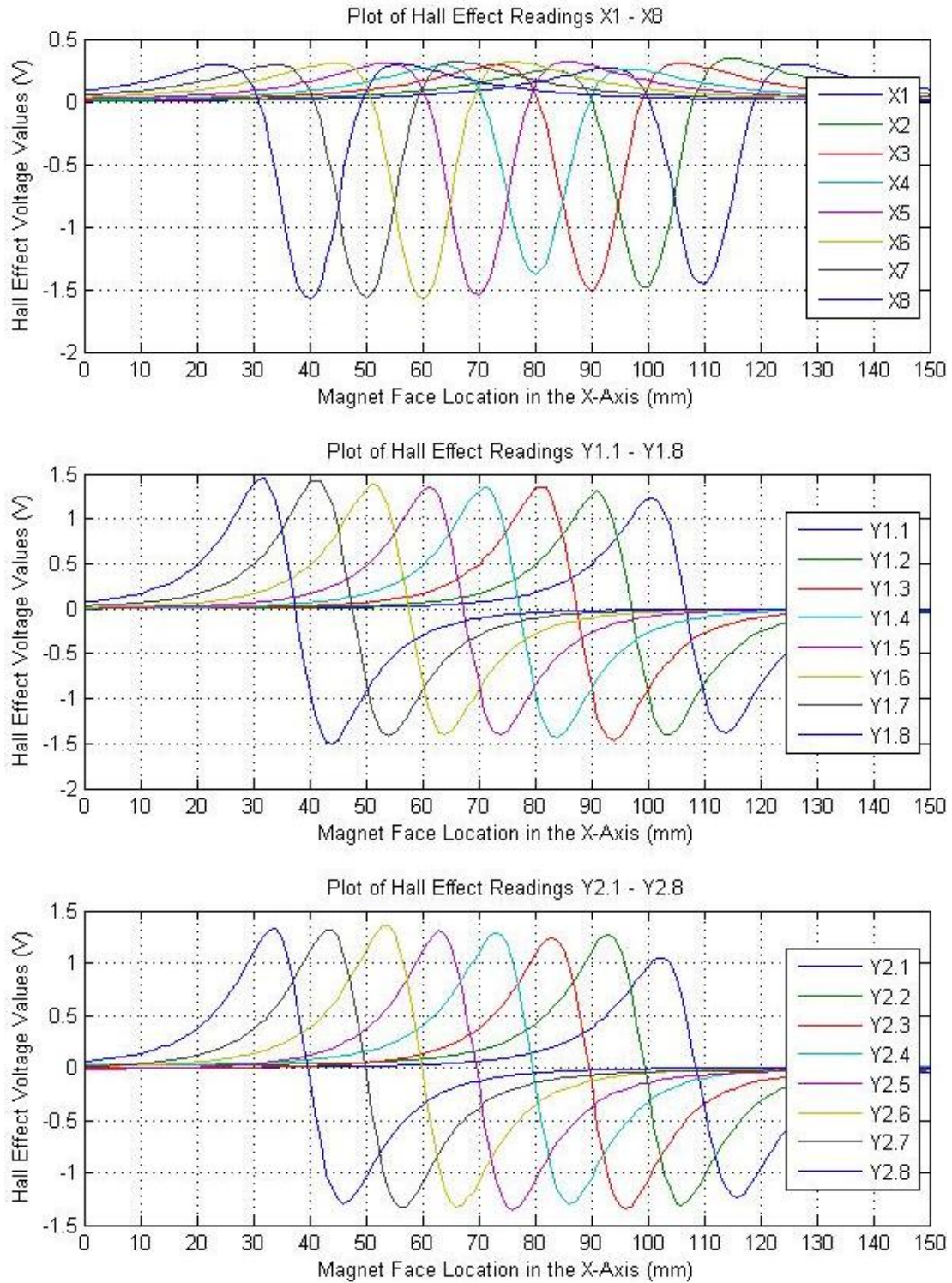


Figure 6.9: Raw voltage data from TR4's 24 sensor channels when a single magnet is passed through the TR4 guide tube

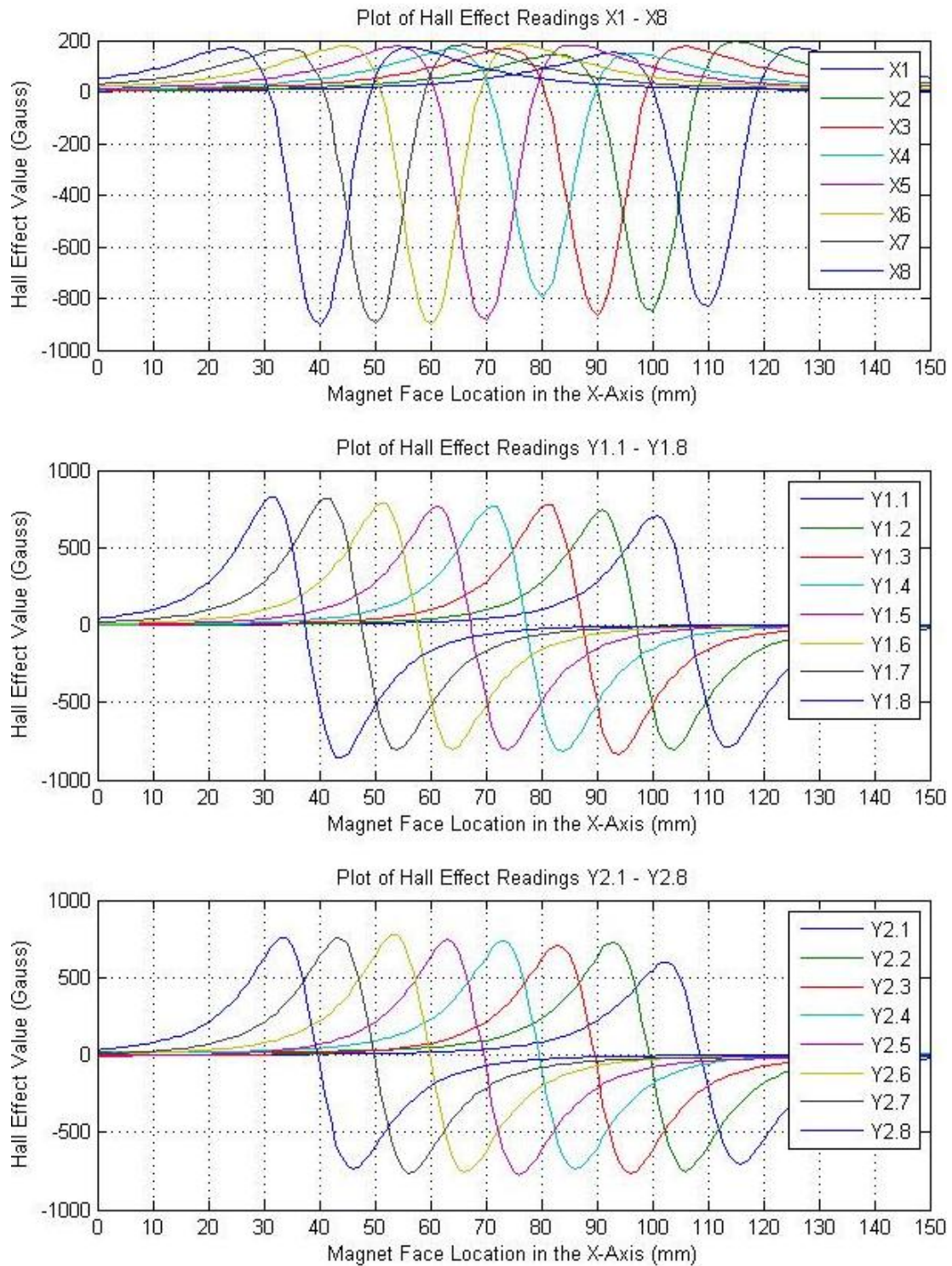


Figure 6.10: Data from the first single magnet calibration experiment with the raw voltage values converted into Gauss

6.3.2 Single magnet calibration swing from mechanical limit

The goal of this testing was to check if translating the magnets in the opposite direction would change the data recorded by the TR4 data acquisition hardware. The only visible difference between the data recorded with this experiment and the previous single magnet calibration swing routine was that the y-axis plots were inverted due to the x-axis being plotted in reverse, figure 6.11.

The same inconsistency in the recorded data, compared to the previous experiment, is visible for the channels affected by misalignment due to super glue problems; X_4 , $Y_{1.1}$ and $Y_{2.1}$, again echoing how accurately the data acquisition hardware has recorded the data. This data was also converted to Gauss, figure 6.12, using equation 5.1 and falls into the expected data range. As before the data was calibrated, section 6.3.3, which matched the data recorded previously. The quality of the data recorded with the TR4 data acquisition hardware is much better than data recorded with TR1, TR2 and TR3, which was the aim of TR4.

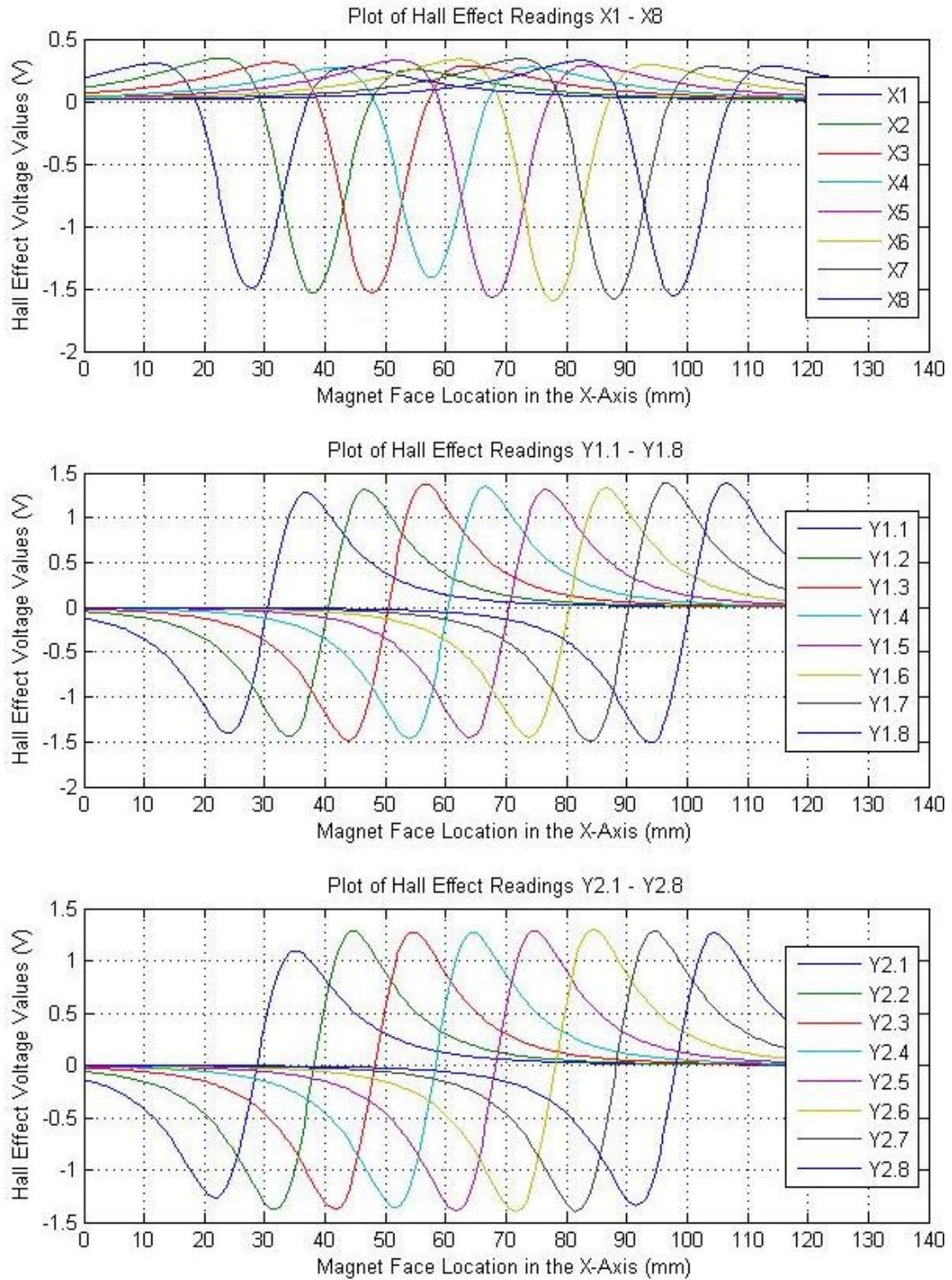


Figure 6.11: Raw voltage data from TR4's 24 sensor channels when a single magnet is passed through the TR4 guide tube from the mechanical testing limit

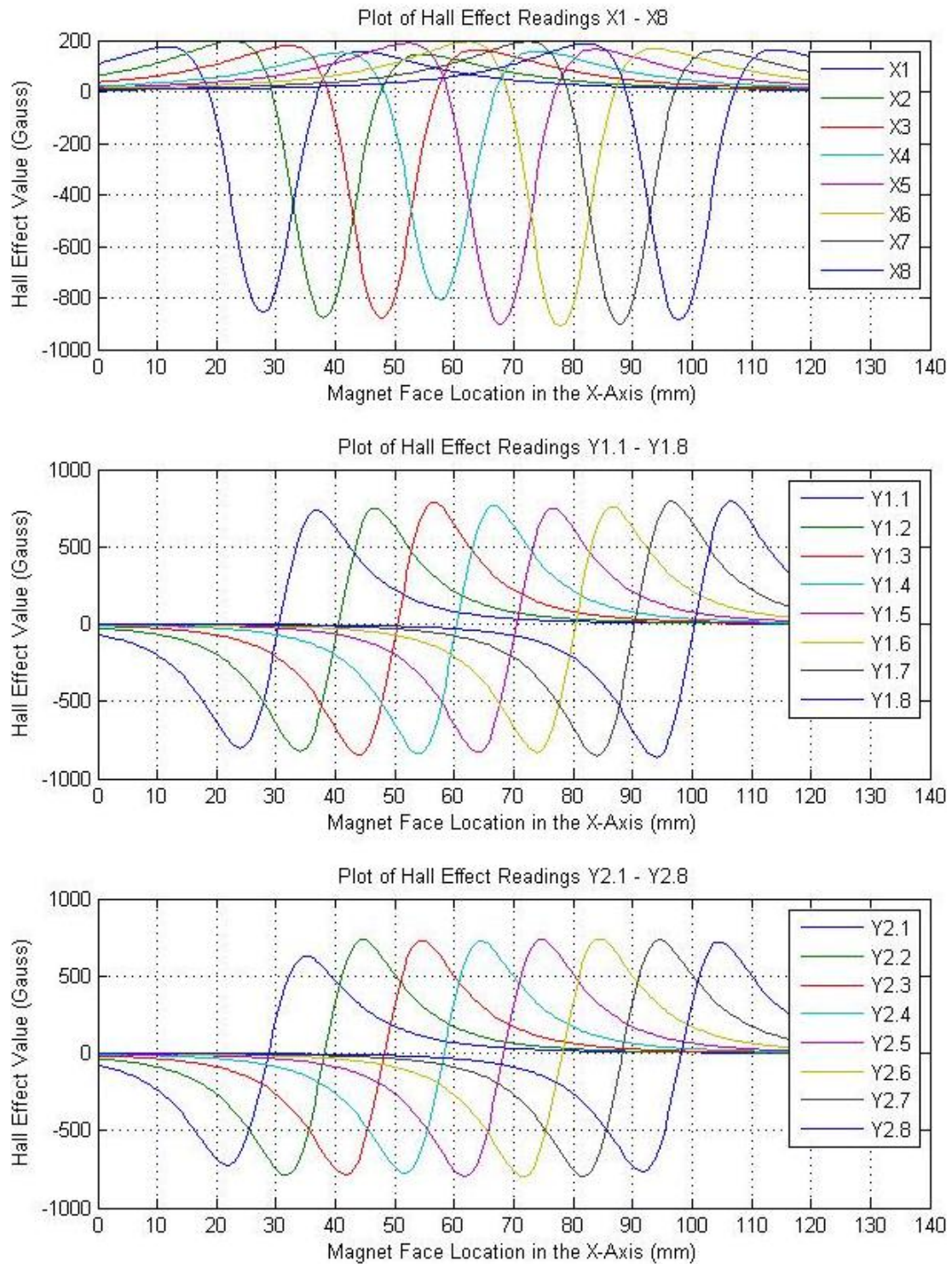


Figure 6.12: Data from the second single magnet calibration experiment with the raw voltage values converted into Gauss

6.3.3 Results after data calibration

The data recorded with TR4 varied due to mechanical misalignment of the SS49E sensors, so some calibration was required to adjust the data to be consistent across all channels. This is an important step as all channels need to give consistent results that can be used for further analysis. The data from the two single magnet swing calibration experiments gives a good reference data set that can be used in conjunction with the Matlab data management and calibration functions, described in sections 5.3.2 and 5.3.2. The data is calibrated by taking the average maximum and minimum data points for all of the SS49E sensors in TR4, to calculate an offset from this average, so each channel can then be scaled to match the correct data range. This corrective scaling can clearly be seen, figures 6.13 and 6.14, for example with the channel X_4 data, where the dotted cyan line represents the original data and the solid cyan line representing the correctly scaled data. These two graphs also show how close some of the channels original data is to the correctly scaled data, for example channels X_8 , X_7 , $Y_{1.4}$, $Y_{1.5}$, $Y_{2.2}$ and $Y_{2.4}$.

The offset and scaling values created by the scaling and calibration functions were added to a Matlab matrix that could be called when analyzing future data, such that the sensors were all now calibrated with respects to each other. This raw data calibration enables the analysis of future data when two magnets are present in the system as the SS49E sensor characteristics are known.

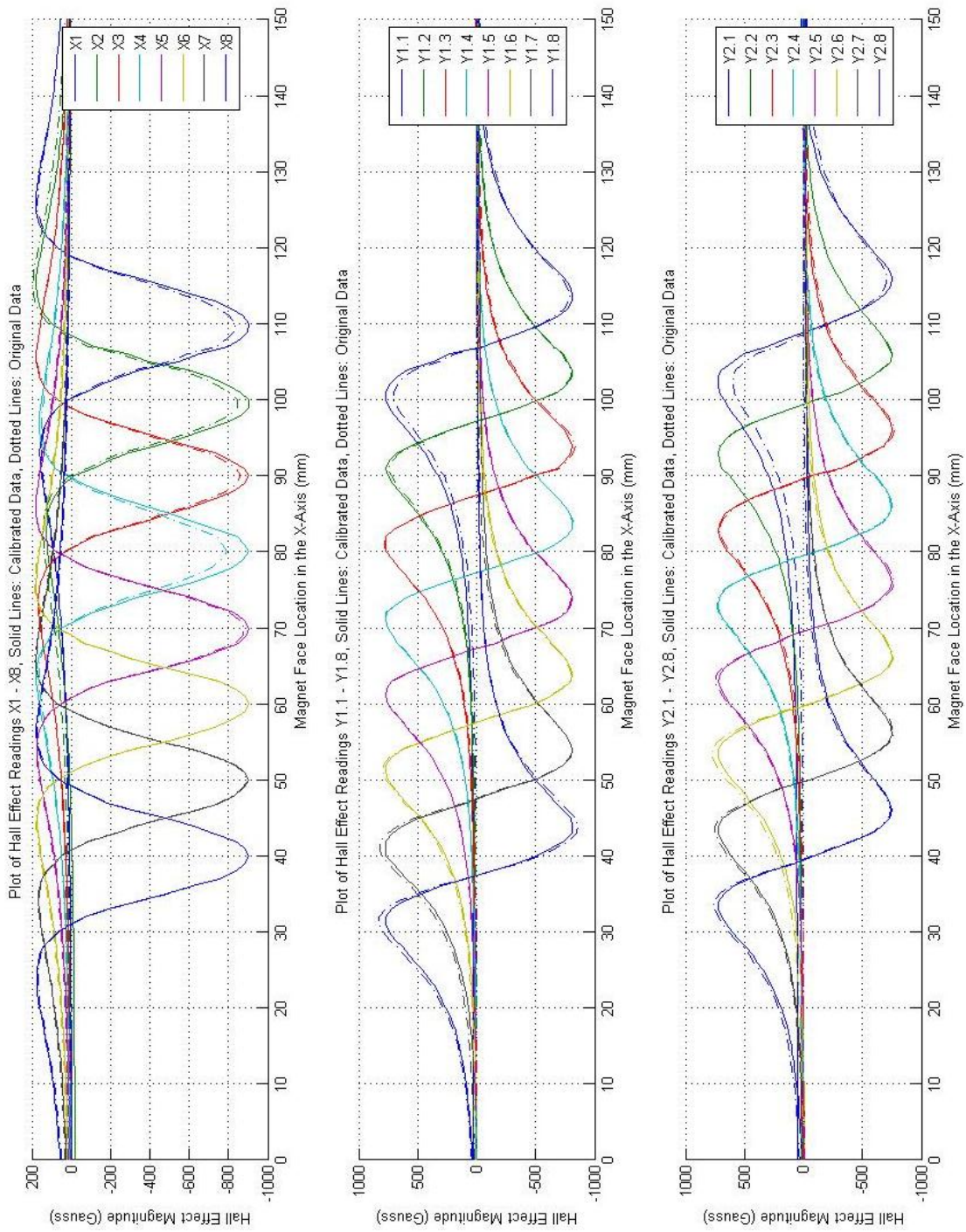


Figure 6.13: Comparison between the raw data (shown as dotted lines) and the calibrated and scaled data (the solid lines) from the first single magnet calibration experiment

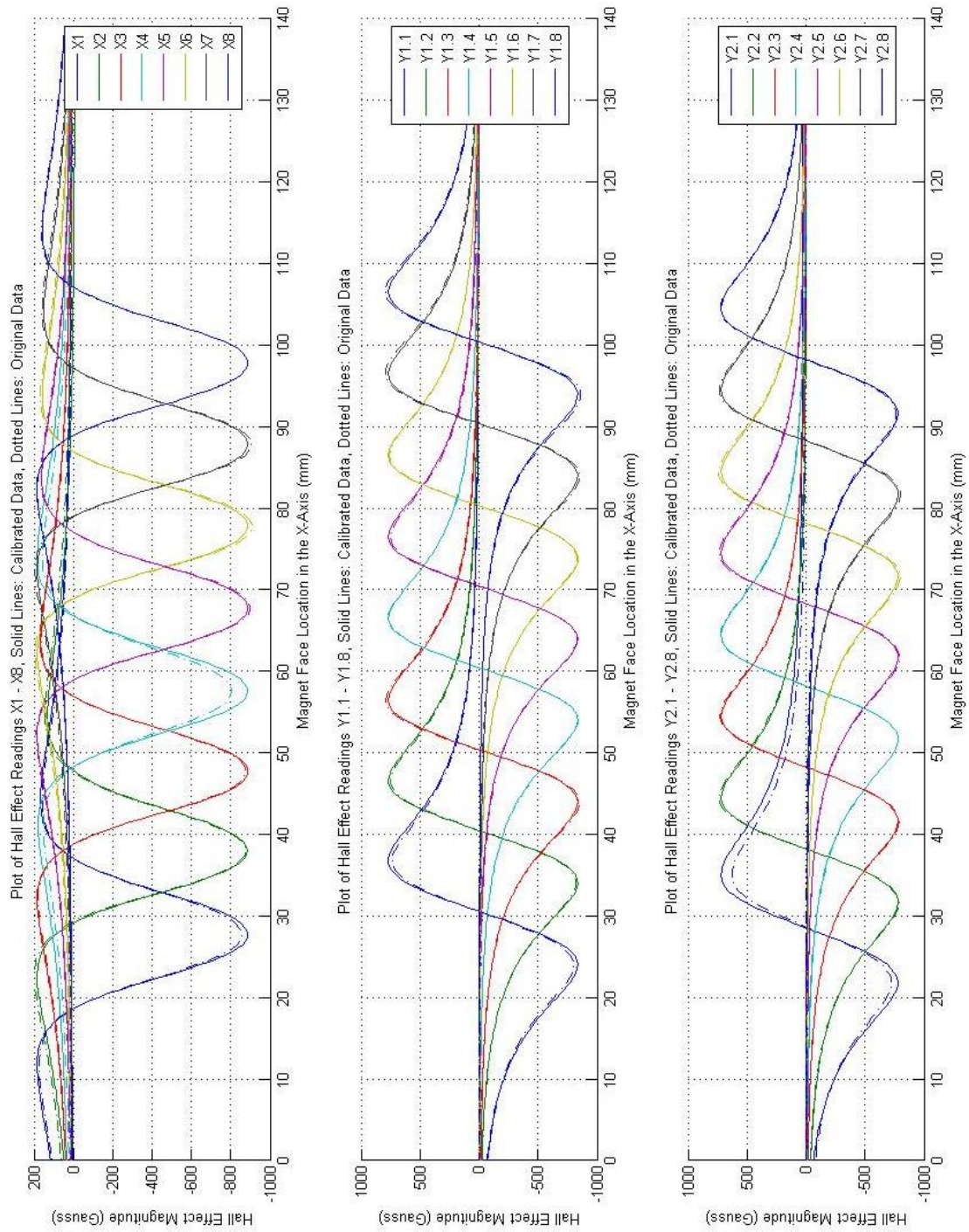


Figure 6.14: Comparison between the raw data (shown as dotted lines) and the calibrated and scaled data (the solid lines) from the second single magnet calibration experiment

6.3.4 Dual magnet suspension results

Once all the calibration steps were completed it was possible to record the data with two magnets present in the testing rig. The testing followed the experimental protocol described in section 5.3.3 for the following fixed magnet positions:

1. Fixed magnet exposed surface positioned at the sensor origin, figure 6.16
2. Fixed magnet positioned at $1.05mm$ from sensor origin to be under the virtual sensing point, figure 6.17
3. Fixed magnet positioned at $5mm$ from sensor origin to be half way between the first two sensor groups, figure 6.18
4. Fixed magnet positioned at $6.05mm$ from sensor origin to be half way between the first two virtual sensor groups, figure 6.19

All data shown in the graphs listed above was passed through the calibration functions to incorporate the data offset and scaling value for all channels generated by the previous experiments.

As there are now two magnets located within TR4 the data looks different, which is most notable in lower value sensors; X_1 to X_4 , $Y_{1.1}$ to $Y_{1.4}$ and $Y_{2.1}$ to $Y_{2.4}$. This can be explained simply as the sensor origin is located at the central sensing point of the third sensor group, so that the magnetic field could be measured behind the fixed magnet as well as in front of it. Therefore this gives a near constant value in the lower value sensors response curves until the magnets are nearly touching, as the magnetic field surrounding the fixed magnet is only affected when the other magnet is in close proximity.

The data graph for when the fixed magnets exposed face is under the first sensor group, figure 6.16, shows clearly the free magnet passing past the sensor groups 4 to 8,

with the response changing most notably in the $Y_{2,4}$ data. The noticeable change in $Y_{2,4}$ shows the curve saturate (≈ 1000 gauss) between $11mm$ and $16mm$ separation between the magnets faces, which is due to the combination of the fields creating a magnetic field strength outside the measurement range of the SS49E sensors. The $Y_{1,3}$, $Y_{1,4}$ and $Y_{2,3}$ sensors also saturate when the magnets face separation is below $20mm$. As the magnets touch, the measurement of magnetic field with sensor X_3 tends to zero, which is due to the magnetic field at the central sensing point in the x-axis having no magnitude and matches the expected data from the simulations performed, section 4.3.

To create a visual representation of the data the equations shown in section 3.5 are combined with known parameters of TR4, to calculate field angles and magnitudes, for each sensor group within TR4 including the virtual sensing points. This creates 16 vectors of field angle and magnitude which can then be displayed graphically. The Matlab data analysis function creates a visual representations of the 16 vectors, figure 6.15, and creates a video showing frame by frame how the magnetic field changes direction at each sensor group with respects to the separation of magnets faces. The video stills in figure 6.15 are taken at the following magnet separations: $20mm$ (figure 6.15a), $15mm$ (figure 6.15b), $10mm$ (figure 6.15c) and $5mm$ (figure 6.15d).

The graphical representation helps visualize how the magnets are reacting to each other and is a useful tool to show visually the magnetic fields direction and magnitude that the sensors are being subjected to. The sensors are displayed in their groups spaced at $10mm$ intervals, with respects to the fixed magnets location and, from empirical data, the location of the free magnet. The sensor groups display clearly the difference in field angle between the central and virtual sensing point y-axis sensors.

This visual analysis and data graphing was performed for all four experiments, as detailed above, to provide a rich set of data analysis that can be used in conjunction

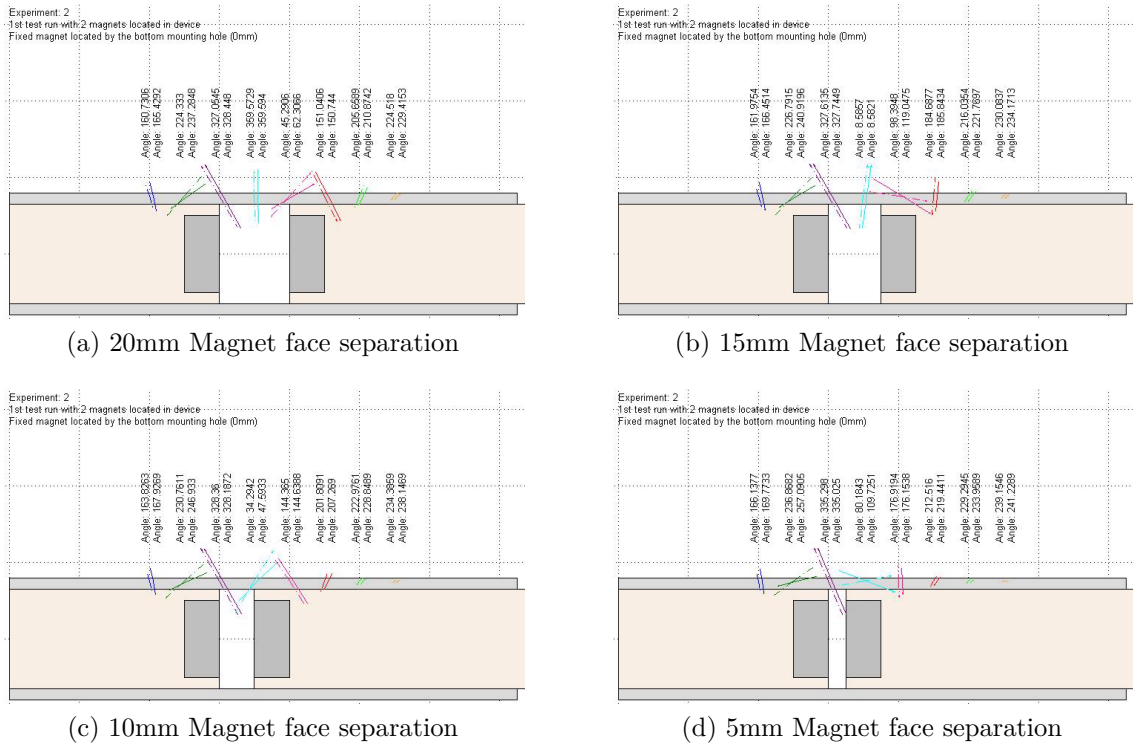


Figure 6.15: Video stills from Matlab showing magnet separation, measured magnetic field magnitude and angle at each sensor group

with the magnet location algorithm to confirm its operation. The experimentation produced very accurate data curves and from the graphical representation of the data it is possible to visually locate where the magnetic fields diverge, thus locating the midpoint between the two magnets.

The magnet separation algorithm, Chapter 6.4, describes how the free magnet location can be found with respect to the calibrated results from these four experiments and compares this back to the results found with TR2, section 6.2.2.

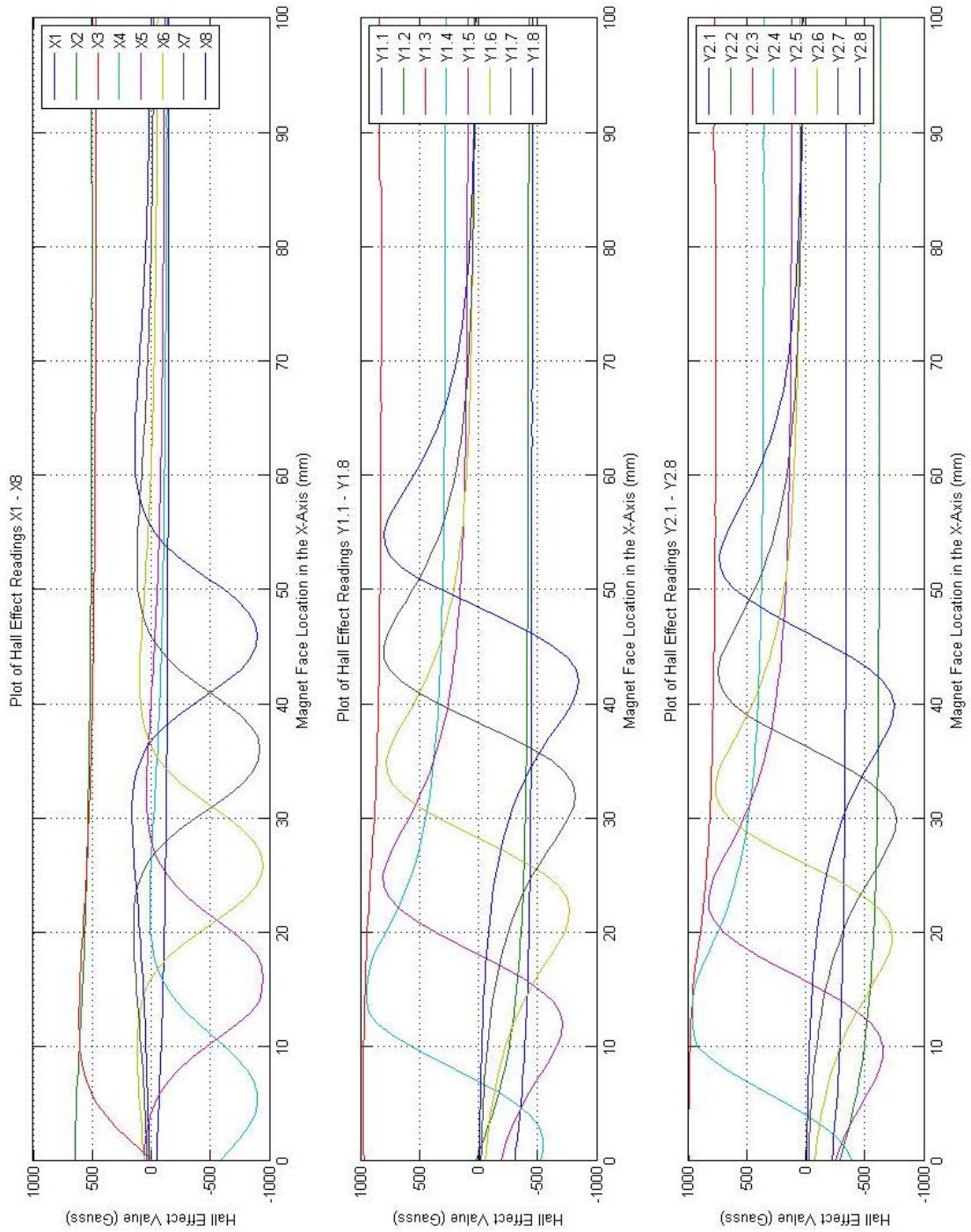


Figure 6.16: Graph showing TR4 experimental data with the fixed magnets exposed face located at sensor zero

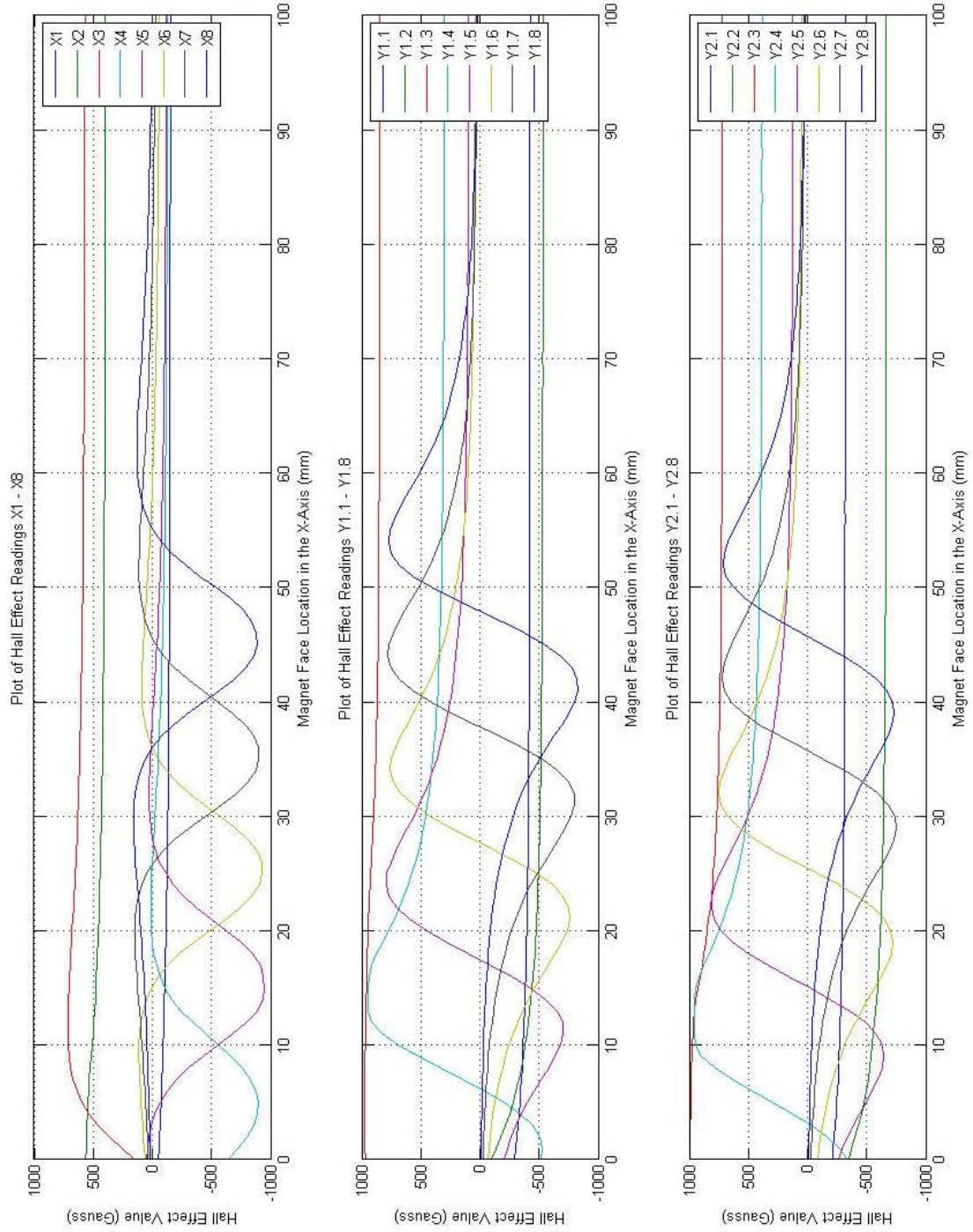


Figure 6.17: Graph showing TR4 experimental data with the fixed magnets exposed face at sensor zero plus 1.05mm

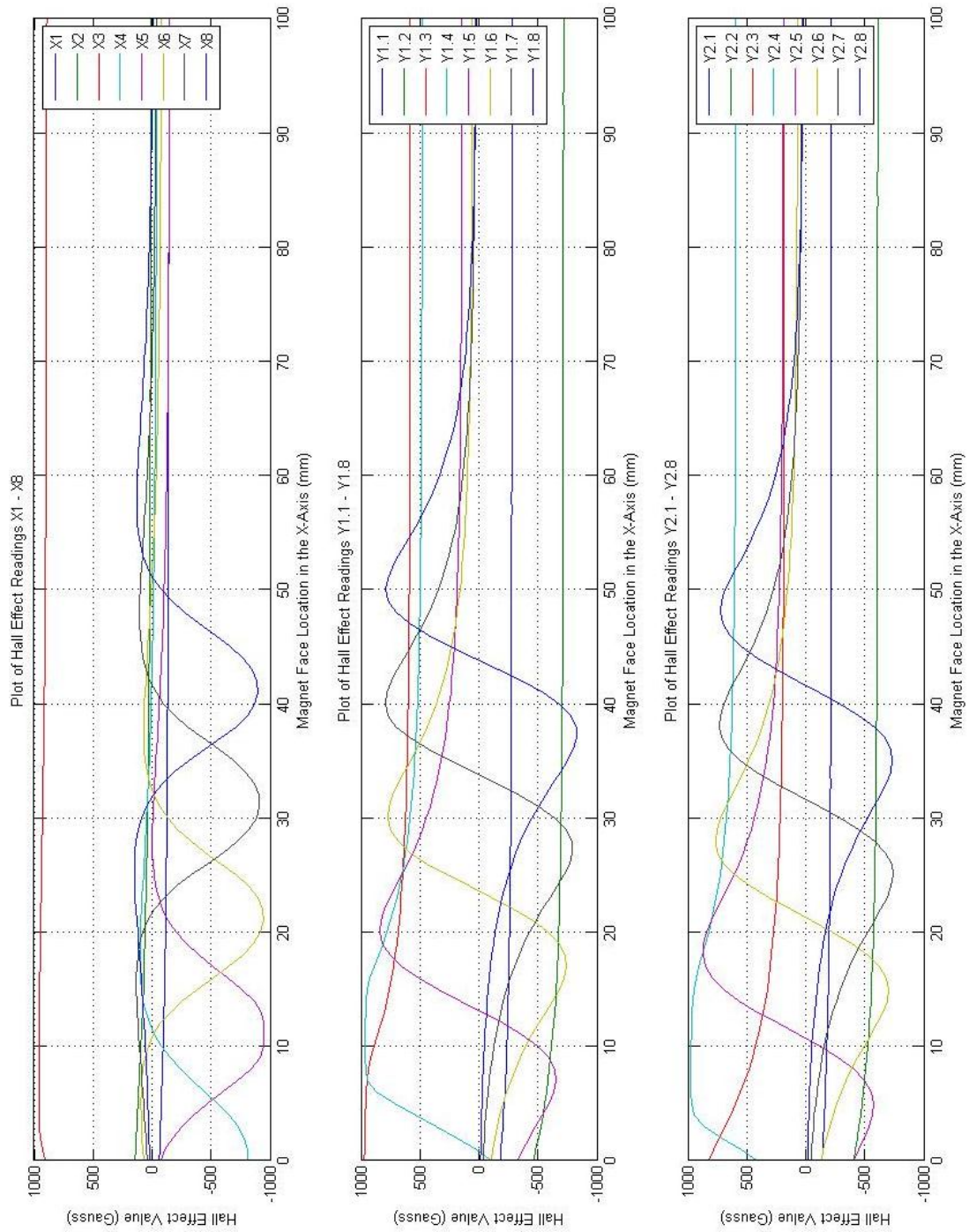


Figure 6.18: Graph showing TR4 experimental data with the fixed magnets exposed face at sensor zero plus 5mm

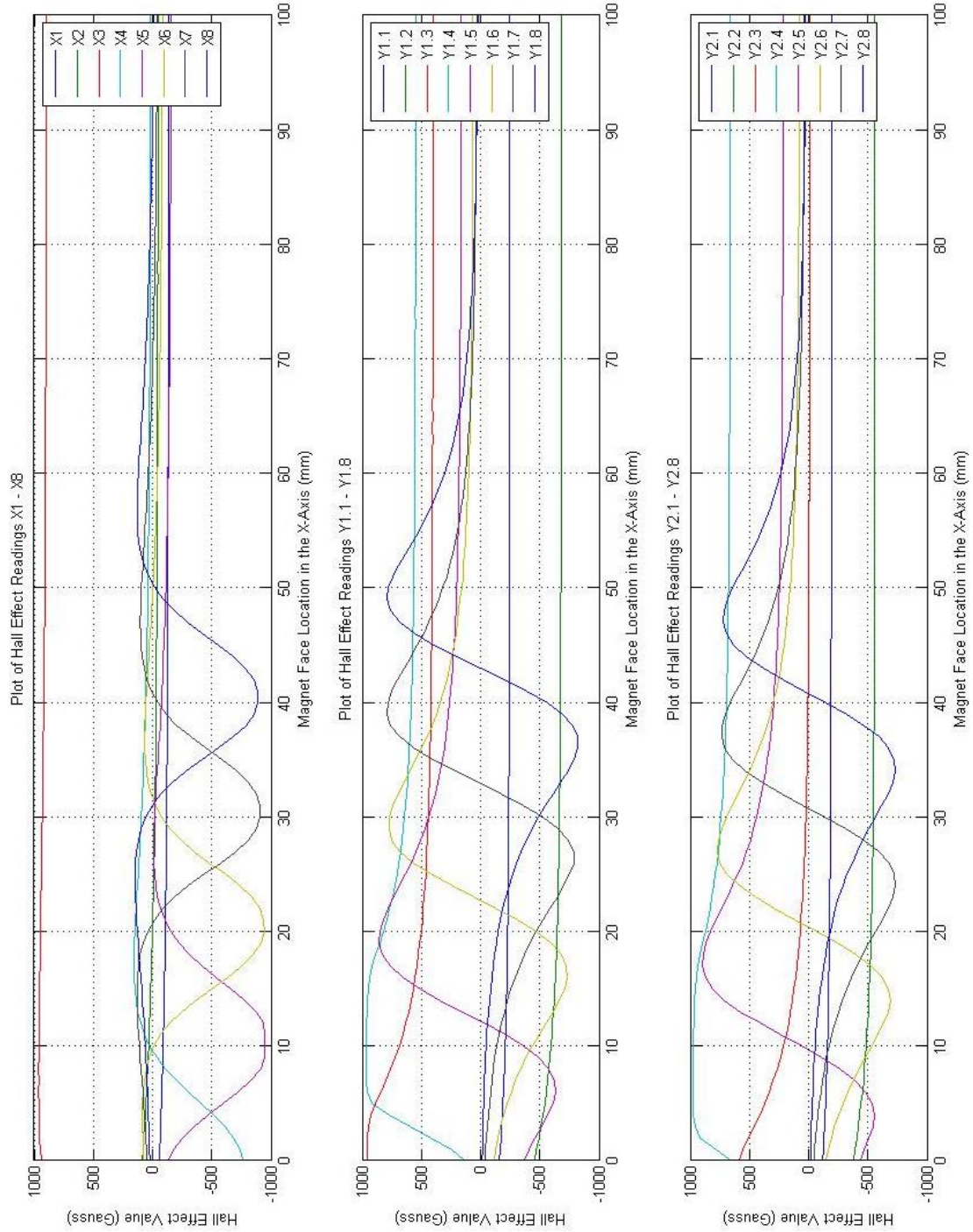


Figure 6.19: Graph showing TR4 experimental data with the fixed magnets exposed face at sensor zero plus 6.05mm

6.4 Curve Fitting

This section describes the curve fitting functions developed for Matlab to create approximations of the real world data using both far field and near field fitting approaches, followed by description and demonstration of the free magnet location algorithm that was developed for and applied to data from TR4, which shows a good correlation between the algorithms output and the expected results, section 6.5.

To try and approximate a better magnetic field fitting function than the Gilbert model, elliptic integrals, equations 3.8 and 3.9 in chapter 3, were used. To use the elliptic integrals a Matlab function was created, which took a single channel of real world y-axis data, so that the x-axis crossing point could be selected, figure 6.20, to extract the gradient at the x-axis crossing point.

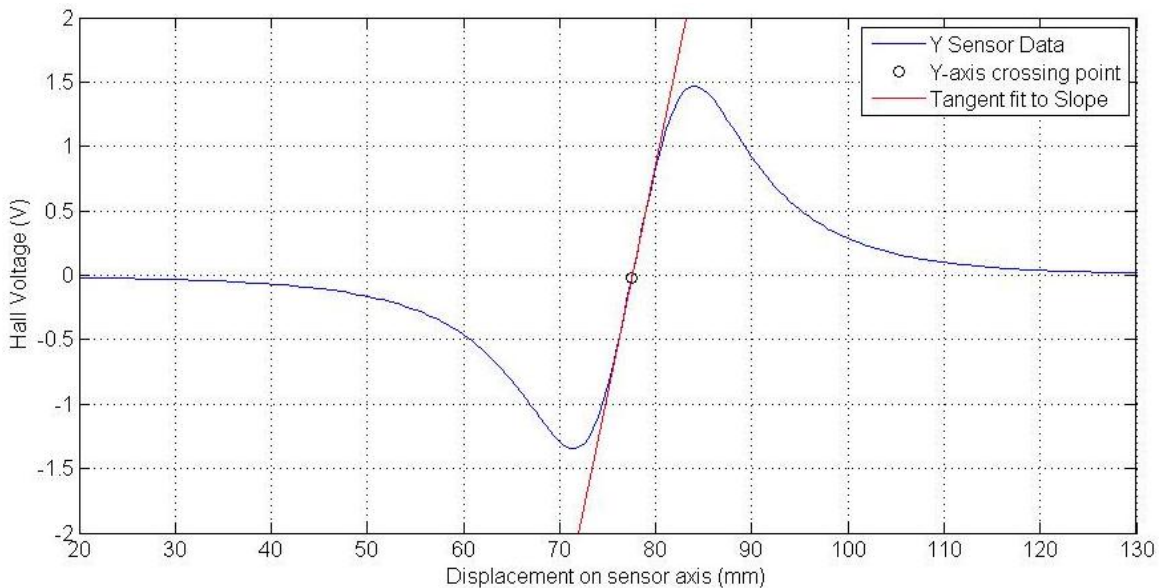


Figure 6.20: Matlab plot of a single y-axis data channel, with the zero crossing selected and a line tangent plotted at that point

This gradient was passed to the elliptic integral function to calculate an estimation of the field magnitude at displacements along the x-axis. The elliptic integral function also generated a fit for the x-axis data from the same sensor group, figure 6.21, which

when plotted on the same axis as the real world data shows a close approximation of the data.

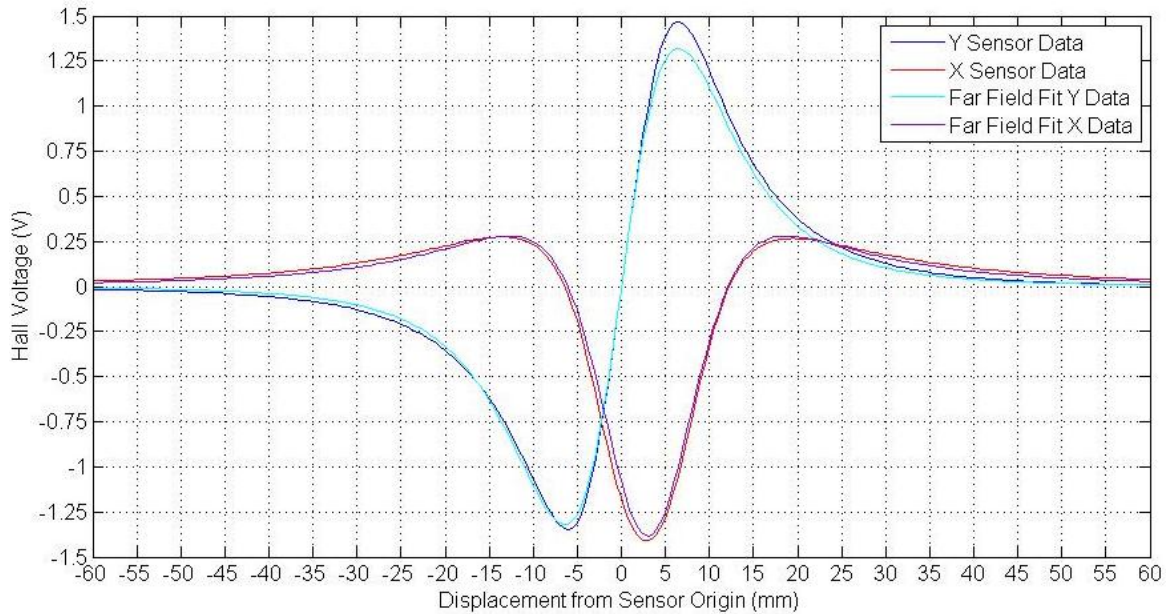


Figure 6.21: Far field fit approximation of real world data using gradient at x-axis crossing point

This graph shows that the x-axis fit is very close, with only a small scaling error which could have been generated by experimental error or a non zero crossing point being selected, with the y-axis data fitting well on the negative side of the data, but the positive side displaying a scaling error. This error was tracked back to the channel that was selected for the fit, as one of the sensors with a blob of super glue under it, which disrupted the real world results.

These results show that it is possible to approximate the magnetic fields measured, but the gradient at the crossing point needs to be known for the fit to align and scale correctly.

6.5 Magnet Separation Algorithm Development

The algorithm used with TR2 to approximate separation between the magnets repelling faces, was modified to incorporate data from eight sensors groups, with two y-axis sensors in each group, rather than the 4 sensors groups found in the TR2 hardware. The algorithm is described and formed into a set of equations so that it can be solved numerically in this section. The results from the algorithm, section 6.6, shows a good correlation between the expected data and the calculated results, proving this approach is valid.

The algorithm is split into 7 key steps:

Step 1: Determine field angle at each sensor group

Determine the magnetic field angle for each sensor group, equation 6.1, using the measured field magnitude in both the x-axis, B_{x_n} and y-axis, B_{y_n} , so that all field angles α_n are stored in degrees as a matrix.

$$\alpha_n = \tan^{-1} \left(\frac{y_n}{x_n} \right) \quad (6.1)$$

Step 2: Find the angle difference between consecutive sensor groups

To find the angle difference between sensor groups, start with the angle of the first sensor group α_n and subtract the angle of the next sensor group α_{n+1} , equation 6.2.

$$\alpha_n - \alpha_{n+1} = \Delta\alpha_n \quad (6.2)$$

Repeat this step for the remaining pairs of sensor groups.

Step3: Locate the midpoint between the magnetic fields

To find the midpoint between the magnetic fields, the matrix of angle differences is searched for the maximum absolute difference value, which indicates that the magnetic field midpoint falls in between these sensors. This is the pseudo code, in Matlab language, to locate the index of the first sensor in the sensor pair that surround the magnetic fields midpoint:

```
Sensor_Index=find(abs(Angle_Matrix)==max(abs(Angle_Matrix)));
```

This sensor index can then be passed to the next step of the algorithm.

Step 4: Data consolidation from sensor index

The sensor index found in the previous step gives the sensor group on one side of the magnetic field midpoint, call this sensor group a, so the next group of sensors along the x-axis, sensor group b, must be positioned on the other side of the field midpoint. The algorithm requires the data of both sensor groups a and b, so this can be extracted from the angle matrix using the sensor index value:

```
Xa = Sensor a location in x-axis
```

```
YSa = Sensor a location in y-axis
```

```
Xb = Sensor b location in x-axis
```

```
YSb = Sensor b location in y-axis
```

```
Aa = Sensor a angle in degrees
```

```
Ab = Sensor b angle in degrees
```

Step 5: Locate the crossing point of the x-axis

The algorithm is now used to resolve the x-axis crossing point x^x of the field tangents. This step, using trigonometry, solves the equations of the field tangent lines, taking

into account the sensor group angles α_n located in the previous step and the sensor locations in 2D Cartesian space. The angle α_n and distance from the magnets central axis y are known so \tan can be used to solve for the x-axis crossing point x^\times .

$$\tan(\alpha_n) = \frac{x_n^\times}{y_n} \Rightarrow x_n^\times = y_n \tan(\alpha_n) \quad (6.3)$$

Step 6: Solve the line equations

The aim of this step is to solve the equations of the 2 lines \underline{r}_n and \underline{r}_{n+1} , so that the following step of the algorithm can find the point at which the lines cross. The point that the two lines cross through follow the same format as each other. The equation of the line \underline{r}_n is made up of two components

$$\begin{bmatrix} x_n \\ y_n \end{bmatrix} \text{ and } \begin{bmatrix} \delta_n \\ \epsilon_n \end{bmatrix} \quad (6.4)$$

Where $\delta_n = x_n + x_n^\times$ and $\epsilon_n = 0$ as there is no difference in the y-axis sensor locations. As the points that the lines \underline{r}_n and \underline{r}_{n+1} cross through are known it is simple to create equations for the lines. If we define the left hand bracket as A and the right hand bracket B then we can build an equation using these variables. For clarity the coefficient symbol for \underline{r}_n is λ and \underline{r}_{n+1} is μ .

$$\begin{aligned} \underline{r}_n &= A_n + \lambda(B_n - A_n) \\ \underline{r}_{n+1} &= A_{n+1} + \mu(B_{n+1} - A_{n+1}) \end{aligned} \quad (6.5)$$

Step 7: Find the intersection point of the lines

Use simultaneous equations to find the intersection point of the lines

$$x_n + \lambda(\delta_n - x_n) = x_{n+1} + \mu(\delta_{n+1} - x_{n+1}) \quad (6.6)$$

$$y_n + \lambda(0 - y_n) = y_{n+1} + \mu(0 - y_{n+1}) \quad (6.7)$$

From equation 6.7 it is clear, after simplification, that $\lambda = \mu$. Substitute λ into equation 6.7 in place of μ and use simultaneous equations to solve. Hence the point of intersection φ can be found

$$\varphi = \begin{bmatrix} x_n + \lambda(\delta_n - x_n) \\ y_n + \mu(0 - y_n) \end{bmatrix} \quad (6.8)$$

To understand this information one must remember that φ is a column vector that describes the crossing point as a 2D Cartesian coordinate. The first element in the column vector λ is the one we are interested in, as it defines the approximate midpoint between the magnetic fields. If you were to take the first elements value λ and double it, the result would represent the location of the free moving magnets face along the x-axis, thus the separation between the magnets

$$x = \lambda \times 2 \quad (6.9)$$

where x is the separation between the two magnet faces and λ is the approximate midpoint between the two magnet faces.

6.6 Magnet Separation Algorithm Results

The free magnet location algorithm, section 6.5, was passed the calibrated data from the four experiments using TR4, to produce figures 6.22 to 6.25. The algorithm that

was run on the TR2 data was slightly different with respect to locating the magnetic field midpoint from field angles, but the line intersection and separation calculation was the same. The data produce by TR2, figures 6.6 & 6.7, showed a close fit to the expected data, but the sensor location accuracy caused the data to drift and have different gradients, $y = -1.6x + 43$ and $y = -1.3x + 36$, to the expected gradient $y = -x + 30$. The experimentation with TR4 had a maximum separation of $100mm$ so the expected gradient of the line produced by the algorithm was $y = -x + 100$ for the four experimental test runs, section 5.3.3.

The first experimental test using TR4 had the fixed magnet face positioned at the sensor origin so the exposed face of the fixed magnet was aligned with the third sensor groups central hall position. The algorithm results from the first experimental data set, figure 6.22, shows a very good correlation between the expected magnet separation and the calculated result. The points circled show where the algorithm was not able to correctly identify the sensor groups that the magnetic field midpoint fell between, which caused the spikes in the algorithm's output. This was due to sensor misalignment, detailed in section 6.3.3, which meant that when the maximum absolute difference between the sensor angles were calculated, step 3 in the algorithm, the wrong group of sensors was selected. The points marked, B and C, show where the algorithm results drift slightly, again due to the sensor misalignment. When the magnets are close together, due to not being extremely magnetically hard, the magnets demagnetize each other a little which cannot be accounted for by the algorithm, thus the drift marked at point A. This is also seen in the data from the TR2 experiments.

The second experimental data run using TR4, figure 6.23, had the fixed magnet located at $1.05mm$ from the sensor origin, thus under the virtual sensing point between the second y-axis and the x-axis sensors. The fit of the Y2 sensor group data is better than in the first experiment as the Y2 sensor group measured on the virtual sensing

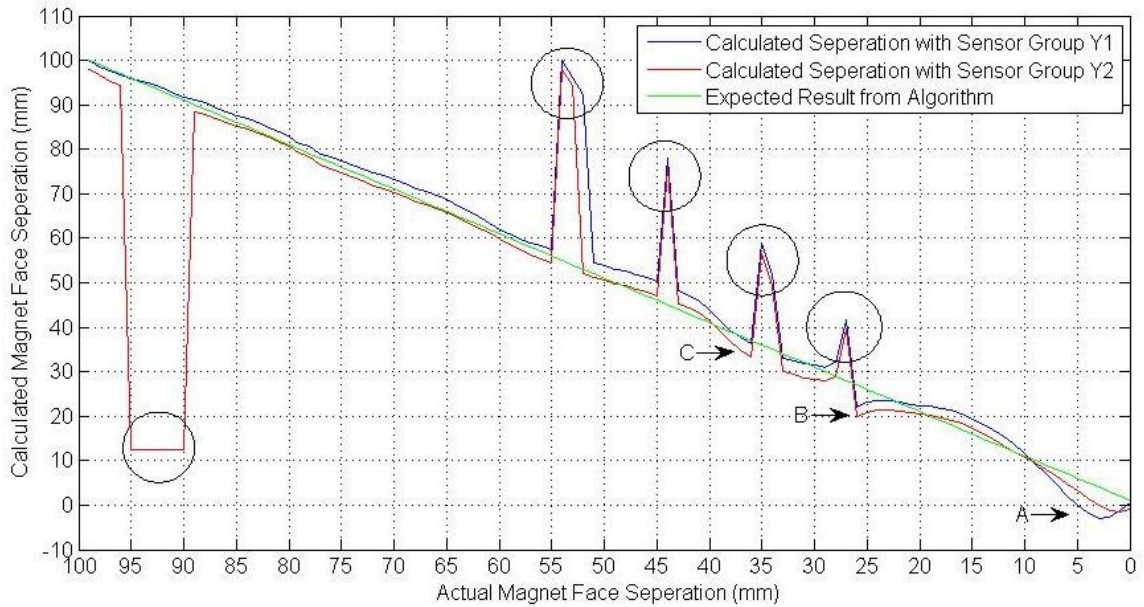


Figure 6.22: Calculated results of magnet location algorithm plotted against expected results for the first experimental data run with TR4

point rather than the sensor origin. As before the spikes in the data that have been circled are due to sensor misalignment causing the midpoint location step to choose the wrong sensor groups. The location of these spikes shows a consistent error across both tests. The points marked, B and C, show similar drift to the first experiment and point A again shows the effects of demagnetization on the field measurements.

The effects of the sensor misalignment are more observable in the results from the third experiment, figure 6.24. This is due to the fixed magnets location being positioned at 5mm from the sensor origin, and thus directly positioned between two of the sensor groups. The spikes in the data again are in roughly the same positions as the first and second experiments. The midpoint location algorithm struggles when the magnets are far apart, the circled data on the left of the graph which can be explained by stray magnetic fields acting upon the sensors with enough effect to rotate the recorded magnetic fields. The midpoint location algorithm is also effected when the magnets

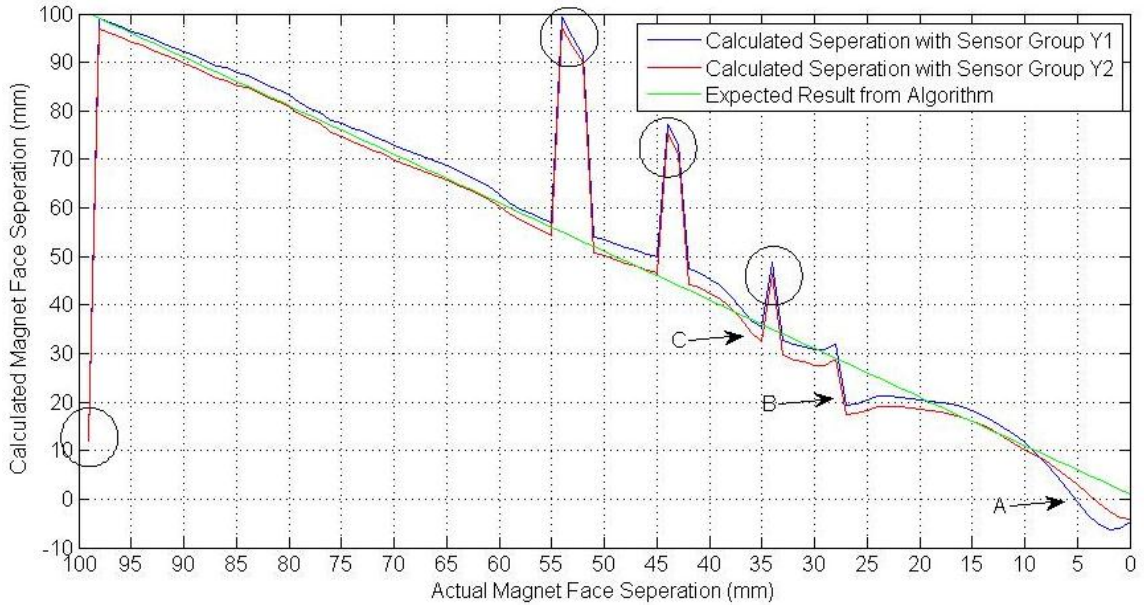


Figure 6.23: Calculated results of magnet location algorithm plotted against expected results for the second experimental data run with TR4

are closer together, data circled at $\approx 40\text{mm}$ which is also seen to a lesser extent in the data from the second test.

The final experimental run with TR4 produced data that looked correct, but when run through the magnet location algorithm, figure 6.25, the midpoint location step failed for most magnet separations. These errors are bounded by the rectangle on the left of the graph. Whilst some of the data has correctly matched the expected data, this shows that the midpoint algorithm is not stable for all cases, when the fixed magnet is too far from the sensor origin, the accuracy of the algorithm drops. Three of the previous data spikes are visible in the same locations as the previous tests as are the points B and C which show sensor drift. Point A also shows the solution sensitivity when magnets are very close, but the algorithm is clearly getting the Y1 sensor groups location wrong as it calculates the magnets have negative separation which is physically impossible.

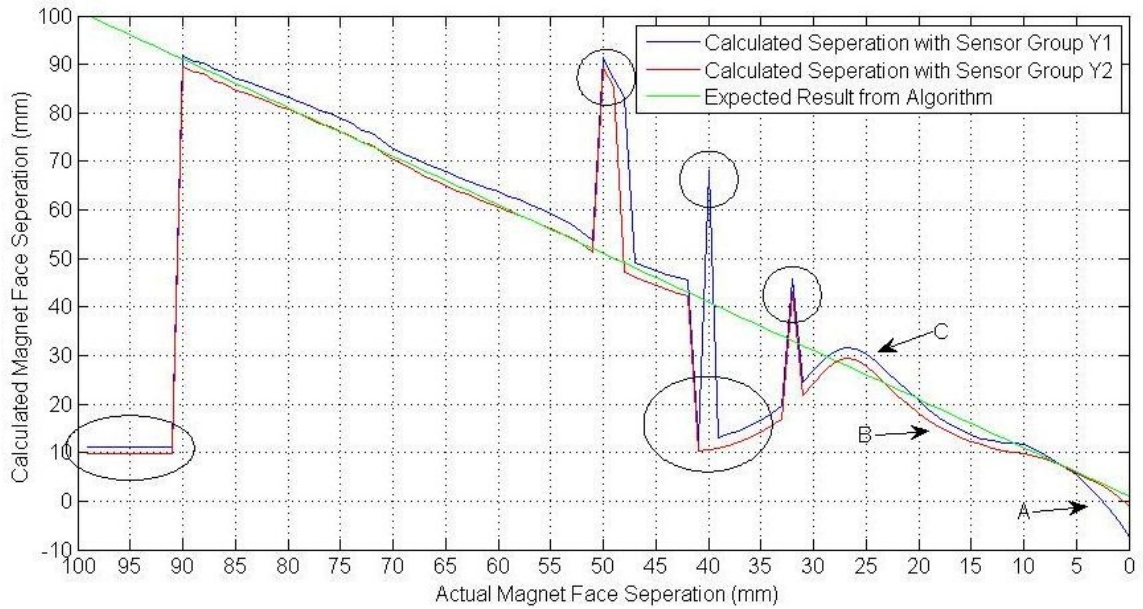


Figure 6.24: Calculated results of magnet location algorithm plotted against expected results for the third experimental data run with TR4

These tests with the free magnet face location algorithm have shown that there is some improvement needed in how the midpoint between the magnetic fields is located, but when sensor groups either side of the magnetic field midpoint are correctly identified, the algorithm is far more accurate than when it was run on the TR2 hardware. This demonstrates that the TR4 hardware is far more accurate and better suited to finding the location of the free magnet through the analysis of magnetic fields that surround the two magnets within the test rig compared to previous test rig experiments.

With some further work the free magnet location algorithm could be employed onto hardware that requires accurate non contact linear positioning. As the hardware is driven by a PIC the data can be directly transmitted back to the control system using a serial connection or even be integrated directly into a closed-loop control system.

To try and explain why the midpoint algorithm is incorrectly selecting sensor groups in some cases, the experimental analysis of the real-world data was extended to include all sensor group pairs, figure 6.26. This graph shows a scatter plot of all calculated

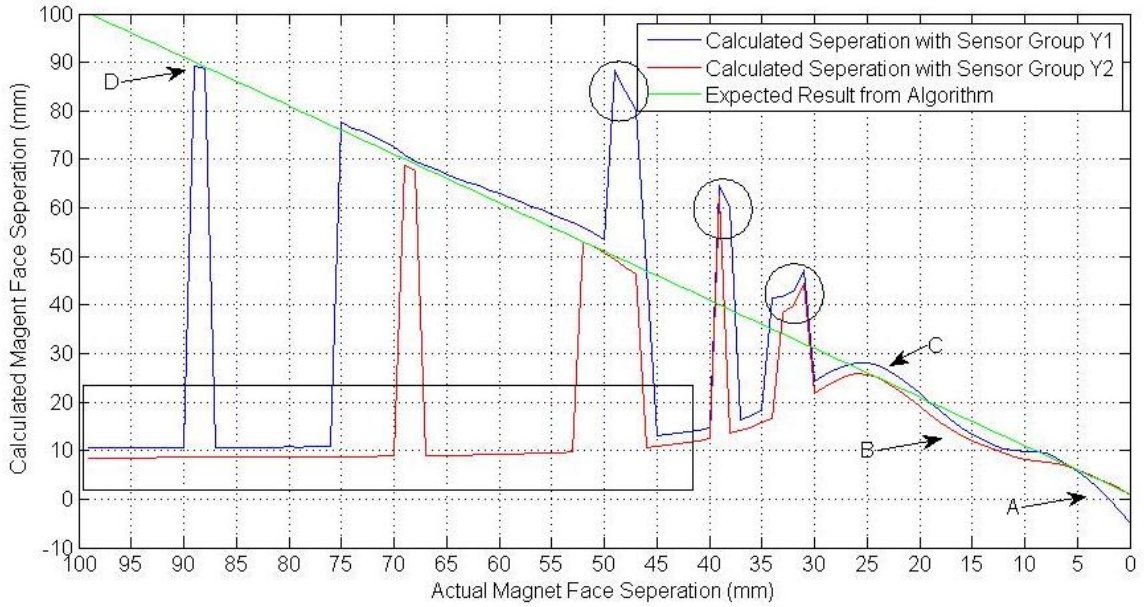


Figure 6.25: Calculated results of magnet location algorithm plotted against expected results for the fourth experimental data run with TR4

midpoints between the sensor pairs, displayed as points, with the results of the original midpoint algorithm overlaid as a solid blue line. The expected results are displayed as a solid red line.

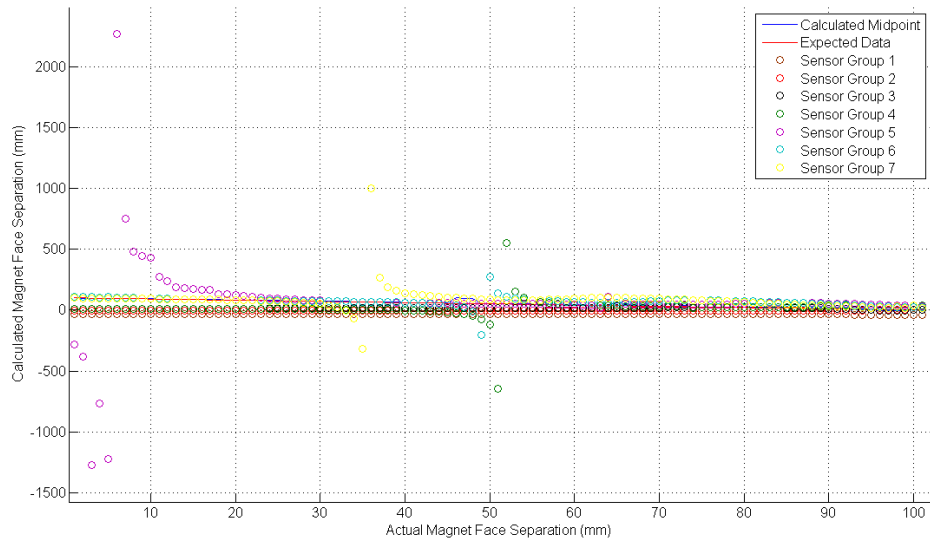


Figure 6.26: Calculated magnetic field midpoints for sensor group pairs, overlay of original algorithm separation prediction (blue line) and expected data (red line)

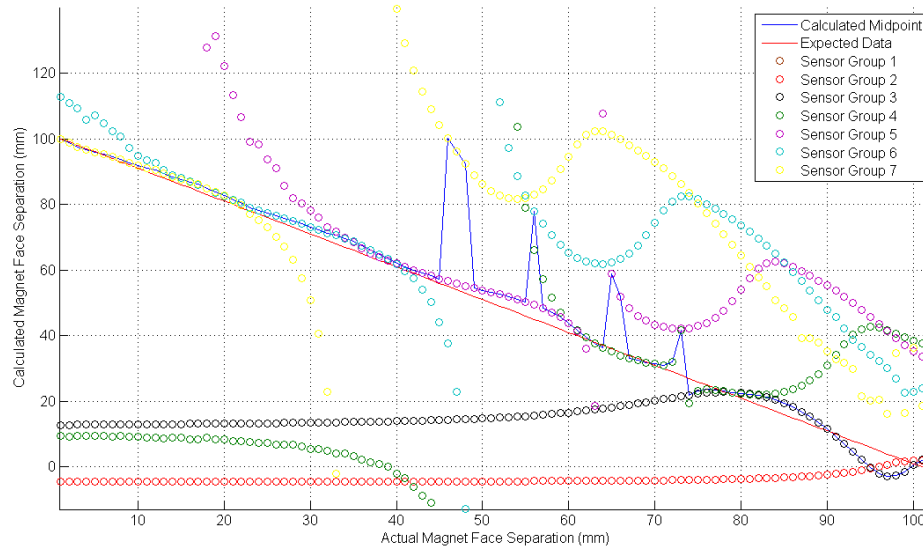


Figure 6.27: Calculated magnetic field midpoints for all sensor groups, overlay of original algorithm separation prediction (blue line) and expected data (red line)

As expected a lot of the data is clearly erroneous, for example the data points that represent negative separations are physically impossible due to the magnets not being able to move to those locations. The data points located above 100mm are also not possible due to the maximum separation of the magnets being physically limited to 100mm , so to improve the visibility of the data, figure 6.27 is an enlargement of the expected data range. In figure 6.27 it is possible to see where the midpoint algorithm has failed to choose the correct sensor pair to determine the separation of the magnets from, as represented by the spikes in the blue line, but the data does clearly show alternative data points that could have been chosen that match the expected data (the red line on the graph) more closely. This shows that with a small modification to the algorithm that selects the sensor groups to use, a more accurately calculated separation between the magnet faces exists, so the separation could be resolved correctly. The shape created by the data points for each sensor group echoes the shape of the data from other groups, showing a strong agreement between the calculated groups analysis of the data, as they are distributed equally along the x-axis.

An alternative approach was to look for symmetry between the magnetic fields. Due to only having a limited number of sensors located in fixed increments along the x-axis it was found to be difficult to visualize the experimental data so the next logical step was to interpolate the field angles between the sensor groups. This was found to be too inaccurate to perform any better than the current midpoint location algorithm. Therefore the approach was modified further, such that all the angles were plotted for each of the sensor groups, to see if there were any patterns that emerged from the data.

The data yielded overlapping S-shaped curves for each of the sensor groups as the magnets were brought together, figure 6.28.

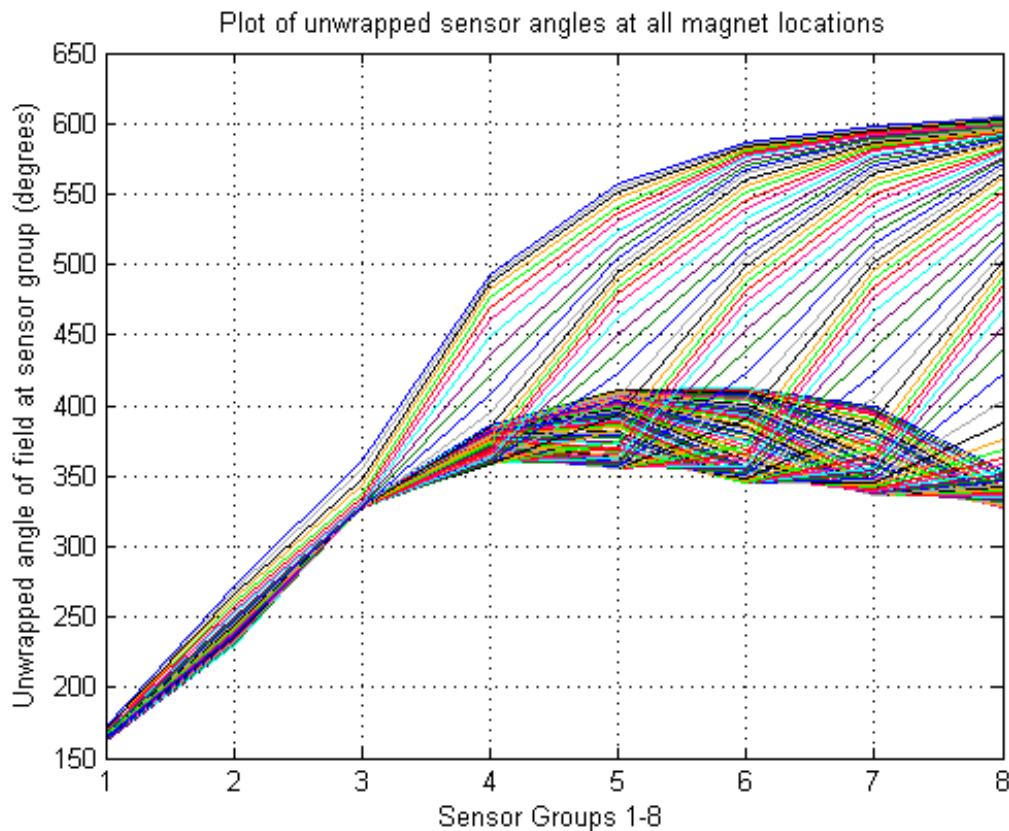


Figure 6.28: Curves produced through analysis of field angle at known sensor locations and displacement of the free moving magnet

A theoretical model for the data displayed in figure 6.28, was developed from the far-fit magnet approximation algorithm. The field angles at known increments along the x-axis, figure 6.29, can be calculated from the superposition of the two magnetic fields due to magnets at A and B . The algorithm was passed the separation S along with the location of a sensor positioned in x and y , therefore by solving for the field magnitude in the x-axis B_x and y-axis B_y the angle of the magnetic field α can be resolved.

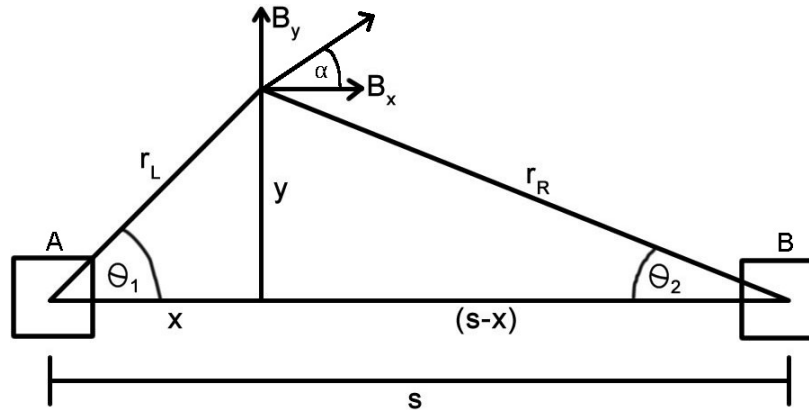


Figure 6.29: Diagram showing the parameter names used in equations 6.10 - 6.13 to modify the far-fit magnetic algorithm and determine field angles at defined points along the x-axis, y-axis with known magnet separation

Equations 6.10 and 6.11 give the combined B_x and B_y values of the fields from the two magnets.

$$B_y = \frac{3 \sin \theta_1 \cos \theta_1}{r_L^3} + \frac{3 \sin \theta_2 \cos \theta_2}{r_R^3} \quad (6.10)$$

$$B_x = \frac{3 \cos \theta_1 - 1}{r_L^3} - \frac{3 \cos \theta_2 - 1}{r_R^3} \quad (6.11)$$

The angle of the field α at point (x, y) is determined from equations 6.12 and 6.13

$$\frac{B_y}{B_x} = \frac{3r_R^3 \sin \theta_1 \cos \theta_1 + 3r_L^3 \sin \theta_2 \cos \theta_2}{r_R^3(3 \cos \theta_1 - 1) - r_L^3(3 \cos \theta_2 - 1)} \quad (6.12)$$

$$\alpha = \tan^{-1} \frac{B_y}{B_x} \quad (6.13)$$

where equation parameters are defined in figure 6.29.

To simplify the process of calculating multiple sensor locations along with magnet displacements a Matlab function, ‘angfun(x,y,S)’, was created. This function was passed the location of the sensor of interest in x and y , as well as the separation between the magnets S and returned the field angle at that point.

The same range of magnet separation displacements as the real-world experimentation was used to create an angle displacement plot that is very similar to the data recorded by TR4, figure 6.30. There is a good correlation between the measured and the theoretical data, with only a minor vertical scaling issue. This scaling issue can be explained by the data normalization step, which took the maximum and minimum sensor values and scaled the real-world data to an average between them, which has shifted the data enough to create this discrepancy.

The S-shaped curves can be interpreted as the magnetic fields rotating about the magnets center, such that with a second magnet in range the curves would have a second local maximum, which creates the S-shaped curve. Further analysis is required to see if additional curve fitting of the data would provide a better estimation of the magnet separation through analysis of field angle only. To illustrate the nature of the curves a simplified view of the field angles are presented in groups, figures 6.31 and 6.32, for each 10mm increment over the displacement between the magnets.

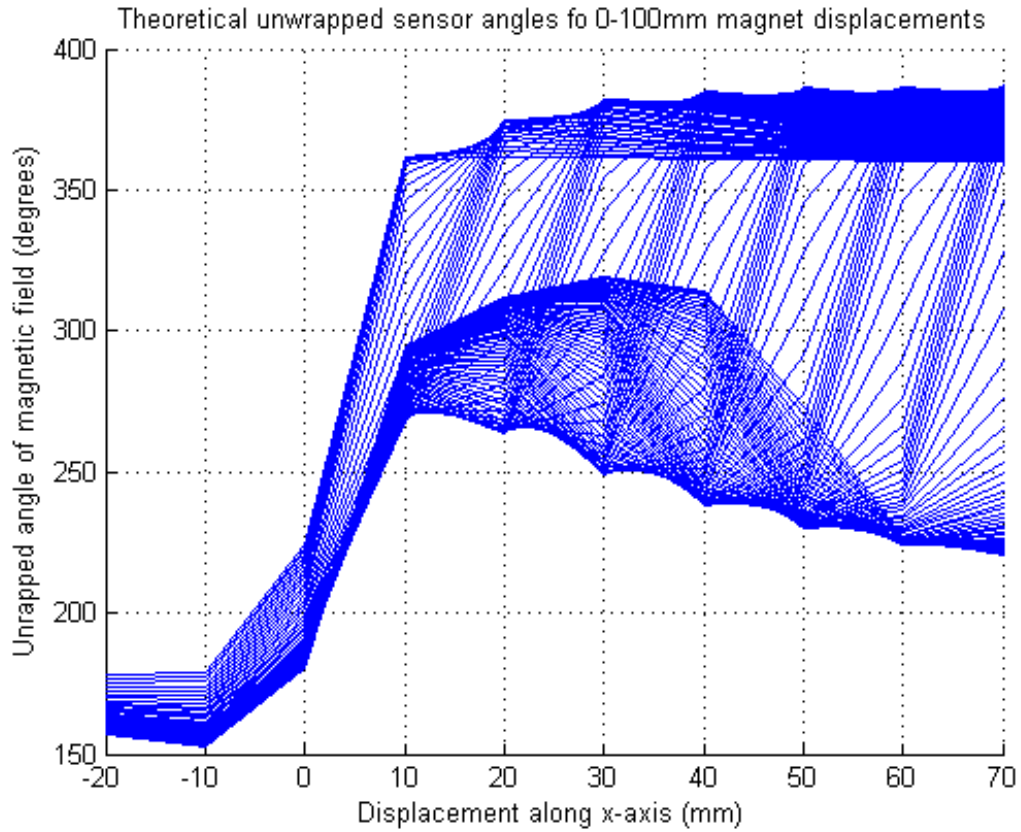
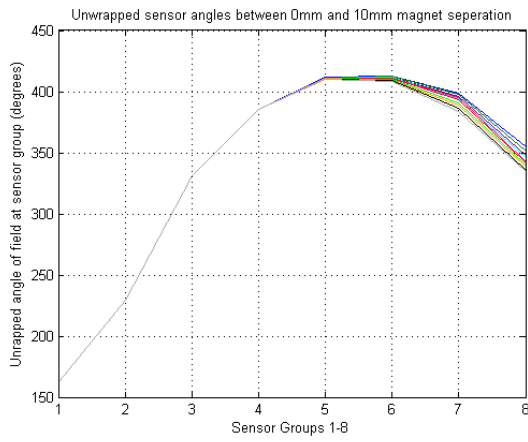
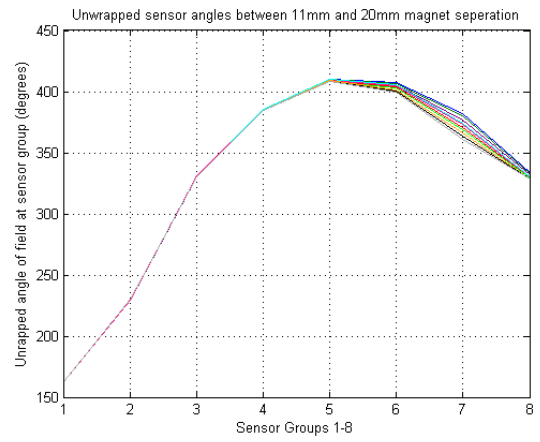


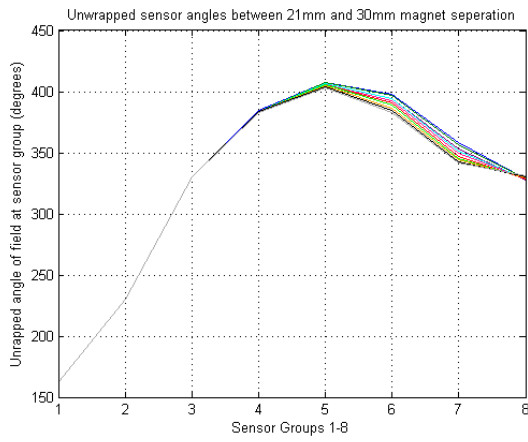
Figure 6.30: Curves produced by Matlab function, $\text{angfun}(x,y,S)$, for the sensors distributed along the x-axis with respects to the field angle for a range of magnet separation displacements



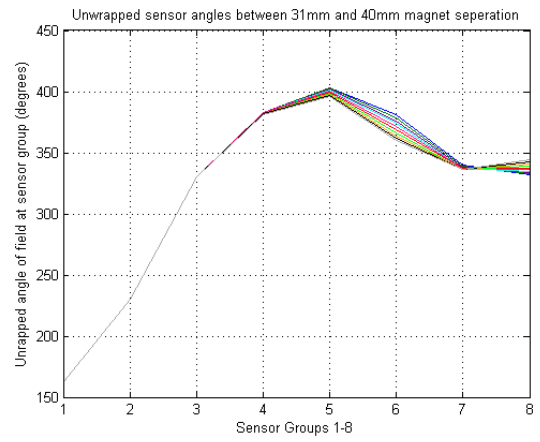
(a) 0-10mm Separation



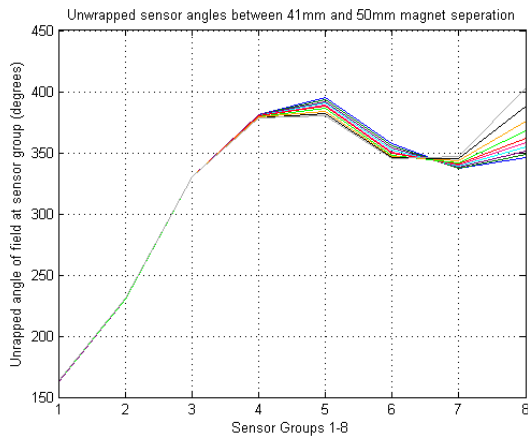
(b) 11-20mm Separation



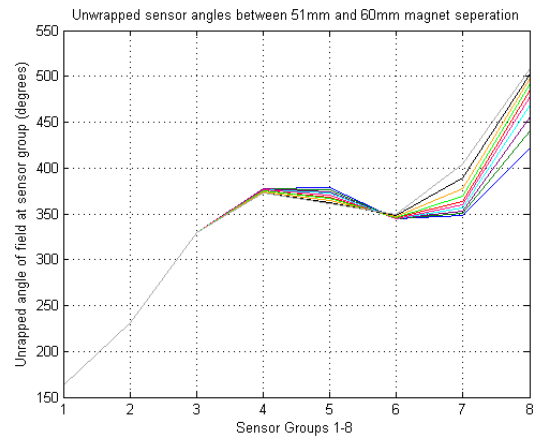
(c) 21-30mm Separation



(d) 31-40mm Separation

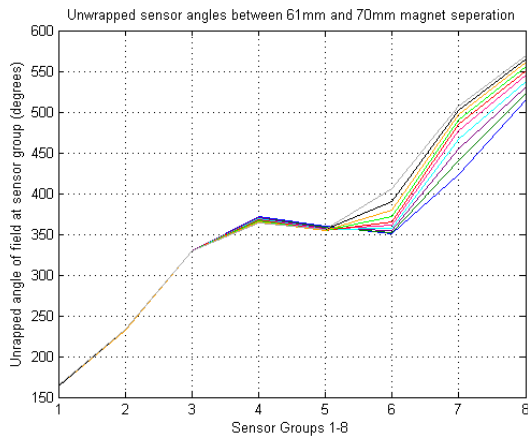


(e) 41-50mm Separation

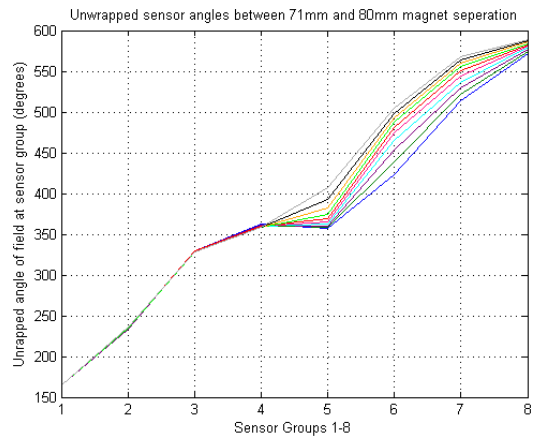


(f) 51-60mm Separation

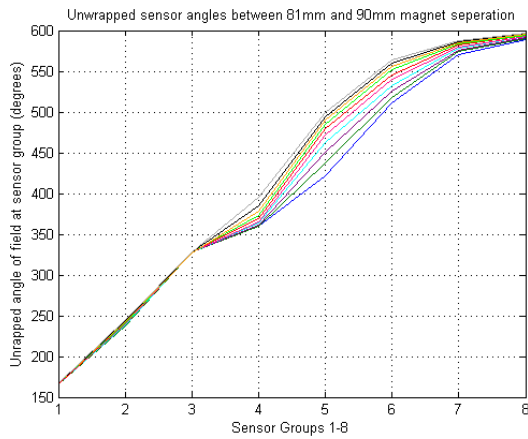
Figure 6.31: Clarified view of S-shaped curves for 10mm increments ranging from 0 to 60mm



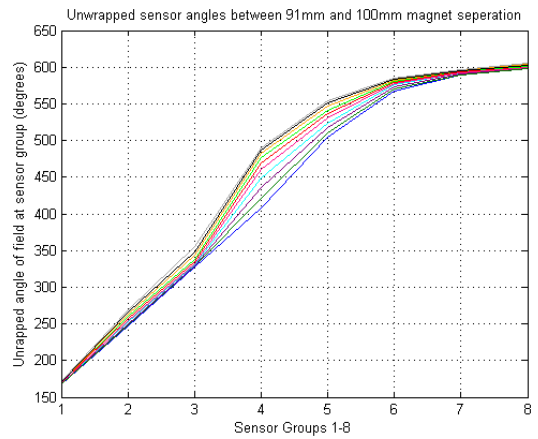
(a) 61-70mm Separation



(b) 71-80mm Separation



(c) 81-90mm Separation



(d) 91-100mm Separation

Figure 6.32: Clarified view of S-shaped curves for 10mm increments ranging from 61mm to 100mm

6.7 Chapter Summary

This chapter started with a discussion on sensor calibration, section 6.1, which included the use of the Helmholtz coil to confirm the accuracy of both the SS49E sensors, that were used for experimental data recording, as well as the FEMM FEA simulations, which ensured accuracy of future simulations. The results from the Helmholtz analysis were extremely accurate, which ensured that all further experimentation was based on known accurate data.

The following section discussed the results from the initial experimental testing rigs, section 6.2, which helped to shape the requirements for the final testing rig TR4. These experiments showed that it was possible to use the basic magnet separation algorithm to estimate the magnet separation, through analysis of the Hall Effect sensor data, but also showed deficiencies in the data capture that needed to be rectified for the final testing rig. The initial testing rigs also helped shape the physical characteristics of TR4 such as the magnets to use, the maximum displacement, the sensor locations, manufacturing techniques and data capture hardware requirements.

The next section of results were specifically targeted at TR4 and the data capture system, section 6.3, which included an analysis of data discrepancies from the sensors within the test rig. The discrepancies were traced back to the misalignment of the sensors as they were mounted into the test rig, with the results section discussing normalisation techniques that were applied to ensure that the data was consistent across all sensor groups. There were some issues discussed such as sensor saturation and resolution that could be investigated further in the future, but the data that was extracted from TR4 was enough to prove the theory of resolving the magnet separation using a set of distributed two dimensional Hall Effect sensing units.

To try and understand the data further, mathematical models for a far-fit estimation of magnetic field magnitude were created, section 6.4, such that curve fitting could be

performed on the raw real-world data. This curve fitting lead to a deeper understanding of the results, but were also used to confirm the results of the magnet separation algorithm.

The development of the magnet separation algorithm, section 6.5, took the raw real-world data from TR4 and tried to calculate the midpoint between the two magnet faces. This task saw custom equations developed to estimate the separation between the magnets, but also to resolve the field angles from the sensor groups.

The final part of this chapter, section 6.6, takes the magnet separation algorithm and proves that it is accurate, although some further development could be done to ensure that the correct sensor groups are chosen for the algorithm to operate on. The separation algorithm was also tested against a different approach for magnetic field analysis, such that the angles recorded at the sensor pairs could be compared against a S-shaped curve function, which would allow for a direct lookup of the data against both known and calculated theoretical values.

Chapter 7

Conclusion & Future Work

This chapter concludes the thesis, drawing together the research performed and results generated through experimentation, so that the original research questions stated in section 1.2 can be answered.

This chapter is divided into 4 main sections to help structure the main findings, section 7.1, followed by a listing of research contributions, section 7.2. Limitations to the work that were found are listed in section 7.3 with the final section of the thesis, section 7.4, stating future work that naturally follows on from the research presented by this thesis. The research questions, from section 1.2, are re-stated and answered in section 7.2. These answers are discussed, giving final conclusions regarding the research performed for this thesis.

7.1 Main Findings

The conclusion of experimental results from TR1 is compared to the Gilbert magnet force model, section 7.1.1, which is followed by a discussion regarding the use of FEMM for magnetic model simulations, section 7.1.2. The magnet separation algorithm results are discussed in section 7.1.3.

7.1.1 TR1 and Gilbert Model conclusions

The testing with TR1, section 6.2.1, enabled the recording of an initial data set so that magnetic repulsion force curves could be experimentally derived. The data gathered from the eight different magnet pairs tested showed that there was a relationship between magnets with similar properties and physical characteristics. When trying to describe an equation to fit the data curves, it was found to be very difficult due to the accuracy of the data recording hardware, such that when the magnetic repulsion force had a very low magnitude the data recorded by the hardware was zero. When trying to fit polynomials to this data, figure 6.3, the results followed roughly the same shape as the data, but were not accurate enough to be used for further testing.

The next test with the results from TR1 was a comparison between the Gilbert model for cylindrical magnets in repulsion, equation 3.17 in section 3.2.3, to the ID54 magnet data. The results of this comparison, figure 6.4, show a poor match between the Gilbert model and the real world data when the separation between the magnets is smaller than the magnets' thickness, but gives a relatively good match when the magnets are far apart. This is due to the Gilbert model not taking into account the magnetic 'hardness' of the material, instead it expects the material to be infinitely 'hard' and so will not demagnetize, which is not possible with real world magnets. Due to this assumption, the Gilbert model is only good at predicting the magnetic force between two magnets with a large separation and therefore is not useful for further experimentation.

The data gathered with TR1 did however find that the magnet most suitable for further experimentation was the ID54 magnet (20mm diameter, 10mm thick, 4600 Gauss (0.46T) with a Ni-Cu-Ni protective coating), due to two magnets producing a useful repulsive force that was sufficient to support a $5kg$ load, with a maximum repulsive force of $10.8kg$. The ID54 magnets produced a strong enough magnetic field

to be measured using hall effect sensors, whilst being a good size to work with. The ID54 magnets were easily mountable in the Delrin magnet holders making them very portable and relatively lightweight.

The experimentation with TR1 formed a lot of the ground work required for the second and third experimental testing rigs, with insights into design considerations and magnetic field characteristics.

7.1.2 FEMM magnetic field modeling conclusion

The FEMM software, detailed in section 4, was used extensively but took a while to get up to speed with. This was because the simulations produced looked correct, but when compared to the real world data the simulations were not accurate, figure 4.6 in section 4.2. The FEMM user interface was difficult to use when defining models to be simulated, as such the best method found to define complex models was to import the model in DXF format from SolidWorks.

Once the model had been drawn or imported into FEMM, the material definitions had to be applied, which was made simpler through the internal library of materials that were already defined. The material definitions could be copied and adapted to create materials that did not already exist, such as the N42 grade material that the ID54 magnets were made from, so that the simulations were defined correctly.

The mesh solver was simple to use and created an unstructured mesh automatically, that the solver would then run on. Once the solver had run, the simulation results could be viewed in a number of ways, with the ability to output data from the software in CSV format.

Whilst basic and initially difficult to use, the FEMM software was proven to be accurate when compared to initial testing and calibration experiment results. The simulation results presented in this thesis are therefore considered as accurate representations of

the expected magnetic fields from real world experimentation.

There are other software packages available to perform FEA and FEM analysis of magnetic systems, but FEMM was suitable for the research performed in this thesis.

7.1.3 Magnet Separation Algorithm Conclusions

The magnet separation algorithm has shown promise in the ability to predict the separation between two magnets in repulsion, through analysis and modeling of the magnetic fields that surround the magnets, however as stated in section 6.7 the separation accuracy depends on some key factors including; alignment and calibration accuracy of the Hall Effect sensors, misalignment of the magnets, sensor resolution around the minimum magnet separation and non-perfect materials which the mathematical models struggle to account for.

The magnet separation algorithm has been shown to work and produce repeatable results, but there is some further work required to ensure that the algorithm is correctly selecting the correct sensor groups needed for further calculation. Whilst this is a problem, the algorithm does produce the correct results when applied to all sensor groups at the same time, but to streamline the process for future work in real-time control, the algorithm should only run on the data from two sensor groups rather than all eight sensor groups. An approach has been detailed to check that the correct sensor group has been selected, section 6.6, as well as another method of data analysis being performed to try and improve the magnet separation estimation.

By recording the magnetic field angle at each of the sensor pairs, the data yielded a range of S-shaped curves that match simulated curves produced using the far-fit magnetic field approximation algorithm, detailed in section 6.4. This is another possible approach for data analysis which could also be experimented with in the future.

7.2 Contributions

There are a number of ways that have been explored within this thesis to isolate a system from mechanical impacts and vibrations, such as material choice in the design of a suspension system, flexible and deformable wheels to absorb surface impacts, passive and active suspension systems found in road vehicles to smooth the ride and research into magnetic compliance to provide a spring like suspension. The research performed has shown that the magnetic spring effect will support a load on two magnets in repulsion that are restricted to a single axis of motion. Magnetic suspension is suitable for most systems that require mechanical isolation due to environmental conditions, section 2.3.1, which would stop oil based suspension damping from operating, whilst requiring no additional energy and only a small additional mass to operate.

This section lists the contributions to science that the author believes this work provides, which are detailed by answering the research questions stated in section 1.2. To conclude this thesis, the original research questions are answered in order:

Can the magnetic ‘spring’ effect be measured and analyzed accurately?

The magnetic spring effect can be accurately measured and characterized through experimentation, section 5.2.1, with the ability to analyze the suspension’s force profile depending on the magnets used. The force profile would need to be adapted for the expected environmental gravity of the target planet that the suspension would be operating on, but this would be a simple conversion to do, section 2.3.2.

Can a good analytical model be found to define the magnetic spring characteristics?

Due to the non-linearity of magnetic fields it is difficult to find a good analytical model to define the magnetic spring effect. The model would need to take into account the ‘hardness’ of the magnet material, as well as the magnetization strength, to be

able to produce accurate results, not currently possible with the Gilbert model. It would be therefore simpler to measure the force produced by the magnets required and use a look-up table of the data as the magnets repulsive force was proven to be very repeatable. The use of elliptic integrals, section 6.4, with the real world data produced a close approximation to the expected magnetic field magnitudes, but this again required the magnetic fields to be measured before the analysis could be performed.

Could the magnetic ‘spring’ effect be utilized in suspension systems for space robotics to increase the space rovers capability?

As the magnetic spring effect is produced mechanically it would be very simple to incorporate into a space based robot, with no additional power requirements and only a small mass increase in the overall suspension design. The suitability of the magnets would need to be tailored to the environment, as they would not be suitable for environments that experience temperatures above the magnet’s Curie point. Future testing is required to see to what extent magnetic compliant suspension improves the handling of space based robots, but the initial testing performed in the lab looks promising.

Can the current inaccuracy in single magnet localization using Hall Effect sensing be improved by employing more sensors or by changing the sensing orientation?

The sensor orientation is the main problem, proven through experimentation, for the location of a magnet using hall effect sensing. By employing more sensors it is possible to define more accurately the location of the magnet, but the orientation must be known to get an exact location. By changing the sensors orientation it is possible to get a different profile of the magnetic field surrounding the magnet, but purely rotating the sensing direction does not improve the localization of the magnet.

Is there a way to accurately localize two magnets using Hall Effect sensing and thus accurately know their separation?

Single axis hall effect sensing is not capable of differentiating between two magnets in a system, even with additional hall effect sensors in an array, due to only reading the magnetic field in one direction. To locate more than one magnet within a system, two dimensional hall effect sensing is required, as the magnetic fields' angle can be resolved as well as the true field magnitude which is not possible with a single axis hall effect system. The algorithm developed for TR2, section 5.2.2, that was expanded for use with TR4, section 6.5, proves that it is possible to locate and resolve the separation between two magnets in repulsion. The data from TR4 shows some of the algorithm limitations, but with additional work this algorithm could provide very accurate positional information for the separation between two magnets in repulsion. The advantage to this form of sensing is that it is non contact so would not change the underlying system dynamics whilst recording the required data.

The original contributions to research developed through this thesis include:

1. Analysis of magnetic suspension for use in suspension systems, specifically in the field of Space Robotics
2. Algorithm development and testing to calculate separation of two identical magnets through analysis of magnetic fields surrounding the magnets
3. Creation of experimental testing hardware to validate the magnet separation algorithm
4. Experimental data generation and analysis using novel techniques

These contributions stand as a testament to the research performed and will support future research in the field of magnetic compliance. The results have been checked

through experimentation, mathematical modeling and simulation, which therefore fills a void of data found when embarking on this thesis and research.

7.3 Limitations of Work

During experimentation there were problems that had to be overcome, even though TR4 was a vast improvement on the previous three testing rigs, so sections 7.3.1 and 7.3.2 discuss possible improvements for the TR4 hardware and software.

Limitations were also found in the magnetic separation algorithm, but a range of techniques have been employed to resolve the issues and new techniques have been developed, section 7.1.3, which will improve future data analysis of magnetic fields using an array of Hall Effect sensors.

Another limitation to work is the difficulty to apply the testing procedures to suspension systems in a space based environment, section 7.3.3.

7.3.1 Possible improvements to Hardware

The hardware produced for TR4 was based on iterations of the experimental testing rigs, so most of the problems had been solved through development, but the TR4 hardware still had room for improvement. The main problem found with the TR4 hardware was the positioning of the SS49E hall effect sensors, as the use of super glue to locate and hold the sensors in place caused some misalignment. To remove this problem, a slower curing super glue could have been used, or even have the sensors positioned and then glued into place after their location was confirmed. The reason that this was not done initially was restricted access to required equipment and materials. The majority of the sensors were positioned correctly, which gave a ground truth during sensor calibration testing, which led to the development of calibration

functions to correct for the sensor misalignment.

The data produced by the TR4 hardware was of far higher quality compared to the experimental testing rigs, due mainly to the integrated data capture and transmission module. This module transferred data with a custom communications protocol which required the re-transmission of data on a regular basis due to not having any underlying error correction. To increase the rate of data transfer from TR4 to the data logging computer, a standardized communications protocol with error correction could be employed. The PIC chip used at the heart of the TR4 hardware is capable of running at a much higher rate for the ADC functions, so could be used to give a constant stream of data showing real-time field measurements, rather than only when requested to send data back by the data logging software. This real-time link could therefore be employed in a control system to provide magnet separation feedback, such that the system could employ some form of control within the suspension.

A final improvement to the hardware could be the use of nylon nuts and thread in place of the brass locating bolt and nuts to make the system truly free of metal (not counting the magnets), as this would reduce the weight of the system and thus allow for faster response to inputs or disturbances.

7.3.2 Possible improvements to Software

The software employed on the TR4 data logging computer used the same communications protocol as the TR4 hardware, which could be replaced with a more robust protocol to improve data transfer. The data logging software was written in C# .net, which enabled multi-threading to improve the efficiency of the data processing and the graphical display routines. The GUI was designed to be used by an experienced user of the system, but if this code was to be released then the user interface would need to be streamlined, to reduce the number of options available and increase intelligibility.

The CSV file generation from the data logging software currently lists all data in a verbose manner, with separators between data runs, as such the data required some intermediate steps before it was usable with Matlab. The CSV files were however very efficient for data storage, with the largest file totaling to $75kB$ after data consolidation, so the experimental runs could have all been saved to a single file without the computer ‘breaking a sweat’.

The software written for Matlab is the result of many software iterations, as such it is large and cumbersome with many sub-sections. The Matlab code has a number of helper functions which are very efficient, similar to using separate header files in C, but for clarity the main body of code could have some of its functions separated out into additional helper functions. The main body of Matlab code contains all of the graphical display functions for many of the graphs and figures within this thesis, as well as the data management functions, which is why the code is included on the thesis DVD and not as an appendix.

The Matlab environment is very capable at processing and displaying data from experimentation, therefore Matlab would not be substituted for another piece of software.

7.3.3 Testing in a ‘Space’ environment

The hardware that has been developed for the research performed has only been tested under Earth-based laboratory conditions.

To test the system to its full capabilities further work will be required to extend the hardware, so that it can initially be tested on simulated terrain outside of the laboratory environment. Further hardware modification will be required if the system is to be tested in either simulated or extraterrestrial conditions, but it would be important to perform this testing to confirm if the system is truly usable for space

robotics. The modifications required for extended testing would include environmental protection, such as radiation hardening of components, extreme temperature protection and possible moisture ingress protection, as well as vibration protection and automated calibration for components.

7.4 Future Work

The future research from this thesis would be in these main areas:

1. Testing the magnetic compliant suspension on a space robot platform operating on expected terrain, for example, a simulated Martian environment.
2. Improving the magnet location and separation algorithm to account for experimental error described in section 6.6, to produce more accurate results.
3. Implementing the TR4 hardware in a real-time control system to adjust the suspension response using damping techniques described in section 2.4.
4. Correcting the magnetic separation algorithm such that the correct sensor group is selected more robustly to produce stronger results.
5. Using the raw real-world data gathered, extend the curve fitting to all data to improve the resolution of look-up tables for real-time control.
6. Extend the research into fitting of S-shaped curves to the magnet field approximations surrounding the magnets.

These areas follow on naturally from the research already performed and described in this thesis, with possible applications and publications in all of these areas.

Bibliography

- [1] Jörg Roth. Rocker-Bogie suspension system wheel positions on different terrain profiles, 2011. URL http://www.wireless-earth.org/private/common_images/RockerBogieSuspension.jpg.
- [2] AUDI of America. The 2011 Audi R8 Spyder 5.2 FSI quattro - Pure Fascination. Date Accessed: 18th December 2012. URL <http://www.eurocarnews.com/76/0/284/0/the-2011-audi-r8-spyder-52-fsi-quattro-pure-fascination.html>.
- [3] Jim Parison. The Bose Ride™ System. Technical report, Bose, 2010.
- [4] D B Bickler. Articulated Suspension System, Patent: 4840394, USA, 1989.
- [5] Doug Coward. Analog Computer Museum and History Center 1939 - Librascope Development Company. Date Accessed: 18th December 2012. URL <http://web.archive.org/web/20080123065301/dcoward.best.vwh.net/analog/libra.htm>.
- [6] Brian D Harrington and Chris Voorhees. The Challenges of Designing the Rocker-Bogie Suspension for the Mars Exploration Rover. Technical report, NASA, 2004.
- [7] Nildeep Patel, Richard Slade, and Jim Clemmet. The ExoMars rover locomotion

- subsystem. *Journal of Terramechanics*, 47(4):227–242, August 2010. ISSN 00224898. doi: 10.1016/j.jterra.2010.02.004. URL <http://linkinghub.elsevier.com/retrieve/pii/S0022489810000182>.
- [8] Astrium. All you want to know about Bridget (ExoMars). Date Accessed: 8th August 2012. URL <http://www.astrium.eads.net/en/articles/all-you-want-to-know-about-bridget.html>.
- [9] Brian H. Wilcox. ATHLETE: A cargo and habitat transporter for the moon. *2009 IEEE Aerospace conference*, pages 1–7, March 2009. doi: 10.1109/AERO.2009.4839568. URL <http://ieeexplore.ieee.org/lpdocs/epic03/wrapper.htm?arnumber=4839568>.
- [10] Feng Chen and Giancarlo Genta. Dynamic modeling of wheeled planetary rovers: A model based on the pseudo-coordinates approach. *Acta Astronautica*, 81(1): 288–305, December 2012. ISSN 00945765. doi: 10.1016/j.actaastro.2012.06.008. URL <http://linkinghub.elsevier.com/retrieve/pii/S0094576512002469>.
- [11] David P Miller and Tze-liang Lee. High-Speed Traversal of Rough Terrain Using a Rocker-Bogie Mobility System. In *Proceedings of Robotics 2002: The 5th International Conference and Exposition on Robotics for Challenging Situations and Environments*, pages 428–434, 2002.
- [12] Peter Omand Rasmussen, Torben Ole Andersen, Frank T Jorgensen, and Orla Nielsen. Development of a High-Performance Magnetic Gear. *IEEE Transactions on Industry Applications*, 41(3):764–770, 2005.
- [13] Viatcheslav Dombrovski, Suresh Tirumalai, Ira Goldberg, and David Driscoll. Magnetic Power Transmission Coupling, Patent: H02K 4900; H02K 4906; H02K 4902; H02K 4910, 2000.

- [14] B. V. Jayawant. *Electromagnetic Levitation and Suspension Techniques*. Edward Arnold (Publishers) Ltd, London, first edition, 1981. ISBN 0-7131-3428-3.
- [15] Richard McElligott. *Magnetic Compliance: A novel approach to compliance in legged robots*. PhD thesis, The University of Reading, UK, 2010.
- [16] Geek3. VectorFieldPlot - Magnetic dipole field around a small current loop. Date Accessed: 8th March 2013. URL <http://commons.wikimedia.org/wiki/User:Geek3/VectorFieldPlot>.
- [17] William Grey Walter. An imitation of life. *Scientific American*, 182(5):42–45, 1950.
- [18] William Grey Walter. A machine that learns. *Scientific American*, 185(2):60–63, 1951.
- [19] Raphael Beatram. Research and applications. Technical Report C, SRI, 1970.
- [20] Hans P Moravec. The Stanford Cart and the CMU Rover. *Proceedings of the IEEE*, 71(7):872–884, 1983.
- [21] Max Bajracharya, Mark W Maimone, and Daniel Helmick. Autonomy for Mars Rovers: Past, Present, and Future. *Computer*, 41(12):44–50, 2008. doi: 10.1109/MC.2008.479.
- [22] S Gabriel Udomkesmalee. Mars Science Laboratory Focused Technology Program Overview. In *IEEE Aerospace Conference*, pages 961–970, 2005. ISBN 0780388704.
- [23] Vladimir Kucherenko, Alexei Bogatchev, and Michel Van Winnendael. Chassis Concepts for the ExoMars Rover. In *Proceedings of the 8th ESA Workshop on Advanced Space Technologies for Robotics and Automation (ASTRA)*, volume c, pages 1–8, 2004.

- [24] Jeongmok Cho, Taegeun Jung, Sung-Ha Kwon, and Joongseon Joh. Development of a Fuzzy Sky-hook Algorithm for a Semi-active ER Vehicle Suspension Using Inverse Model. In *IEEE International Conference on Fuzzy Systems*, pages 1550–1556. IEEE, 2006. ISBN 0780394895.
- [25] Randel A Lindemann and Chris J Voorhees. Mars Exploration Rover Mobility Assembly Design, Test and Performance. In *IEEE International Conference on Systems, Man and Cybernetics*, pages 450–455, 2005.
- [26] Antonin Svboda. *Computing Mechanisms and Linkages*. McGraw-Hill Book Company, New York, Massachusetts Institute of Technology Radiation Laboratory Series, 1948.
- [27] William S. Hammack. The Whiffletree. Date Accessed: 20th October 2012. URL www.engineerguy.com/videos/video-whiffletree.htm.
- [28] William F. Voit. Machine Operation and Some Major Design Crossroads of the Selectric Typewriter. In *Design Engineering Conference and Show*, New York, 1963. The American Society of Mechanical Engineers.
- [29] B. W. Whittwer. A History of the Development of the IBM Selectric. In *Design Engineering Conference and Show*, New York, 1963. The American Society of Mechanical Engineers.
- [30] S. A. Okcuoglu. Input Motion Synthesis and Analysis for the IBM Selectric Selection System. In *Design Engineering Conference and Show*, New York, 1963. The American Society of Mechanical Engineers.
- [31] NASA. Wheels in the Sky. Date Accessed: 8th August 2012. URL <http://marsrover.nasa.gov/spotlight/wheels01.html>.

- [32] Nildeep Patel, Richard Slade, and Jim Clemmet. Evolution of the ExoMars Rover Locomotion subsystem. In *16th International Conference of the International Society for Terrain-Vehicle Systems (ISTVS)*, number 2, pages 1–14, 2008.
- [33] Nildeep Patel, Richard Slade, and Jim Clemmet. Traction performance trials of the ExoMars Rover breadboard. In *11th European Regional Conference of the International Society for Terrain-Vehicle Systems (ISTVS)*, pages Vol. 3, No. 5, 2009.
- [34] Yoji Kuroda, Koji Kondo, and Kazuaki Nakamura. Low Power Mobility System for Micro Planetary Rover “ Micro5 ”. In *The 3rd International Symposium on Artificial Intelligence, Robotics and Automation in Space - iSAIRAS*, pages Vol. 440, p. 77. ESTEC, 1999.
- [35] Baichao Chen, Rongben Wang, Yang Jia, Lie Guo, and Lu Yang. Design of a high performance suspension for lunar rover based on evolution. *Acta Astronautica*, 64 (9-10):925–934, May 2009. ISSN 00945765. doi: 10.1016/j.actaastro.2008.11.009. URL <http://linkinghub.elsevier.com/retrieve/pii/S0094576508003706>.
- [36] Robert Bauer, Winnie Leung, and Tim Barfoot. Development of a Dynamic Simulation tool for the ExoMars Rover. In *The 8th International Symposium on Artificial Intelligence, Robotics and Automation in Space - iSAIRAS*, number August, pages 311–314. ESTEC, 2005.
- [37] David P Miller, Tim S Hunt, and Matt J Roman. Experiments and Analysis of the Role of Solar Power in Limiting Mars Rover Range. In *Proceedings of the 2003 IEEE/RSJ International Conference on Intelligent Robots and Systems*, number October, pages 317–322, Las Vegas, Nevada, 2003. ISBN 0780378601.

- [38] Brian K Muirhead. Mars Rovers, Past and Future. Technical report, Jet Propulsion Laboratory, California Institute of Technology, 2004.
- [39] J Yuh. Underwater Robotics. In *Proceedings of the 2000 IEEE International Conference on Robotics and Automation*, number April, pages 932–937, 2000. ISBN 0780358864.
- [40] Daniel P Scharf, Fred Y Hadaegh, and Scott R Ploen. A Survey of Spacecraft Formation Flying Guidance and Control (Part I): Guidance. In *Proceedings of the 2003 American Control Conference*, number Part I, pages 1733–1739, 2003. ISBN 0780378962.
- [41] Lieng-Huang Lee. Adhesion and cohesion mechanisms of lunar dust on the moon’s surface. *Journal of Adhesion Science and Technology*, 9(8):1103–1124, 1995.
- [42] Alex Macdiarmid and Quanterion Solutions. Thermal Cycling Failures - Part One of Two. *Journal of the Reliability Information Analysis Center*, (January), 2011.
- [43] BBC. 1967: Three astronauts die in Apollo 1 tragedy. Date Accessed: 12th December 2012. URL http://news.bbc.co.uk/onthisday/hi/dates/stories/january/27/newsid_3392000/3392419.stm.
- [44] Catherine L Thornton and James S Border. Radiometric Tracking Techniques for Deep - Space Navigation. Technical report, Jet Propulsion Laboratory, California Institute of Technology, 2000.
- [45] James E. Potter and Robert G. Stern. Statistical Filtering of Space Navigation Measurements. Technical report, Massachusetts Institute of Technology, 1963.
- [46] Kazuya Yoshida. Space Robot Dynamics and Control: To Orbit, From Orbit,

- and Future. Technical report, Department of Aeronautics and Space Engineering, Tohoku University, 1993.
- [47] Howie Choset and David Kortenkamp. Path Planning and Control for AERCam, a Free-flying Inspection Robot in Space. Technical report, Texas Robotics and Automation Center, Carnegie Mellon University, 1999.
- [48] R. Mitcheltree, A. Steltzner, A. Chen, M. SanMartin, and T. Rivellini. Mars Science Laboratory Entry Descent and Landing System Verification and Validation Program. *2006 IEEE Aerospace Conference*, pages 1–6, 2006. doi: 10.1109/AERO.2006.1655799. URL <http://ieeexplore.ieee.org/lpdocs/epic03/wrapper.htm?arnumber=1655799>.
- [49] David W Way, Richard W Powell, Allen Chen, Adam D Steltzner, A Miguel San Martin, P Daniel Burkhart, and Gavin F Mendeck. Mars Science Laboratory: Entry, Descent and Landing System Performance. In *2006 IEEE Aerospace Conference*, pages 1–39, 2006.
- [50] Charles Elachi. Engineering Challenges in Space Exploration. Date Accessed: 20th April 2012, 2012. URL http://www.raeng.org.uk/events/pdf/International_Lecture_March_2012.pdf.
- [51] Guy Webster. NASA’s Hibernating Mars Rover May Not Call Home. Date Accessed: 12th December 2012. URL http://www.nasa.gov/mission_pages/mer/news/mer20100730.html.
- [52] A.J.S Rayl. Mars Exploration Rovers Update: Spirit Gains A little Power, Opportunity Loses a Little Steam. Date Accessed: 10th October 2012. URL <http://www.planetary.org/explore/space-topics/space-missions/mer-updates/2009/02-28-mer-update.html>.

- [53] Satish Krishnan and Christopher J. Voorhees. The use of harmonic drives on NASA's Mars Exploration Rover. Technical report, Jet Propulsion Laboratory, California Institute of Technology, 2003.
- [54] Randel A. Lindermann, Donald B. Bickler, Brian D. Harrington, Gary M. Ortiz, and Christopher J. Voorhees. Mars Exploration Rover Mobility Development. *IEEE Robotics and Automation Magazine*, pages 19–26, June 2006.
- [55] P.C. Leger, a. Trebi-Ollennu, J.R. Wright, S.a. Maxwell, R.G. Bonitz, J.J. Biesiadecki, F.R. Hartman, B.K. Cooper, E.T. Baumgartner, and M.W. Maimone. Mars Exploration Rover Surface Operations: Driving Spirit at Gusev Crater. *2005 IEEE International Conference on Systems, Man and Cybernetics*, 2:1815–1822. doi: 10.1109/ICSMC.2005.1571411. URL <http://ieeexplore.ieee.org/lpdocs/epic03/wrapper.htm?arnumber=1571411>.
- [56] Shunichi Makita. Non-Contact Magnetic Gear for Micro Transmission Mechanism Koji. In *An Investigation of Micro Structures, Sensors, Actuators, Machines and Robots*. *IEEE*, pages 125–130, 1991.
- [57] K. Atallah and D. Howe. A novel high-performance magnetic gear. *IEEE Transactions on Magnetics*, 37(4):2844–2846, July 2001. ISSN 00189464. doi: 10.1109/20.951324. URL <http://ieeexplore.ieee.org/lpdocs/epic03/wrapper.htm?arnumber=951324>.
- [58] K Atallah, S D Calverley, and D Howe. Design, analysis and realisation of a high-performance magnetic gear. In *IEE Electronic Power Applications*, pages 135–143, 2004. doi: 10.1049/ip-epa.
- [59] Kais Atallah, Jan Rens, Smail Mezani, David Howe, The Sheffield Biocubator, S Sheffield, Faculté Sciences, and Vandoeuvre Nancy. A Novel “ Pseudo ” Direct-

- Drive Brushless Permanent Magnet Machine. *IEEE Transactions on Magnetics*, 44(11):4349–4352, 2008.
- [60] Jacob Rabinow. The Magnetic Fluid Clutch. In *AIEE Transactions*, pages 1308–1315, 1948.
- [61] Steve Constantinides. NdFeB for High Temperature Motor Applications. In *SMMA Fall Technical Conference*, pages 1–33. Arnold Magnetic Technologies, 2004.
- [62] Brad Paden, Nelson Groom, and James F. Antaki. Design Formulas for Permanent-Magnet Bearings. *Journal of Mechanical Design*, 125(4):734, 2003. ISSN 10500472. doi: 10.1115/1.1625402. URL <http://link.aip.org/link/JMDEDB/v125/i4/p734/s1&Agg=doi>.
- [63] Nicholas A Greatrex, Daniel L Timms, Nobuyuki Kurita, Edward W Palmer, and Toru Masuzawa. Axial Magnetic Bearing Development for the. *IEEE Transactions on Biomedical Engineering*, 57(3):714–721, 2010.
- [64] Shanbao Cheng and Steven W Day. Design and Control of Hybrid Magnetic Bearings for Maglev Axial Flow Blood Pumps. In *International Conference on Advanced Intelligent Mechatronics*, pages 187–192, 2010. ISBN 9781424480302.
- [65] A Chambers, R K Fitch, and B S Halliday. Basic Vacuum Technology. In *Basic Vacuum Technology*, chapter Vacuum Mat, page 108. IOP Publishing Ltd, 1989. ISBN 0-85274-128-6.
- [66] G. R. Polgreen. Magnetic System of Transportation, Patent: 3158765, USA, 1964.
- [67] P. K. Sinha. *Electromagnetic Suspension: Dynamics and Control, IET Control Edition*. Institution of Engineering and Technology, 1987. ISBN 978-0863410635.

- [68] Geoffrey A Long, O James Fiske, and Brad E Paden. Design of a Small-Scale Prototype for a Stabilized Permanent Magnet Levitated Vehicle. Technical Report 88, 2008.
- [69] O J Fiske. The Magtube low cost maglev transportation system. In *The 19th International Conference on Magnetically Levitated Systems and Linear Drives*, Dresden, Germany, 2006.
- [70] Kee-Bong Choi, Young Geun Cho, Tadahiko Shinshi, and Akira Shimokohbe. Stabilization of one degree-of-freedom control type levitation table with permanent magnet repulsive forces. *Mechatronics*, 13(6):587–603, July 2003. ISSN 09574158. doi: 10.1016/S0957-4158(02)00032-6. URL <http://linkinghub.elsevier.com/retrieve/pii/S0957415802000326>.
- [71] W. Robertson, B. Cazzolato, and a. Zander. A multipole array magnetic spring. *IEEE Transactions on Magnetics*, 41(10):3826–3828, October 2005. ISSN 0018-9464. doi: 10.1109/TMAG.2005.854981. URL <http://ieeexplore.ieee.org/lpdocs/epic03/wrapper.htm?arnumber=1519458>.
- [72] Timothy H Boyer. The force on a magnetic dipole. *American Journal of Physics*, 56(8):688–692, 1988. doi: 10.1119/1.15501.
- [73] Kar W. Yung, Peter B. Landecker, and Daniel D. Villani. An analytic solution for the force between two magnetic dipoles. *Magnetic and Electrical Separation*, 9(1):39–52, 1998. ISSN 1055-6915. doi: 10.1155/1998/79537. URL <http://www.hindawi.com/archive/1998/079537/abs/>.
- [74] David Vokoun, Marco Beleggia, Luděk Heller, and Petr Šittner. Magneto-static interactions and forces between cylindrical permanent magnets. *Journal of Magnetism and Magnetic Materials*, 321(22):3758–3763, November 2009.

- ISSN 03048853. doi: 10.1016/j.jmmm.2009.07.030. URL <http://linkinghub.elsevier.com/retrieve/pii/S030488530900746X>.
- [75] P Hammond. Electromagnetism for Engineers, An Introductory Course. pages 91–94. Oxford University Press, 4th edition, 1997. ISBN 0198562985.
- [76] John Mellor-crummey. Introduction to Simulation. Date Accessed: 18th May 2012. URL [www.cs.rice.edu/~sim\\$johnmc/comp528/lecture-notes/Lecture19.pdf](http://www.cs.rice.edu/~sim$johnmc/comp528/lecture-notes/Lecture19.pdf).
- [77] Robert Lee Hotz. Mars Probe Lost Due to Simple Math Error. Date Accessed: 18th May 2012, October . URL <http://articles.latimes.com/1999/oct/01/news/mn-17288>.
- [78] S Robinson. *Simulation: The Practice of Model Development and Use*. Wiley, 2004. ISBN 978-0-470-84772-5.
- [79] Roger McHaney. *Understanding Computer Simulation*. BookBoon, 2009. ISBN 9788776815059.
- [80] Abdunaser Sayma. *Computational Fluid Dynamics*. Ventus Publishing ApS, 2009. ISBN 9788776814304.
- [81] David Gossard and Kenji Shimada. Bubble Mesh: Automated Triangular Meshing of Non-Manifold Geometry by Sphere Packing. pages 409–419, 1995.
- [82] Jonathan Richard Shewchuk. Delaunay refinement algorithms for triangular mesh generation. *Computational Geometry*, 22(1-3):21–74, May 2002. ISSN 09257721. doi: 10.1016/S0925-7721(01)00047-5. URL <http://linkinghub.elsevier.com/retrieve/pii/S0925772101000475>.

- [83] Fei Shi and Xianghuai Dong. 3D numerical simulation of filling and curing processes in non-isothermal RTM process cycle. *Finite Elements in Analysis and Design*, 47(7):764–770, July 2011. ISSN 0168874X. doi: 10.1016/j.finel.2011.02.007. URL <http://linkinghub.elsevier.com/retrieve/pii/S0168874X11000345>.
- [84] Fabio Luise, Giorgio Grezzani, and Diego Bon. *Using FEMM software tool*. Electric Drive Laboratory, 2006.
- [85] David Meeker. Finite Element Method Magnetics User’s Manual. Technical report, IEEE, 2003.
- [86] Nathan Ida. *Nondestructive Testing Handbook Volume 5: Electromagnetic Testing*. American Society for Nondestructive Testing, third edit edition, 2004. ISBN 1571170464.
- [87] Dupont Engineering Polymers. Delrin with ‘ Design with Delrin ’ Data at your fingertips. Date Accessed: 15th May 2012. URL <http://plastics.dupont.com/plastics/pdflit/europe/delrin/dwdnav.pdf>.
- [88] ST Microelectronics. LD117A Series Low Drop Fixed and Adjustable Positive Voltage Regulators. Technical Report January, 2003.
- [89] Laird Technologies. BTM410/411 Bluetooth AT Data Module. Technical report, Laird Technologies.
- [90] Microchip Technology. PIC18F87K22 Family Datasheet. Technical report, 2010.
- [91] Honeywell. Honeywell SS49E Datasheet. Technical report, Honeywell.
- [92] Laird Tech. BTM410/411 Data Module User Manual Version 3.0. Technical Report 2, Laird Technologies, February 2012.

-
- [93] Kristjan Jonasson. RGB triple of color name V.2. Date Accessed: 12th December 2012. URL <http://www.mathworks.co.uk/matlabcentral/fileexchange/24497-rgb-triple-of-color-name-version-2>.
- [94] Microchip Website. Date Accessed: 10th April 2012. URL <http://www.microchip.com/>.
- [95] Microchip Technology. PIC18F87K22 Family Data Sheet 1-Mbit Enhanced Flash Microcontrollers with 12-Bit ADC and nanoWatt XLP Technology. Technical report, 2011.

Appendix A

Helmholtz Coil Full Derivation

This appendix delivers the full derivation of the Helmholtz Equations used in section 3.3. Two derivations are necessary; one to derive an expression which resolves the magnetic field strength at any point along the central axis of the coils and a second derivation to determine magnetic field strength at the midpoint of the central axis between two coils.

The derivations begin with equation A.1 which is derived from Biot-Savart's Law and is given by

$$B = \frac{\mu_0 I R^2}{2(R^2 + x^2)^{3/2}} \quad (\text{A.1})$$

Where B is the magnetic field, μ_0 is the permeability of free space, I is the current within the coil, R is the coil radius and x is the distance from the coil on the central axis.

When the number of turns n in each coil is introduced, equation A.1 becomes

$$B = \frac{\mu_0 n I R^2}{2(R^2 + x^2)^{3/2}}. \quad (\text{A.2})$$

First the expression to find B at any point will be derived. Each coil is mirrored about a point x and the two coils are separated by radius R , so the coils are positioned at $x \pm \frac{R}{2}$ which is substituted into equation A.2 to give

$$B = \frac{\mu_0 n I R^2}{2 \left(R^2 + (x \pm (R/2))^2 \right)^{3/2}} \quad (\text{A.3})$$

Which, by separating out the constants, can be re-written as

$$B = \frac{\mu_0 n I R^2}{2} \left(\frac{1}{\left(R^2 + (x \pm R/2)^2 \right)^{3/2}} \right). \quad (\text{A.4})$$

By assigning B_1 to the magnetic field strength due to coil 1 and B_2 to the magnetic field strength due to coil 2, the magnetic field strength B can be defined by $B = B_1 + B_2$. Since B_1 and B_2 are given by

$$B_1 = \frac{\mu_0 n I R^2}{2} \left(\frac{1}{\left(R^2 + (x - R/2)^2 \right)^{3/2}} \right)$$

and

$$B_2 = \frac{\mu_0 n I R^2}{2} \left(\frac{1}{\left(R^2 + (x + R/2)^2 \right)^{3/2}} \right)$$

the magnetic field strength at any point can be found by equation A.5

$$B = \frac{\mu_0 n I R^2}{2} \left(\frac{1}{\left(R^2 + (x - R/2)^2 \right)^{3/2}} + \frac{1}{\left(R^2 + (x + R/2)^2 \right)^{3/2}} \right). \quad (\text{A.5})$$

To demonstrate the effect of two coils on the magnetic field strength along the central axis, figure A.1 shows the calculated field strength plotted against the measurement point x . The two smaller amplitude curves represent the magnetic fields generated by

B_1 and B_2 , with the larger curve confirming their summation.

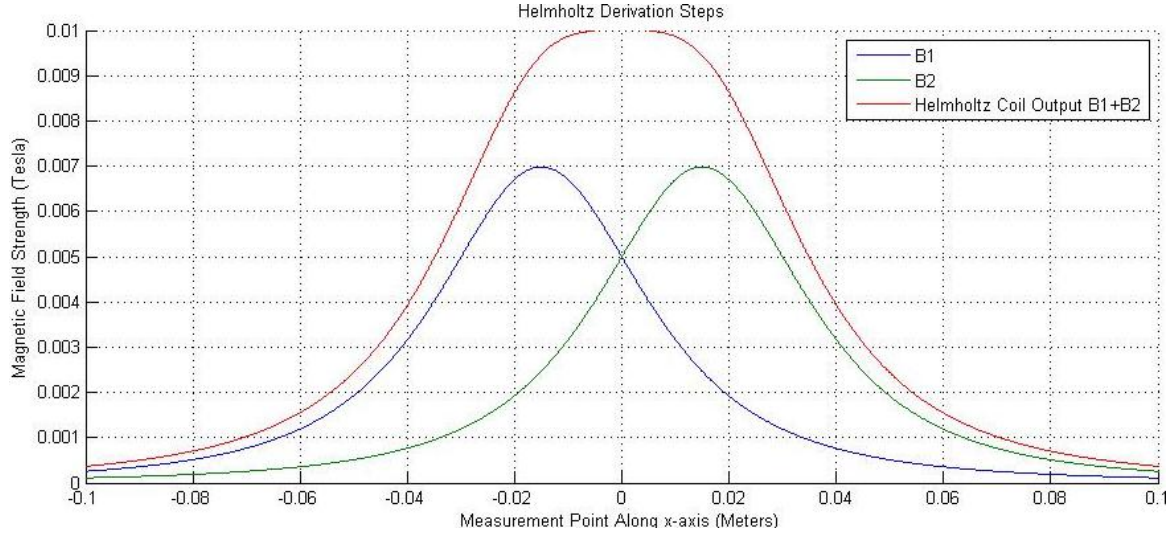


Figure A.1: Graph showing magnetic field strength of B_1 , B_2 and full Helmholtz coil

The larger amplitude curve has been proven experimentally, section 4.4, vindicating the derivation.

For the derivation of the expression to determine the field strength at the midpoint between two coils, the x term is static and as such equation A.2 does not require the additional complexity of replacing x by $x \pm R/2$ so the x term is replaced instead by $R/2$ and equation A.2 is multiplied by 2 since there are two coils to give

$$B = \frac{2\mu_0 n I R^2}{2(R^2 + (R/2)^2)^{3/2}} = \frac{\mu_0 n I R^2}{(R^2 + (R/2)^2)^{3/2}}. \quad (\text{A.6})$$

Since

$$\begin{aligned} R^2 + \left(\frac{R}{2}\right)^2 &\equiv R^2 + \frac{R^2}{4} \\ &\equiv R^2 \left(1 + \frac{1}{4}\right) \\ &\equiv \frac{5}{4}R^2 \end{aligned} \quad (\text{A.7})$$

Equation A.6 is re-written to give

$$B = \frac{\mu_0 n I R^2}{\left(\frac{5}{4} R^2\right)^{3/2}}. \quad (\text{A.8})$$

Also note that

$$\begin{aligned} \left(\frac{5}{4} R^2\right)^{3/2} &\equiv \left(\frac{5}{4}\right)^{3/2} (R^2)^{3/2} \\ &\equiv \left(\frac{5}{4}\right)^{3/2} R^3 \end{aligned} \quad (\text{A.9})$$

So that equation A.8 becomes

$$B = \frac{\mu_0 n I R^2}{\left(\frac{5}{4}\right)^{3/2} R^3} \quad (\text{A.10})$$

Which simplifies to

$$B = \frac{\mu_0 n I}{\left(\frac{5}{4}\right)^{3/2} R} = \left(\frac{4}{5}\right)^{3/2} \frac{\mu_0 n I}{R}. \quad (\text{A.11})$$

The simplified equation can now be rearranged to solve for other factors such as current required to drive the coil or the number of turns needed to produce a magnetic field of specific magnitude. These are given by

Solve for:

$$\begin{aligned} \text{Radius of Coils} \quad R &= \left(\frac{4}{5}\right)^{3/2} \frac{\mu_0 n I}{B} \\ \text{Number of turns} \quad n &= \frac{RB}{(4/5)^{3/2} \mu_0 I} \\ \text{Current in Coils} \quad I &= \frac{RB}{(4/5)^{3/2} \mu_0 n} \end{aligned} \quad (\text{A.12})$$

Appendix B

Helmholtz Coil Manufacture

The physical manufacture of the Helmholtz coil, specified in chapter 3.3.2, is described in this appendix. The Helmholtz coil used needs to produce a constant field of 100 Gauss (0.01 Tesla), so by plugging this value into equation 3.24 the Helmholtz coil required 667 coils powered by a constant direct current of 1A.



Figure B.1: 3D Printing of the Helmholtz coil bobin

The design was manufactured using a 3D additive plastic printing technique which whilst relatively quick and versatile posed some considerations that needed to be addressed, including heat dissipation of the coils, orientation of the print, accuracy of dimensions and print depth of layers. The heat dissipation of the coils was important as the plastic used for printing, Acrylonitrile Butadiene Styrene (referred to as ABS), is a thermoplastic which softens under heat causing it to lose its structural strength and shape. Thermoplastics have two important temperatures to be aware of, the Glass Transition T_g and Melting Point T_m , which govern their properties. The Glass Transition T_g temperature is the transition point at which the thermoplastic changes from a solid to a molten state so that it can be molded into a useful shape. The melting point T_m is the point at which the thermoplastic becomes unusable due to the chemical bonds breaking down and as such cannot be exceeded during manufacture or use. Not all thermoplastics including ABS have a true melting point due to being amorphous, but the Glass transition point of ABS is $105^\circ C$. To avoid over-heating the ABS and causing it to become soft it was important to know how warm the coils would get during use, which was done very simply with a temperature probe as the coil would not be powered for long periods. If the coils were left running for much more than 30 minutes then some calculation would have been necessary, but after 10 minutes of constant use the coils could be picked up without needing gloves. The contingency plan was to surround the coils with dry ice (frozen Carbon Dioxide CO_2), but this was never required. When using 3D additive printing it is vital to get the orientation correct, otherwise the part can fracture when subjected to a load or not be physically sturdy enough when compressed. The print quality also depends on the orientation as the printer deposits plastic in layers, so for example printing a circle will be much higher quality when printed flat onto the build surface of the machine compared to being created from multiple layers and printed vertically. The design required the coil

diameter to be constant to create the best possible coils and as such the orientation chosen for printing can be seen in figure B.1. The 3D printer deposits layers that are 0.01 inches thick ($0.254mm$) which has to be taken into account as these are not SI units. To get a constant and accurate print from the system, all measurements in the vertical direction need to be divisible by this, otherwise the software that drives the printer could get confused and produce varying thickness walls in the design. As all the vertical measurements in the coil design only required $\pm 0.3mm$ accuracy this was not a major problem to overcome as the layer thicknesses were rounded to fit the machines tolerance.



(a) Side view of the SS49E sensor located near a magnet attached to the lathe chuck



(b) Close up view of the SS49E sensor in position to record the rotations of the lathe chuck

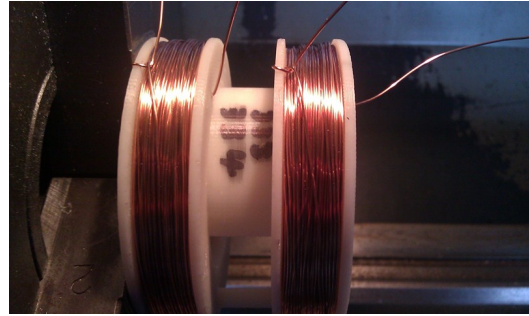
Figure B.2: Rotation counting using a magnet attached to the lathes chuck and a SS49E sensor

The 3D printer is capable of producing complex 3D designs due to its ability to print a support material as well as the build material ABS. The support material Polyvinyl alcohol (PVA) is extruded in the same way as the ABS (melting point of $180^{\circ}C$), but is readily dissolved in agitated water at about $70^{\circ}C$. After the 3D printing was completed (6.5 hours to print and a further 2 hours in the water bath to remove the PVA support material) the bobbin part was ready to have the coils wound onto it to create the Helmholtz coil. This bobbin was dried overnight by storing it in a sealed beaker along with a desiccant (packets of silica gell) and was then loaded onto

a Colchester lathe.



(a) Fully wound helmholtz coil still mounted on the lathe chuck



(b) Side view of the fullt wound Helmholtz coil with coil count indicated

Figure B.3: Fully wound Helmholtz coil after wire turns had been added to the 3D printed bobbin

The lathe did not have a turn counter so a solution was devised using a spare magnet attached to the lathes chuck and a spare SS49E hall effect sensor suspended on a plastic rod near the rotating magnet, figure B.3. The sensor counted the number of rotations of the lathes chuck by recording the field measurements from the hall effect sensor and displayed them on a 7-SEG display, figure B.4, so that the correct number of copper wire turns could be wound onto the bobbin.

The copper wire had an enamel coating so multiple coils could be laid without the need for insulation between them. Once the first coil was wound onto the bobbin, the wires were secured and the second coil was created. The coils were joined in series, so that the current could flow through both coils to produce a field in the same direction. At this point the coils total resistance was measured to see if it matched the calculated value, otherwise modifications to the current would need to be made to get the Helmholtz coil to operate in the correct way.

The Helmholtz coil was placed under a translation stage, so that the magnetic field profile of the coil could be verified, figure B.5, using a calibrated hall probe. Once the field had been confirmed to match the FEMM simulation, section 4.4, the SS49E

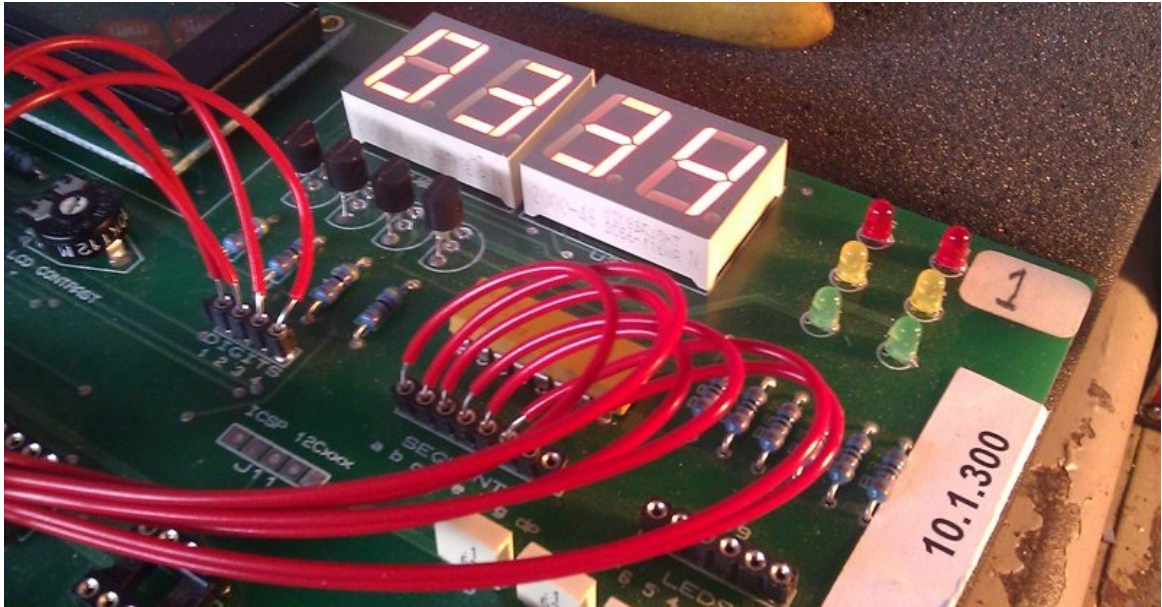


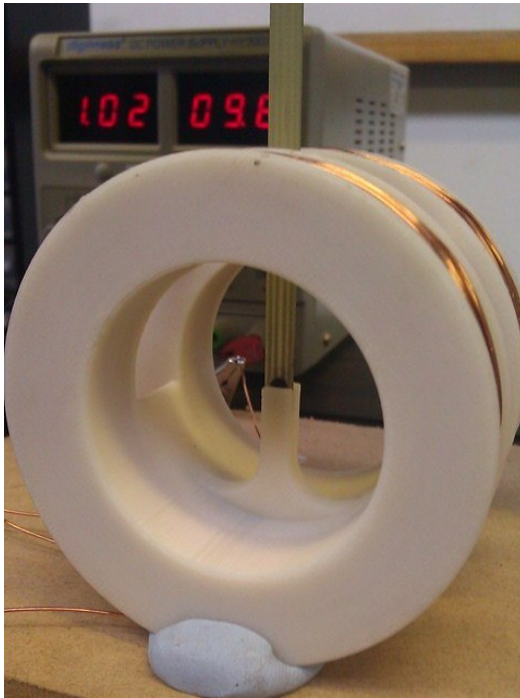
Figure B.4: Coil counting display built on a PIC development board to process the analog input from the SS49E sensor

sensors could be checked to see if they produced the expected output when exposed to a 100 Gauss magnetic field.

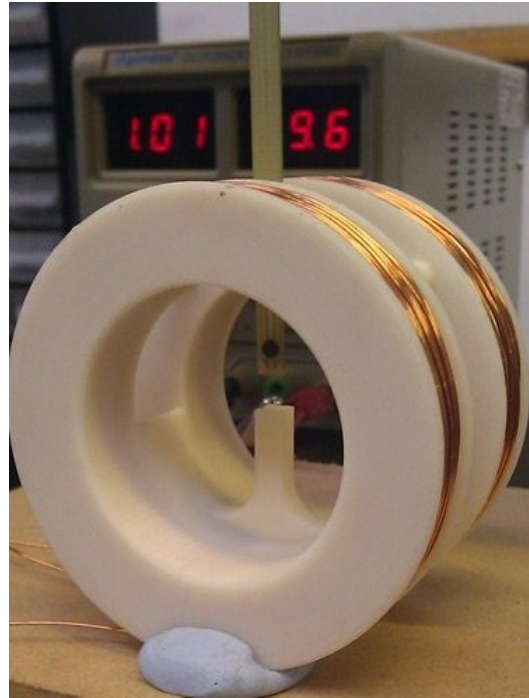
Figure B.6 shows a close up of the coil with the calibrated hall probe in the very center of the coil, where it read 100 Gauss, as well as at 10mm displacement. The translation stage allowed for very accurate movements to create consistent data. The stabilized laboratory DC power supply is visible in the background showing the current on the left and voltage on the right. The current value drifted from the expected 1A because the coils resistance changed due to temperature, so was monitored closely during experimentation. The figure shows 102 and 101 on the displays, because the decimal point is not visible. The sensors performed as expected, thus the Helmholtz coil proved that the SS49E sensors were accurate and could be used for further experimentation.



Figure B.5: Translation stage and experimental setup to move the hall sensing devices through the Helmholtz coil



(a) Calibrated hall probe at the magnetic field center



(b) Calibrated hall probe displaced by 10mm from magnetic field center

Figure B.6: Close up of Calibrated hall probe within the Helmholtz coil

Appendix C

Single Hall Effect sensor calibration using a Helmholtz Coil

This appendix shows the data recorded during calibration testing of a single SS49E Hall Effect sensor using a Helmholtz coil, compared to measurements taken with a calibrated hall probe and the simulated results from FEMM.

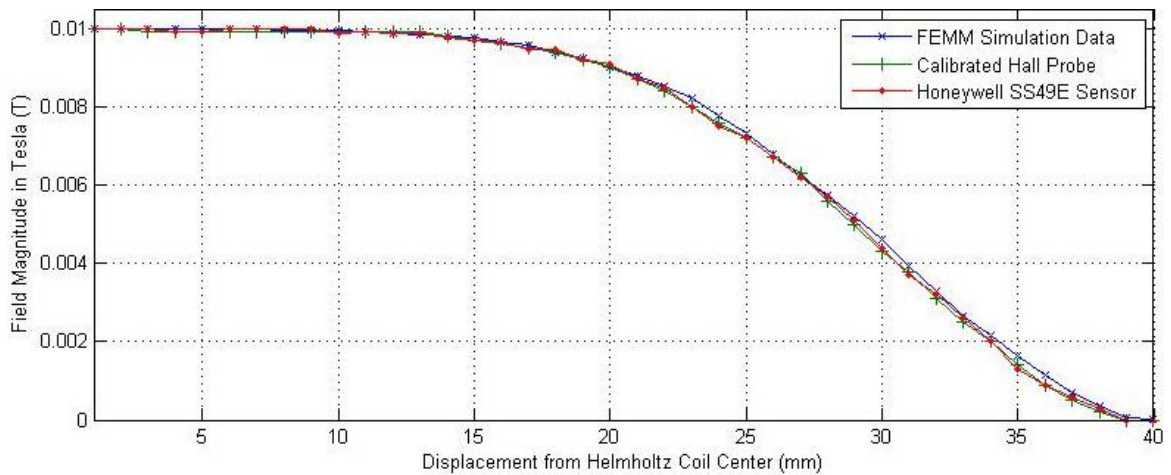


Figure C.1: FEMM simulation and Hall Effect measurements of the Helmholtz Coil

Dis	FEMM	Cal	SS49E	Dis	FEMM	Cal	SS49E
0	9.98E-03	1.00E-02	1.00E-02	21	8.53E-03	8.40E-03	8.50E-03
1	9.98E-03	1.00E-02	1.00E-02	22	8.21E-03	8.00E-03	8.00E-03
2	9.98E-03	9.90E-03	1.00E-02	23	7.78E-03	7.60E-03	7.50E-03
3	9.98E-03	9.90E-03	9.90E-03	24	7.31E-03	7.20E-03	7.20E-03
4	9.98E-03	9.90E-03	9.90E-03	25	6.78E-03	6.70E-03	6.70E-03
5	9.98E-03	9.90E-03	1.00E-02	26	6.22E-03	6.30E-03	6.20E-03
6	9.97E-03	9.90E-03	1.00E-02	27	5.74E-03	5.60E-03	5.70E-03
7	9.97E-03	9.90E-03	1.00E-02	28	5.22E-03	5.00E-03	5.10E-03
8	9.96E-03	9.90E-03	9.98E-03	29	4.59E-03	4.30E-03	4.40E-03
9	9.95E-03	9.90E-03	9.89E-03	30	3.95E-03	3.80E-03	3.70E-03
10	9.93E-03	9.90E-03	9.90E-03	31	3.29E-03	3.10E-03	3.20E-03
11	9.90E-03	9.90E-03	9.87E-03	32	2.67E-03	2.50E-03	2.60E-03
12	9.85E-03	9.90E-03	9.88E-03	33	2.15E-03	2.00E-03	2.00E-03
13	9.81E-03	9.80E-03	9.78E-03	34	1.63E-03	1.40E-03	1.30E-03
14	9.75E-03	9.70E-03	9.70E-03	35	1.15E-03	9.00E-04	9.00E-04
15	9.67E-03	9.60E-03	9.65E-03	36	7.07E-04	5.00E-04	6.00E-04
16	9.56E-03	9.50E-03	9.45E-03	37	3.73E-04	2.00E-04	3.00E-04
17	9.41E-03	9.40E-03	9.45E-03	38	3.87E-05	0.00E+00	0.00E+00
18	9.24E-03	9.20E-03	9.20E-03	39	1.46E-05	0.00E+00	0.00E+00
19	9.02E-03	9.00E-03	9.10E-03	40	0.00E+00	0.00E+00	0.00E+00
20	8.78E-03	8.70E-03	8.70E-03				

Table C.1: Table showing the Magnetic Field Strengths in Tesla (T) with respects to Displacement (mm). Column headings: Dis (Displacement), FEMM (FEMM Software), Cal (Calibrated Hall Probe) and SS49E (SS49E Sensor)

Appendix D

Group Calibration of Sensors

This appendix shows the data recorded during the group sensor calibration routine with a graph of the data displaying all 24 sensor channels.

Channel	Voltage in V								
	0.000	0.100	0.200	0.300	0.400	0.500	0.600	0.700	0.800
1	0.006	0.103	0.203	0.305	0.405	0.504	0.606	0.704	0.804
2	0.006	0.103	0.202	0.305	0.405	0.504	0.605	0.704	0.804
3	0.007	0.103	0.203	0.305	0.405	0.503	0.604	0.704	0.804
4	0.006	0.103	0.202	0.304	0.404	0.504	0.605	0.704	0.804
5	0.007	0.103	0.203	0.305	0.404	0.504	0.605	0.703	0.804
6	0.007	0.103	0.203	0.305	0.405	0.504	0.604	0.703	0.804
7	0.007	0.103	0.203	0.305	0.404	0.503	0.605	0.704	0.804
8	0.008	0.103	0.203	0.305	0.404	0.503	0.605	0.704	0.805
9	0.007	0.103	0.202	0.304	0.404	0.504	0.606	0.705	0.804
10	0.006	0.104	0.202	0.305	0.404	0.503	0.605	0.704	0.804
11	0.007	0.103	0.202	0.305	0.405	0.504	0.604	0.704	0.803
12	0.007	0.103	0.202	0.305	0.404	0.503	0.605	0.704	0.803

13	0.006	0.103	0.202	0.304	0.404	0.503	0.604	0.704	0.804
14	0.006	0.103	0.202	0.304	0.404	0.504	0.604	0.704	0.803
15	0.007	0.103	0.202	0.305	0.405	0.503	0.605	0.704	0.804
16	0.007	0.103	0.202	0.305	0.403	0.504	0.605	0.704	0.804
17	0.005	0.102	0.202	0.305	0.405	0.504	0.605	0.704	0.803
18	0.007	0.103	0.202	0.304	0.404	0.504	0.604	0.704	0.804
19	0.006	0.103	0.202	0.305	0.404	0.503	0.605	0.703	0.804
20	0.007	0.103	0.203	0.305	0.405	0.503	0.605	0.704	0.803
21	0.006	0.103	0.204	0.304	0.404	0.503	0.605	0.703	0.804
22	0.006	0.103	0.202	0.304	0.405	0.505	0.605	0.704	0.803
23	0.006	0.103	0.202	0.305	0.404	0.504	0.604	0.704	0.804
24	0.007	0.103	0.202	0.305	0.404	0.504	0.605	0.704	0.804
Max	0.008	0.104	0.204	0.305	0.405	0.505	0.606	0.705	0.805
Min	0.005	0.102	0.202	0.304	0.403	0.503	0.604	0.703	0.803
Avg	0.007	0.103	0.202	0.305	0.404	0.504	0.605	0.704	0.804
Diff	0.003	0.002	0.002	0.001	0.002	0.002	0.002	0.002	0.002
Channel	Voltage in V								
	0.900	1.000	1.100	1.200	1.300	1.400	1.500	1.600	1.700
1	0.904	1.002	1.105	1.204	1.300	1.402	1.502	1.602	1.701
2	0.905	1.002	1.105	1.204	1.300	1.402	1.502	1.601	1.701
3	0.904	1.002	1.106	1.204	1.301	1.401	1.502	1.601	1.702
4	0.904	1.002	1.105	1.204	1.300	1.401	1.502	1.603	1.701
5	0.904	1.002	1.106	1.204	1.300	1.402	1.502	1.601	1.702
6	0.904	1.003	1.105	1.204	1.301	1.402	1.502	1.602	1.702
7	0.904	1.002	1.105	1.204	1.300	1.402	1.502	1.602	1.702

8	0.904	1.002	1.106	1.204	1.300	1.401	1.503	1.601	1.702
9	0.904	1.002	1.105	1.203	1.300	1.401	1.502	1.602	1.701
10	0.904	1.002	1.105	1.205	1.300	1.401	1.502	1.602	1.702
11	0.904	1.002	1.106	1.204	1.301	1.402	1.502	1.603	1.702
12	0.904	1.002	1.105	1.205	1.301	1.401	1.502	1.602	1.702
13	0.903	1.002	1.106	1.204	1.300	1.402	1.502	1.602	1.701
14	0.903	1.002	1.105	1.204	1.301	1.401	1.503	1.602	1.702
15	0.904	1.002	1.106	1.204	1.301	1.402	1.502	1.602	1.701
16	0.904	1.002	1.105	1.204	1.300	1.401	1.503	1.602	1.702
17	0.904	1.002	1.105	1.203	1.300	1.402	1.502	1.601	1.702
18	0.904	1.002	1.105	1.204	1.300	1.401	1.502	1.601	1.702
19	0.904	1.002	1.106	1.204	1.300	1.402	1.502	1.602	1.702
20	0.904	1.002	1.106	1.204	1.300	1.402	1.502	1.602	1.702
21	0.903	1.002	1.105	1.205	1.300	1.401	1.502	1.602	1.701
22	0.904	1.002	1.106	1.204	1.300	1.402	1.503	1.601	1.702
23	0.904	1.002	1.106	1.204	1.300	1.401	1.502	1.602	1.701
24	0.904	1.002	1.106	1.205	1.300	1.402	1.502	1.602	1.702
Max	0.905	1.003	1.106	1.205	1.301	1.402	1.503	1.603	1.702
Min	0.903	1.002	1.105	1.203	1.300	1.401	1.502	1.601	1.701
Avg	0.904	1.002	1.105	1.204	1.300	1.402	1.502	1.602	1.702
Diff	0.002	0.001	0.001	0.002	0.001	0.001	0.001	0.002	0.001
Channel	Voltage in V								
	1.800	1.900	2.000	2.100	2.200	2.300	2.400	2.500	2.600
1	1.803	1.904	2.003	2.105	2.205	2.291	2.396	2.514	2.614
2	1.803	1.905	2.003	2.105	2.205	2.291	2.396	2.515	2.613

3	1.803	1.905	2.003	2.105	2.205	2.292	2.397	2.515	2.613
4	1.802	1.905	2.002	2.105	2.205	2.291	2.397	2.514	2.612
5	1.803	1.905	2.003	2.104	2.205	2.291	2.398	2.514	2.613
6	1.803	1.905	2.003	2.105	2.206	2.291	2.397	2.514	2.613
7	1.803	1.904	2.003	2.104	2.206	2.291	2.397	2.514	2.613
8	1.803	1.905	2.003	2.105	2.206	2.291	2.397	2.514	2.613
9	1.803	1.905	2.003	2.104	2.206	2.291	2.396	2.515	2.613
10	1.803	1.904	2.002	2.105	2.206	2.291	2.397	2.514	2.613
11	1.803	1.904	2.003	2.105	2.205	2.291	2.397	2.515	2.614
12	1.803	1.905	2.003	2.104	2.205	2.292	2.397	2.514	2.613
13	1.803	1.905	2.003	2.104	2.206	2.291	2.396	2.515	2.612
14	1.803	1.904	2.003	2.106	2.206	2.291	2.397	2.514	2.613
15	1.802	1.905	2.003	2.104	2.206	2.292	2.397	2.515	2.613
16	1.802	1.905	2.002	2.106	2.206	2.291	2.396	2.514	2.613
17	1.802	1.905	2.002	2.105	2.206	2.291	2.396	2.515	2.613
18	1.802	1.905	2.002	2.106	2.206	2.291	2.397	2.515	2.613
19	1.803	1.906	2.003	2.105	2.205	2.292	2.398	2.515	2.614
20	1.803	1.904	2.003	2.104	2.206	2.290	2.398	2.514	2.612
21	1.803	1.904	2.003	2.104	2.205	2.290	2.397	2.514	2.614
22	1.804	1.905	2.003	2.105	2.206	2.291	2.396	2.515	2.612
23	1.803	1.905	2.003	2.105	2.205	2.292	2.396	2.515	2.613
24	1.803	1.905	2.002	2.104	2.206	2.291	2.397	2.515	2.613
Max	1.804	1.906	2.003	2.106	2.206	2.292	2.398	2.515	2.614
Min	1.802	1.904	2.002	2.104	2.205	2.290	2.396	2.514	2.612
Avg	1.803	1.905	2.003	2.105	2.206	2.291	2.397	2.515	2.613
Diff	0.002	0.002	0.001	0.002	0.001	0.002	0.002	0.001	0.002

Channel	Voltage in V								
	2.700	2.800	2.900	3.000	3.100	3.200	3.300	3.400	3.500
1	2.703	2.803	2.903	3.004	3.106	3.205	3.304	3.404	3.505
2	2.703	2.802	2.903	3.003	3.105	3.206	3.304	3.404	3.505
3	2.703	2.804	2.904	3.004	3.105	3.205	3.304	3.403	3.505
4	2.703	2.803	2.904	3.004	3.105	3.205	3.303	3.404	3.505
5	2.704	2.803	2.904	3.003	3.104	3.206	3.304	3.404	3.505
6	2.704	2.804	2.904	3.005	3.104	3.206	3.304	3.404	3.504
7	2.703	2.803	2.903	3.004	3.105	3.206	3.304	3.404	3.504
8	2.703	2.803	2.904	3.005	3.105	3.206	3.304	3.403	3.505
9	2.703	2.803	2.904	3.004	3.105	3.206	3.303	3.404	3.505
10	2.704	2.803	2.903	3.004	3.105	3.206	3.304	3.404	3.506
11	2.703	2.802	2.903	3.004	3.105	3.205	3.304	3.402	3.505
12	2.704	2.803	2.904	3.004	3.105	3.206	3.304	3.403	3.504
13	2.703	2.803	2.903	3.004	3.104	3.205	3.304	3.403	3.506
14	2.704	2.803	2.904	3.005	3.106	3.206	3.303	3.405	3.505
15	2.703	2.803	2.904	3.004	3.104	3.207	3.302	3.403	3.506
16	2.704	2.803	2.903	3.005	3.104	3.206	3.304	3.405	3.505
17	2.704	2.803	2.902	3.005	3.104	3.206	3.305	3.404	3.505
18	2.703	2.802	2.905	3.004	3.105	3.206	3.304	3.403	3.505
19	2.703	2.802	2.903	3.005	3.105	3.206	3.303	3.403	3.505
20	2.704	2.803	2.904	3.005	3.104	3.205	3.304	3.404	3.504
21	2.703	2.804	2.904	3.004	3.106	3.206	3.304	3.405	3.505
22	2.702	2.803	2.904	3.005	3.105	3.207	3.304	3.404	3.505
23	2.703	2.802	2.903	3.005	3.103	3.206	3.304	3.404	3.504

	2.704	2.804	2.904	3.004	3.105	3.206	3.305	3.404	3.505
24	2.704	2.804	2.904	3.004	3.105	3.206	3.305	3.404	3.505
Max	2.704	2.804	2.905	3.005	3.106	3.207	3.305	3.405	3.506
Min	2.702	2.802	2.902	3.003	3.103	3.205	3.302	3.402	3.504
Avg	2.703	2.803	2.904	3.004	3.105	3.206	3.304	3.404	3.505
Diff	0.002	0.002	0.003	0.002	0.003	0.002	0.003	0.003	0.002
Channel	Voltage in V								
	3.600	3.700	3.800	3.900	4.000	4.100	4.200	4.300	4.400
1	3.605	3.703	3.796	3.898	3.997	4.101	4.199	4.304	4.403
2	3.605	3.703	3.797	3.898	3.997	4.101	4.199	4.304	4.403
3	3.604	3.703	3.797	3.898	3.998	4.101	4.199	4.304	4.403
4	3.604	3.704	3.797	3.898	3.997	4.102	4.201	4.303	4.401
5	3.605	3.704	3.798	3.898	3.998	4.103	4.200	4.304	4.402
6	3.604	3.701	3.797	3.899	3.998	4.101	4.200	4.303	4.402
7	3.604	3.702	3.797	3.899	3.997	4.100	4.200	4.304	4.402
8	3.606	3.703	3.797	3.898	3.997	4.101	4.199	4.304	4.402
9	3.606	3.703	3.797	3.899	3.997	4.101	4.200	4.304	4.403
10	3.606	3.702	3.797	3.899	3.996	4.100	4.200	4.302	4.404
11	3.604	3.703	3.797	3.898	3.997	4.100	4.200	4.304	4.401
12	3.605	3.702	3.798	3.898	3.998	4.102	4.201	4.303	4.402
13	3.605	3.702	3.798	3.898	3.997	4.102	4.199	4.303	4.402
14	3.606	3.702	3.797	3.899	3.996	4.102	4.201	4.304	4.402
15	3.603	3.703	3.796	3.898	3.997	4.100	4.200	4.304	4.401
16	3.605	3.703	3.797	3.899	3.996	4.100	4.199	4.304	4.402
17	3.606	3.702	3.797	3.899	3.997	4.101	4.199	4.303	4.403
18	3.606	3.703	3.797	3.900	3.997	4.101	4.199	4.304	4.403

19	3.605	3.704	3.797	3.899	3.997	4.100	4.199	4.304	4.402
20	3.605	3.702	3.798	3.898	3.997	4.101	4.200	4.303	4.401
21	3.605	3.702	3.797	3.899	3.996	4.100	4.199	4.303	4.401
22	3.605	3.702	3.797	3.898	3.998	4.101	4.200	4.304	4.401
23	3.606	3.703	3.797	3.900	3.996	4.101	4.200	4.303	4.403
24	3.605	3.703	3.798	3.899	3.997	4.102	4.199	4.303	4.404
Max	3.606	3.704	3.798	3.900	3.998	4.103	4.201	4.304	4.404
Min	3.603	3.701	3.796	3.898	3.996	4.100	4.199	4.302	4.401
Avg	3.605	3.703	3.797	3.899	3.997	4.101	4.200	4.304	4.402
Diff	0.003	0.003	0.002	0.002	0.002	0.003	0.002	0.002	0.003
Channel	Voltage in V								
	4.500	4.600	4.700	4.800	4.900	5.000			
1	4.505	4.605	4.693	4.793	4.892	4.99			
2	4.507	4.606	4.693	4.793	4.890	4.993			
3	4.506	4.605	4.693	4.791	4.891	4.992			
4	4.505	4.606	4.694	4.792	4.892	4.991			
5	4.506	4.605	4.693	4.792	4.891	4.991			
6	4.505	4.604	4.693	4.793	4.891	4.993			
7	4.506	4.605	4.693	4.792	4.892	4.991			
8	4.505	4.606	4.693	4.793	4.892	4.990			
9	4.506	4.605	4.693	4.794	4.891	4.992			
10	4.505	4.605	4.693	4.793	4.891	4.993			
11	4.506	4.607	4.694	4.792	4.890	4.992			
12	4.504	4.605	4.693	4.793	4.892	4.992			
13	4.504	4.605	4.693	4.791	4.891	4.992			

14	4.505	4.604	4.693	4.794	4.893	4.991
15	4.506	4.605	4.693	4.792	4.891	4.992
16	4.506	4.605	4.694	4.793	4.891	4.991
17	4.507	4.605	4.694	4.794	4.891	4.993
18	4.506	4.604	4.694	4.792	4.890	4.991
19	4.505	4.606	4.692	4.791	4.890	4.993
20	4.506	4.606	4.692	4.792	4.891	4.993
21	4.504	4.605	4.694	4.791	4.891	4.990
22	4.505	4.604	4.692	4.793	4.893	4.991
23	4.504	4.604	4.693	4.793	4.892	4.991
24	4.507	4.605	4.693	4.792	4.890	4.991
Max	4.507	4.607	4.694	4.794	4.893	4.993
Min	4.504	4.604	4.692	4.791	4.890	4.990
Avg	4.505	4.605	4.693	4.792	4.891	4.992
Diff	0.003	0.003	0.002	0.003	0.003	0.003

Table D.1: Hall Effect Sensor Data for Group Calibration

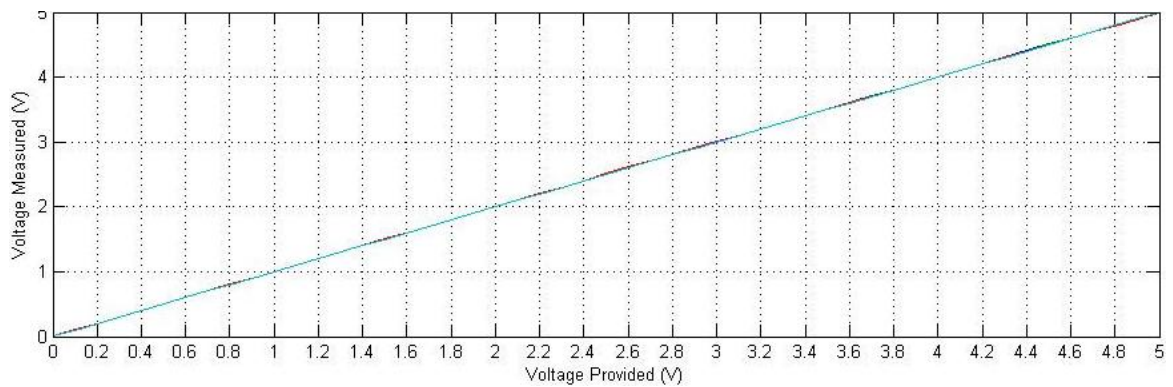


Figure D.1: Plot of 24 ADC channels provided voltage against voltage measured after group calibration test

Appendix E

Simulink models for data capture

The Simulink models described in this appendix are from testing performed with TR2 and TR3.

Figure E.1 shows the data capture model for TR2, which logged to a CSV file 'multi.mat'. This data recording was triggered by pressing the 'space bar' on the computers keyboard. Simulink model to record data with TR2 and TR3

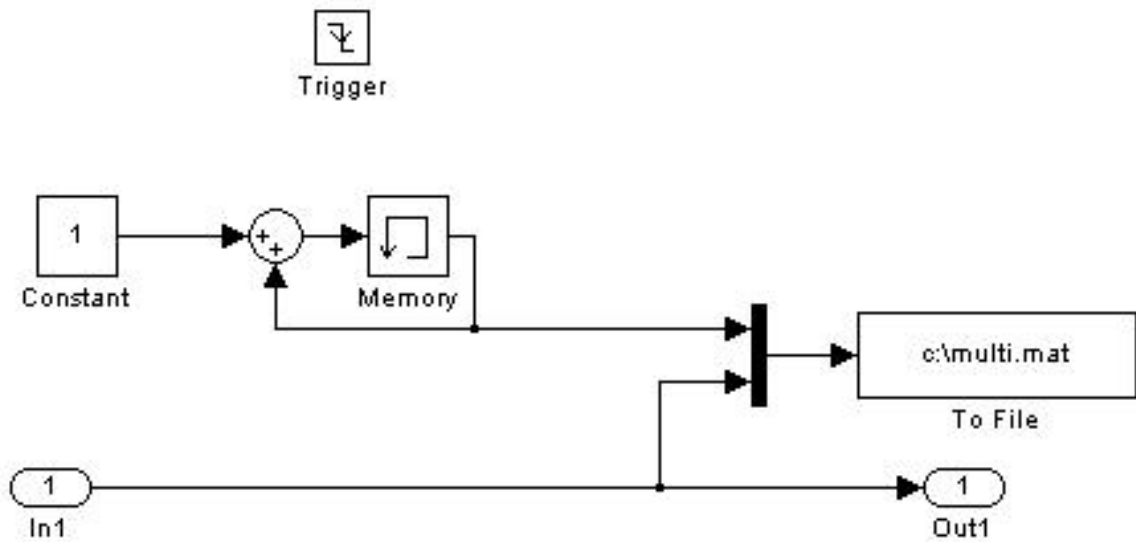


Figure E.1: TR2 Data logging Simulink model

Figure E.2 shows the data capture model for TR3, which logged to a CSV file

'8Sensors.mat'. This data recording was triggered by the hand held microswitch through the trigger block. This model had the addition of a scope to visualize data as it was recorded to insure that the recording step had been performed. Simulink model to record data with TR2 and TR3

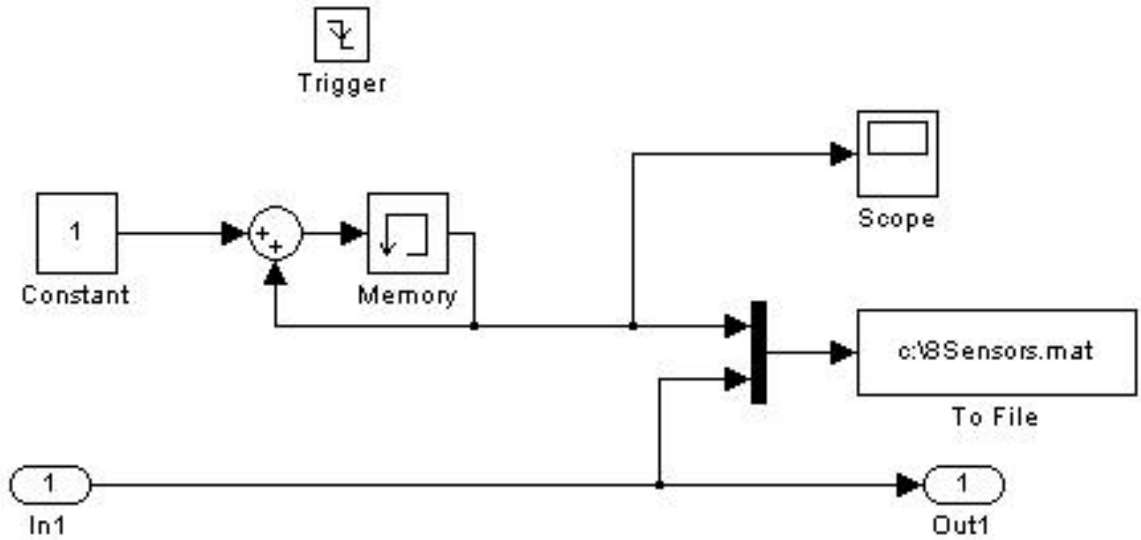


Figure E.2: TR3 Data logging Simulink model

Figure E.3 shows the analog input handling Simulink model for TR3. This enabled the sensor offsets to be set at time of data recording to avoid having to do this in code to the data during processing. This model also shows the digital input used to trigger the data capture. The scope block gave a raw display of the data as it was recorded.

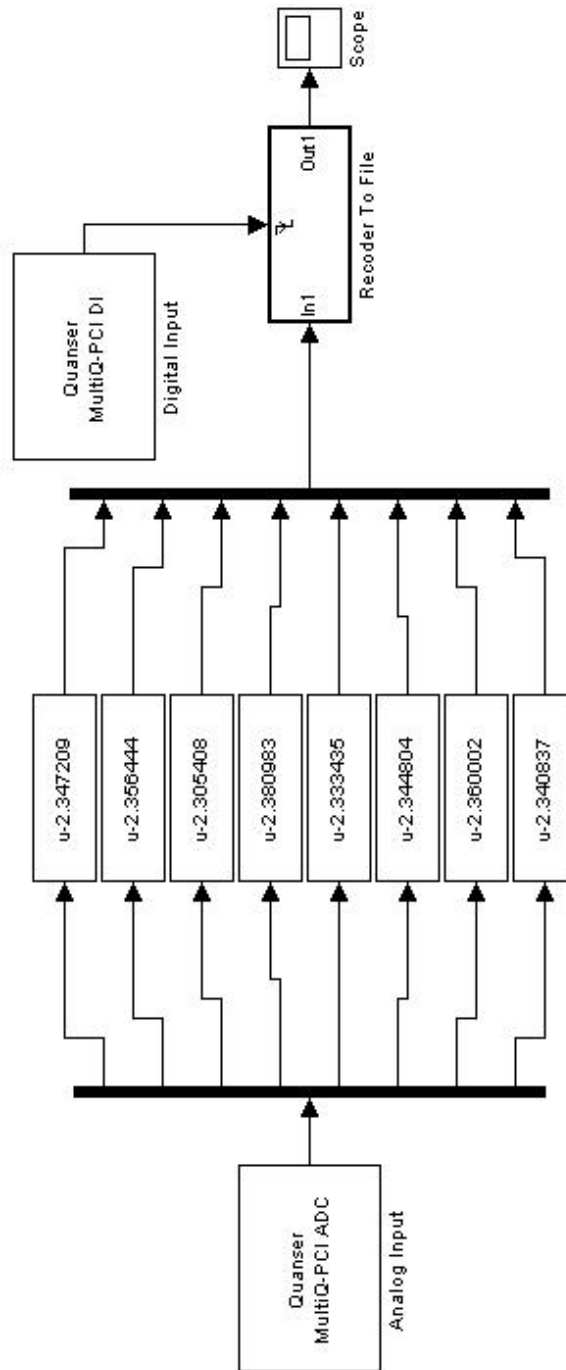


Figure E.3: TR3 analog input handling Simulink model

Appendix F

Test Rig 4 SolidWorks models for manufacture

These models were created in SolidWorks and manufactured to create TR4. The models are listed in this order:

Static Holder The static magnet holder has two small mounting holes, so that its position relative to the sensor origin can be changed depending on the experiment performed. The holder also has a larger mounting hole to add structural strength to TR4 when it is assembled.

Dynamic Holder The dynamic magnet holder, referred to in the thesis as the free magnet holder, has a single locating hole to align the magnet holder inside the guide tube. The holder has a polished surface to reduce the friction between it and the guide tube with an outside diameter just smaller than the inside diameter of the guide tube to run freely.

Guide Tube The guide tube is manufactured from extruded acrylic plastic and has the sensor mounting points milled into the tube's surface. The guide tube also has

multiple mounting points to work with the static and dynamic magnet holders and has a $3mm$ wall thickness for strength. This image shows the mounting points for the x-axis sensors and the first group of y-axis sensors.

Guide Tube 16.5 Deg The guide tube requires a second set of y-axis sensors to be mounted with a rotation of 16.5 degrees from the first set of sensors about the central tube axis. This drawing shows the definition of the sensor mounting profile.

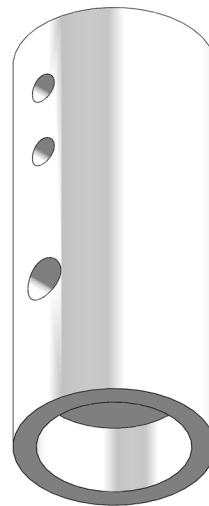
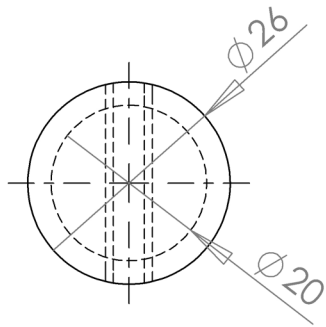
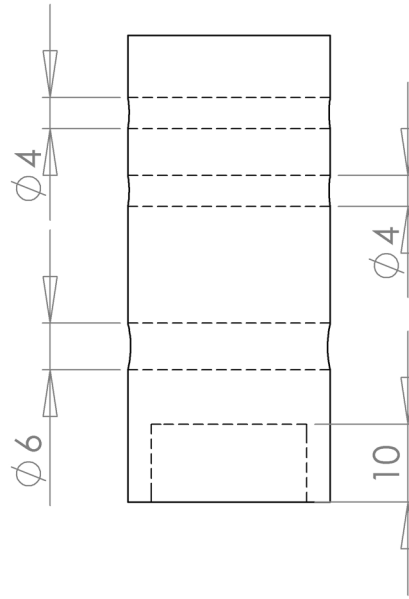
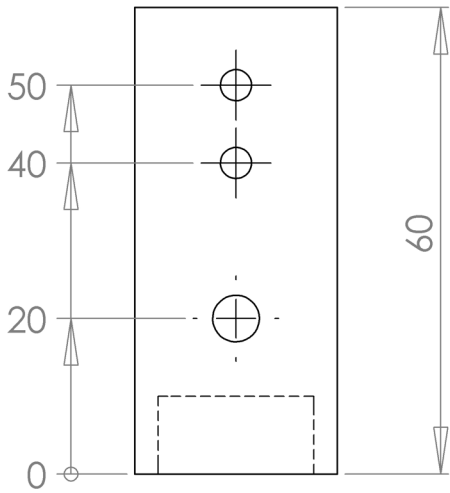
Tool End Cap Two of these parts were used to make up the cutting jig to clamp the guide tube in the CNC milling machine. The central hole had studding passed through to clamp the two ends together using nuts, with four mounting holes used to locate the guide tube at 90 degree intervals.

Tool Holder These plates were designed to hold the end caps in place during manufacture of the guide tube. The mounting holes allowed for the 16.5 degree rotation for the sensors as well as the 90 degree rotation when cutting the mounting holes.

Final Assembly Top Top down view of the TR4 final assembly showing the x-axis and first y-axis sensors positioned above the central axis of the device. The second set of y-axis sensors are located in their mounting points with the 16.5 degrees rotation about the central axis.

Final Assembly Side Side view of the TR4 final assembly showing the sensors mounted with their electrical contacts positioned ready for mounting onto the TR4 data logging hardware. The static magnet holder is positioned at the sensor origin, with the dynamic holder positioned at its mechanical limit.

Final Assembly Isometric Isometric view of the TR4 final assembly, showing the magnet (in blue) located within the fixed magnet holder. This view gives an idea of scale with respect to the separation between the magnet and the sensors array.



UNLESS OTHERWISE SPECIFIED:
 DIMENSIONS ARE IN MILLIMETERS
 SURFACE FINISH:
 TOLERANCES:
 LINEAR:
 ANGULAR:

FINISH:

DEBUR AND
 BREAK SHARP
 EDGES

DO NOT SCALE DRAWING

REVISION

	NAME	SIGNATURE	DATE		
DRAWN					
CHK'D					
APP'VD					
MFG					
Q.A					

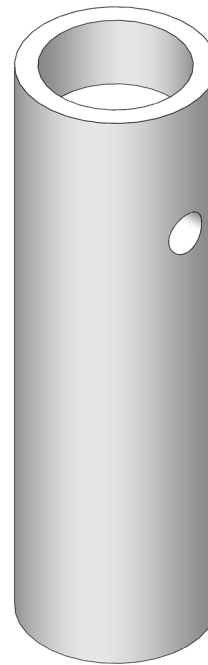
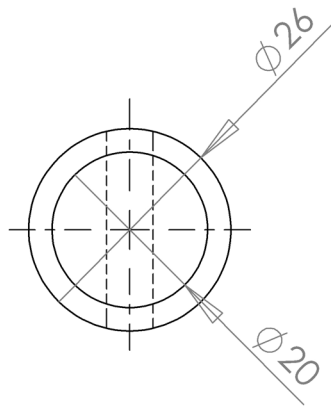
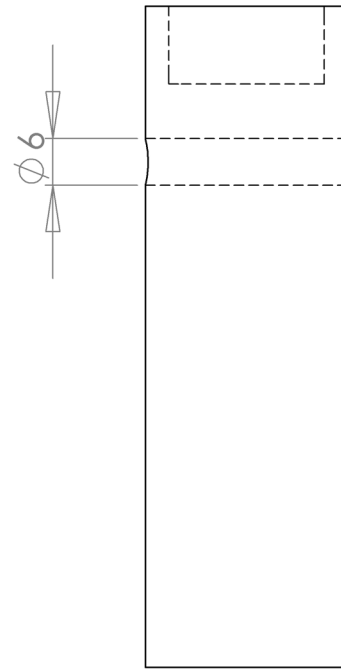
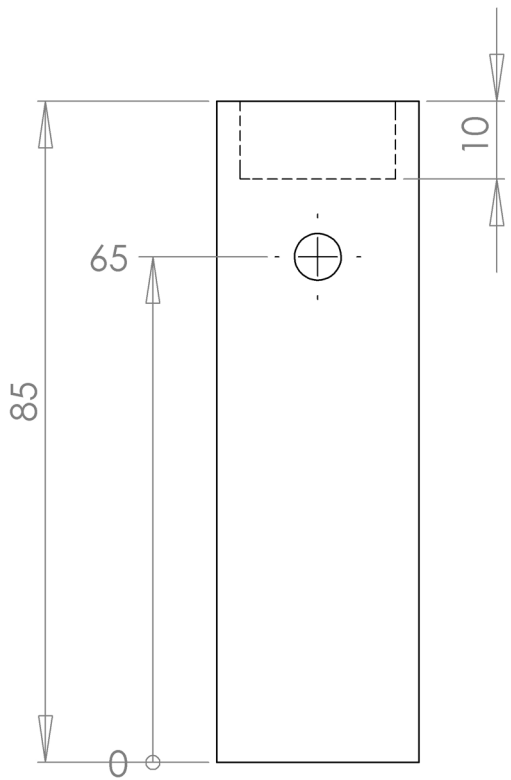
TITLE:	
DWG NO.	Static Holder
	A4

MATERIAL:

DWG NO.

Static Holder

A4



UNLESS OTHERWISE SPECIFIED:
 DIMENSIONS ARE IN MILLIMETERS
 SURFACE FINISH:
 TOLERANCES:
 LINEAR:
 ANGULAR:

FINISH:

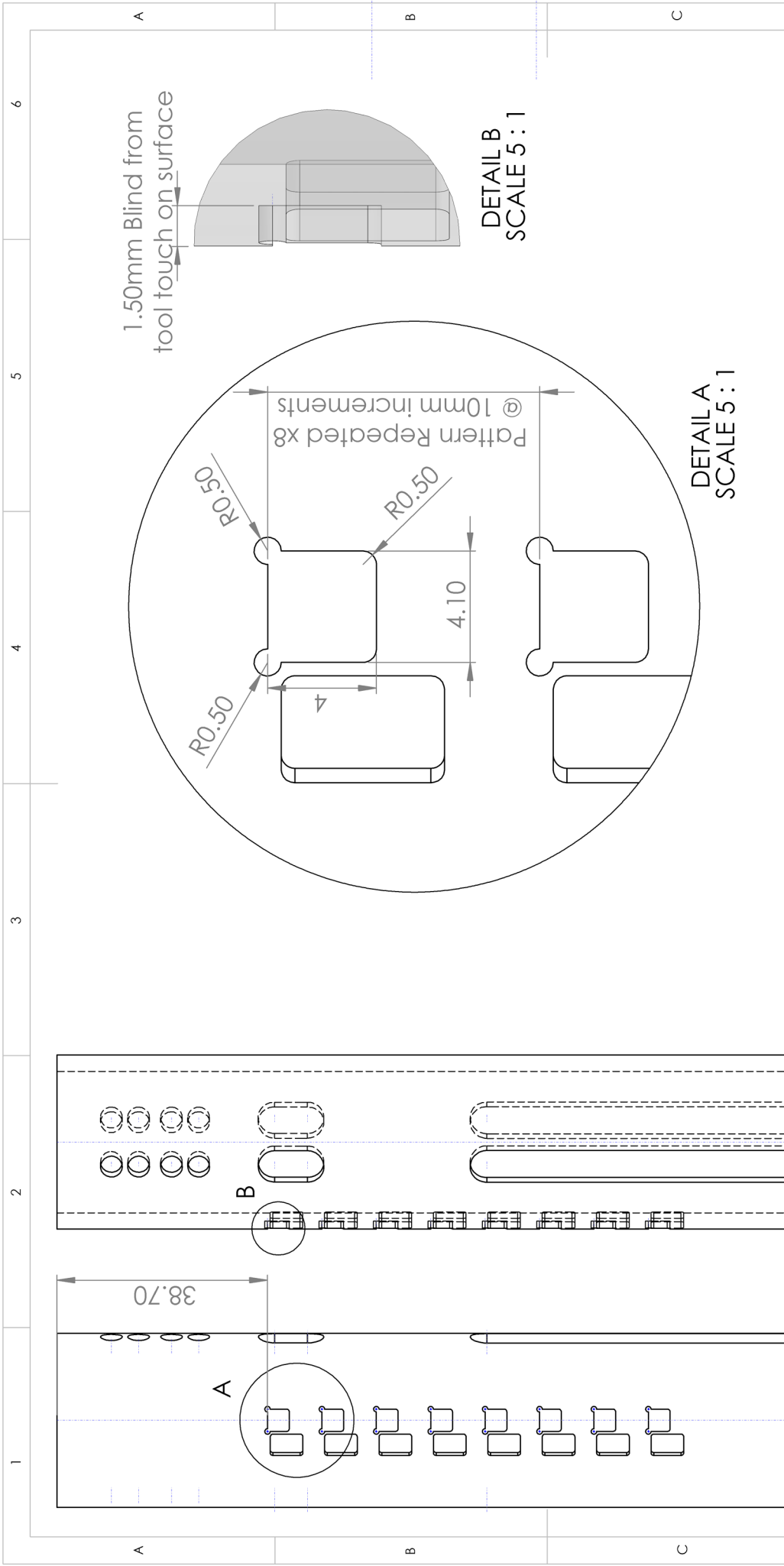
DEBUR AND
 BREAK SHARP
 EDGES

DO NOT SCALE DRAWING

REVISION

	NAME	SIGNATURE	DATE		
DRAWN					
CHK'D					
APP'V'D					
MFG					
Q.A					
				MATERIAL:	

TITLE:	
DWG NO.	Dynamic Holder
	A4



UNLESS OTHERWISE SPECIFIED: DIMENSIONS ARE IN MILLIMETERS		FINISH:		DEBUR AND BREAK SHARP EDGES		DO NOT SCALE DRAWING		REVISION	
SURFACE FINISH:		TOLERANCES:		NAME		SIGNATURE		DATE	
LINEAR:		ANGULAR:		DRAWN		CHK'D		APP'VD	
				MFG		Q.A		MATERIAL:	
				TITLE:					
				WEIGHT:		SCALE:1:2		SHEET 1 OF 1	

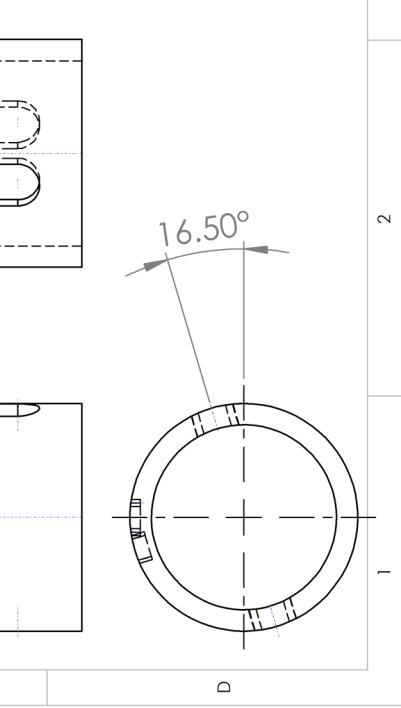
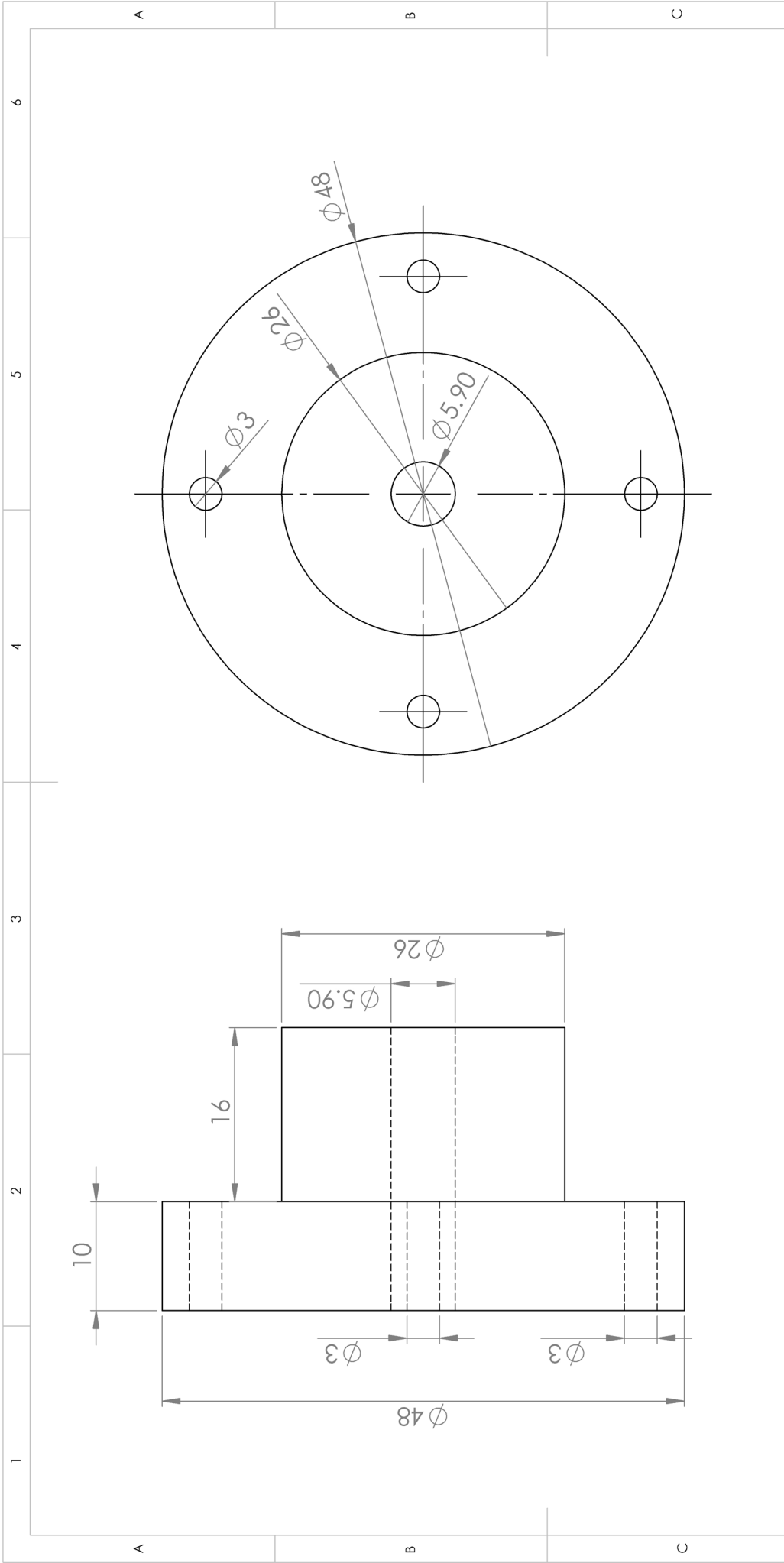
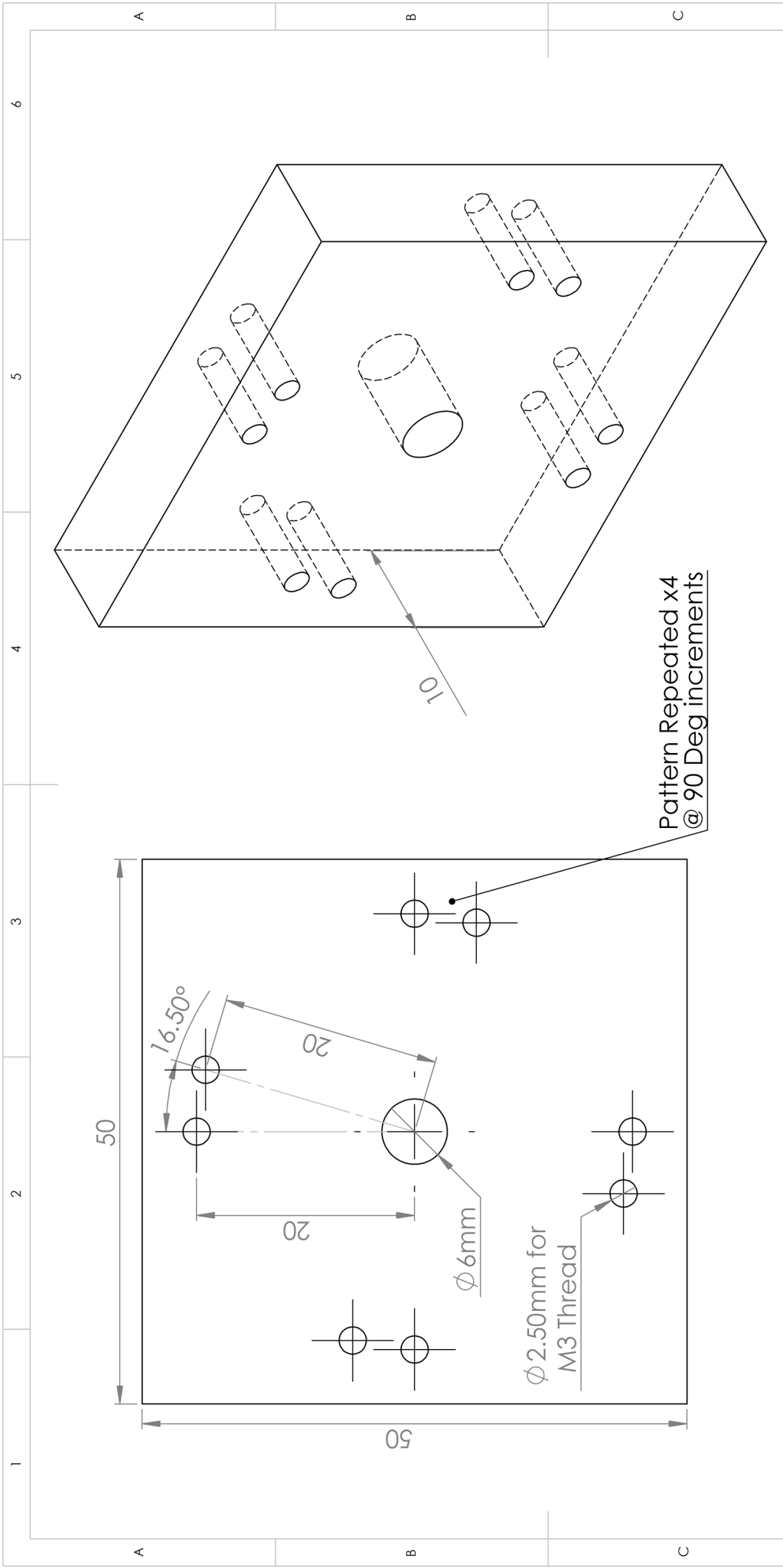


FIG. NO. **Guide Tube 16.5 Deg**

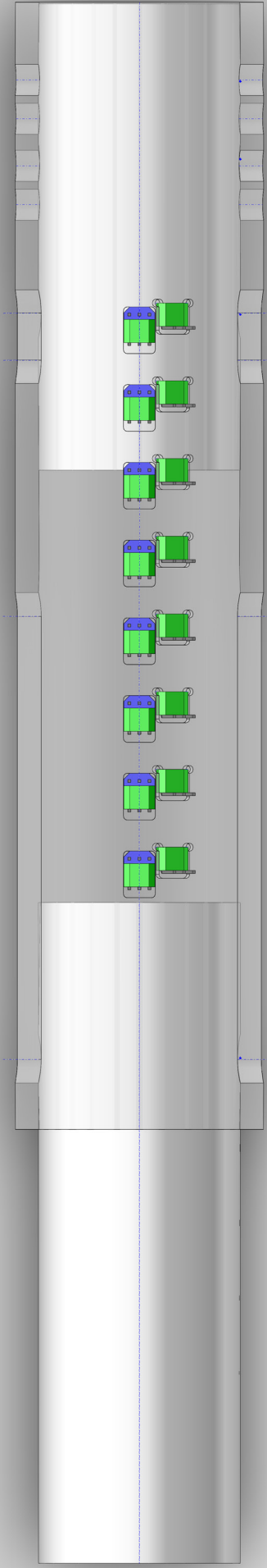


UNLESS OTHERWISE SPECIFIED: DIMENSIONS ARE IN MILLIMETERS		FINISH:		DEBUR AND BREAK SHARP EDGES		DO NOT SCALE DRAWING		REVISION	
SURFACE FINISH:									
TOLERANCES:		LINEAR:							
		ANGULAR:							
NAME	SIGNATURE	DATE	TITLE:						
DRAWN									
CHK'D									
APP'VD									
MFG									
Q.A									
			MATERIAL:		DWC No. Tool End Cap x2 A4				
			WEIGHT:		SCALE: 1:1 SHEET 1 OF 1				

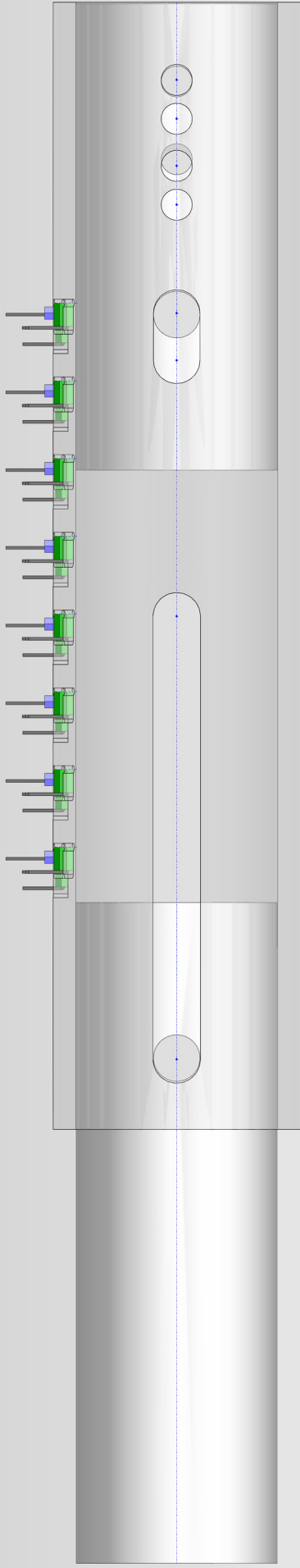


UNLESS OTHERWISE SPECIFIED: DIMENSIONS ARE IN MILLIMETERS		FINISH:		DEBUR AND BREAK SHARP EDGES		DO NOT SCALE DRAWING		REVISION	
SURFACE FINISH:									
TOLERANCES:									
LINEAR:									
ANGULAR:									
NAME		SIGNATURE		DATE		TITLE:		DWC NO.	
DRAWN								A4	
CHK'D								Tool Holder x2	
APP'VD								SCALE:1:1	
MFG								SHEET 1 OF 1	
Q.A								WEIGHT:	
								MATERIAL:	

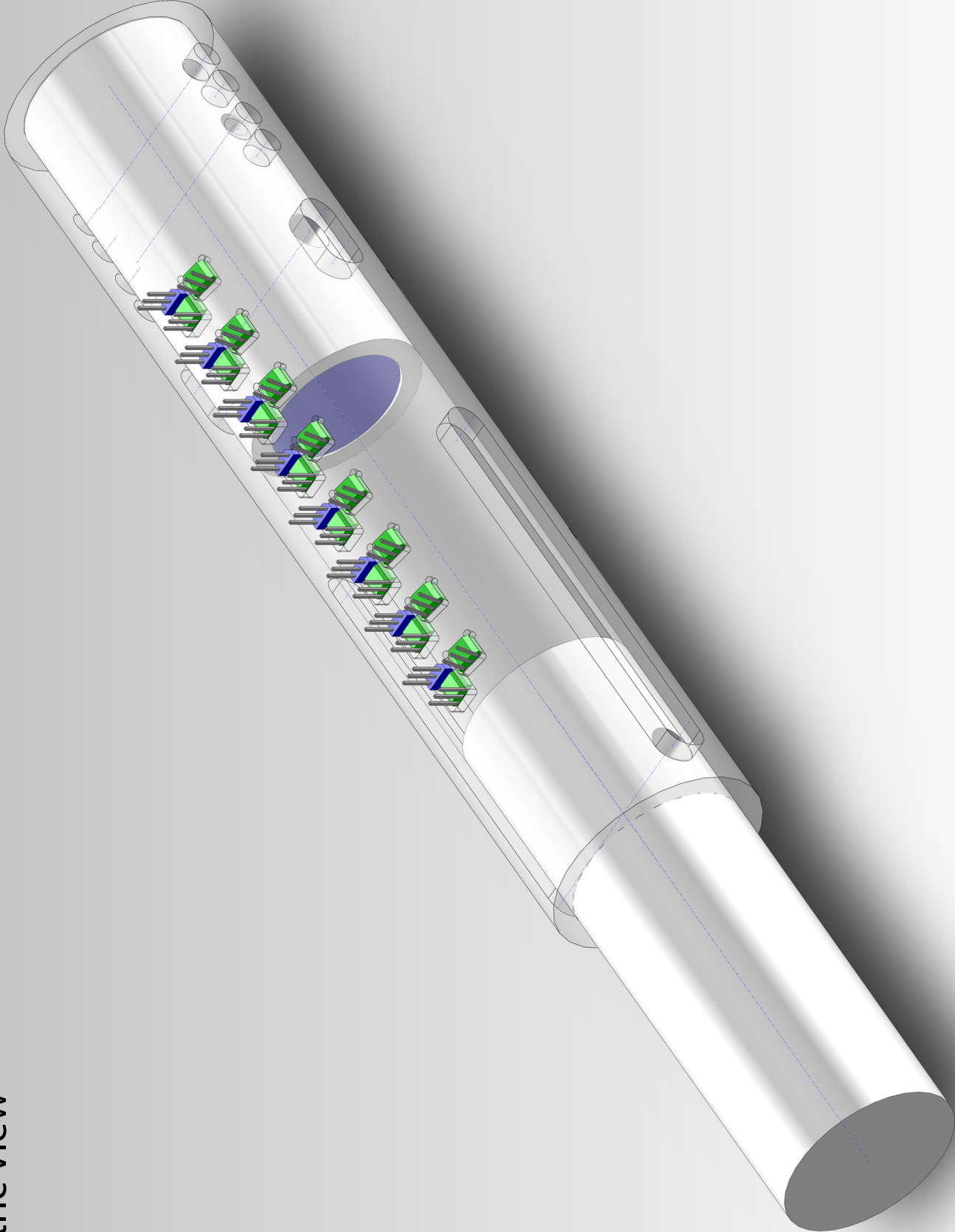
Final TR4 Assembly
Top View



Final TR4 Assembly
Side View



Final TR4 Assembly
Isometric View

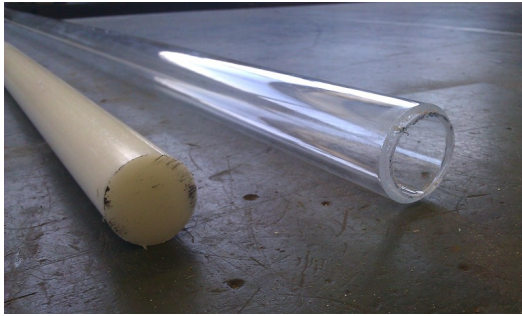


Appendix G

Work log for the manufacture of Test Rig 4

The test rigs (TR2 and TR3) used the same manufacturing techniques as TR4, but TR4 used additional processes such as the cutting profiles for the sensor placement, so this appendix can be considered as the full description of processes used in the manufacture of all testing rigs. Test rig 4 is essentially a copy of test rig 3, but used an integrated electronics package, with Bluetooth communications, instead of the massively long and complicated wire link to the computer. This work log was taken from my personal website, which is used to keep account of work progress, that describes the manufacturing process for TR4 including the tools used and the steps required to insure optimal results.

I started today with the same acrylic tubing and Delrin rod that I have used for test rig's 1-3. First I cut the acrylic tube to roughly 150mm being careful not to chip the ends (this makes for a better finish). Once cut, the acrylic tube will need to be machined down to the correct length. I used a Colchester 600 Center lathe to machine



(a) Delrin rod and acrylic tube



(b) Material cut to roughly the right length

Figure G.1: Raw material used for the construction of Test Rig 4

the parts for all my test rigs.



(a) Colchester 600 Center lathe

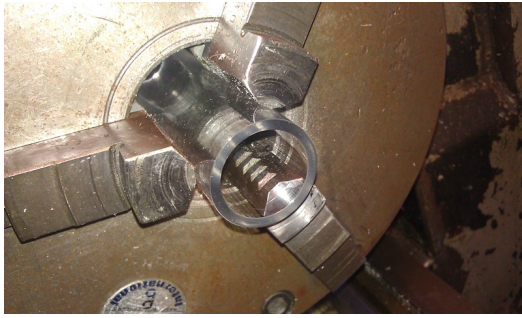


(b) Facing off the acrylic tube

Figure G.2: The lathe used for manufacture with acrylic being turned

The 3 tooth jaw grips securely without crushing the parts, and 770 rpm cuts beautifully with an aluminium grade (designed to cut aluminium) cutting tip. After the end had been faced off, it was time to de-bur and polish the tube ends. This serves 3 purposes; it makes the tube look better, it strengthens the tube (no areas for cracks to form) and it makes the Delrin rod run smoothly over the edges so that it doesn't jam.

Now that the acrylic rod is polished at one end, it is measured and marked off at 145mm (the required final length) and the cutting and polishing process is repeated on the unfinished end. Once this is done, the part is tested for compliance to specs using a precision measuring device called a digital caliper. This makes sure that the part is



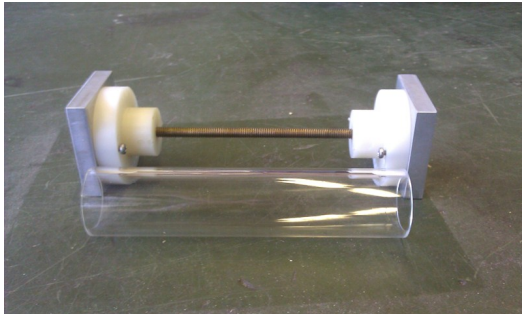
(a) Acrylic tube end after polishing



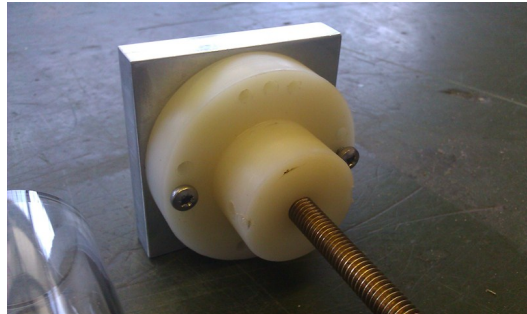
(b) Acrylic tube after polishing

Figure G.3: Acrylic tube after preparation with lathe

accurate before the next process step. To move onto the next processing step, which uses a 3 axis CNC, the tube needs to be mounted in a jig so that it can be positioned on the CNC's cutting area. This jig has been designed to support the tube and to stop it from twisting whilst it is machined.



(a) Side view of the sensor profile cutting jig and the polished guide tube

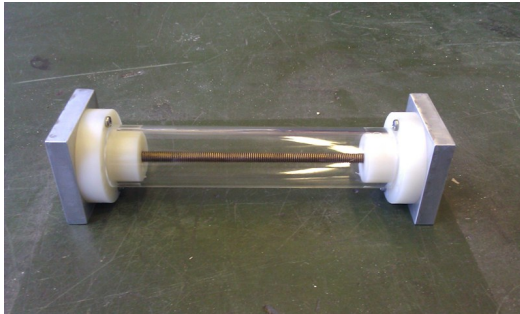


(b) Cutting jig end cap to center the acrylic tube with screws for the rotation positioning

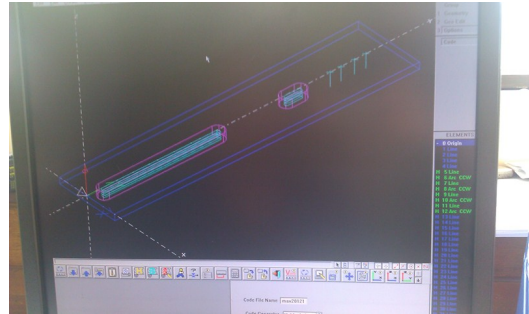
Figure G.4: The cutting jig to hold the guide tube in the CNC milling machine during cutting

The jig centers the tube within a 50x50mm square (nice round numbers helps reduce errors when calibrating the CNC) and has additional tapped holes so that the part can be rotated at a set angle, for when the sensor mounting points are machined. The cutting jig has a piece of brass studding passed from one end to the other, so that when two nuts at either end are tightened, it sandwiches the two end caps together

and holds the guide tube in place.



(a) The cutting jig with the acrylic tube mounted



(b) SmartCAM Interface with program 1 displayed

Figure G.5: Guide tube in cutting jig ready for the first profile to be machined

The next step is to take the 3D design of my tube, and export it from SolidWorks into SmartCAM, a piece of software that performs CNC tool path generation. This software calculates the path and program that the CNC machine will use to create the desired cuts in the acrylic tube. This design is quite complicated, so the CNC machine needs 3 different programs to complete all the desired work:

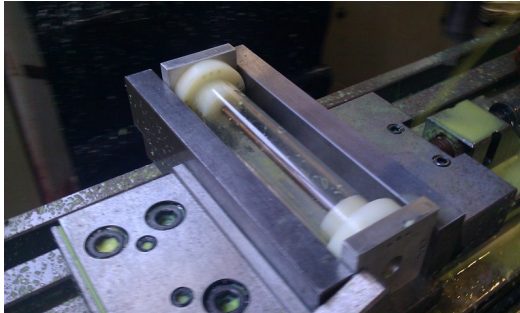
Program 1: Tool paths for milling the four 4mm mounting holes and the 6mm wide mounting slot in the static holder end of the tube, as well as the 6mm wide guide slot for the dynamic holder, so that it can move up and down whilst having its rotation constrained.

Program 2: Tool paths used to mount the dual sensor array. The dual sensor array mounting holes are blind (not cut all the way through the tube) so that the sensors are near but not interfering with the moving parts of the test rig.

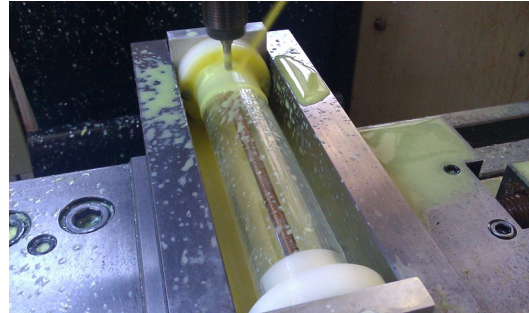
Program 3: Tool paths used to mount the remaining sensors. These sensors are mounted in much the same way as in program 2, but the tube will need to be rotated 15.5 degrees so that the mountings do not interfere with the other sensors.

With the CNC programs created it is then time to position the cutting jig onto the CNC machine, clamp it in place and using a wobbler (a ball bearing on the end of a

ground rod) set the datum points for the machine. Once the datum points were set and verified, the first program was set running.



(a) The cutting jig positioned and clamped on the CNC machine



(b) Program 1 running with coolant to stop the plastic from melting

Figure G.6: Cutting the first profile into the guide tube

You can see in the picture that the program was run a second time after the cutting jig had been rotated through 180 degrees. This created symmetrical cuts on either side of the tube, so that the free magnet could not twist during testing. The symmetrical cuts also meant that the mounting holes lined up, allowing for simple fixing of components.



(a) Cutting rig after second run of program 1

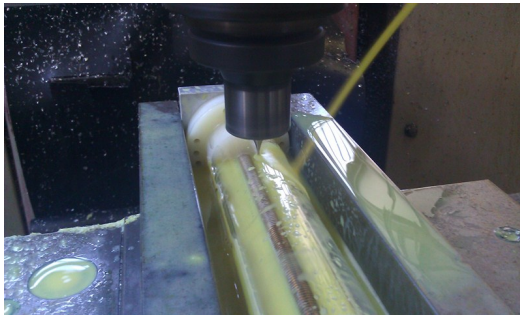


(b) Close up of the static end 4mm mounting holes and slot

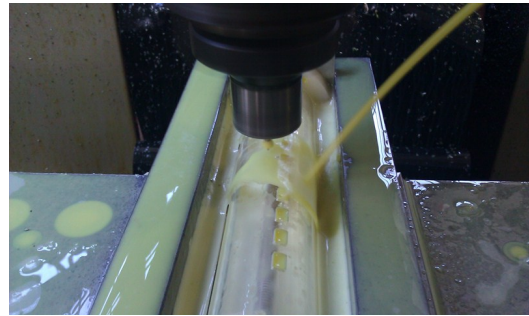
Figure G.7: The guide tube after the first program had been completed

The tube was then put back into the CNC machine but this time set at a 90 degree angle to machine program 2. The result of program 2 is a visible 2mm deep blind cut of the dual sensor mounting profile. This profile will allow the sensors to sit very close to the Delrin runner that will be inside the tube (holding a magnet), without

interfering with the Delrin runner in any way. The profile aids in the sensor placement as the sensors can be pushed (under a microscope) until they are perfectly flush with the profile, which will create a near perfect sensor alignment, which is important when it comes to calibration and taking readings.



(a) 1mm diameter three flute cutter controlled by program 2



(b) Program 3 running after the acrylic tube was rotated 15.5 degrees in the cutting jig

Figure G.8: Guide tube during the second and third cutting profile programs

The cutting jig was then adjusted, so that the tube was rotated through 15.5 degrees to cut the final program. This was a simple procedure and only required four screws to be adjusted to complete the rotation. This jig has been excellent, and I am very glad I kept it after it was used in the manufacture of the 3rd test rig.



(a) Cutting jig after all three programs had been run



(b) Close up of the two sensor mounting profiles

Figure G.9: Guide tube after the second and third cutting profile programs

Once the machining was completed the jig was removed from the CNC machine and the tube was extracted from the jig. The tube went through a cold wash with soap to

remove any remaining cutting coolant and swarf from the manufacturing process and was then dried with soft paper towels to avoid scratching the surface of the tube.



(a) Side view of the guide tube



(b) The sensor mounting profiles cut into the surface

Figure G.10: The guide tube after machining and washing to remove coolant and swarf. All that remains to do on the tube before it is finished is to fine tune the sharp edges that are left after the CNC cutting, and give the tube a final polish before mounting the sensors and components onto it.

The next step in the manufacturing process is to produce the magnet holders. These are machined from Delrin rod and fit inside the guide tube. The first step is to face off the Delrin rod and bore out a hole for the magnet to be housed in.



(a) Delrin rod held in chuck ready for facing and cutting



(b) Cutting the magnet holder into the end of the Delrin rod

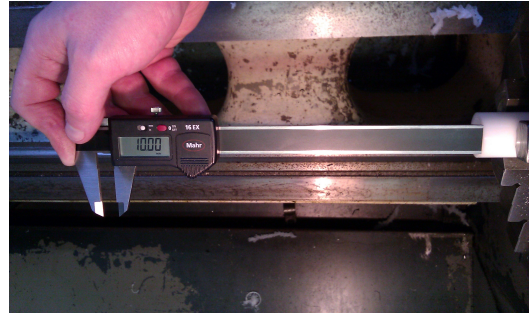
Figure G.11: Manufacturing one of the TR4 magnet holders from Delrin

Once the magnet holder is cut the dimensions need to be checked using a digital caliper, to insure that they match the tolerances in the TR4 design. The design called

for a friction fit around the magnet, as such the readings expected from measurements were 20mm diameter and 10mm depth.



(a) Checking the diameter of the magnet holder



(b) Checking the depth of the magnet holder

Figure G.12: Measurement to insure the magnet holder matches design tolerances

The magnet was also glued in place to stop it falling out if bumped, as such a hole behind the magnet holder was drilled to act as a reservoir for excess glue that may have been applied, to insure the magnet sits flush inside its holder.



(a) Cleaning the Delrin rod to give a shiny low friction surface



(b) Surface of the Delrin rod after cleaning and polishing

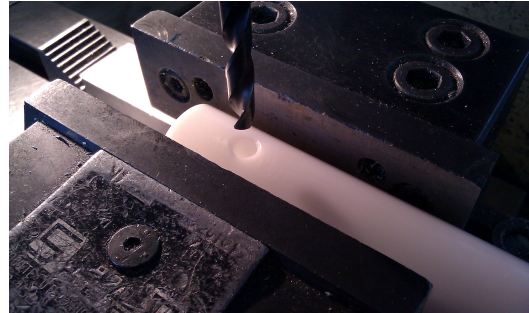
Figure G.13: The cleaner the surface of the Delrin, the lower the friction

The magnet holders need to run as freely as possible against the acrylic guide tube, one of the reasons Delrin was chosen, so the magnet holder was polished using a very fine grit wet-and-dry paper, followed by a polishing compound on a soft rag. The result of this polishing was a very shiny and low friction surface. Once the magnet holders were polished, they were checked to see if they matched the expected dimensions using a caliper. Once confirmed, a miniature milling machine was used to bore the mounting

holes into the magnet holders. The mini milling machine was numerically controlled, rather than controlled by a computer, which gave cutting accuracy of $\pm 0.01\text{mm}$.



(a) The numerically controlled mini milling machine



(b) Hole to locate the magnet holder within the guide tube

Figure G.14: Location hole positioned through the magnet holder

The magnet holder was held firmly in the machine's chuck and the mounting hole was drilled through the holder. The fixed magnet holder had two additional locating holes drilled so that the fixed magnet could be moved depending on the experiment performed. Once the mounting holes were drilled through the magnet holder, it was checked to see how well it fitted inside the guide tube, as any misalignment would cause friction between the magnet holder and the guide tube. The holder was also tested to its mechanical limit to check that the dimensions were correct.

The parts that make up TR4 are shown, including the two magnet holders, the guide tube, four brass washers, two brass bolts, two brass nuts, a nylon threaded rod and two nylon nuts and two magnets (one magnet is already inside one of the magnet holders). The brass nuts and bolts were used as they are non magnetic and it was not possible to source nylon bolts and nuts in this size.

The next step was to mount the magnet inside the magnet holders using a blob of epoxy resin glue. The magnets non-exposed faces were coated in the epoxy glue and additional glue was applied to the inside faces of the magnet holder. The magnet was



(a) Magnet holder inside the guide tube



(b) Magnet holder at mechanical limit with guide tube

Figure G.15: Magnet holder located within the guide tube



(a) Finished plastic parts



(b) Components to assemble TR4

Figure G.16: Component parts of TR4

then inserted into the holder and clamped in place for three hours until the epoxy had hardened. Once hardened the magnet holders were mounted inside the guide tube, such that the mass of the guide tube was supported by the magnet in the free moving magnet holder.



(a) Magnet holder with an ID54 magnet inside



(b) TR4 supported by the free moving magnet holder

Figure G.17: TR4 magnet holder with magnet and side view of guide tube with both magnet holders mounted

The guide tube finally had the sensors super glued into the sensor profiles cut into the side of the tube and then the TR4 data capture PCB was attached and soldered into place.

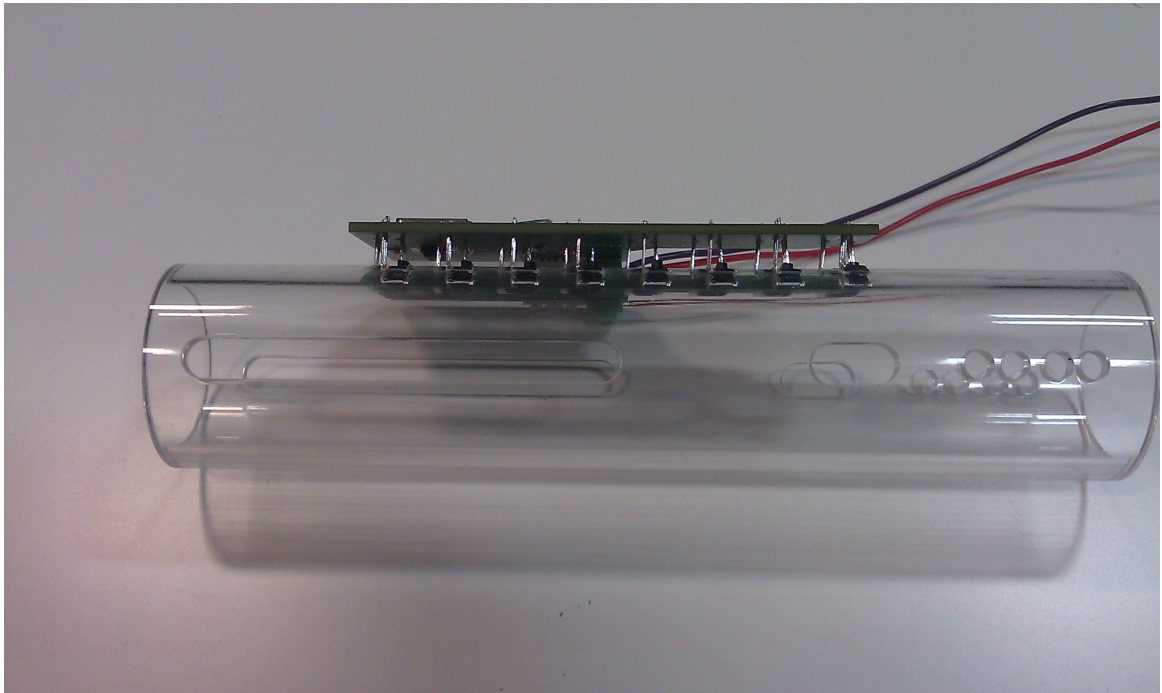


Figure G.18: TR4 with sensors mounted on the guide tube

Appendix H

TR4 Circuit and PCB

This appendix shows the final circuit design, created using EagleCAD, of TR4.

The TR4 schematic, figure H.1, includes a microprocessor, a bluetooth communications module and the hall effect sensor array, along with the supporting passive components required for device operation. The bill of materials, table H.1, details all the parts required to build the TR4 PCB.

The final TR4 PCB design created with EagleCAD, figures H.2 & H.3, are shown with and without ground planes for clarity, with the final manufactured PCB shown in figure H.4.

The total cost of components for two PCB's to be manufactured came to £119.99 inc. VAT, with the PCB manufacture of two board totaling to £102.59 inc. VAT, giving a total cost for the two TR4 sensing and data capture PCB's of £222.58.

Part ID	Device Details	Value
C1	Capacitor Size 0603	100nF
C2	Capacitor Size 0603	10uF
C3	Capacitor Size 0603	10uF
C4	Capacitor Size 0603	100nF
C5	Capacitor Size 0603	100nF
C6	Capacitor Size 0603	100nF
C7	Capacitor Size 0603	100nF
C8	Capacitor Size 0603	100nF
IC1	Power Regulator	LD117AS33TR
J1	Power Connector	2 Pins
R1	Resistor Size 0603	10k
R2	Resistor Size 0603	470R
R3	Resistor Size 0603	22K
U1	Microprocessor	PIC18F87K22
U2	Hall Sensor Array	SS49E
X1	ICD2 Programming Header	5 Pins

Table H.1: Bill of materials for TR4 PCB

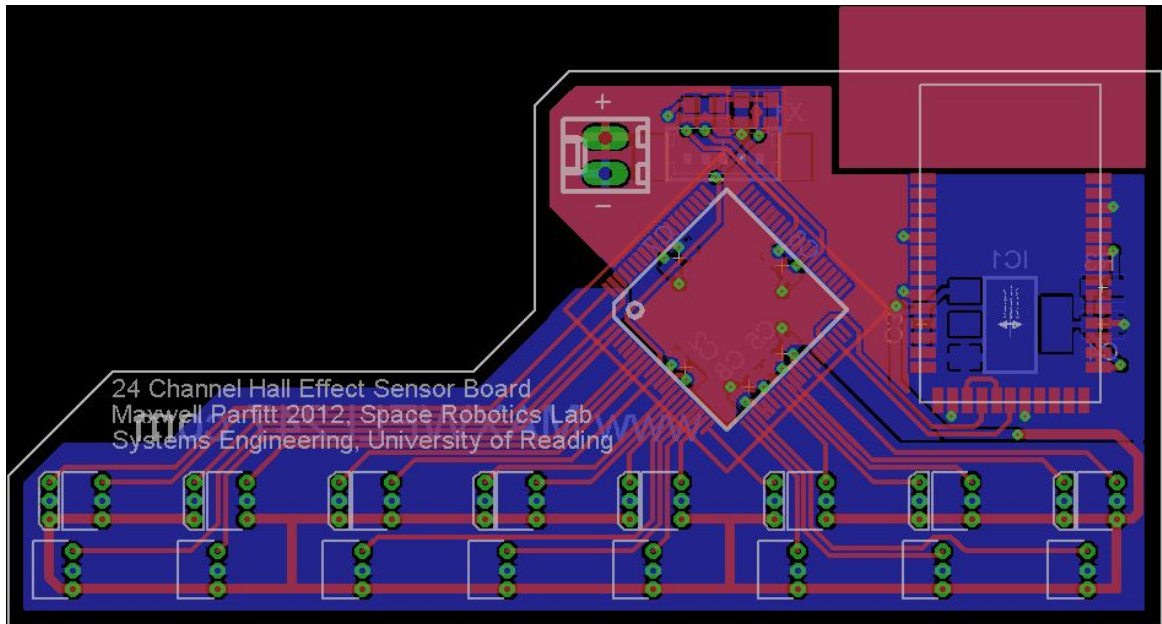


Figure H.2: TR4 PCB with ground planes (Top Layer, Red, Bottom Layer, Blue)

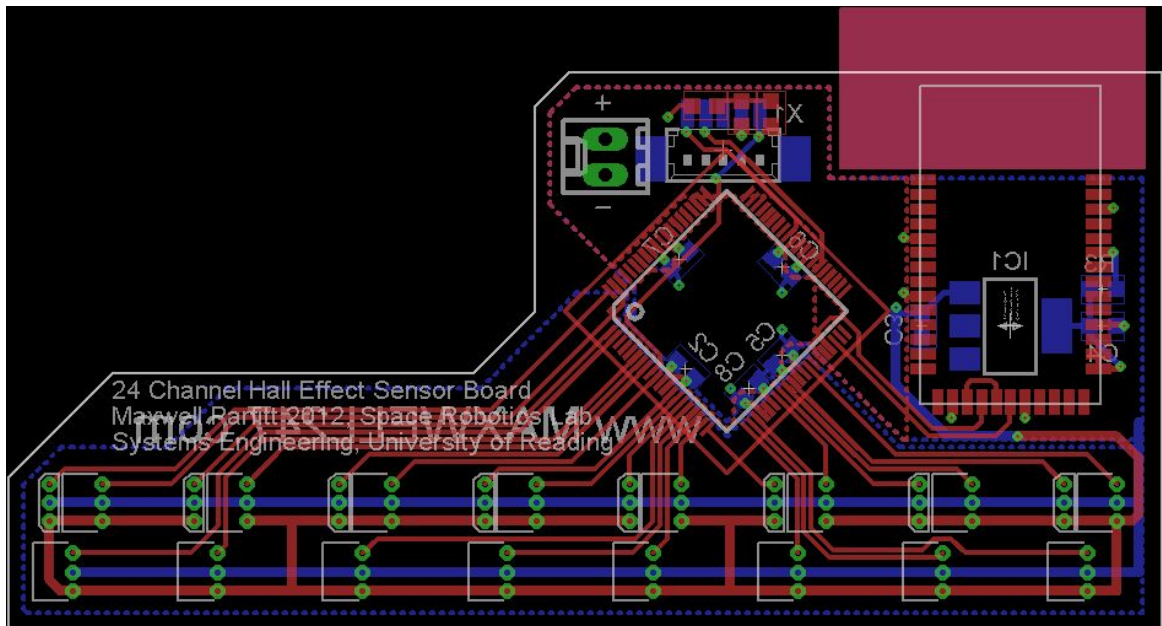


Figure H.3: TR4 PCB with no ground planes (Top Layer, Red, Bottom Layer, Blue)

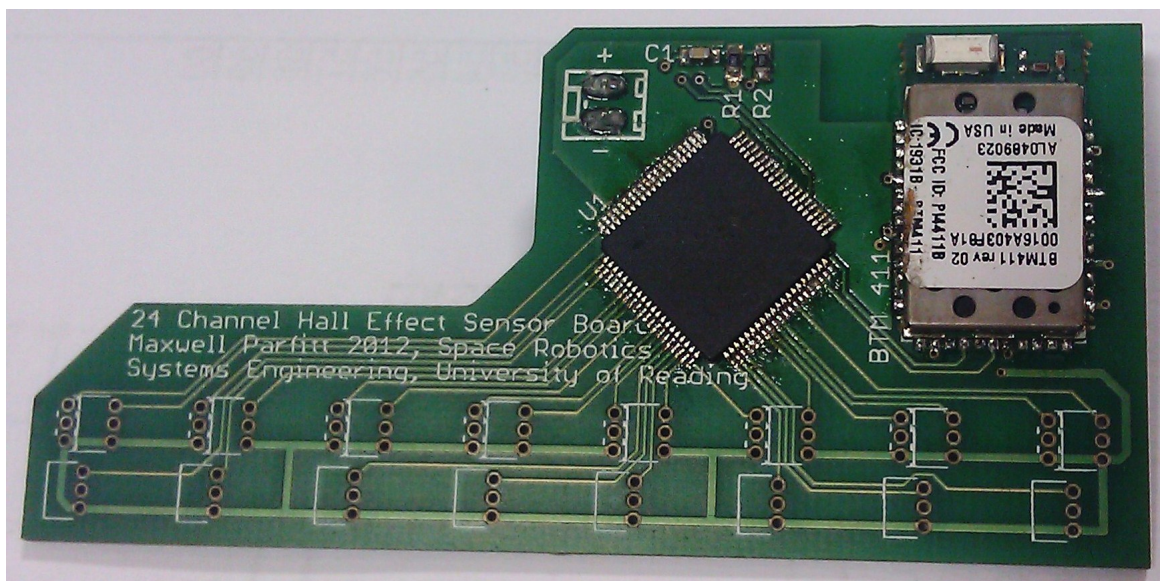


Figure H.4: TR4 PCB after population with components

Appendix I

Published paper from ASTRA 2011
conference proceedings

MAGNETIC COMPLIANT SUSPENSION CONCEPT FOR SPACE ROBOTICS

Maxwell Parfitt, Gerard McKee

School of Systems Engineering, University of Reading, Reading, Berkshire, RG6 6AY, UK
m.r.parfitt@reading.ac.uk, g.t.mckee@reading.ac.uk

Abstract – This paper proposes a Dual-Magnet Magnetic Compliance Unit (DMCU) for use in medium sized space rover platforms to enhance terrain handling capabilities and speed of traversal. An explanation of magnetic compliance and how it can be applied to space robotics is shown, along with an initial mathematical model for this system. A design for the DMCU is proposed along with a 4-wheeled DMCU Testing Rig.

Index Terms – Magnetostatics, Robot Motion, Space exploration, Space vehicles

1. INTRODUCTION

Robotics systems are a very important part of space exploration. There is currently much interest in enhancing the versatility of space robotic rovers. Current rover configurations have limitations due to the forces generated when impacting objects whilst traversing unstructured terrain. These limitations are necessary to maintain system stability and increase the chassis/rovers life-span by reducing mechanical vibrations which transfer to the equipment contained within the rover. Therefore the rovers speed is limited to reduce the magnitude of forces that occur during these impacts. Unstructured terrain also limits the maximum distance a robot can travel autonomously as the chassis design and capabilities restrict the path that the rover can navigate. If the rover could increase speed whilst maintaining stability over more complex terrain then the maximum distance that the rover could traverse could be greatly increased

Current robotics systems have used a number of approaches to incorporate compliance, such as material choices, traditional spring based suspension and active suspension. The Mars Exploration Rover (MER) [1], for example used mainly Titanium due to its strength to weight ratio, but also its ability to flex thus reducing some of the impact stresses generated during the rovers operation. The NASA Athlete [2], on the other hand, is able to actuate all of its legs so terrains that would normally be impassable to wheeled robots can be walked over by reconfiguring the robots chassis.

This paper proposes that certain limitations can be improved with the application of magnetic compliance to the chassis design. Magnetic compliance exploits the non-linear repulsive forces between opposing magnetic poles to create a compliant suspension system. The design, development and initial evaluation of a

prototype dual-magnet magnetic compliance unit is presented and this paper describes a mathematical model for the compliance unit and compares the model with practical experimental data. The paper also discusses the development of the compliance unit, which required careful consideration of material properties with respects to magnetic fields and parasitic losses. For example if the chassis was made of Aluminium then the proximity of the magnetic compliance unit would generate Eddy (Foucault) Currents, thus introducing a damping effect within the compliance.

Paper Outline: Section 2 reviews a range of current rover systems and some of the limitations that they are subject to. Section 3 discusses the terrain handling requirements of space robotic rovers. Section 4 introduces magnetic compliance with initial mathematical models and testing. Section 5 describes the design of a prototype dual magnet compliance unit based on the results presented in Section 4 and a test rig that is currently under development to support further research.

2. SPACE EXPLORATION ROVERS

There have been many different rover systems used over the last 30 years for planetary surface exploration with the most successful to date being the MER platform [1]. The MER design was based on the Sojourner Rover [3] after very successful operation on the surface of Mars. The MER addressed some problems that were experienced with the Mars Pathfinder mission [4] which included the wheel design for soft surface traversal and lower nominal ground pressure, as well as the ability to communicate directly back to Earth rather than via a relay on the Descent Lander. The ExoMars Rover [5] currently being developed by the European Space Agency (ESA) will be fitted with more sophisticated object avoidance technology which should improve the robots surface traversal capabilities. A wide range of issues must be addressed, therefore, to enhance the capability of space robotic rovers. The following subsections consider rover limitations, environmental factors and communication constraints.

2.1. Rover Limitations

Rover systems on Mars all have to adapt to difficult terrain, which is why extensive testing is performed on

Earth [6] before a rover is put into service. The most successful chassis designs used in planetary exploration rovers are based on the rocker-bogie [7] design, as this keeps all wheels passively in contact with the surface whilst distributing load evenly. The rocker-bogie allows the rovers wheels to traverse objects larger than their diameter, so that normally impassable terrain to wheeled robots can be driven over without the need for constant course adjustments which consumes a lot of power.

The rocker-bogie system uses solid linkages, without compliance built into them, which means that the rovers speed needs to be limited to maintain stability over obstacles and not subject the rover to excessive forces or vibrations that occur when a wheel impacts an object. If these limitations were not in place the rover would suffer damage, such as torsional stress to the leg supports or excessive vibrations whilst moving over larger rocks and uneven terrain.

When navigating autonomously a rover has to choose its path based on observations of the terrain as well as computation to confirm that it can safely traverse an obstacle. This takes time and often requires an operator on Earth to decide if the risk involved with the rovers current path is acceptable to the mission. If the rovers navigation system can see a clear and relatively smooth path ahead of the rover then it will travel as fast as it can to its next predefined coordinate, but with the limitations to the rovers speed to reduce vibrations this top speed is often not more than $10\text{cm}\cdot\text{s}^{-1}$ ($0.1\text{m}\cdot\text{s}^{-1}$) which greatly limits the distance that the rover can travel in a communications window with Earth. For example the MER is capable [8] under no load of a speed of $4.6\text{cm}\cdot\text{s}^{-1}$ ($0.046\text{m}\cdot\text{s}^{-1}$) and at full load a top speed of $2.6\text{cm}\cdot\text{s}^{-1}$ ($0.026\text{m}\cdot\text{s}^{-1}$).

2.2. Environment Factors

Surface composition can vary greatly depending on planet and even the location that a rover lands. Surfaces can range from deep drifts of loose dust [9] to huge boulder fields [10] which makes wheel design on the rover critical to mission success. The nominal ground pressure (NGP) is a calculation [11] that can help choose wheel parameters for a mission to limit wheel sinkage and resistance to motion. The calculation takes into account the number of wheels a robot has, the wheel width and radius as well as the robots weight. A low NGP will help the rover to traverse soft or loose surfaces, but the rover will also need to have enough traction whilst on the surface otherwise the robots motion will be very inefficient. The traction required to move the robot also affects the amount of torque that the drive train in the rover would need to generate, as the rover still has to be able to move in the event of drive failure in one or two of its wheels.

2.3. Communication Constraints

Communications lag is an important factor in how autonomous a rover has to be, as sending commands to Mars for example can take up to 20 minutes (depending on orbits around the sun), which would be 40 minutes round trip time for the operator on Earth to get updated position telemetry. This lag drastically reduces the amount of time for a decision to be made as to the rover's next move, because connections to Mars are made during a communications window which varies in length due to relative orbits. These windows can happen very far apart if Mars is orbiting the other side of the sun to Earth, as the sun blocks all communications with Mars.

3. TERRAIN HANDLING REQUIREMENTS

3.1. Drive Torques and Impact Forces

The drive train of space rovers needs to produce enough torque to not only move the rover but also lift it over obstacles and drive up slopes. If the rover is driving on a slope then it will be subject to the gravity of the planet that it is on which is rarely the same as the gravity on earth, for example the gravity on Mars [12] is roughly 38% of Earth's, meaning that 100kg on Earth would be roughly 38kg on Mars. This would make a rover tested on Earth much more capable on Mars as it would require less power to traverse objects and terrain. For example Eq. 1 shows the torque required (τ) for a 250mm diameter wheel (0.25m) to move a mass of 30kg up a 20° (θ) slope under normal Earth gravity ($9.81\text{m}\cdot\text{s}^{-2}$), with Eq. 2 showing the same situation but under Martian gravity ($3.72\text{m}\cdot\text{s}^{-2}$).

$$\tau = (0.25 \times 9.81 \times 30) \sin \theta = 25.1Nm \quad (1)$$

$$\tau = (0.25 \times 3.72 \times 30) \sin \theta = 9.54Nm \quad (2)$$

The above comparison shows that a motor in the drive train might be strained during testing on Earth but would be much more capable on the surface of Mars.

Even though these forces are reduced when operating on Mars the rover will still have to cope with impacts when its wheels climb over obstacles, which can create short, high magnitude vibrations that travel through the chassis and can damage the internal circuitry. Using the same values as before, the impulse force can be calculated Eq. 3 assuming that the wheel impacting a rock creates a step input and that the rover comes to a complete stop (v_1) in 0.5s (Δt), with an initial speed (v_0) of $0.046\text{m}\cdot\text{s}^{-1}$.

$$F = \frac{mv_1 - mv_0}{\Delta t} = \frac{30 \times (0 - 30) \times 0.046}{0.5} \quad (3)$$

$$= -2.76\text{kg} \cdot \text{ms}^{-1}$$

This force is negative because the impulse force is acting in opposition to the forward motion of the rover. The key to creating a durable chassis and reducing vibrations transferred to the rover is to reduce the magnitude of impulse forces that the rover is subject to.

3.2. Wheel Traction on Difficult Terrain

When driving over soft surfaces such as sand, not only does a rover require enough traction to move, but it needs a large enough surface area in contact with the ground to stop it from sinking into the surface and burying its wheels. To overcome this rovers need a low NGP with large diameter tyres to spread its weight. To help increase wheel traction on terrain such as soft sand or loose dust, rover designs have incorporated spikes into the surface of their wheels to allow them to claw their way over obstacles. For example, the MER rovers included paddles [13] around the wheels to help drag the rover over the soft sand. Wheels can incorporate compliance to aid traction; for example letting some air pressure out of a pneumatic tyre will increase the tyre's grip on a road car, but in space rovers pneumatic tyres are not practical. Instead the MER wheels were made from aluminium and had spiral shaped spokes linking the drive train on the wheels hub to the wheels rim. This spiral linkage could flex slightly allowing the rover to maintain pressure on the ground and deform slightly under impact conditions to reduce the impulse forces transferred to the rover's chassis if it was to drop off a rock (Fig. 1).



Figure 1. Spiral spokes that provide contact compliance in the MER Platform. (Courtesy NASA/JPL-Caltech)

3.3. Suspension in Current Rovers

Classical suspension systems which incorporate springs and dampers are widely used in road vehicles, but rarely in space robotics which normally favour solid linkage type suspensions such as the rocker-bogie which is used in the MER, Sojourner and ExoMars. Robots like the

NASA Athlete and the MTR [14] use active suspension, where all the links in the chassis can be independently controlled and positioned. This gives the rover the ability to adapt its shape to the environment or obstacle that it is traversing. Active suspension requires more power compared to the rocker-bogie type, but it does allow the robot to traverse more challenging terrain. The NASA Athlete is able to lock its wheels and use them as feet that can be lifted individually allowing the robot to walk, which is very useful in boulder fields where wheels alone could get stuck. There has been some work done to incorporate magnetic compliance into legged robotics [15] which reduced the power required whilst the robot was moving, but this approach has yet to be applied to wheeled robots.

4. MAGNETIC COMPLIANCE

Magnetic compliance exploits the non-linear repulsive forces between two magnets which have been placed in opposition - opposing magnetic poles facing each other - to offer a novel suspension mechanism for robots [15]. We propose that this suspension mechanism can be applied to a space robotic rover to decouple it from the surface it is traversing, so that impacts do not damage the system.

This paper proposes using a number of magnetic compliance units on the wheel supports in a rover so that vibrations and displacements are handled as close to the ground as possible, although it would also be possible to mount a small compliance unit near the warm electronics box to add further isolation for the internal control circuitry.

4.1. Mathematical Model

Eq. 4 was used to simulate the initial magnet model (Fig. 2). This took into account variables including the magnets dimensions, field strengths and separation between magnet faces.

$$F = \frac{\pi\mu_0}{4} M^2 R^4 \left[\frac{1}{x^2} + \frac{1}{(x+2t)^2} - \frac{2}{(x+t)^2} \right] \quad (4)$$

μ_0 is the permeability of the intervening medium, in this case free space, R is the radius of the magnets in question. M is defined in Eq. 5 as the magnetic flux density B_0 divided by the permeability of the intervening medium μ_0 which is the same as before. The thickness of the magnets t is also required, as is the distance between their respective magnetic faces x . The resulting force F is measured in Newtons and is observed as the result of the variables and the interactions between them.

$$M = \frac{B_0}{\mu_0} \quad (5)$$

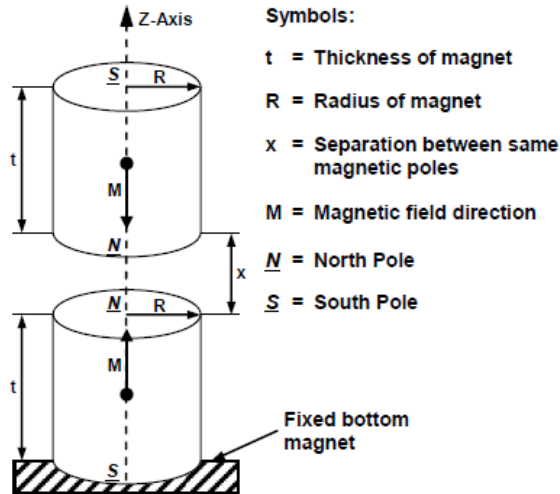


Figure 2. Two concentric cylindrical permanent magnets held so that the bottom magnet is fixed and the top magnet can only move in the z-axis.

4.2. Static Load Testing

Static load testing was carried out using a digital load cell (Fig. 3) made from steel. All ferrous metals will affect magnetic fields, but non-ferrous metals can also create disturbances to magnetic fields. This is due to an effect called Foucault Currents, which are present when passing a magnet past certain metals. For the static load testing a mixture of Delrin and mahogany was used to house the magnets, which de-coupled the magnets from the steel of the load cell.

To test the N42 Grade Neodymium Magnets a range of diameters, thicknesses and strengths were tested, with the final 10 magnets (Tab. 1) being mounted into the load cell for compression testing.



Figure 3. The testing rig, showing two magnets in the middle of a test sequence contained within the mahogany supports which de-couple the magnets from the steel frame of the load cell.

Table 1. Magnets tested in the load cell (Fig.3)

Magnet ID	17	19	20	21	23
Radius (mm)	2.5	2.5	2.5	2.5	3
Thickness (mm)	1	5	10	20	1
Magnitude (Tesla)	0.20	0.59	0.46	0.66	0.20
Magnet ID	33	34	43	44	54
Radius (mm)	4	4	5	5	10
Thickness (mm)	8	30	5	10	10
Magnitude (Tesla)	0.56	0.66	0.51	0.52	0.46

These magnets were compressed together giving a range of force measurements at varying distances between the magnets. These were then plotted against the theoretical data generated by Eq. 4. These plots are shown in Fig. 4 for one of the magnets, ID54.

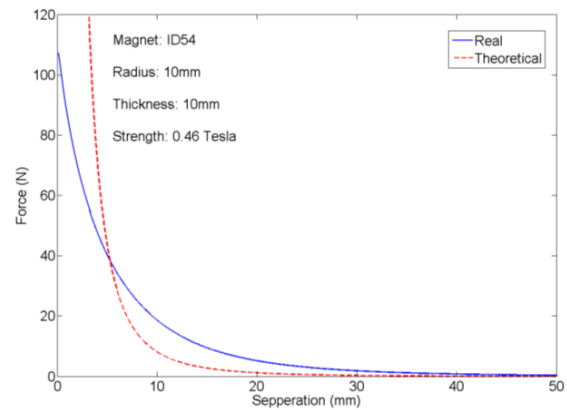


Figure 4. Graph showing the separation (mm) between the two ID54 magnets against the repulsive Force measured in Newtons (N).

The real world magnets whilst having a similar response to the theoretical did not achieve the same maximum force and deviated from the expected results. This is due to the N42 Grade Neodymium not being 'perfect'. In reality the magnetic material has imperfections and the opposing magnets will tend to de-magnetise each other.

The practical experiments show that the mathematical model requires further development, especially when the distance between the magnetic faces is less than the thickness of the magnets. This is being investigated as part of further research. Eq. 6 is a modification of Eq. 4 to express this observation.

$$F = \frac{\pi\mu_0}{4} M^2 R^4 \left[\frac{1}{x^2} + \frac{1}{(x+2t)^2} - \frac{2}{(x+t)^2} \right] \quad (6)$$

$\xrightarrow{\text{approx}}$ when $x > t$

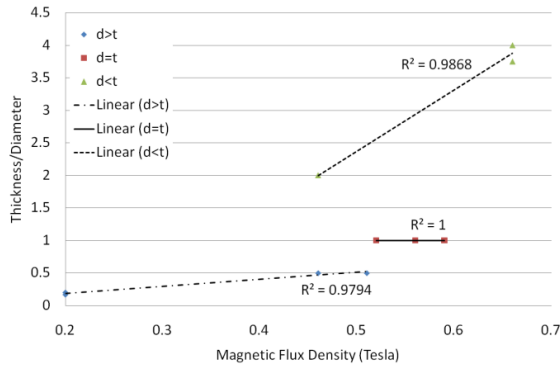


Figure 5. Analysis of the crossing points between the real and theoretical data from all the magnets. Plot Thickness/Diameter against Magnetic Flux Density.

Analysis of crossing points between the theoretical and real world data, when plotted against magnetic flux density, for all magnets (Fig. 5) shows a strong correlation of results between magnets that have proportional dimensions. The trend lines generated show how closely they fit the data and are assigned to magnets with similar proportions.

5. PROTOTYPE DUAL-MAGNET COMPLIANCE UNIT

5.1. Design and Development of the DMCU

The design of the prototype Dual-Magnet Magnetic Compliance Unit (referred to as the DMCU from here on) was based on the initial magnet testing and included two of the ID54 N42 Neodymium magnets. The choice to use these specifications of magnets was so that at a resting state the magnets had a separation of 50mm and could take a maximum of 10kg load at full compression. This would allow a robot with 4 of the compliance units to support a 10kg payload whilst keeping a 4 times safety factor in case of a large impact.



Figure 6. The prototype Dual-Magnet Magnetic Compliance Unit (DMCU). The bottom magnet is visible and the DMCU is held together with brass locating nuts, which will be replaced with nylon bolts in the final implementation of the suspension.

To avoid disturbances to the magnetic field, clear acrylic plastic was used in conjunction with Delrin, as these materials satisfied all the design constraints whilst not affecting the magnetic field.

The clear acrylic plastic also enabled real time video analysis of the system as the Delrin magnet holders could be clearly seen through the casing. The magnets were mounted inside the end of a Delrin rod (Fig. 6), which runs inside the acrylic tubing.

Delrin was chosen as it has a low friction coefficient when used in conjunction with acrylic and is simple to form into usable shapes. The DMCU locks the motion of the Delrin runner to the z-axis only, for simple modelling as well as keeping the operation of the device as accurate as possible. The acrylic tube had a locating slot milled into the sides which stopped the suspension from twisting during operation, so that when wheels are mounted to the bottom they do not rotate around the z-axis.

5.2. DMCU Robot Test Rig

A simple 4-wheeled test rig which incorporates 4 compliance units was also designed to use 4 of the DMCU modules (Fig. 7). The test rig allows each leg to be adjusted so that the angle of attack can be locked between $\pm 45^\circ$ from vertical, as it is rare to have the wheels mounted directly below the chassis, whilst measuring response to terrain profiles.



Figure 7. The DMCU Robot Test Rig with 4 of the DMCU modules attached.

This testing rig is currently being upgraded with accurate electronic sensing equipment so that more detailed analysis of system response can be performed as well as instrumented wheels for feedback of motion as the rover is run over a set of predefined testing environments. The final upgraded test rig will replace the brass locating nuts and the tilting axle with nylon bolts so that the magnetic fields are not affected during testing. Once the upgrades to the DMCU Robot Test Rig are complete, a range of tests will be performed.

These will range from simple drop tests, to see how the system would respond to a simulated planetary landing to driving over pre-defined terrain profiles, which would test how accurate the system model is compared to the real world responses. The electronics that are currently being integrated into the DMCU Robot Test Rig will enable real-time monitoring and recording of the robots motion with respects to the start position, using sensor fusion between a 3axis accelerometer and a 3 axis gyroscope which can be polled at 1kHz and above. This will enable a range of testing data to be analysed and will give a benchmark for further experimentation as well as giving real-time feedback to a visual display. These experiments will provide data which when analysed will aid in the future expansion and development of the DMCU principles for application to space rover suspension systems, specifically the Rocker-Bogie which was described in Section 2.

6. CONCLUSION

The speed a rover can traverse difficult terrain is currently an important research area. In this paper we have considered a number of issues which are concerned with speed of traversal. The paper proposes an approach to rover suspension based on magnetic compliance. The modelling, design and development of a Dual-Magnet Magnetic Compliance Unit (DMCU) was described. Further research will investigate enhancements to the mathematical models and will experimentally evaluate the DMCU using a novel test rig that is under development. Our conclusion, based on our initial observations of the DMCU Robot Test Rig is that magnetic compliance can indeed enhance the versatility of space robotic rovers.

7. REFERENCES

1. J. Krajewski, et al., *MER: From Landing to Six Wheels on Mars...Twice*. IEEE International Conference on Systems, Man & Cybernetics, 2005.
2. B. Wilcox, *ATHLETE: A Cargo and Habitat Transporter for the Moon*. Aerospace conference, 2009 IEEE, 2009.
3. H. W. Stone, *Mars Pathfinder Microrover: A Small, Low-Cost, Low-Power Spacecraft*. JPL TRS 1992+, 1996.
4. R. Volpe, *Navigation Results from Desert Field Tests of the Rocky 7 Mars Rover Prototype*. The International Journal of Robotics Research, Vol.18, No. 7, 1999: p. 669-683.
5. M. V. Winnendaal, P. Baglioni, and J. Vago, *Development of the ESA ExoMars Rover*. Proc. of 'The 8th International Symposium on Artificial Intelligence, Robotics and Automation in Space', 2005.
6. E. Tunstel, et al., *Fido Rover Field Trials as Rehearsal for the NASA 2003 Mars Exploration Rovers Mission*. Automation Congress, Proceedings of the 5th Biannual World 2002: p. 320-327.
7. Bickler, D., 1989 - *United States Patent 4840394*. 1989.
8. A. Randel, et al., *Mars Exploration Rover Mobility Development*. IEEE Robotics & Automation Magazine, 2006.
9. L. Taylor, et al., *The Lunar Dust Problem: From Liability to Asset*. 1st Space Exploration Conference: Continuing the Voyage of Discovery, 2005.
10. R. Schroeder and M. Golombek, *Mars Exploration Rover Landing Site Boulder Fields*. Lunar and Planetary Science XXXIV, 2003.
11. A. Ellery, *An Introduction to Space Robotics* 2008: pp. 32, Springer. 32.
12. F. Cain. *Gravity on Mars*. [cited 2011; Available from: <http://universetoday.com>].
13. D. Akin (2009)) *Case Study: Mars Rovers*. Principles of Space Systems Design, pp. 16.
14. Mechatronics, Z.O. *Multi-Tasking Rover*. Available from: www.01mech.com.
15. R. McElligott and G. McKee, *Magnetic Compliance in Legged Robots*. Proceedings of the 9th International Conference on Climbing and Walking Robots (CLAWAR), 2006: p. 104-108.

Figure 1. Courtesy of NASA/JPL-Caltech, Image URL: http://marsrover.nasa.gov/gallery/spacecraft/images/mer2002_1106_b231.jpg

Appendix J

Published poster presentation from
ASTRA 2011 conference

Magnetic Compliant Suspension Concept for Space Robotics

Maxwell Parfitt¹ | Gerard McKee²

Novel approach to suspension systems for a medium sized rover

This paper proposes a Dual-Magnet Magnetic Compliance Unit (DMCU) for use in medium sized space rover platforms to enhance terrain handling capabilities and speed of traversal. An explanation of magnetic compliance and how it can be applied to space robotics is shown, along with an initial mathematical model for this system. A design for the DMCU is proposed including a 4-legged DMCU Testing Rig.

Magnetic Compliance

Magnetic compliance exploits the non-linear repulsive forces between two magnets which have been placed in opposition – opposing magnetic poles facing each other – to offer a novel suspension mechanism for robots [1]. We propose that this suspension mechanism can be applied to a space robotic rover to decouple it from the surface that it is traversing, so that impacts experienced do not damage the system.

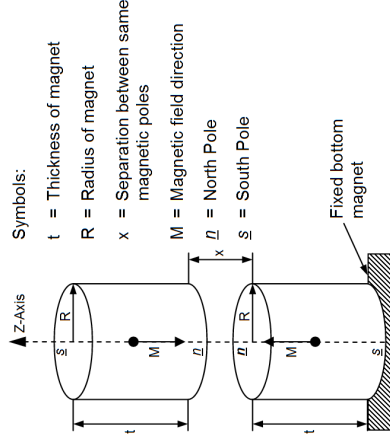


Figure 1: The compliance model showing variables

Figure 1 shows the experimental setup for the DMCU using two cylindrical magnets. All magnets used in our experiments are constructed from N42 Grade Neodymium which is considered an extremely hard magnetic material.

This consideration does not take into account de-magnetisation forces which the magnets exert on each other when compressed together. The motion of the magnets is constrained to the Z-Axis.

DMCU Mathematical Model

The equation below was used to model the DMCU shown in the previous figure. This model was used to determine the resting state of the DMCU when under no load, which was then used in the physical design of the DMCU.

$$F = \frac{\mu_0 \mu_r M^2 R^4}{4} \left[\frac{1}{x^2} + \frac{1}{(x+2t)^2} - \frac{2}{(x+t)^2} \right]$$

The equation uses the same variables as the figure in the previous column, with M defined as the magnetic flux density divided by the permeability of the intervening medium μ_0 , in this case free space.

This model considers that the magnets are 'perfect' and very magnetically hard, but in reality the magnets have imperfections, allowing de-magnetisation forces to affect the magnetic field strength. This effect can be clearly seen on the graph below.

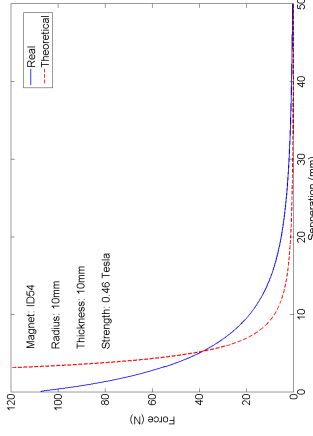


Figure 2: Theoretical and Real-World Results

This data was recorded by recreating the system model in a load cell which could perform static load testing. This system allowed the testing of many different magnets, which lead to a revision of the equation above. This revision of the equation states that the model is approximately true when the separation between the magnets is greater than the thickness of the magnets (when $x > t$).

Prototype Dual-Magnet Compliance Unit

The prototype design uses two N42 Grade Neodymium magnets with a radius and thickness of 10mm. These magnets were chosen as they had a resting separation of 50mm whilst still being able to support a maximum load of 10kg. The materials used for construction of the DMCU are clear acrylic plastic and Delrin, as these materials satisfied all the design constraints whilst not affecting the magnetic fields of the two magnets housed within the DMCU. The prototype DMCU is shown in Figure 3.



Figure 3: Prototype DMCU assembled

DMCU Robot Test Rig

A simple 4-wheeled test rig incorporating 4 compliance units was also designed to use 4 of the DMCU modules. The test rig allows each leg to be adjusted so that the angle of attack is locked between $\pm 45^\circ$ from vertical and is made from the same materials as the DMCU. Figure 4 shows the test rig including 4 DMCU modules, without the wheels mounted. This test rig will be used for future testing, and is currently having the measurement electronics installed. These measurement devices will help evaluate the model.



Figure 4: DMCU Robot Test Rig with 4 DMCU modules

Conclusions

The speed a rover can traverse difficult terrain is currently an important research area.

Our initial observation is that magnetic compliance can enhance the versatility of space robotic rovers.

Further research will investigate enhancements to the mathematical model and will experimentally evaluate the DMCU.

References

- [1] R. McElligott and G. McKee, "Magnetic Compliance in Legged Robots", Proceedings of the 9th International Conference on Climbing and Walking Robots (CLAWAR), pp. 104-108, 2006

Contact information

1. m.r.parfitt@reading.ac.uk Space Robotics Lab, School of Systems Engineering, University of Reading, Whiteknights, RG6 6AY, UK
 2. g.t.mckee@reading.ac.uk Computer Science, School of Systems Engineering, University of Reading, Whiteknights, RG6 6AY, UK
- www.reading.ac.uk/sse - www.arl.reading.ac.uk